REFERENCE COPY

CONFIDENTIAL
UNCLASSIFIED

NATIONAL AERONAUTICS AND SPACE ADMINISTRATION

Space Programs Summary No. 37-36, Volume I

for the period September 1, 1965 to October 31, 1965

The Lunar Program

(Title Unclassified)

Classification Changed to UNCLASSIFIED
JPL Letter on Authority NASA-Langley
dtd Nov. 4, 1970, Signed by W. E. Hanson
Date: Jan. 4, 1971 By: A. Castain

JET PROPULSION LABORATORY
LIBRARY
JAN 1 1966

151
Copy No.

CALIFORNIA INSTITUTE OF TECHNOLOGY

JET PROPULSION LABORATORY
CALIFORNIA INSTITUTE OF TECHNOLOGY
PASADENA, CALIFORNIA

November 30, 1965

LAB-C00044

CONFIDENTIAL
GROUP 4 Downgraded at 3 year intervals; 12 years.

UNCLASSIFIED

141896

Preface

The *Space Programs Summary* is a six-volume, bimonthly publication that documents the current project activities and supporting research and advanced development efforts conducted or managed by JPL for the NASA space exploration programs. The titles of all volumes of the *Space Programs Summary* are:

Vol. I. The Lunar Program (Confidential)

Vol. II. The Planetary–Interplanetary Program (Confidential)

Vol. III. The Deep Space Network (Unclassified)

Vol. IV. Supporting Research and Advanced Development (Unclassified)

Vol. V. Supporting Research and Advanced Development (Confidential)

Vol. VI. Space Exploration Programs and Space Sciences (Unclassified)

The *Space Programs Summary*, Vol. VI consists of an unclassified digest of appropriate material from Vols. I, II, and III; an original presentation of technical supporting activities, including engineering development of environmental-test facilities, and quality assurance and reliability; and a reprint of the space science instrumentation studies of Vols. I and II.

W. H. Pickering

W. H. Pickering, *Director*
Jet Propulsion Laboratory

Space Programs Summary No. 37-36, Volume I

Copyright © 1965, Jet Propulsion Laboratory, California Institute of Technology

Prepared under Contract No. NAS 7-100, National Aeronautics & Space Administration

This document contains information affecting the national defense of the United States, within the meaning of the Espionage Laws, Title 18, U.S.C., Sections 793 and 794, the transmission or revelation of which in any manner to an unauthorized person is prohibited by law.

UNCLASSIFIED

Contents

I. *Surveyor* Project 1

A. Introduction 1
B. System Engineering 2
C. System Analysis 5
D. Launch Vehicle Integration 40
E. Launch Operations 44
F. System Testing 50
G. Scientific Payload 56
H. Flight Control 66
I. Electronics 70
J. Electrical Power Supply 77
K. Thermal Control 81
L. Engineering Mechanics 88
M. Propulsion 94
N. Spaceflight Operations 102

References 104

UNCLASSIFIED

I. *Surveyor* Project

A. Introduction

Calculated to span the gap between the *Ranger* flights and Project *Apollo*, the *Surveyor* spacecraft is designed to take the next step in lunar technology by attempting soft landings on the Moon. The first launches will be engineering test missions to demonstrate system capability up to soft landing, and limited post-landing operations. The engineering payload includes elements of redundancy, diagnostic telemetry, touchdown instrumentation, and survey TV.

Following the engineering test missions, *Surveyor's* objectives are to extend our knowledge of lunar conditions and to verify suitability of *Apollo* landing sites. The science payload is planned to consist of two-camera TV, micrometeorite ejecta, single-axis seismometer, alpha particle scattering, soil sampler, and touchdown dynamics experiments.

Hughes Aircraft Company, Space Systems Division, is under contract to develop and fabricate the first seven spacecraft. The launch vehicle is a combination *Atlas/Centaur*. The JPL Space Flight Operations and Deep Space Network (Mission Operations System) will be utilized for flight control and tracking. The earliest practical launch is presently anticipated for the first quarter of 1966.

The major portion of the following material relating to the *Surveyor* spacecraft system was derived from material prepared by the Hughes Aircraft Company; articles prepared by the JPL Technical Sections are identified by footnotes to the article titles. The principal model designations and vehicles discussed are defined in Table 1.

Table 1. Model and vehicle designations

Designation	Description
SC-1–4	Flight spacecraft with engineering payload
SC-6–8	Flight spacecraft with scientific payload
A-21	Model designation for spacecraft with engineering payload (SC-1–4)
A-21A	Model designation for spacecraft with scientific payload (SC-6–8)
T-21	Model A-21 prototype system test spacecraft
SC-5	Model A-21A proof test model spacecraft
T-2	Simplified spacecraft for evaluation of terminal descent propulsion and flight control
S-2	Test spaceframe for vibration, shock, and static structural tests
S-6, -7	Test spaceframe for vernier propulsion system tests
S-9	Structural test model
S-10	Temperature control model

B. System Engineering

1. A-21 Spacecraft Configuration

The first four flight spacecraft (Model A-21) are designed to carry an engineering instrument payload to evaluate spacecraft performance and lunar soft-landing characteristics. The current A-21 weight summary is shown in Table 2. The A-21 balance summary showing the cg location is given in Table 3.

Table 2. A-21 spacecraft weight summary

Item	Current design weight, lb
Total separated weight	2183.49
Basic bus	696.72
Usable propellant	1423.27
Engineering payload	63.50

Table 3. A-21 spacecraft weight and balance summary

Condition	Weight, lb	Vertical center of gravity Z[a], in.	Lateral center of gravity X, in.	Lateral center of gravity Y, in.
Spacecraft after Centaur separation	2183.49	12.02	0.07	−0.22
Maximum touchdown	647.59	16.80	0.08	−0.25
Minimum touchdown	601.18	17.59	0.09	−0.23

[a]Inches above landing gear hinge line (Spacecraft Station 47.48).

2. SC-1 Spacecraft Special Tests

a. Transient monitoring of command lines. Transient monitoring of command lines test was performed for evaluation of a representative sample of command lines to determine what transients exist in the spacecraft command lines. A flight configuration spacecraft was operated through various major sequences containing those modes that required switching of large currents. No irregularities were observed during the testing; however, firm conclusions cannot be formulated since the data have not yet been reduced and analyzed.

b. Auxiliary engineering signal processor/engineering signal processor (AESP/ESP) simultaneous operation. While operating the T-21 spacecraft in transponder mode, the coast phase commutator was accidentally commanded on. This occurred with the ESP operating in Mode 2. The result of this simultaneous operation was a loss of command link capability. A special test was conducted to determine if this condition would cause the same loss of command capability on the SC-1 spacecraft. The spacecraft configuration was in the flight-control coast phase while monitoring telemetry via coast-mode telemetry mode. The procedure was to operate the AESP in coast and thrust modes while commanding each of the ESP modes on. The converse configuration was also sequenced. The ESP was operated in each of its four modes while commanding the coast and thrust modes. Results of this testing did not duplicate the loss of command link exhibited on T-21. Test conclusions show that, although both commutators can be operated simultaneously, no loss of command capability would result from such a configuration on the SC-1 spacecraft. Reasons for such a condition occurring on T-21 could lie in the differences of the boost regulators on T-21 and SC-1. The T-21 control item has a cycling dump characteristic, which could cause the central decoder unit to cease normal operation.

c. Telemetry channel verification. A special test was conducted to verify telemetry signals that had not been previously verified at the spacecraft systems level. These included all data link, landing gear position potentiometer, shock absorber strain gage, vernier engine strain gage, and reference voltage telemetry signals. A programmed automatic telemetry evaluation temperature assessment of all thermal sensors was made shortly after application of spacecraft power to verify that all thermal sensors were indicating close to room temperature.

d. Narrow-band/wide-band switching problem. A test was performed to determine if transients were being generated within the spacecraft and causing the transmitter to switch from NBVCXO to WBVCXO. Photographs covering the test were examined and showed no transients capable of causing the problem. It was later verified on the unit level that the cause of the problem was in the transmitter.

e. Power bus noise test. A special test was performed on the SC-1 spacecraft to determine the characteristics of noise appearing on power buses at various control item interfaces. The test was performed as an overall noise investigation of the *Surveyor* spacecraft. Noise measurements were taken on the power buses with the spacecraft operating in those configurations that were likely to result in the maximum noise generation. Photographs were taken of the power buses for each configuration. Also, the +22-v unregulated power input and all power outputs of the boost regulator were monitored on a magnetic tape recorder. The data taken during the test are being reduced and analyzed. The completed data will consist

of scope photographs, power spectral density plots, and average peak-to-peak noise levels.

f. RF group noise test. A special test was performed on the SC-1 spacecraft to evaluate the RF group in the noise environment and to define the noise applied to the RF group in a system configuration. Various command lines, power buses, and telemetry lines were monitored using a magnetic tape recorder. During the recording, all spacecraft commands that might result in either transient or steady-state noise were sent. The data taken during the test are being reduced and analyzed. The completed data will consist of peak levels and duration of all noise transients and a printout of pulse-code modulated data on transmitter/receiver telemetry lines.

3. A-21A Spacecraft Configuration

Spacecraft for the fifth, sixth, and seventh *Surveyor* flights have the A-21A (scientific instrument payload) configuration for analysis of lunar surface characteristics. During this reporting period, the A-21A model was the subject of detailed definition leading to a design "freeze" and evaluation of the present configuration (Fig. 1) and performance data.

Among the major characteristics of the present A-21A spacecraft design are an injected weight of 2480.81 lb (including a 7.50-lb weight contingency and a payload capacity of 124.72 lb), a 50-m/sec midcourse correction capability, and a 45-deg lunar approach angle. The weight summary is shown in Table 4. The A-21A balance summary showing the cg location is given in Table 5. Tables 6 and 7 give summaries of electrical energy at

Table 4. A-21A spacecraft weight summary

Item	Current design weight, lb
Total separated weight	2480.81
Basic bus	737.67
Usable propellant	1618.42
Scientific payload	124.72

Table 5. A-21A spacecraft weight and balance summary

Condition	Weight, lb	Vertical center of gravity Z[a], in.	Lateral center of gravity X, in.	Lateral center of gravity Y, in.
Spacecraft after Centaur separation	2480.81	11.86	−0.37	−0.13
Maximum touchdown	790.74	16.67	0.44	−0.15
Minimum touchdown	717.58	17.44	−0.48	−0.17

[a]Inches above landing gear hinge line (Spacecraft Station 47.48).

Table 6. Summary of electrical energy at touchdown[a]

Item	Energy, w-hr
Required system energy	
Nominal	6111
Dispersion (±5%)	±306
Net solar panel energy (70.4 × 61.8 hr)	
Nominal	4351
Dispersion (±5%)	±218
Solar intensity variation (±3%)	±131
Net battery energy used through touchdown	
Nominal	1760
Dispersion (rss)	±376
Solar intensity variation (±3%)	±131
Maximum battery energy used through touchdown	2267
Main battery energy at launch	
Nominal	3800
Dispersion	±200
Battery energy remaining at touchdown	
Nominal	2040
Minimum	1333

[a]Transit time = 62.9 hr.

Table 7. Telecommunication and signal processing performance summary

Simultaneous approach TV and energy data	
TV signal-to-noise ratio	≥ 35–37 db
Engineering data bit-error rate	$\leq 3 \times 10^{-3}$
Survey TV	
Video signal-to-noise ratio	33–38 db
Frame identification bit-error rate	$\leq 3 \times 10^{-3}$
Soil mechanics/surface sampler	
Accelerometer channel signal-to-noise ratio	≥ 41.1 db
Other channel signal-to-noise ratios	> 50 db
Seismometer signal-to-noise ratio	> 50 db
Alpha scattering instrument count bit-error rate	$\leq 3 \times 10^{-3}$
Micrometeorite ejecta detector bit-error rate	$\leq 3 \times 10^{-3}$
Touchdown dynamics instrumentation system	
Real-time data signal-to-noise ratio	18 db
Recorded data signal-to-noise ratio	> 50 db
Engineering data bit-error rate	$\leq 3 \times 10^{-3}$
Emergency mode TV signal-to-noise ratio	≥ 17 db

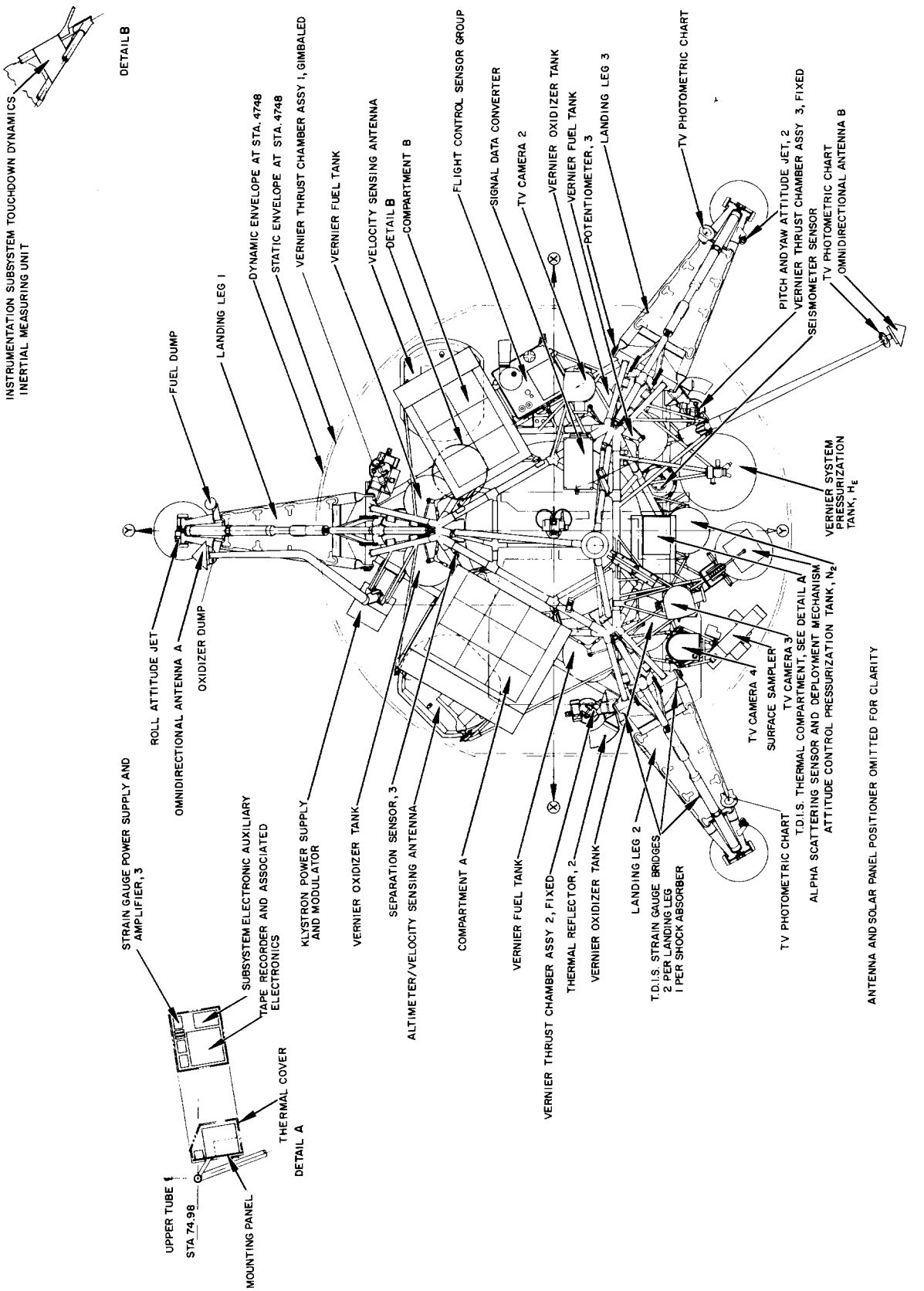

Fig. 1. *Surveyor A-21A* spacecraft (midcourse configuration)

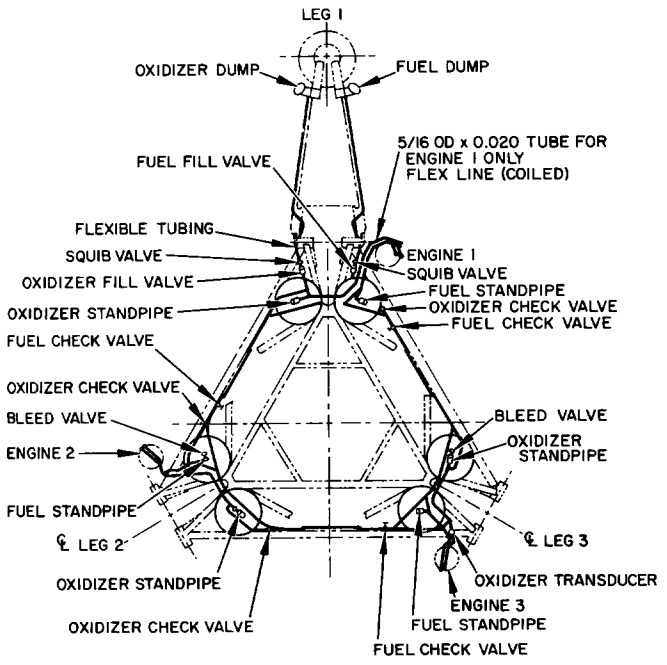

Fig. 2. A-21A spacecraft propellant lines

touchdown and telecommunication and signal processing performance. Fig. 2 shows propellant lines.

In Table 8 JPL Specification 30240D requirements for the A-21A spacecraft are given versus present A-21A performance data. Table 9 compares performances of the A-21 and A-21A spacecraft. After evaluation of the present A-21A configuration and performance data, a design deviation was approved which is the basis now for A-21A spacecraft design. In Table 10 the design deviation data are compared with JPL Specification 30240D requirements.

Table 8. JPL Specification 30240D requirements versus A-21A spacecraft performance data

Item	JPL 30240D requirements	Performance data
Separated weight	2450 lb	2480.81 lb
Trajectory type	Direct ascent or parking orbit	Direct ascent or parking orbit
Maximum midcourse maneuver capability	50 m/sec	50 m/sec
Maximum incidence angle	45 deg	45 deg
Survival		
predawn	20 hr	67 hr max
postsunset	150 hr	195 hr max
Payload	114 lb	124.72 lb

Table 9. A-21/A-21A performance comparison

Item	A-21	A-21A
Trajectory type	Parking orbit or direct ascent	Parking orbit or direct ascent
Midcourse correction capability	50 m/sec max; 0 m/sec min	50 m/sec max; min not specified
Main-retro maximum thrust	10,000 lb	11,500 lb
Main-retro burn time	39 sec	44 sec
Allowable thrust misalignment	0.19 in.	0.165 in.
Altitude marking radar range	60 mi max	70 mi max
Approach angles	0 to 25 deg	0 to 45 deg
Allowable MR burnout velocity	250–525 ft/sec	300–410 ft/sec
Number of commands for descent TV	Nine commands per mode change + 1 command per picture (~ 117 command total)	Three commands
Payload	62 lb	124.72 lb

Table 10. Comparison of approved A-21A design configuration with JPL Specification 30240D requirements

Item	JPL 30240D requirement	Approved design deviation data
Injected weight, lb	2450	2470
Payload weight, lb	114	125
Contingency weight, lb	—	12
Midcourse correction capability, m/sec	50	50
Lunar approach angle capability, deg	45	45
Approach TV installed	Yes	No

C. System Analysis

1. *Atlas-Centaur 6/Surveyor Dynamic-Model 2 (AC-6/SD-2) Flight Path and Simulated Midcourse Maneuver*

a. Introduction. For the AC-6/SD-2 task, the flight-path analysis area was manned by the complete *Surveyor* Flight Path Analysis and Command (FPAC) team. This

effort was a joint JPL-Hughes operation staffed by 16 members from JPL and 11 from Hughes. The staff was augmented by seven people from the *Surveyor* Spacecraft Performance Analysis and Command (SPAC) team working, for this mission only, under the auspices of the FPAC Director.

The space flight operations plan required the support planned for the *Surveyor* mission during the period from launch (L) − 1 hr through the midcourse maneuver (approximately L + 15½ hr). Orbit computations were made, trajectories computed, and midcourse maneuver studies carried out on a schedule dictated by the *Surveyor* FPAC sequence of events, the sole exception being that dual computing configurations were used only until L + 2 hr. At this point, the available computing facilities were reduced to a single 7044-1301-7094 complex.

SPAC personnel were available during the prelaunch Spaceflight Operations Facility–Eastern Test Range (SFOF–ETR) spacecraft frequency measurement period, and to generate the required commands to execute the simulated midcourse maneuver. Frequency measurements, analysis, and validation are required at L − 40 min and again at L − 20 min. The resulting data were used to generate initial acquisition data for the Deep Space Instrumentation Facility at Johannesburg, South Africa (DSIF 51).

Very few problems were experienced in the standard sequence of events during the actual flight. The usual program input errors and data processing system failures caused the operation to lag in the sequence — at one point, by as much as 45 min. It is felt, however, that this problem would have been alleviated with dual computing capability. The major difficulty encountered during the flight was the failure of the system and/or equipment to place incoming tracking data on disk. Recovery time was minimized by reading the missing tracking data directly onto disk from the input/output console in the user areas. Throughout the mission, tracking data cards were punched in near real-time by the recently installed IBM 047 tape-to-card machines.

b. Prelaunch frequency data. During the prelaunch countdown, five frequency reports were sent from ETR to the SFOF. The reports were sent at the beginning and end of the L − 90-min hold, at L − 40, L − 20, and L − 5. The narrow-band voltage-controlled crystal oscillator (NBVCXO) frequency varied between 2294.999567 and 2294.999700 Mc, and the receiver best-lock frequency varied between 2113.309456 and 2113.310560 Mc. These frequencies were indicative of compartment temperatures at liftoff somewhere between 95 and 105°F. The fluctuations in frequencies correlated until the gantry was removed.

The detected static phase-error voltage at best lock fluctuated between 0.055 and 0.275 v because of the long-term drift of the telemetry subcarrier oscillator. This drift was equivalent to only 0.1%; however, in terms of different frequencies at S-band, this was equivalent to about 20 kc. This fluctuation was not considered to be serious and had no affect on the frequency predictions made by the Tracking Data Analysis (TDA) Group. In summary, the frequency data received from ETR was on time and the data were near predictions based on previous data taken during the time the spacecraft was at Cape Kennedy. In addition, the interface between the telecommunication analyst from the Spacecraft Performance Analysis Area and the TDA Group was found to be very satisfactory.

c. Launch phase. The SD-2 *Surveyor* dynamic model was launched from ETR at Cape Kennedy, Florida, on Wednesday, August 11, 1965, using a General Dynamics/Convair (GD/C) *Atlas/Centaur* (AC-6) boost vehicle. Launch occurred at 14:31:04.430 GMT. At 2 sec after liftoff, the launch vehicle began a programmed roll that oriented the vehicle from an azimuth of 115 deg to a launch azimuth of 94.54 deg. At 15 sec, a programmed pitchover maneuver was initiated. The *Atlas* booster engines were shut off, and jettisoned. The *Atlas* sustainer engine continued to provide thrust. The insulation panels and the payload shroud were jettisoned. The sustainer engine was shut off, and *Atlas/Centaur* staging occurred at 236.6 sec after liftoff.

At 244.04 sec, the *Centaur* main engines were started, and injection into the transit trajectory occurred at 679.2 sec after liftoff, when the *Centaur* main engines were cut off. The spacecraft was physically separated from the *Centaur* vehicle at 747.8 sec. The *Centaur* was then turned 180 deg and a retro maneuver was initiated. Mark time for retro start was never received in real-time. Completion of this retro maneuver occurred at 1855 sec after liftoff. The launch-phase ascent trajectory profile is shown in Fig. 3.

d. Actual SD-2 trajectory. The converged injection conditions for each orbit are shown in Table 11. The conditions are Earth-fixed spherical coordinates plus the conventional geocentric conic conditions defined at injection. Injection, or *Centaur* main engine cutoff, occurred at 14:42:23.6 GMT on August 11, 1965, at a geocentric latitude and longitude of 23.0 and 307.4 deg, respectively.

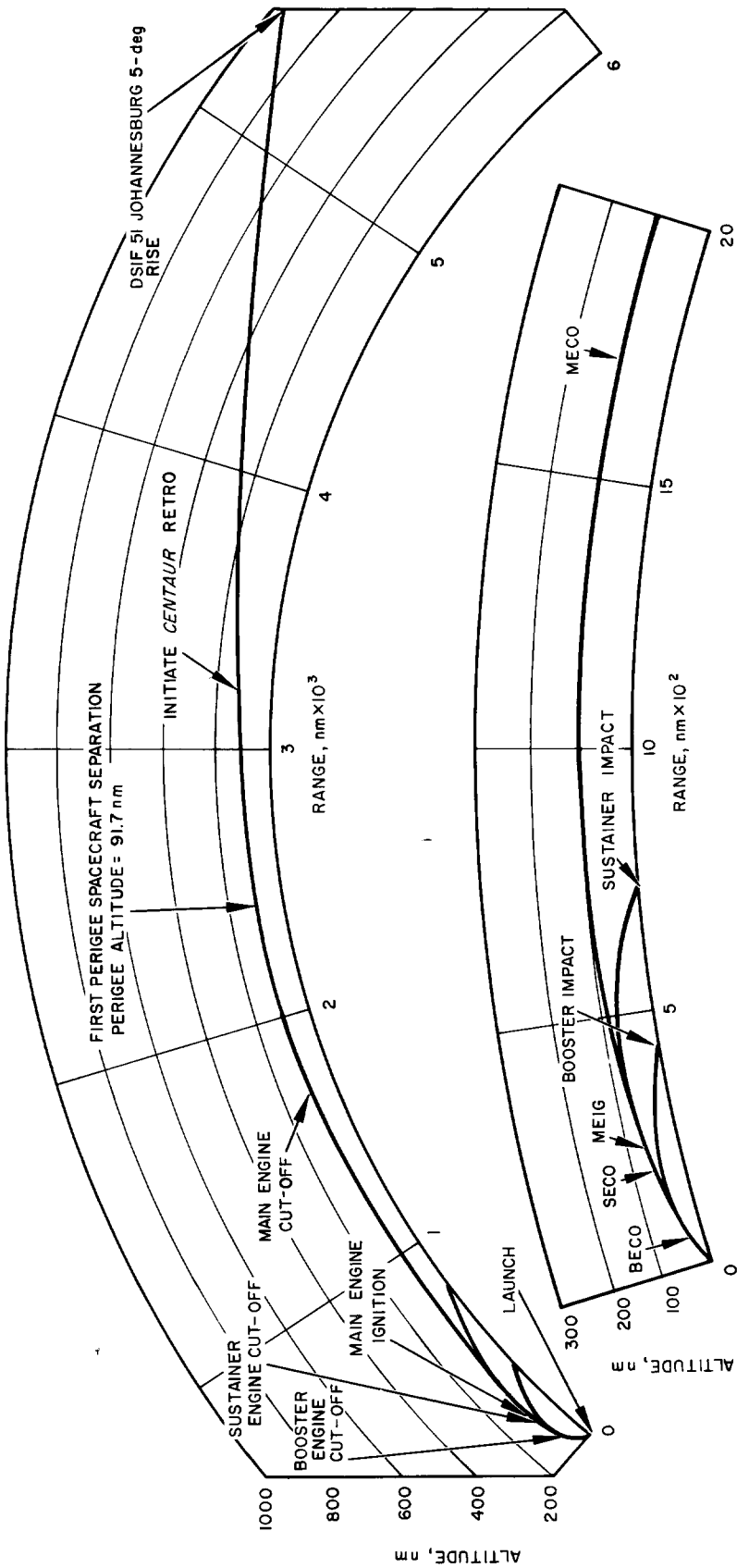

Fig. 3. AC-6 launch-phase ascent trajectory profile

Table 11. AC-6 in-flight orbit considerations

Orbit identification	Time of orbit computation		Converged conditions at injection epoch in Earth-fixed spherical coordinates plus general characteristics of geocentric conic				
	Begin, min	End, min	Epoch	RAD, km	LAT, deg	LONG, deg	VE, km/sec
ETR check orbit (Run A)	$L + 34$	$L + 48$	14:42:20.000	6563.4495	23.087784	307.10446	10.542155
ETR check orbit (Run B)	$L + 48$	$L + 86$	14:42:20.000	6564.1396	23.088054	307.10245	10.557471
Predict orbit (PROR X)	$L + 105$	$L + 135$	14:42:20.000	6563.3407	23.093267	307.10115	10.558396
Predict orbit (PROR Y)	$L + 76$	$L + 97$	14:42:23.600	6556.0415	23.107560	307.42427	10.565206
Initial condition evaluation (ICEV Y)	$L + 169$	$L + 208$	14:42:23.600	6559.7202	23.027988	307.44090	10.561752
Preliminary Maneuver (PREL Y)	$L + 235$	$L + 284$	14:42:23.600	6561.4858	22.983421	307.44538	10.560087
Data consistency (DACO YA)	$L + 388$	$L + 403$	14:42:23.600	6561.9200	22.981194	307.45212	10.559713
Data consistency (DACO YB)	$L + 440$	$L + 452$	14:42:23.600	6562.3867	22.956494	307.45092	10.559343
Data consistency (DACO YC)	$L + 454$	$L + 468$	14:42:23.600	6561.5465	22.984250	307.44711	10.560042
Data consistency (DACO YD)	$L + 524$	$L + 550$	14:42:23.600	6561.2422	22.991257	307.44367	10.560274
Last premaneuver (LAPM)	$L + 759$	$L + 794$	14:42:23.600	6561.7322	22.980665	307.44907	10.559884
Final inflight orbit using all DSIF data	$L + 1860$	$L + 1980$	14:42:23.600	6561.6091	22.983811	307.44802	10.559996

RAD = spacecraft geocentric radius distance
LAT = spacecraft geocentric latitude
LONG = spacecraft geocentric longitude
VE = spacecraft Earth-fixed velocity

UNCLASSIFIED
CONFIDENTIAL

Converged conditions at injection epoch in Earth-fixed spherical coordinates plus general characteristics of geocentric conic

PTE, deg	AZE, deg	SMA, km	ECC	INC, deg	C3, km^2/sec^2	LAN, deg	APF, deg	TA, deg
−2.8566045	108.01691	303581.60	0.97843017	28.565739	−1.3129934	359.07270	130.46118	−5.5552489
−3.1621513	107.98213	413468.43	0.98416925	28.547242	−0.96404126	359.12713	130.98789	−6.1316076
−3.1525788	107.97835	415328.63	0.98424180	28.549350	−0.95972346	359.13773	130.95715	−6.1128689
−2.9658687	108.14078	413807.92	0.98419636	28.650829	−0.96325035	359.22236	130.81417	−5.7515553
−2.9687724	108.14846	414897.80	0.98422910	28.592391	−0.96072002	359.13695	130.93280	−5.7567737
−2.9698174	108.15419	415489.00	0.98424733	28.560529	−0.95935302	359.08165	131.00046	−5.7585904
−2.9688228	108.16254	415559.82	0.98424894	28.563377	−0.95918953	359.07226	131.01334	−5.7566370
−2.9592810	108.22496	415462.52	0.98424388	28.578747	−0.95941417	358.94049	131.11696	−5.7381579
−2.9695271	108.15569	415532.55	0.98424882	28.562003	−0.95925246	359.08188	131.00096	−5.7580236
−2.9740291	108.12628	415532.89	0.98424969	28.551202	−0.95925169	359.13471	130.95816	−5.7667422
−2.9680672	108.16557	415525.75	0.98424808	28.564666	−0.95926818	359.06357	131.01701	−5.7551891
−2.9693615	108.15662	415503.92	0.98424758	28.562167	−0.95932070	359.08078	131.00253	−5.7576991

PTE = pitch angle of spacecraft Earth-fixed velocity vector with respect to local horizontal
AZE = azimuth angle of spacecraft Earth-fixed velocity vector measured east of true north
SMA = semimajor axis
ECC = eccentricity
INC = inclination of orbital plane to equation plane
C3 = twice energy (vis viva energy integral)
LAN = longitude of ascending mode
APF = argument of pericenter
TA = true anomaly

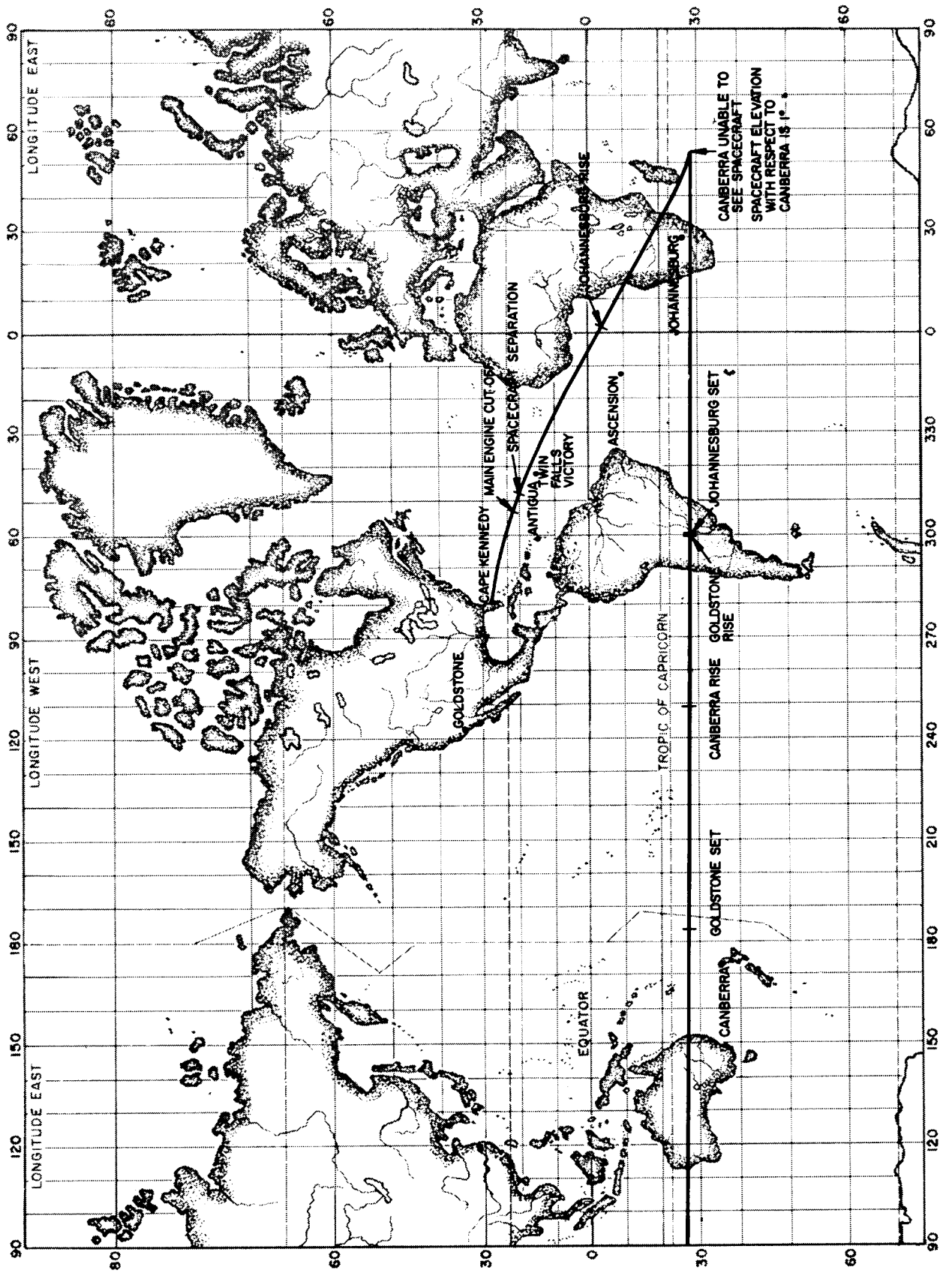

Fig. 4. AC-6 Earth-tracked trajectory

The *Centaur*/spacecraft combination was in the sunlight at injection and never entered the Earth's shadow during the expected lifetime of 20 hr. The predicted view periods for the Johannesburg, Goldstone, and Canberra tracking stations are shown in Table 12. Fig. 4 shows the Earth's track of AC-6. Fig. 5 plots the probe geocentric radius and velocity versus time from main engine cutoff. The Sun-probe-Moon, Earth-probe-Moon, and Earth-probe-Sun angles versus time from main engine cutoff are shown in Fig. 6.

Table 12. SD-2 view period summary

DSIF station	Event	Time past epoch, hr:min:sec	Greenwich Mean Time, (date)	hr:min:sec
	Start epoch	00:00:00	Aug 11, 65	14:42:24
51 Johannesburg	5-deg elevation rise	00:12:08	11	14:54:32
51 Johannesburg	90-deg hour angle set	11:09:00	Aug 12	01:51:24
11 Goldstone	5-deg elevation rise	11:11:30	12	01:53:54
42 Canberra	5-deg elevation rise	14:44:19	12	05:26:43
11 Goldstone	5-deg elevation set	19:15:00	12	09:57:24
51 Johannesburg	5-deg elevation rise	23:25:40	12	14:08:04
42 Canberra	5-deg elevation rise	28:29:21	12	19:11:44
11 Goldstone	5-deg elevation rise	35:30:52	Aug 13	02:13:16
51 Johannesburg	90-deg hour angle set	35:52:30	13	02:35:54
42 Canberra	5-deg elevation rise	39:12:19	13	05:54:43

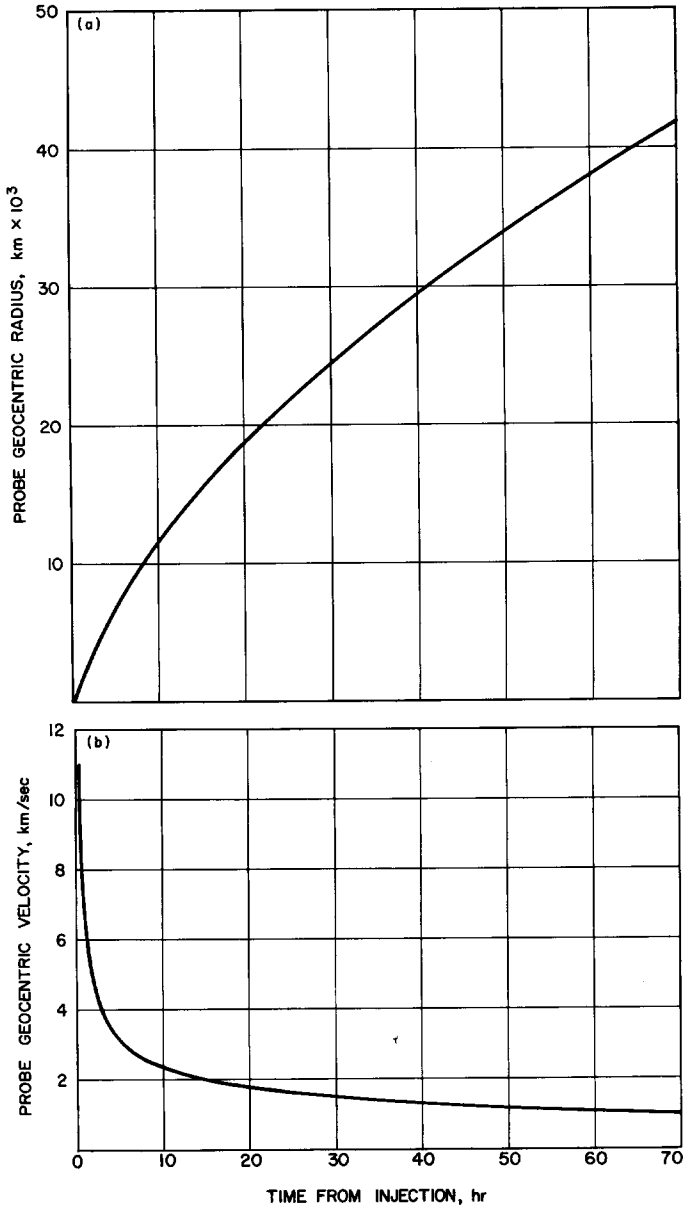

Fig. 5. Probe parameters vs time from injection: (a) geocentric radius; (b) geocentric velocity

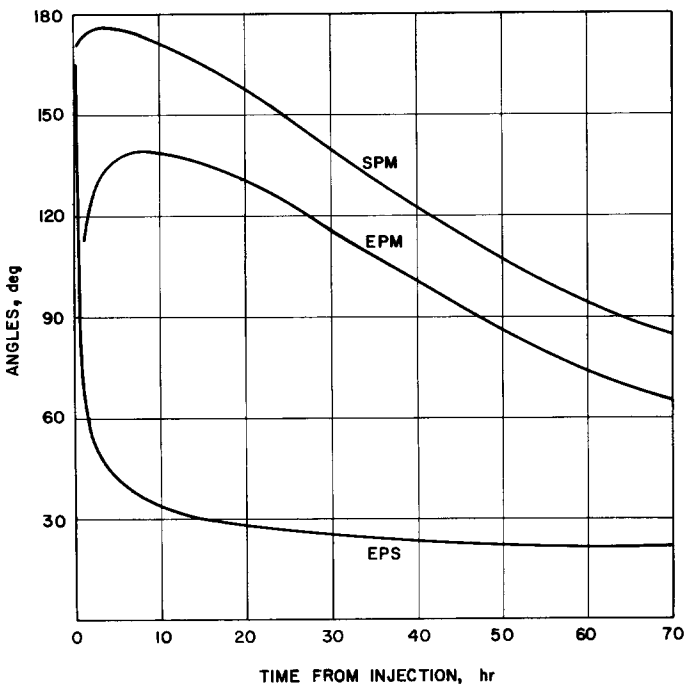

Fig. 6. Earth–probe–Sun (EPS), Sun–probe–Moon (SPM), and Earth–probe–Moon (EPM) angles as function of time for injection

Using the best set of injection conditions available, the spacecraft trajectory was integrated out for 100 days from main engine cutoff. A plot of the trajectory projection on the Earth's equatorial plane is shown in Fig. 7. Although the trajectory was chosen from one that was targeted to impact the Moon and biased in time to preclude impact, it came relatively close to the Moon on its return to Earth. The radius of closest approach is 66,000 km. The original orbit is perturbed considerably during this pass of the Moon. To illustrate the magnitude of this perturbation, a plot of the orbital energy versus time from main engine cutoff is shown in Fig. 8.

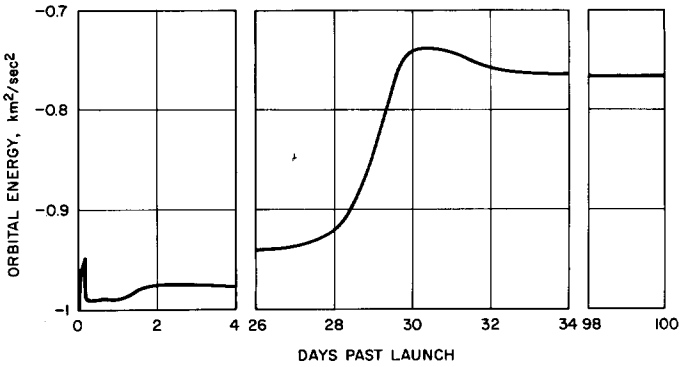

Fig. 8. Orbital energy vs time

e. Simulated trajectory. As previously noted, the nominal trajectory was targeted for an actual launch date of September 28, 1965. The spacecraft was launched, per this launch window, on August 11, 1965. To satisfy test support requirements for morning through early afternoon launches, 6 hr were added to the targeted launch window. Simulated lunar trajectories and corresponding midcourse corrections were computed in real-time by using the converged orbit determination program, Earth-fixed spherical conditions, and the appropriate September 28 injection epoch. Table 13 summarizes the simulated lunar parameters for selected orbit computations. For launch data presented in Table 13, AC-6 was targeted so that impact would occur on the lunar surface at a latitude of −3.75 deg and a longitude of 337.25 deg.

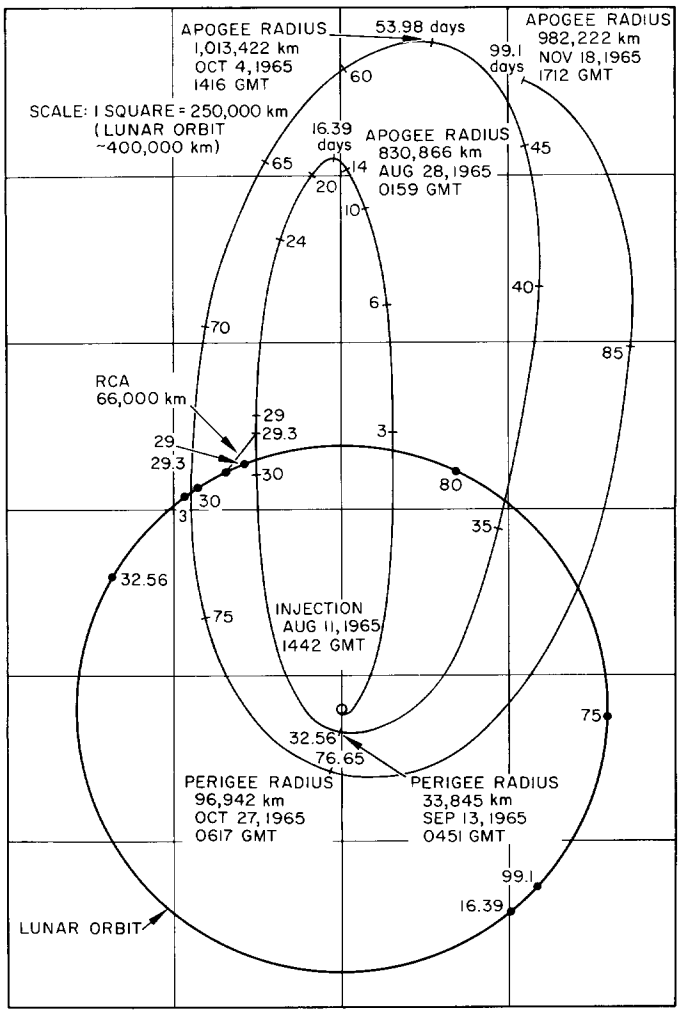

Fig. 7. Actual AC-6 trajectory in Earth's equatorial plane

Fig. 9 shows the approximate relationship between the simulated impact points and the targeted aiming point. If the spacecraft were on a lunar trajectory, unbraked impact would have occurred in the crater, Copernicus, only 15 deg from the desired landing site. The grouping of trajectory solutions using the injection conditions of the various converged orbit determination runs (i.e., PROR X, PROR Y, DACO YA, DACO YB) is shown in Fig. 10. During the flight, the impact points varied from the floor of the crater to the east wall. The final in-flight orbit, computed *after* the nominal midcourse maneuver time, showed an unbraked impact at 9.96 deg latitude and 341.13 deg longitude. Because of the added complication of changing the injection epoch, no orbit determination statistics were mapped to the Moon.

f. Simulated midcourse correction. The *Surveyor* midcourse correction computed to enable the spacecraft to soft land at the desired landing site, −3.75 deg latitude and 337.25 deg longitude, was 18.5 m/sec. This maneuver is well within the maximum midcourse correction capability of the SC-1 spacecraft. Fig. 11 shows the maximum capability for the simulated launch date as a function of the uncorrected impact velocity. Also shown are the

Table 13. AC-6 orbit computations

Orbit identification	Computer station	Data used in orbit	Simulated target parameters								
			B, km	B-TQ, km	B-RQ, km	Flight time, hr	Impact velocity, km/sec	Latitude, deg	Longitude, deg	Arrival GMT, hr:min:sec	Flight-path angle, deg
ETR check orbit (Run B)	X	Antigua 7-point range 8-point angles Twin Falls 14-point range 15-point angles	1138	—	—	62.10	2.676	13.24	340.23	22:36:49	−75.3
PROR X	X	Antigua 7-point range Twin Falls 14-point range DSIF 51 173-point doppler 236-point angles	1033	431	−939	61.98	2.676	9.98	340.61	22:32:43	−74.1
PROR Y	Y	DSIF 51 175-point doppler 217-point angles	915.8	887	−229	62.01	2.676	−6.67	345.5	22:34:48	−75.9
ICEV Y	Y	DSIF 51 256-point doppler 301-point angles	915.8	598	−634	61.98	2.676	4.12	342.36	22:33:09	−75.9
PREL Y	Y	DSIF 51 336-point doppler 402-point angles	1064	465	−957	61.97	2.676	10.16	341.42	22:32:19	−73.6
DACO YA	Y	DSIF 51 576-point doppler 447-point angles	1053	439	−957	61.97	2.676	10.31	340.89	22:32:23	−73.8
DACO YB	Y	DSIF 51 577-point doppler	1188	507	−1074	61.97	2.676	12.33	343.11	22:31:48	−71.6
DACO YD	Y	Antigua 7-point range Twin Falls 14-point range DSIF 51 778-point doppler	1053	461	−947	61.97	2.676	9.99	341.26	22:32:18	−73.8
LAPM Y	Y	Antigua 1-point range DSIF 51 793-point doppler DSIF 11 19-point doppler	1066	461	−961	61.97	2.676	10.27	341.38	22:32:16	−73.6
Last inflight orbit	Y	DSIF 11 133-point doppler DSIF 42 42-point doppler DSIF 51 792-point doppler	1048	455	−944	61.97	2.676	9.96	341.13	22:32:09	−73.9

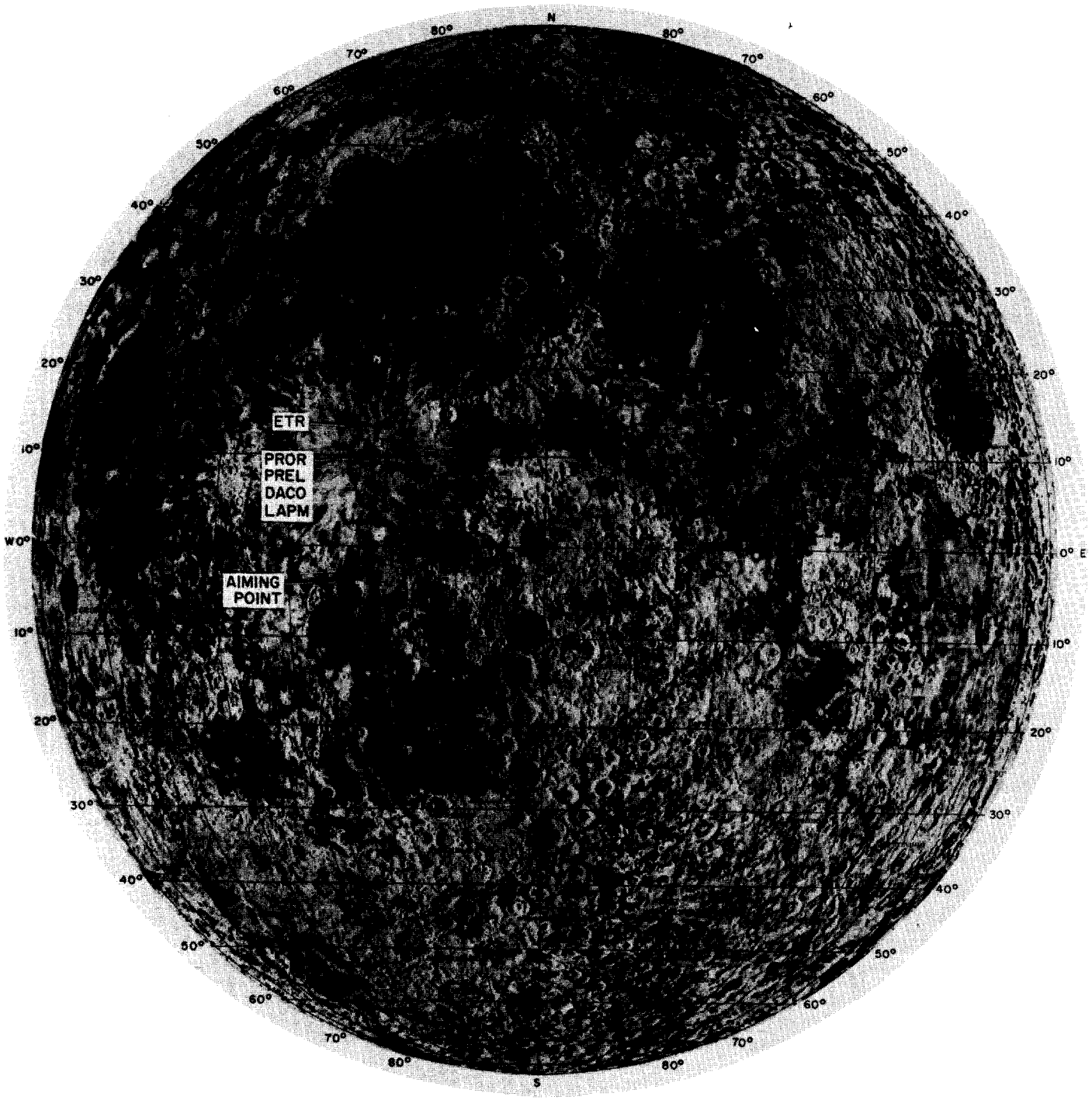

Fig. 9. AC-6 simulated impact points and targeted aiming point on the Moon

UNCLASSIFIED

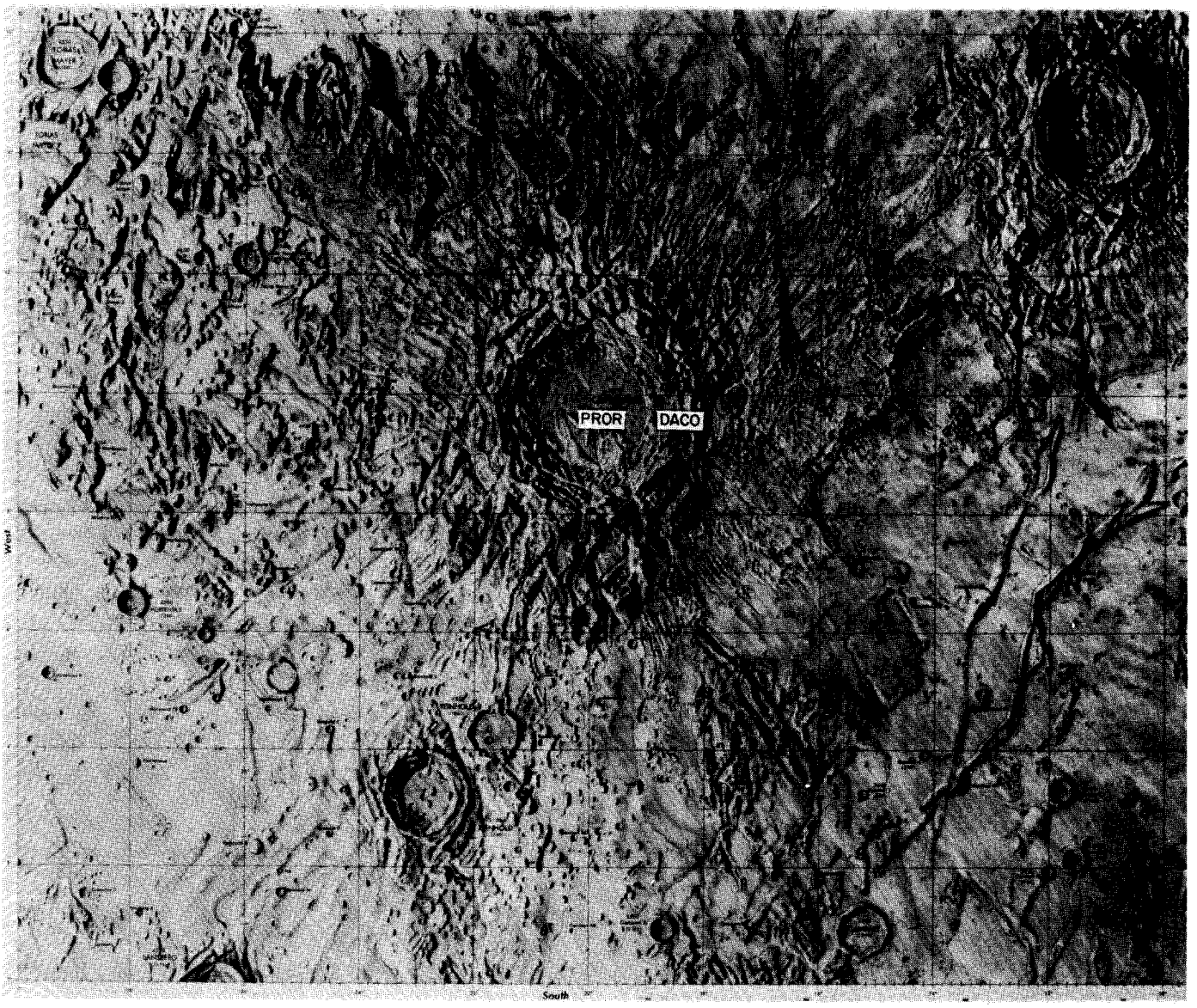

Fig. 10. AC-6 uncorrected impact points on the Moon

UNCLASSIFIED

effective lunar radius and the estimated 3σ *Centaur* injection guidance dispersions. The midcourse capability contours are shown in the conventional *R-S-T* coordinate system defined in Ref. 1. As required by the sequence of events, the final correction was based on the results of the last premaneuver orbit (LAPM YA) available at $L + 794$ min. The results of this orbit and the aiming point are shown in Fig. 11. The simulated midcourse maneuver time was 15.69 hr after injection. This time was found to be a good compromise between pre- and postmaneuver Goldstone visibility. The maneuver epoch was September 29, 1965, 00:24:00 GMT.

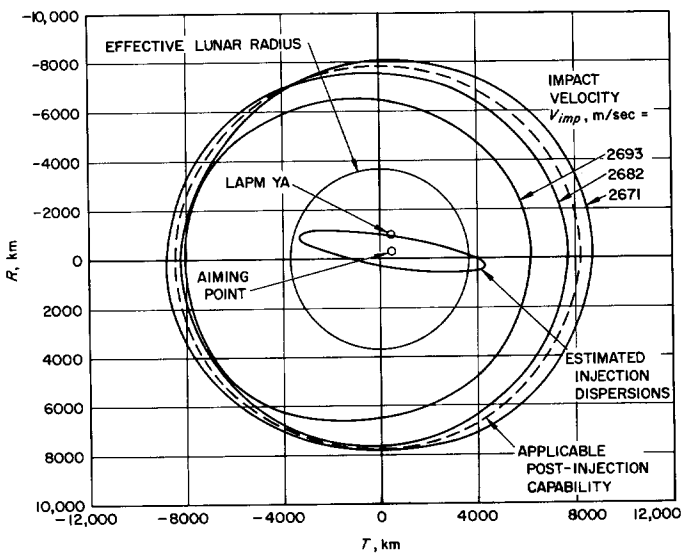

Fig. 11. AC-6 15.5-hr midcourse capability contours

Table 14 summarizes the results of the nominal correction. The required component in the critical plane, to correct miss only, was found to be 4.25 m/sec. The component in the noncritical direction, which results from an optimum selection of flight time, main retro burnout velocity, and vernier propulsion system fuel margin, was 18.04 m/sec. If the maneuver strategy were to correct miss plus flight time, the required noncritical component would have been -14.5 m/sec, giving a total of approximately 15 m/sec. Fig. 12 shows the complete spectrum of flight times, burnout velocities, and fuel margins as a function of the velocity in the noncritical direction (U_3). Also indicated are the values selected by the *Surveyor* guidance logic that are required to correct to the nominal flight time.

g. Landing site errors. An important consideration in the midcourse maneuver analysis is a study of the premaneuver predicted landing site dispersions. Because of tracking and midcourse execution errors, the dispersions of the lunar surface were predicted to be within 55.3 km (3σ). Fig. 13 shows the landing area in relation to these errors.

h. Additional maneuver considerations. Following computation of the magnitude and direction of the midcourse vector ($\Delta V_{M/C}$), four pairs of attitude maneuvers were calculated and compared with respect to pre-stored omni-antenna patterns in the midcourse command pro-

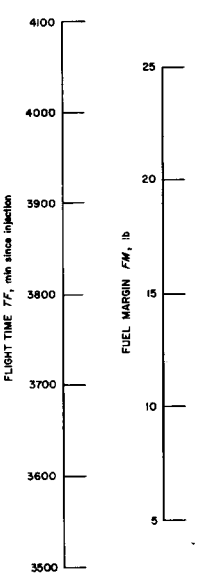

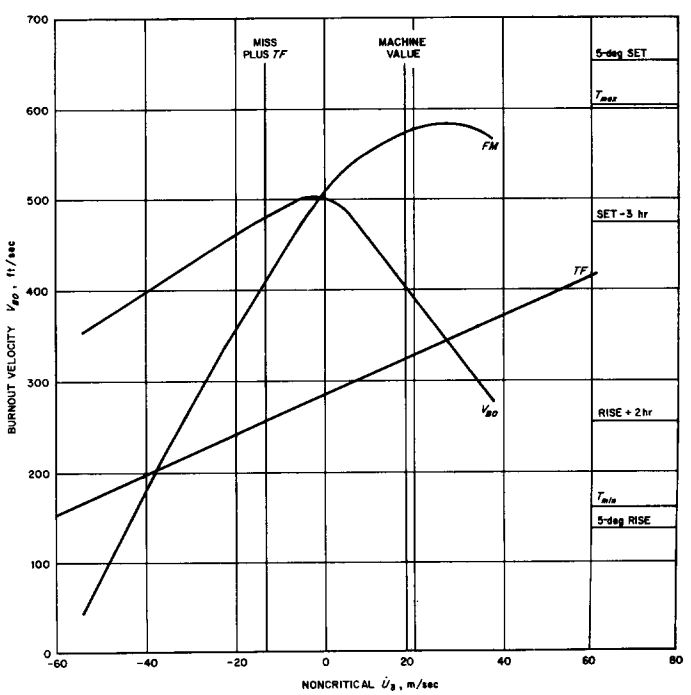

Fig. 12. AC-6 flight time, fuel margin, and burnout velocity vs velocity in the noncritical direction

UNCLASSIFIED

Table 14. Critical midcourse and terminal maneuver parameters

Item	No midcourse maneuver	15.5-hr midcourse maneuver	40-hr midcourse maneuver
Midcourse data			
Time, (date) hr:min:sec GMT		Sep 29, 65 00:24:00	Sep 30, 65 00:42:23.60
Critical component (miss), m/sec	0	4.25	8.01
Noncritical component, m/sec	0	18.04	16.67
Magnitude, m/sec	0	18.51	18.51
Propellant weight, lb	0	15.1	15.1
Roll, deg-sec	0	33.44, 66.89	
Yaw, deg-sec	0	149.54, 299.08	
Engine burn time, sec	0	18.94	
Omni-antenna	B	B	B
Maneuver execution errors, km	0	28	14
Terminal data			
Latitude, deg	10.17	−3.75	−3.74
Longitude, deg	341.42	337.24	337.26
Impact time, (date) hr:min:sec GMT	Sep 30, 65 22:32:19.35	Sep 30, 65 23:10:20.27	Sep 30, 65 22:39:50.57
Incidence angle, deg	16.39	8.47	8.02
Impact velocity, m/sec	2676.39	2667.68	2668.98
Touchdown time, (date) hr:min:sec GMT	Sep 30, 65 22:35:5.82	Sep 30, 65 23:12:51.50	
Burnout velocity, ft/sec	512.04	395	404
Burnout alternator, ft	43,788.94	31,542.13	
Fuel margin, lb	19.28	20.9	20
Descent propellant, lb	141.71	124.8	125.7
Nominal descent time, sec		126.01	
Roll, deg-sec	73.29, 146.58	67.65	
Yaw, deg-sec	143.08, 286.17	143.56	
Ignition delay, sec	5.85	7.59	

gram. Fig. 14a shows the trace of the DSIF vector, in spacecraft coordinates, for each maneuver pair superimposed on the contour antenna pattern of Omni-antenna A. Fig. 14b shows the DSIF traces for Omni-antenna B. Since any one maneuver pair will correctly position the spacecraft prior to midcourse, the pair that maximizes mission success through continuous, high antenna gain and maximum Sun-lock time was chosen. Of the four pairs the roll-pitch maneuver placed the DSIF in a relatively low gain area of the initial Omni-antenna B. However, the roll-yaw pair of the three remaining maneuver sequences allowed the DSIF to remain in the best gain region for both maneuvers and *simultaneously* permitted continuous Sun lock throughout the roll. The roll-yaw pair was therefore selected as 33.44 and 149.54 deg, respectively. The required engine burn time was 18.94 sec.

i. Simulated terminal phase. Key terminal parameters indicate that the terminal descent phase would have been nominal with an associated high probability of success. The key parameters are as follows: pre- and post-landing Goldstone visibility of 3 and 5½ hr, respectively, an unbraked impact velocity of 2667.18 m/sec, a nominal main retro burnout velocity of 395 ft/sec, a fuel margin of 20.9 lb, and a main retro ignition delay of 7.59 sec. Fig 15 is a plot of range versus velocity for the vernier phase of the AC-6 mission based on the 15.69-hr midcourse correction. The "O" markings represent the actual range-velocity profile from burnout to touchdown. The radar constraints and the 3σ dispersion ellipse about the burnout point are superimposed on the plot. The expected conditions are well within the constraining limits.

The required vernier fuel margin, as a function of main retro burnout velocity, to accommodate the various dispersions is shown as Fig. 16. The required fuel margin at the nominal burnout point is 10.5 lb. The predicted fuel margin of 20.95 lb was well above the requirement. For the terminal attitude maneuvers, a roll, yaw sequence was chosen: roll = 67.65 deg; yaw = 143.56 deg.

In a manner analogous to the midcourse maneuver determination, using plots of constant antenna gain contours, Omni-antenna B was chosen for the entire maneuver. No switching of omni-antennas was necessary for this choice.

UNCLASSIFIED

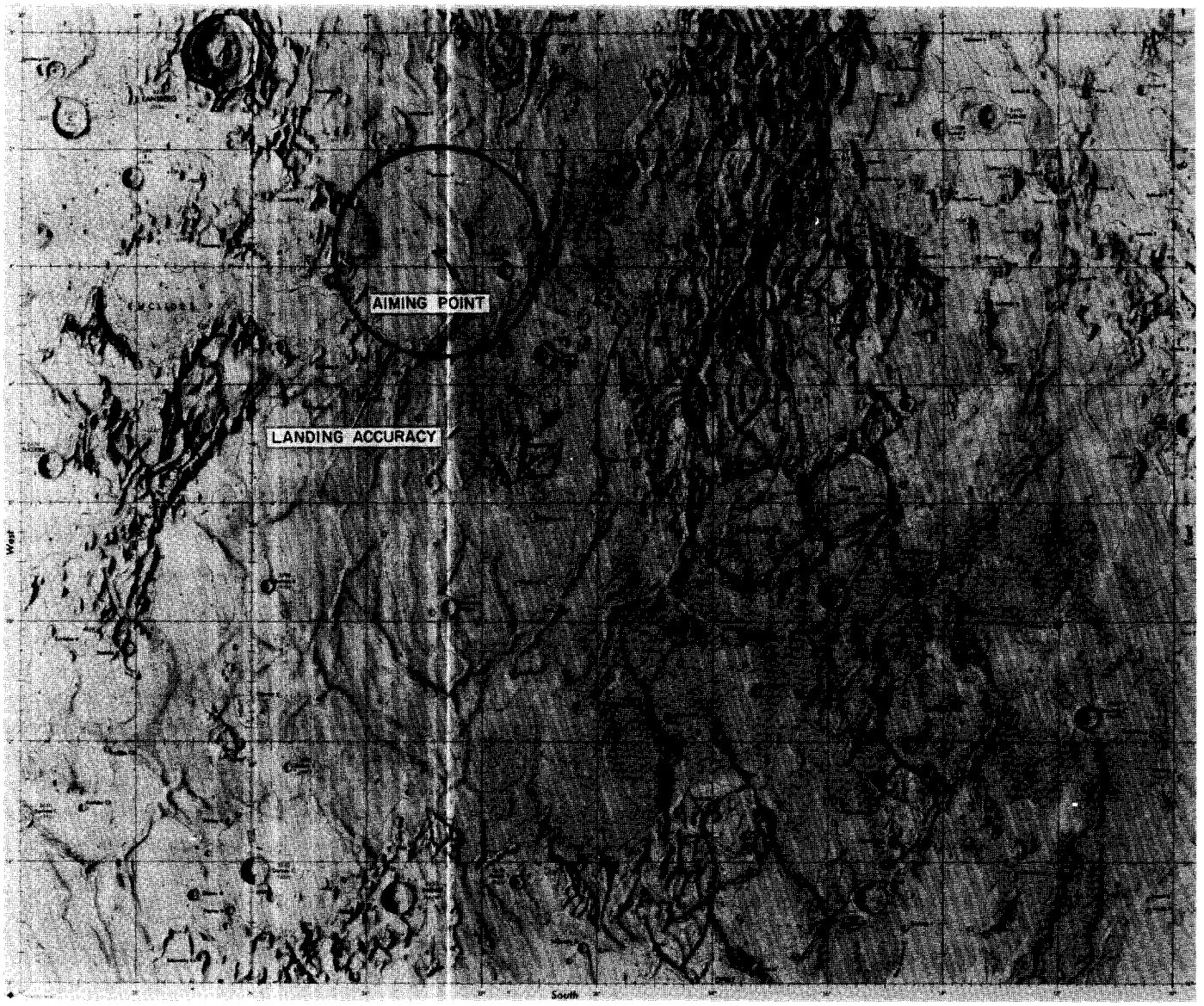

Fig. 13. AC-6 aiming point on the Moon

UNCLASSIFIED

The following list presents important events associated with the terminal descent phase. All times occurred on September 30, 1965.

Event	hr:min:sec GMT
Earliest planar array erection	22:32:30.854
Earliest first maneuver	22:39:50.854
Earliest second maneuver	22:47: 6.152
1000-mi mark	22:58:45.772
Altitude marking radar enable	23: 9: 6.316
Radar trigger	23: 9:43.270
Main retro phase start	23: 9:50.854
Impact	23:10:20.266
Vernier phase start	23:10:45.494
Touchdown	23:12:51.502

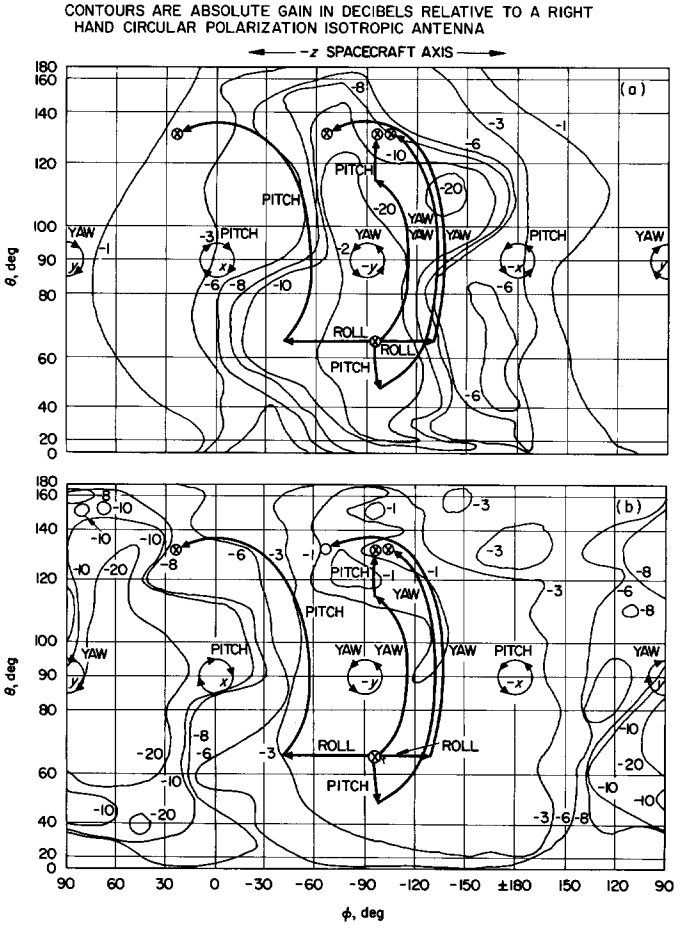

Fig. 14. Contour antenna pattern minimum coverage: (a) Arm A; (b) Arm B

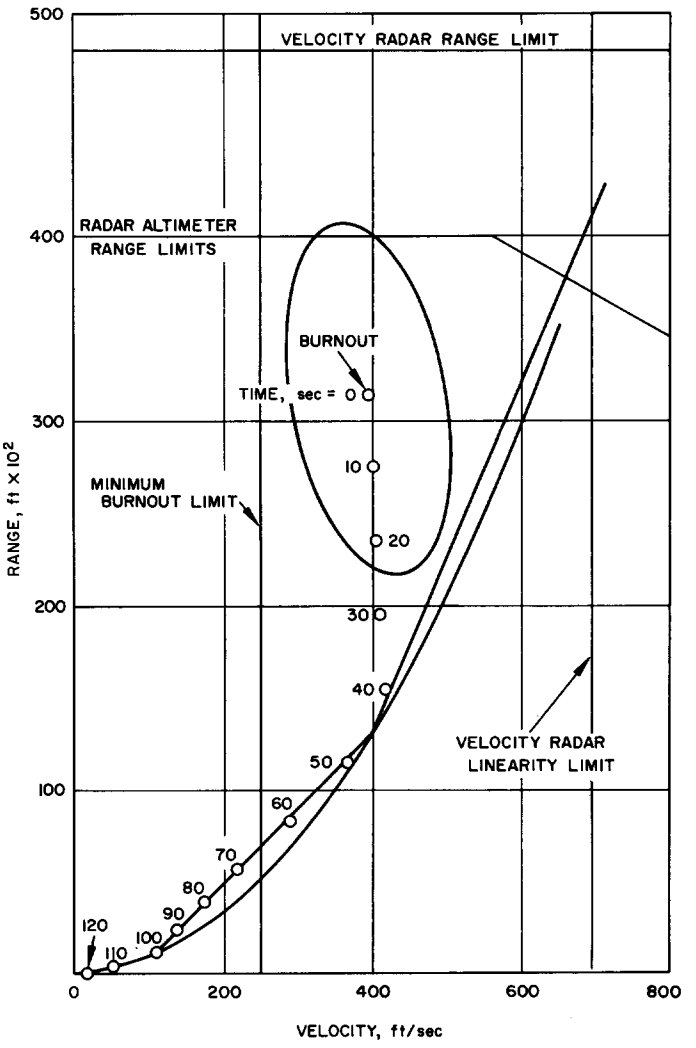

Fig. 15. AC-6 vernier descent-phase velocity-range rate limit

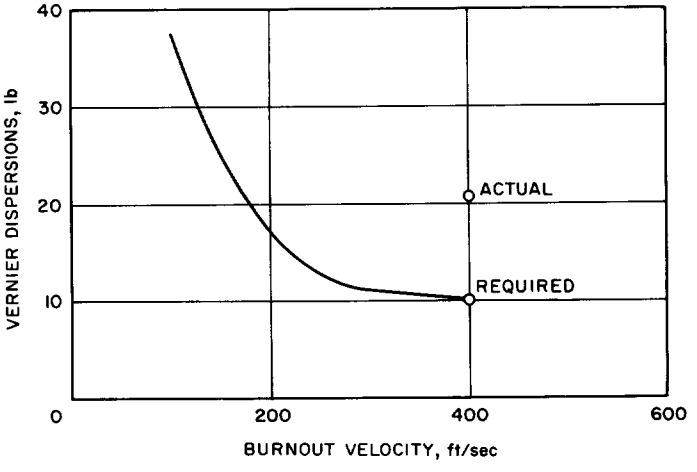

Fig. 16. AC-6 minimum fuel margin vs burnout velocity

The required 40-hr correction and the associated terminal parameters are tabulated in Table 14. The magnitude of the maneuver was found to be 18.5 m/sec, approximately the same as at 15.69 hr. The apparent paradox is a result of the *Surveyor* midcourse guidance logic and will occur whenever small misses are encountered.

2. Launch Window and Impact Velocity Study for 63-hr Direct Ascent Trajectories (March–November 1967)

A study of the launch windows and impact velocities for 63-hr direct ascent trajectories during the March–November 1967 launch periods was conducted: its purpose was to provide data in support of the A-21A design effort.

The data are obtained from a two-body conic trajectory program and are corrected on the basis of *n*-body integrated trajectory results. The conic boost model of the program is updated to include the AC-6 closed-loop trajectory data from Ref. 2.

a. Ground rules. The following ground rules were used for the design of the lunar transit trajectories:

(1) The *Atlas/Centaur* boost vehicle as defined for *Surveyor* direct ascent launches is used.

(2) Launches take place from Cape Kennedy with the launch azimuth restricted to lie between 80 and 115 deg east of true north.

(3) Direct ascent boost trajectories are used with weight constraints on the launch window for *Atlas/Centaur* zero flight performance reserve (FPR). The weight constraint used (6413 lb) is a value representative of the A-21A/114 missions and was determined from Refs. 3 and 4. The perigee of the transit trajectory is 90 nm.

(4) The time periods of interest are the direct ascent launch periods from late March to early November 1967.

(5) Flight times in the order of 63 hr are considered.

(6) Arrival at the Moon is constrained to take place between 2 hr after Goldstone rise and 3 hr before Goldstone set. Goldstone rise and set refer to the times of the Moon's rise and set with respect to the Goldstone Deep Space Network as determined by a 5-deg elevation angle.

(7) Only days with launch windows greater than 0 min are considered.

(8) For the A-21A/114 missions, the lunar lighting requirements at arrival are a minimum of 72 hr of post-landing sunlight before sunset or a maximum of 20 hr of darkness before sunrise.

b. Results. The typical variation of lunar impact speed with arrival time at constant launch azimuth (or FPR) is illustrated in Fig. 17. Any trajectory that arrives in the lightly shaded area bounded by the arrival time constraints and the opening and closing launch azimuths (or FPR) will satisfy the launch and arrival constraints thus far imposed. To design trajectories across the arrival window, the impact speed is held constant. The arrival window, then, is further bounded by lines of constant impact speed as seen in Fig. 17. For the days considered in this study, the window opens at the FPR limit and closes at the 115-deg launch azimuth limit.

The variation of unbraked lunar impact speed for all direct ascent launch days in the periods of interest is presented in Fig. 18. The significance of the bars is illustrated in Fig. 17; each bar represents the possible daily variation of impact speed in the arrival window. It is not possible to design constant impact speed trajectories across all periods considered without loss of launch window or violation of the arrival time constraints.

Fig. 19 presents the launch windows for each of the launch periods in the period of interest. All days with non-zero launch windows are presented.

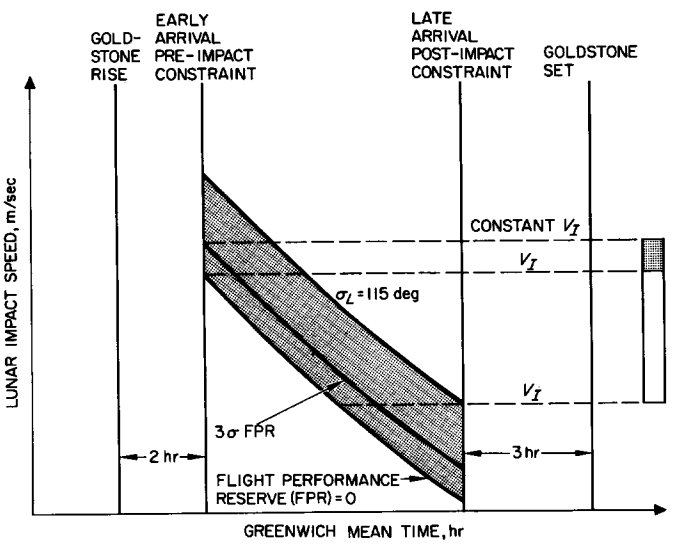

Fig. 17. Goldstone arrival window

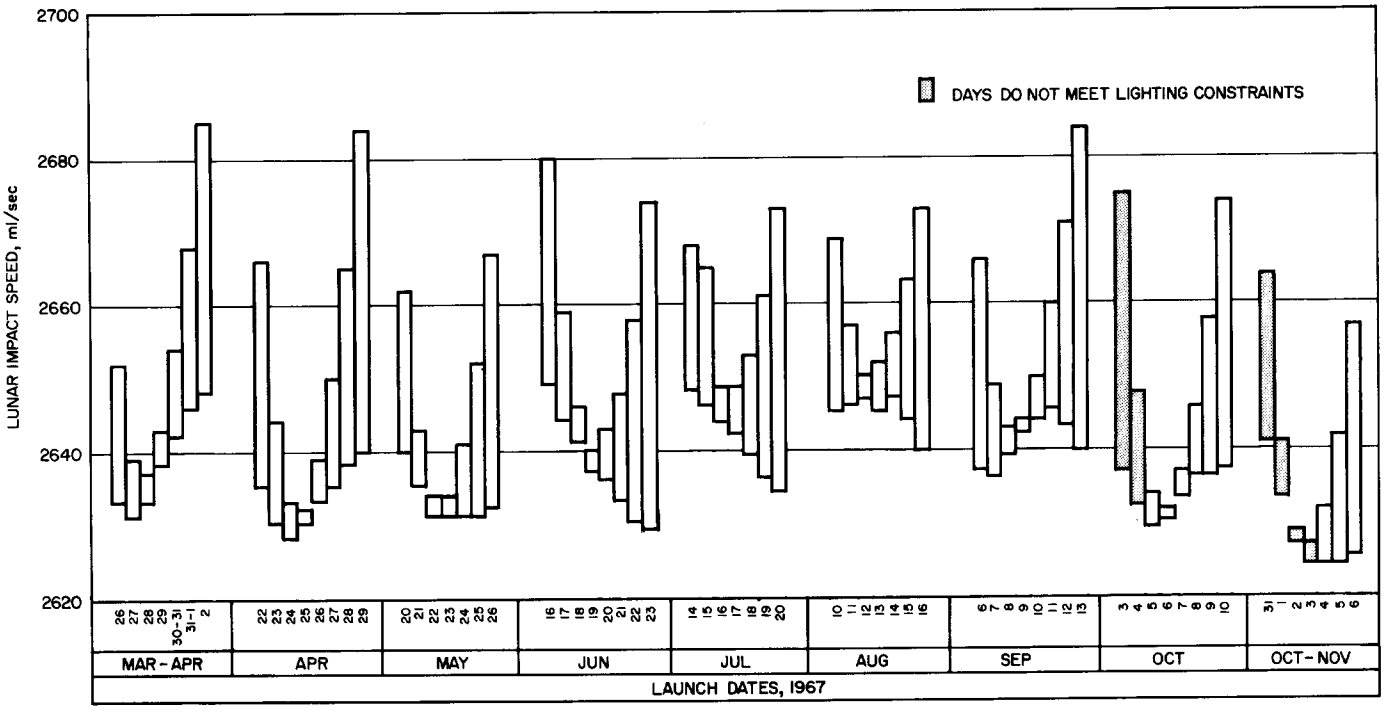

Fig. 18. Variation of direct-ascent impact speed, 1967 (flight time = 63 hr)

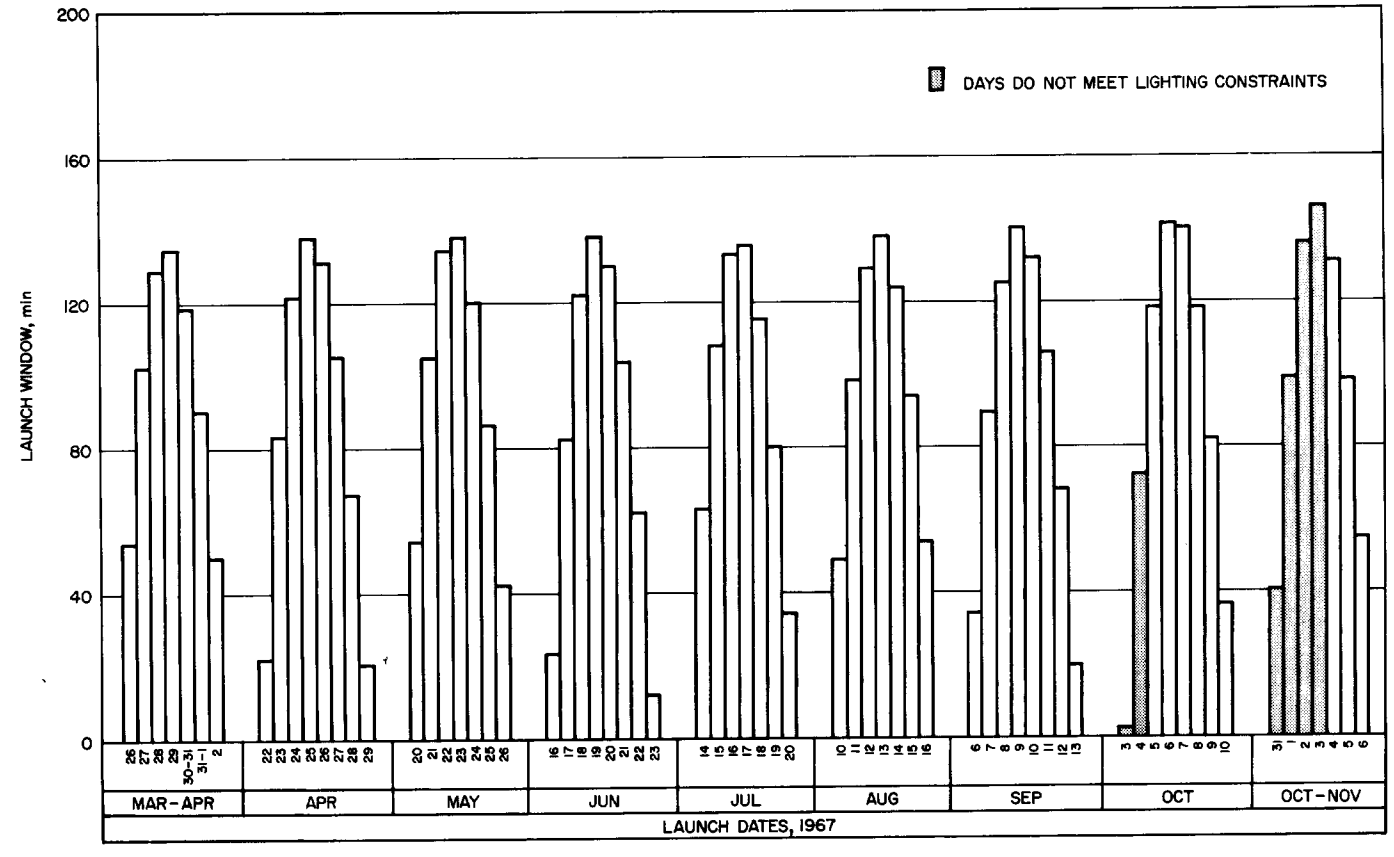

Fig. 19. Direct-ascent launch windows, 1967 (flight time = 63 hr)

3. Trajectory Aspects of Particle Interference with Canopus Sensor

a. Introduction. Loss of Canopus lock was experienced on a number of occasions during the *Mariner IV* flight. The accepted explanation is that particles (probably dust) were knocked off the spacecraft by the impact of meteoroids. Some of these particles, of sufficient size and reflectivity to interfere with the normal operation of the sensor, subsequently drifted into its field of view. The possibility of a similar problem with *Surveyor* has led to a study of particle trajectories. Related studies are being performed to determine the physical characteristics and initial velocities of the particles, and the effect on the Canopus sensor of extraneous particles in its field of view. Specific questions answered here are:

(1) Given the origin of a particle on the spacecraft, what is the probability that it will drift into the sensor field of view?

(2) Given that the particle passes through the field of view, what is the distribution of its distance from the sensor at the point nearest the sensor axis?

(3) How does the time spent in the field of view vary with distance along the sensor axis?

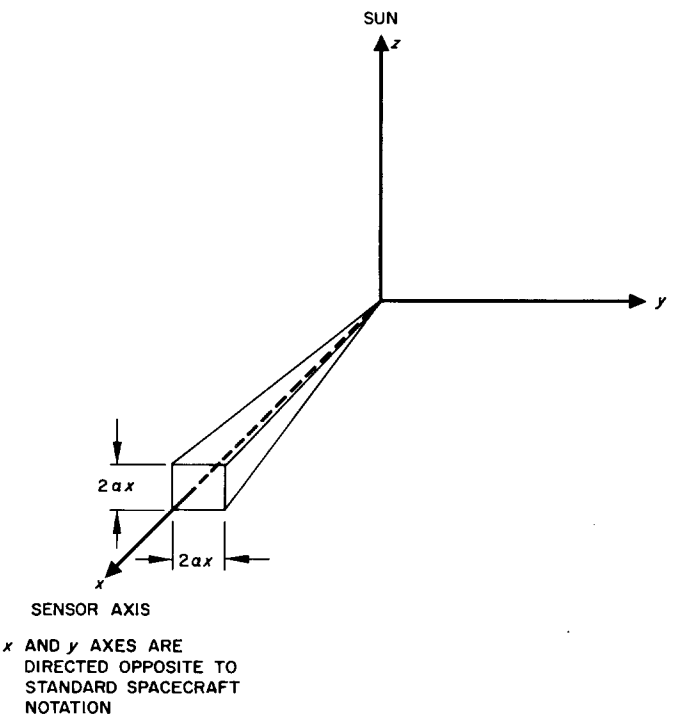

Fig. 20. Spacecraft–Sun geometry

b. Particle acceleration. Since only that portion of the trajectory in the neighborhood of the spacecraft is of interest, it is assumed that there is no motion relative to the spacecraft due to gravitational forces external to the particle-spacecraft system. The gravitational attraction of the spacecraft on a particle may also be neglected, since it produces an acceleration much smaller than that due to solar pressure.

The principal departure from linear motion is, in fact, the result of solar pressure. It is easily shown that the acceleration due to solar pressure is given by

$$a = \frac{K(A/V)p}{\rho} \tag{1}$$

where p = solar pressure = 0.462×10^{-4} dyne/cm^2 on a black body whose surface is normal to incident radiation, A = area normal to spacecraft—Sunline subtended by particle, V = volume of particle, ρ = density of particle (assumed homogeneous), and K = factor that takes into account orientation and reflectivity of surface intercepting solar radiation, $0 \leq K \leq 2$.

The analysis will be confined to spherical particles, in which case

$$a = \frac{0.346 \times 10^{-4}}{\rho R} \text{ cm/sec}^2 \tag{2}$$

Eq. (2) reflects the fact that $K = 1$ for a spherical particle, provided the percentage of incident energy reflected is the same for all points on the particle surface. It will be assumed that the particles are typically described by the parameters $\rho = 1$ g/cm^3 and $R = 0.0035$ cm, so that $a = 0.01$ cm/sec^2.

c. Assumptions. The pertinent geometry is shown in Fig. 20 for the standard cruise attitude, i.e., locked to the Sun and Canopus. The origin is taken at the Canopus sensor. Note that the x and z axes are directed oppositely to the usual spacecraft notation. The field of view is assumed to have a square cross section with a linear dimension of $2\alpha x$, i.e., the half-angle of the field-of-view cone is α. A particle is defined to pass through the field of view if, and only if, its trajectory intersects the x, y plane within the field of view. In this event, the z component of the distance traveled in the field of view will be assumed equal to $2\alpha x$.

In identifying the sources of particles that are most likely to pass through the field of view, the important

considerations are the size of the surface presented to approaching meteoroids and the position of the surface relative to the field of view. The initial position of the particle is designated by the triplet, x_0, y_0, z_0. The initial velocity is assumed to be spherically distributed, so that the initial components $\dot{x}_0$, $\dot{y}_0$, $\dot{z}_0$, are independent random variables. Furthermore, the component velocities are assumed to be drawn from a normal distribution with standard deviation σ. For convenience, $\dot{z}_0$ is, for the most part, treated parametrically rather than as a random variable; however, in all such cases its magnitude is assumed equal to σ.

It is also assumed that the particles are never in shadow after separation from the spacecraft, so that they are subjected to constant solar pressure. The major violation of this assumption occurs in the case of particles originating on the lower surface of the solar panel. However, because of the position of the panel in the cruise position, those particles that drift into the field of view spend only a relatively short time in the shadow.

d. Time spent in field of view. Because of solar pressure, a particle originating at a positive value of z_0 passes through the x, y plane exactly once. If a particle originating at a negative value of z_0 passes through the x, y plane, it does so twice. With $t = 0$ taken as the time at which the particle is separated from the spacecraft, the time of passage through the x, y plane is

$$t = \frac{1}{a}\left[\dot{z}_0 \pm (\dot{z}_0^2 + 2a\, z_0)^{1/2}\right] \tag{3}$$

For positive z_0, only the plus sign is relevant. Should the particle pass through the field of view, the time spent there is

$$\Delta t = \frac{2\alpha x}{(\dot{z}_0^2 + 2\, a\, z_0)^{1/2}} \tag{4}$$

Note that Δt is independent of the sign of z_0.

Fig. 21 contains plots of Δt versus x for several of the more likely particle sources and several values of $|\dot{z}_0|$. For positive z_0 the curves indicate that, unless the source is close to the x, y plane, the time spent in the field of view is relatively independent of $\dot{z}_0$, provided $|\dot{z}_0| < 1.0$ cm/sec.

For the sources located at negative z_0, the chosen values of $\dot{z}_0$ are somewhat greater than those required to penetrate the x, y plane. The latter velocities are 0.55 cm/sec for the flight control sensor group, 0.71 cm/sec for the velocity sensing antenna, and 1.41 cm/sec for Landing Leg 3. When z_0 is negative, the particle may pass through the field of view once, twice, or not at all. If the particle passes through the field of view twice, the value of x, and hence Δt, is generally different in the two directions.

e. Probability of passage through the field of view. *Case I:* $z_0 > 0$. In this case the particle always passes through the x, y plane. The particle passes through the field of view if, at the time of passage through the x, y plane, $x > 0$ and $|y| < \alpha x$. The joint probability of a particle's passing through the field of view (FOV) at a given value of x, $p(x, \text{FOV})$, depends, for a given particle source, only on $\dot{z}_0$. In the case of the solar panel, for example, the following values of z_0 were considered: 1.5, 1.15, 0.70, or -10.0, and 0.41 or -0.72 cm/sec. The corresponding values of the total probability of passing through the field of view are 0.010, 0.0114, 0.0078, and 0.00036.

Case II: $z_0 < 0$. The particle passes through the x, y plane in this case only if $\dot{z}_0 > (-2\, a\, z_0)^{1/2} \triangleq z_{0m}$. If this condition holds, the particle will be considered to pass completely through the field of view if $x > 0$ and $|y| < \alpha x$ on either passage through the x, y plane. Should this condition not hold, the assumption is that the particle does not enter the field of view. In other words, the possibility of the particle's being "turned around" while in the field of view is not considered.

f. Conclusions. Under the assumptions inherent in the model that has been used to analyze the particle dynamics, it may be concluded that not more than 2% of the particles leaving any point on the spacecraft pass through the field of view. For sources located at negative x_0 (this includes all significant sources except Landing Leg 3), the fraction of particles passing through the field of view is strictly limited to 1.6%. The principal assumption required to draw this conclusion is that the initial velocity component in the x, y plane is circularly distributed. Only in the case of the planar array, whose surface is nearly normal to the x-axis in the cruise position, might this not be a good assumption.

Of all the particles separated from the spacecraft, the fraction that enter the field of view is much smaller than 1%, since only those sources and initial velocities that tend to maximize the probability of entering the field of

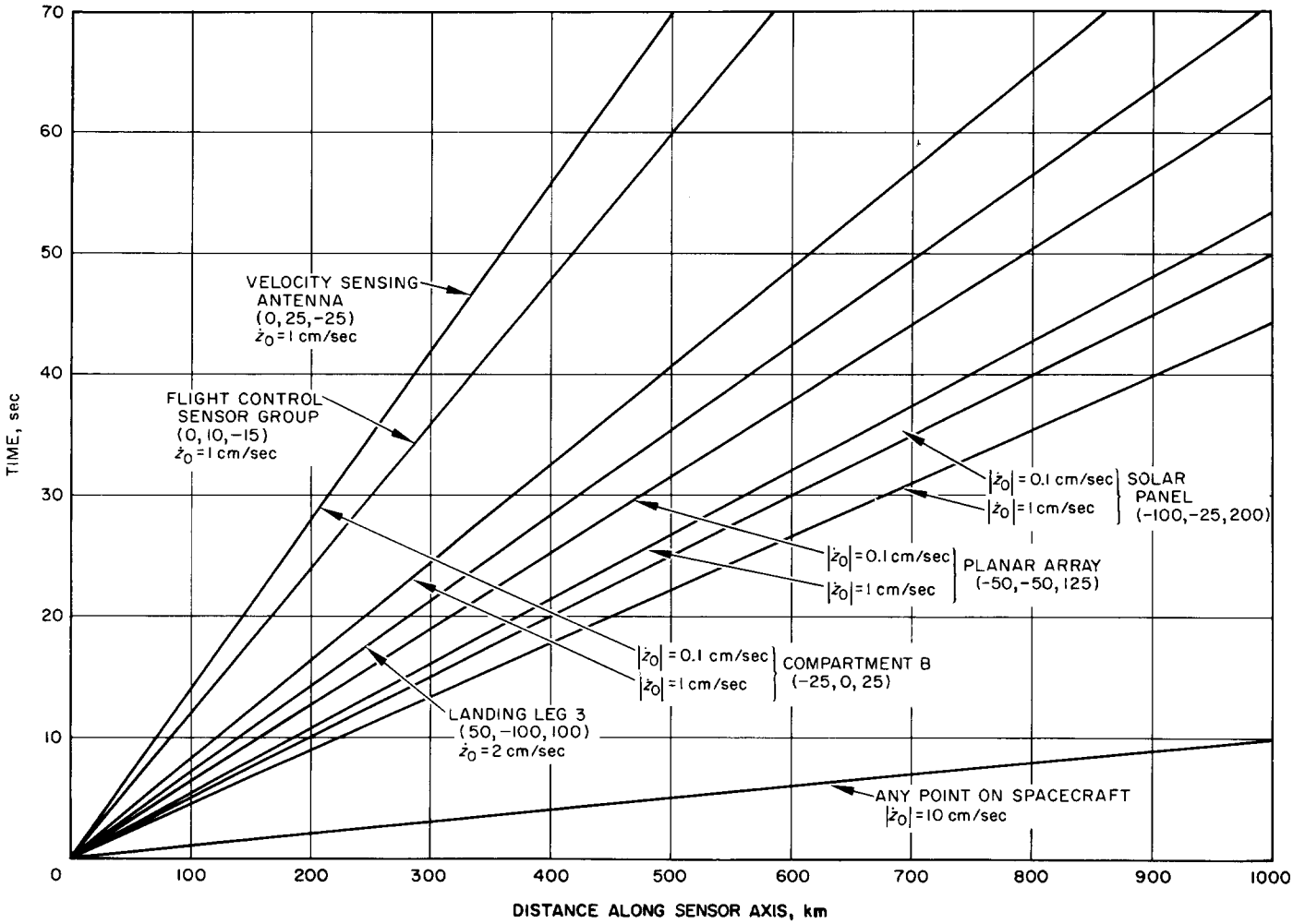

Fig. 21. Time spent in field of view

view have been examined. The most important unknown factor is the distribution of separation velocities. Regardless of the nature of this distribution, however, it seems safe to conclude that not more than 0.2% of the separated particles enter the field of view. Should the separation velocities be characteristically much smaller than 1 cm/sec, the percentage would be substantially less.

An idea of the distribution of times spent in the field of view can be obtained by correlating $p(x, \text{FOV})$ for initial conditions yielding large values for the probability of entering the field of view with the curves in Fig. 21. It is found that the times are typically 10 to 20 sec. Considerably larger times would be encountered, however, should large values of $\dot{x}_0$ be accompanied by small values of $\dot{z}_0$, contrary to the assumption that $\sigma = |\dot{z}_0|$. This is most likely in the case of the planar array. For $\dot{z}_0 = 0$, it can be shown that a particle entering the field of view at $x = 1000$ cm (requiring that $\dot{x}_0 = 6.3$ cm/sec) after being separated from the planar array would remain there for 63 sec.

Finally, it should be noted that the assumptions made about the physical characteristics of the particles affect their motion only through the parameter a. Should the particles be either denser or larger than assumed, a would be reduced. This would have the effect of shifting $p(x, \text{FOV})$ in the direction of increasing x, particularly for z_0 large and positive, and small $|\dot{z}_0|$. The time spent in the field of view would increase for two reasons—first, because of the increased z-distance traveled in the field of view at the larger values of x and second, because of the smaller value of $\dot{z}$ when the particles reach the x, y plane. As an example, for a particle separated from the solar panel with $\dot{z}_0 = 1.15$ cm/sec, if a is halved, the time in the field of view would increase from 15 to 37 sec.

4. DSIF Antenna Constraint on Spacecraft Trajectory

A cursory investigation of the trajectory data for the November launch window revealed that it is possible for the Sun to be very near the RF axis of the Deep Space Instrumentation Facility (DSIF) antenna for portions of the mission. The Sun is a very strong noise source and, consequently, can severely degrade telecommunication link performance if the DSIF antenna is pointing toward it. The severity of the problem is a function of how far the Sun is off the RF axis, the time in the mission that the alignment occurs, and the duration of the alignment.

Experimental data have been provided by JPL showing the signal-to-noise ratio (S/N) degradation observed as a function of the angle between the center of the Sun and the DSIF boresight axis. Fig. 22 is a copy of these data, with the exception that the abscissa is related to the Sun-probe-station (SPS) angle. The three curves represent various system noise temperatures with the middle curve of 50°K being the most representative for *Surveyor*. SPS angles greater than 177 deg appear to be critical in terms of S/N degradation, whereas angles below 170 deg appear to have negligible effect on the telecommunication system performance.

An investigation of the telecommunication system performance for launch dates in December 1965 was undertaken. For each opening and closing of the firing window, the SPS angle was determined as a function of time from injection. The S/N decrease, in db, was determined from Fig. 22 (using the 50°K curves); worst case conditions, Figs. 23a and b (window opening and closing), are

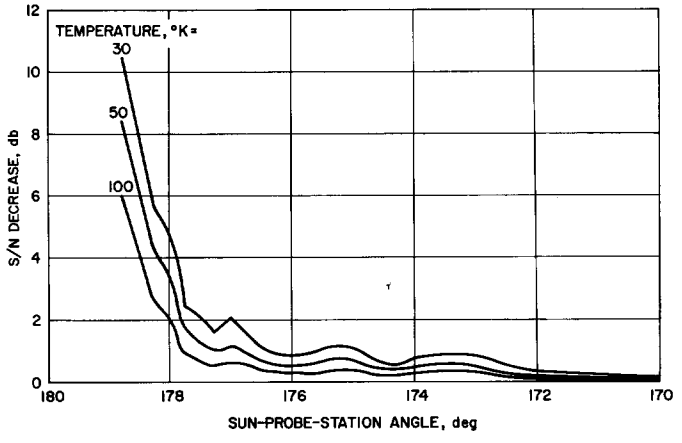

Fig. 22. Signal-to-noise ratio degradation vs Sun-probe-station angle

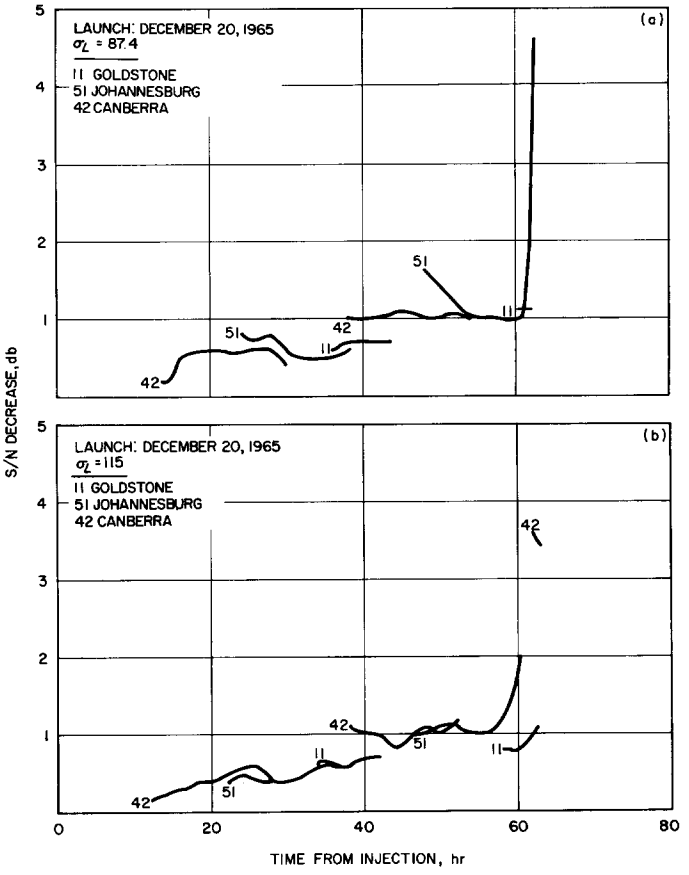

Fig. 23. Signal-to-noise decrease vs time from injection

presented for December 20, 1965. The trajectories for this date appear to yield the worst S/N decrease. For instance, DSIF Station 51, Johannesburg, may experience a 4.5-db decrease in the S/N near lunar encounter if the spacecraft is launched on December 20, 1965, at a launch azimuth (σ_L) of 87.4 deg.

5. Intensity and Spacecraft Coordinates of Earth and Moon for November and December 1965

Selected *Surveyor* trajectories (Table 15) have been examined to determine the intensity (total brightness) and spacecraft coordinates of the Earth and Moon as a function of time from injection.

The first two trajectories in each launch period bound the range of launch azimuths for those days. All others represent the opening or lowest possible launch azimuth. The spacecraft coordinates of the Earth and Moon at any given time from injection are relatively invariant for all trajectories throughout a launch day. For this reason,

Table 15. Selected trajectories

Launch date (1965)	Launch azimuth, deg	Figure numbers			Firing window
		Coordinates		Intensity (total brightness)	
		θ	ϕ		
Nov 20	105.3	1	2	3	Opening
Nov 20	115	4	5	6	Closing
Nov 21	96.3	7	8	9	Opening
Nov 22	90.3	10	11	12	Opening
Nov 23	87.3	13	14	15	Opening
Nov 25	91.7	16	17	18	Opening
Nov 26	98.4	19	20	21	Opening
Nov 27	108.1	22	23	24	Opening
Dec 17	110.5	25	26	27	Opening
Dec 17	115	28	29	30	Closing
Dec 18	99.5	31	32	33	Opening
Dec 19	91.8	34	35	36	Opening
Dec 20	87.4	37	38	39	Opening
Dec 21	86.6	40	41	42	Opening
Dec 22	89.4	43	44	45	Opening
Dec 24	104.9	46	47	48	Opening

only window openings were considered for most days. The spacecraft coordinate system is shown on Fig. 24. These cruise mode coordinates are valid only when the spacecraft is locked to both the Sun and the star Canopus (Ref. 5).

Representative data are shown for a launch date of December 21, 1965. Figs. 24 and 25 show θ as a function of time and ϕ as a function of time, respectively, for the Earth and Moon mass centers, and for three DSIF stations, Goldstone, Canberra, and Johannesburg. Please note the two different scales for the angle ϕ. The angles on each plot under the label "Terminal Conditions" are the spacecraft coordinates of the Earth, Moon, or DSIF station that will exist if the planar array antenna is aligned with Goldstone prior to retro. Fig. 26 illustrates how the intensity of the Earth and Moon varies through the same trajectory.

6. *Mission Effects of Solar Focusing by RADVS[1] Antenna*

Possible effects on the *Surveyor* mission of restrictions placed on the angle between the Sun and the RADVS antenna centerline have been investigated. The restriction is caused by concentration of solar energy by the near-parabolic antenna into a spot of light on the antenna

[1]Radar altimeter and doppler velocity sensor.

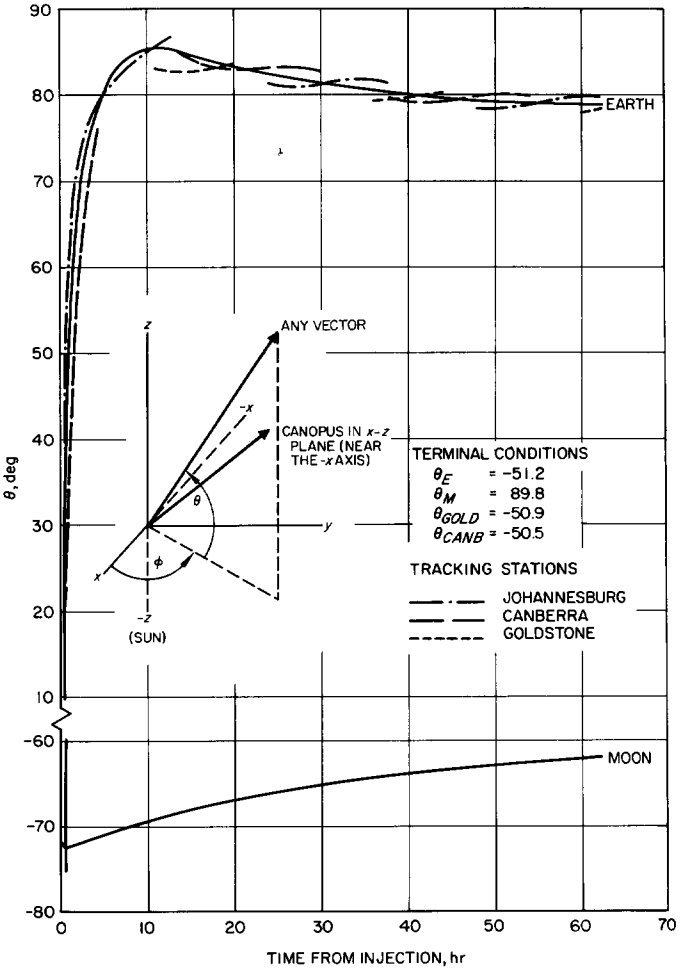

Fig. 24. Angle θ of Earth, Moon, and DSIF stations vs time from injection

septum, and the subsequent possibility of thermal damage to the septum. The study investigated the effects on the November launch period of an optimistic and pessimistic set of angular restrictions.

a. Possible angular constraints. The optimistic constraint is that the Sun must not be allowed steady-state within a zone of ± 35 deg in the plane of the septum and ± 10 deg normal to the plane of the septum. This constraint corresponds roughly to the analytical results in the preliminary Ryan Aeronautical Company report, which suggests corresponding constraints of ± 25 and ± 10–15 deg.

A series of experiments conducted at Hughes Aircraft Company using a light meter and a thermal model of the RADVS antenna indicates a more pessimistic steady-state constraint. Using as a criterion a reduction in concentrated light at the septum to approximately one-fourth

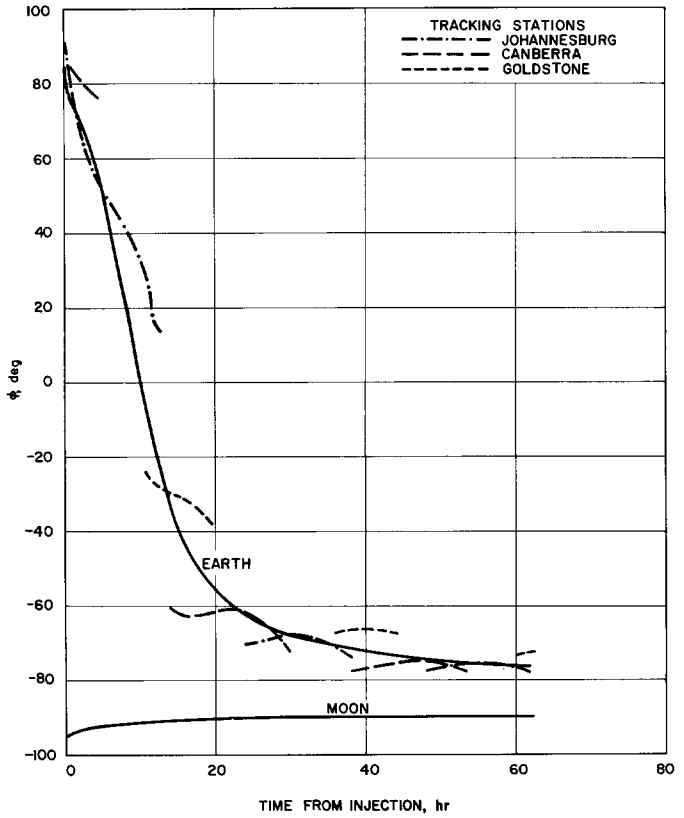

Fig. 25. Angle ϕ of Earth, Moon, and DSIF stations vs time from injection

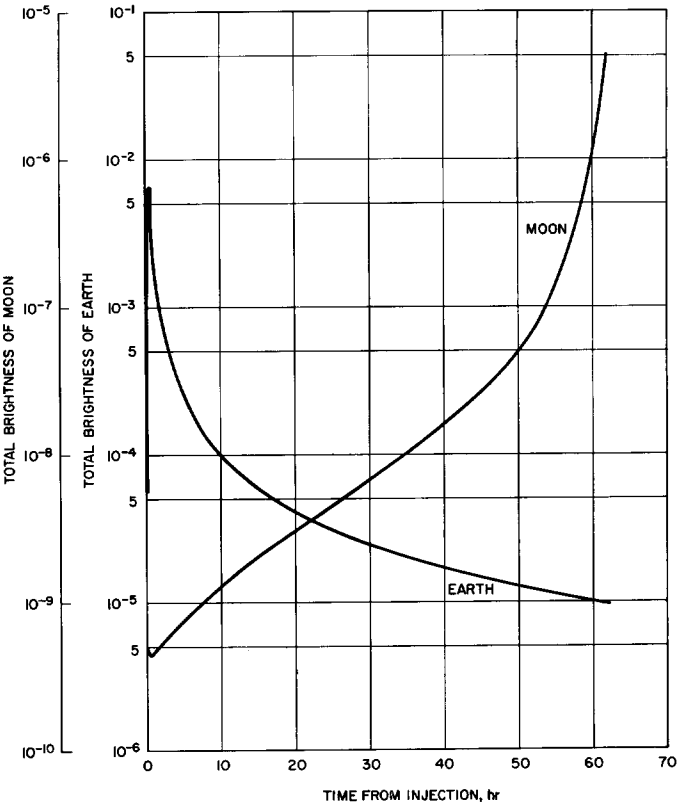

Fig. 26. Total brightness of Earth and Moon vs time from injection

the peak value at normal incidence, the angular constraints are ±55 deg in the plane and ±45 deg normal to that plane of the septum. This is termed the pessimistic constraint. Using the spacecraft coordinate system given in Fig. 27, both sets of constraints are shown in Fig. 28. The above steady-state constraints are assumed to apply while the spacecraft is under inertial attitude control or in a rate-stabilized mode with a maximum rate of 0.51 deg/sec. It is questionable whether the Sun may be allowed to enter these areas while the spacecraft is performing angular maneuvers at 0.5 deg/sec. The preliminary Ryan analytical results indicate that for a very rough surface the temperature rise would be on the order of 150°F, and for a smooth surface it might be 400°F or more (the hard limit is 550°F). Thus it seems doubtful whether angular maneuvers can be performed through the restricted regions.

b. Mission effects. Possible mission effects during post-separation midcourse and terminal phases are discussed below for the November launch period. There is, of course, no problem during the coast phases of the mission since the $-z$-axis is pointed at the Sun (see Fig. 27).

Post-separation phase. The tipoff rates imparted at separation are of a random nature. For the purposes of this analysis, it is assumed that the rate is 3 deg/sec (specification value) and is a combination of pitch and yaw only (no roll). This rate is damped out in approximately 29 sec, with a total angular displacement of 44 deg. At this time the spacecraft enters a rate-stabilized mode with a maximum angular rate of 0.051 deg/sec. The erection of the solar panels begins at separation and is completed in 580 sec. The Sun acquisition maneuver begins immediately thereafter, with a 0.5-deg/sec roll in the negative direction (pitch and yaw axes still in the rate-stabilized mode) until the Sun is acquired by the secondary Sun sensor.[2] The maneuver is then completed by a positive yaw aligning the Sun with the $-z$-axis.

The situation for the November launch period is shown in Fig. 28. The location of the Sun in spacecraft

[2] For the SC-1 spacecraft only; for all subsequent spacecraft plus the SC-1 flight programmer spare, the Sun acquisition maneuver begins at 51 sec after separation and thereafter takes place concurrently with solar panel erection, which begins at separation.

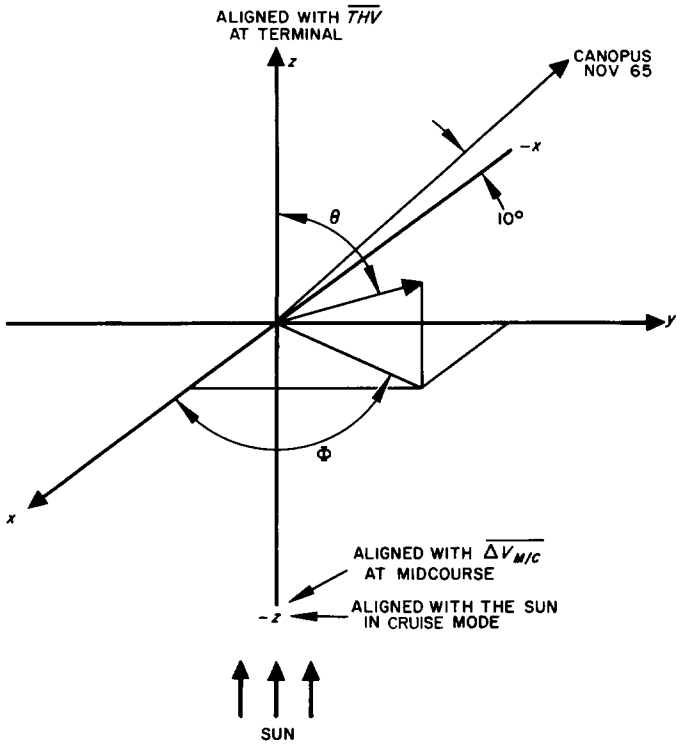

Fig. 27. Spacecraft coordinate system

coordinates during this period is indicated. For the trajectory that results in the Sun being closest to the restricted areas (November 20 launch, opening of the firing window), the extreme positions of the Sun at initiation of Sun acquisition are also indicated. It is assumed that both the tipoff rate of 3 deg/sec and the rate in the rate-stabilized mode are in the same plane and in the same direction, resulting in a maximum possible angular displacement under any circumstances of

$$44 + 0.051\,(580 - 29) = 72 \text{ deg}$$

As shown, a significant portion of cases is within the restricted area defined by the pessimistic constraint.

For a number of trajectories in the November period, the spacecraft is in the Earth's shadow at injection. The maximum time spent in the shadow is 10 min on November 20, decreasing to zero on November 26. Thus, on November 20 the spacecraft will be leaving the shadow at approximately the time the Sun acquisition maneuver begins. As the launch period progresses, the shadow time decreases but the Sun location moves away from the restricted area until the fourth day (November 23), when there is no possibility of the Sun entering the pessimistic

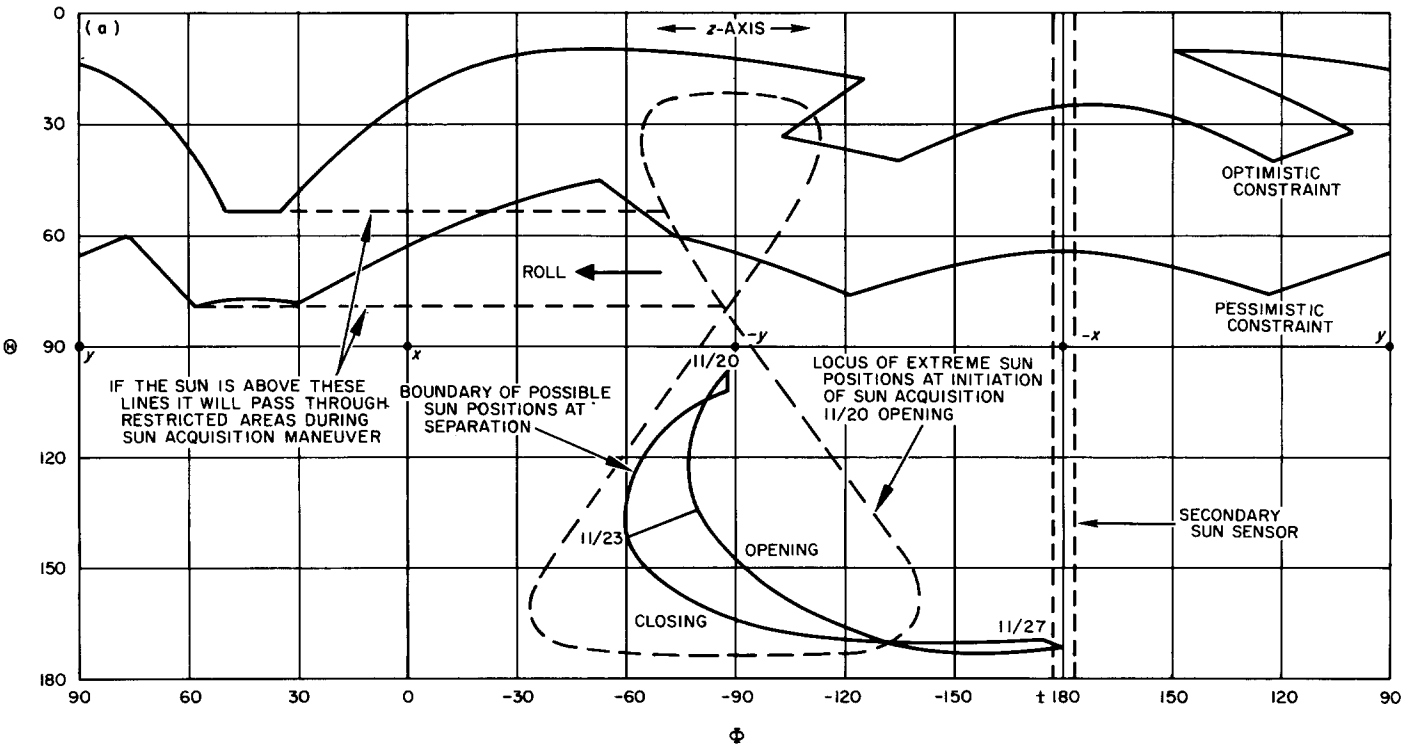

Fig. 28a. RADVS focusing investigation (pre-separation phase)

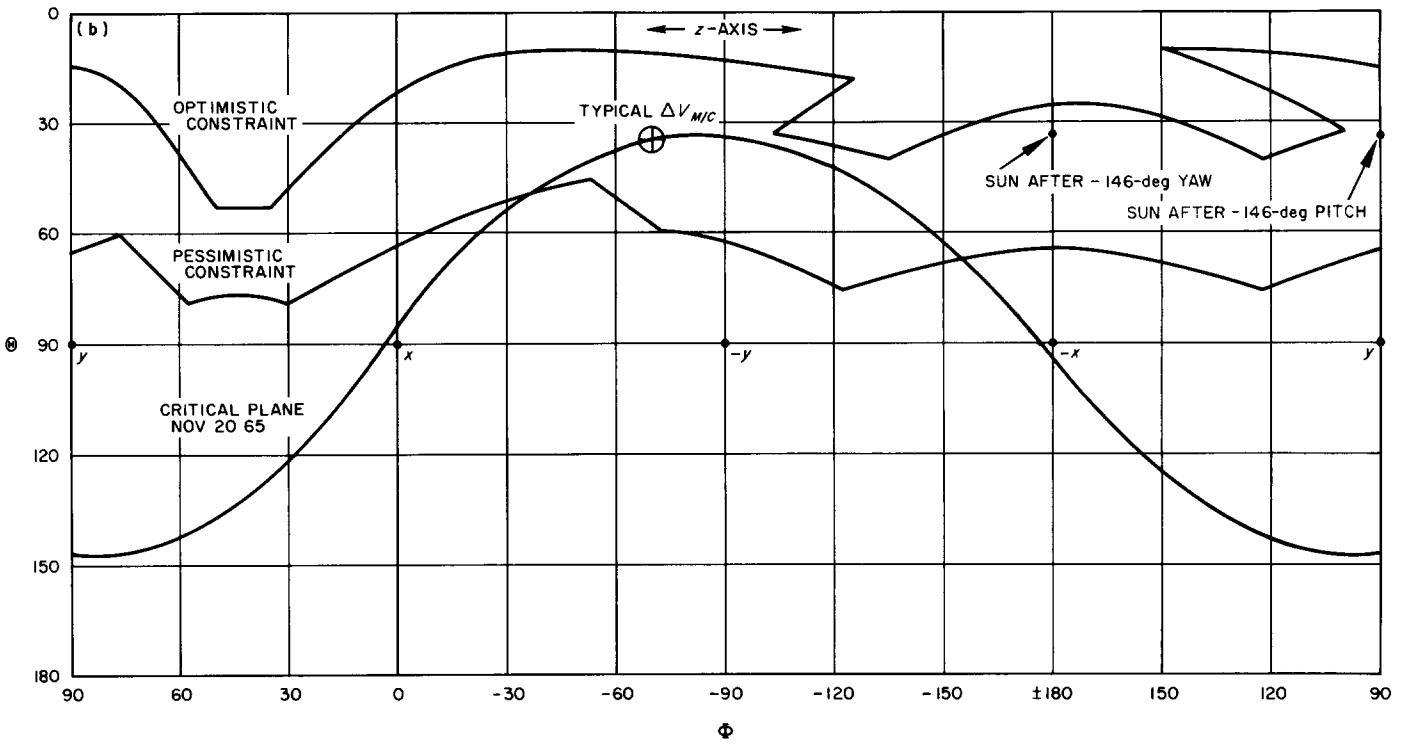

Fig. 28b. RADVS focusing investigation (midcourse phase)

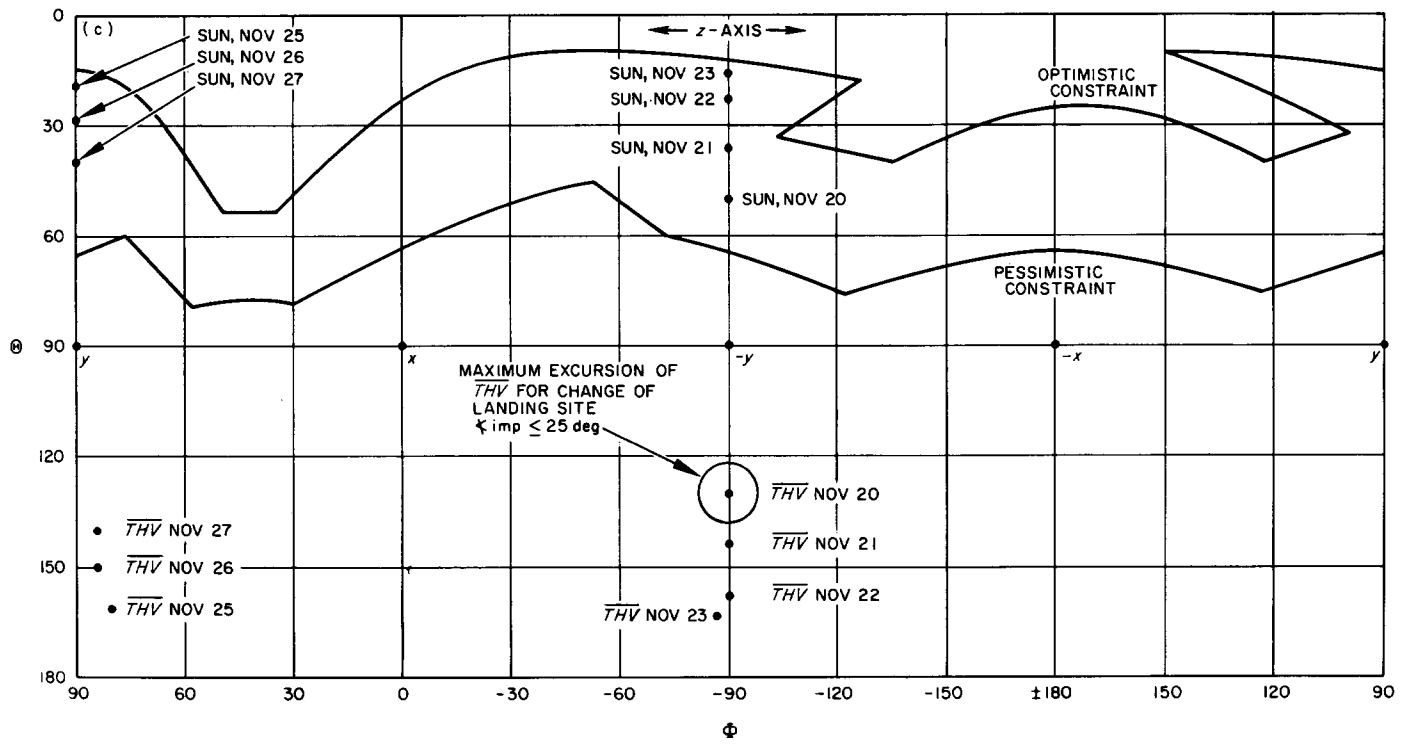

Fig. 28c. RADVS focusing investigation (terminal phase)

restricted area. On November 20 and 21 there is some probability that the Sun will enter the restricted area while the spacecraft is in the rate-stabilized mode and not in the shadow; however, the probability is relatively small. On November 20 there is a fairly large probability, approaching 50%, that the spacecraft will have to travel through the restricted area while rolling at 0.5 deg/sec in the Sun acquisition maneuver.

c. Midcourse phase. (See Figs. 27 and 28). In order to successfully execute the midcourse correction, the spacecraft $-z$-axis must be aligned with the computed midcourse correction vector ($\overline{\Delta V_{M/C}}$), which may occur anywhere in spacecraft coordinates and is composed of a critical plane component (to correct miss only) and a noncritical direction component ($\dot{U}_3$). The $\dot{U}_3$ component will make no first-order change in lunar miss and is used to optimize terminal constraints such as arrival time, main retro burnout velocity, and fuel margin. It is vectorially added to the required critical plane component to form $\overline{\Delta V_{M/C}}$. The location of the critical plane component is necessarily a function of injection errors; hence, the total $\overline{\Delta V_{M/C}}$ may have any location in spacecraft coordinates.

Alignment of the $-z$-axis with $\overline{\Delta V_{M/C}}$ may then cause the Sun to be placed in an unacceptable zone.

A typical $\overline{\Delta V_{M/C}}$ location, in spacecraft coordinates, prior to the midcourse attitude maneuvers is shown in Fig. 28b. In this case the correction is in the critical plane. Alignment of the spacecraft $-z$-axis with this vector will require a positive roll of 20 deg followed by a negative pitch of 146 deg, or a negative roll of 70 deg followed by a negative yaw of 146 deg. During the roll maneuver the position of the Sun remains aligned with the $-z$-axis (along the bottom line of Fig. 28b). However, during the negative pitch maneuver the Sun will move up the $\Phi = 90$-deg line to a position within 34 deg of the $+z$-axis. Or, after the negative yaw maneuver, the Sun will lie on the $\Phi = \pm 180$-deg line 34 deg below the $+z$-axis. Clearly, these two final Sun positions are unacceptable in the light of the pessimistic constraint and possibly marginal with respect to the optimistic constraint.

The critical plane for November 20, 1965, is shown in Fig. 28b for a midcourse maneuver approximately 15 hr after injection. The critical planes for the remaining days of the November launch opportunity tend to approach the $\Theta = 90$-deg line more closely as a result of the changing trajectory-Sun-Moon-Canopus geometry. Table 16 indicates that 27% of the November 20 critical plane is within the pessimistic zone and 17% of the November 21 critical plane lies in the pessimistic region. Here the pessimistic zone is defined to be any region within 45 deg of the spacecraft $+z$-axis and the optimistic zone to be within 10 deg of the spacecraft $+z$-axis. Obviously, if the Sun is maneuvered into the optimistic constraint where $\Theta = 20$ deg and $\Phi = \pm 180$ deg, a final roll maneuver of 55 or -55 deg will remove the Sun from the region without changing the orientation of the spacecraft $-z$-axis (aligned with $\overline{\Delta V_{M/C}}$). Alternately,

Table 16. Percentage of critical plane corrections (miss only) that will place Sun in RADVS constraint zone

Launch date (1965)	Optimistic zone[a]	Pessimistic zone[b]
Nov 20	None	27
Nov 20	None	17
Nov 22	None	None
Nov 23	None	None
Nov 25	None	None
Nov 26	None	None
Nov 27	None	None

[a]Within 10 deg of spacecraft + z-axis.
[b]Within 45 deg of spacecraft + z-axis.

Table 17. $\dot{U}_3$ component requirements to prevent Sun from entering pessimistic zone[a]

Launch date (1965)	$\dot{U}_3$ requirement, m/sec	Total $\overline{\Delta V_{M/C}}$ requirement, m/sec	Resultant terminal effects			
			Impact velocity, m/sec	Flight time, min	Burnout velocity, ft/sec	Fuel margin, lb
Nov 20	−16.3	52.5	+9.8	−41.0	+20.0	Slight
Nov 21	− 5.2	50.4	+3.2	−13.0	−10.0	Negligible

[a]50-m/sec critical plane component located in worst position in critical plane.

angular maneuvers could be performed to avoid entering the optimistic zone entirely. Table 16 also shows that the critical planes for the remaining days of the November opportunity never peak higher than the $\Theta = 45$-deg line.

Table 17 shows the $\dot{U}_3$ component requirements necessary to prevent the Sun from entering the pessimistic zone, given the critical plane component oriented in the worst possible direction ($\Theta = 33$ deg, $\Phi = -86$ deg). The sign and value of the $\dot{U}_3$ component must be such that the resultant total $\overline{\Delta V_{M/C}}$ will lie below the $\Theta = 45$-deg line; the pitch or yaw then required to align $\overline{\Delta V_{M/C}}$ with the z-axis will never align the Sun *above* the 45-deg line. Only launches on November 20 and 21 have been considered; the latter days of the launch opportunity do not violate the pessimistic region. The resultant terminal effects shown in Table 17 indicate that when $\overline{\Delta V_{M/C}}$ is changed by varying $\dot{U}_3$ to avoid the RADVS constraints, the effect is significant, though not sufficient to seriously degrade terminal descent mission success. However, the total $\overline{\Delta V_{M/C}}$ above 50 m/sec must be manually timed, which will result in landing accuracy degradation by perhaps 100 km, larger than the current expected standard error.

Table 18 shows, for both optimistic and pessimistic zones, the $\dot{U}_3$ requirement, given $\overline{\Delta V_{M/C}}$ of 50 m/sec initially aligned with spacecraft $+z$-axis (the worst possible direction) for November 20, 1965. The necessary variation of $\dot{U}_3$ with regard to the pessimistic zone will degrade mission success; the necessary manual timing of the maneuver will cause a reduction in landing accuracy on the order of double the specified requirement.

d. Terminal phase. The terminal-phase attitude maneuver sequence reorients and aligns the spacecraft $+z$-axis with the computed thrust vector $\overline{THV}$. To a first approximation, $\overline{THV}$ lies along the spacecraft velocity vector at retro ignition; hence, the orientation of $\overline{THV}$ depends on launch date and the selected landing site.

Worst day, November 23. The position of the Sun after the terminal attitude maneuvers is 16 deg from the $+z$-axis. As shown in Fig. 28c this is at best marginal for the optimistic zone and unacceptable for the pessimistic zone. Also, as indicated, selection of a new landing site will not provide an acceptable Sun position (within the soft-landing limits of the spacecraft).

Best day, November 20. The Sun position after the terminal attitude maneuvers is 50 deg from the $+z$-axis; this is reasonable for the optimistic zone, but unacceptable for the pessimistic zone.

In conclusion, in the terminal phase all days of the launch opportunity will place the Sun within 50 deg and possibly within 16 deg of the spacecraft $+z$-axis. Consideration of the pessimistic constraints will thus preclude successful mission capability in the November launch opportunity.

e. Conclusions. The most serious problem arises in the terminal phase of the mission. For the assumed pessimistic constraint on all days of the November period, the Sun is within the restricted area, precluding the possibility of a successful soft landing. Furthermore, one day (November 23) is within 5 deg and two days (November 22 and 25) are within 10 deg of the optimistic boundary. It should be noted that this is the ± 10-deg normal to the septum boundary, which is, according to the Ryan data, possibly ± 10–15 deg. Thus, it appears that at least one launch day in the November

Table 18. $\dot{U}_3$ component requirements to remove Sun from either zone

RADVS zone	$\dot{U}_3$ requirement, m/sec	Total $\overline{\Delta V_{M/C}}$ requirement, m/sec	Resultant terminal effects			
			Impact velocity, m/sec	Flight time, min	Burnout velocity, ft/sec	Fuel margin, lb
Optimistic	− 9.5	51.0	5.7	−23.7	14.0	Negligible (sufficient fuel margin remains)
Pessimistic	−37.3	62.4	22.4	−93.5	11.0	Serious (margin reduced to 0–1σ region)

[a]50-m/sec correction initially aligned in worst possible direction. Launch date: Nov, 1965, the worst day of launch opportunity.

period may be lost, and another two days may be marginal even with the most optimistic constraints.

The problems arising during the post-injection and midcourse phases are less clearly defined, because of their statistical nature. However, it appears that the midcourse maneuver will be severely restricted with the pessimistic constraints sometimes resulting in a degradation of the probability of mission success. The post-separation phase problem depends primarily upon the transient constraints that will be placed upon 0.5-deg/sec maneuvers. These constraints are not well defined.

It should be emphasized that the above results are for the November launch period only. The results for subsequent months may or may not be similar.

7. Compensation of Spacecraft Mechanization Errors

The possibility of reducing landing site errors and main retro burnout dispersions through the compensation of spacecraft mechanization errors has been explored periodically and, in some instances, action has been initiated. The various methods of compensation investigated, their significance, and present status are presented in this discussion. The methods considered are those that can be implemented through additional programming to the midcourse and terminal guidance program (Ref. 1), and/or additions to the spaceflight operations sequence of events (Ref. 6). In general, the compensation schemes discussed are based on spacecraft parameter measurements obtained from the preflight test data and in-flight telemetry data.

The specific values of some of the data used in this study are obsolete and should not be used to draw specific quantitative conclusions; however, the general concepts and conclusions, which are independent of the data differences, are still valid.

Fig. 29 is a plot of midcourse velocity magnitude and angle error as a function of the magnitude of the velocity correction. Also shown is the corresponding landing site error, which is the resultant system parameter of concern. Three cases are shown—uncompensated, present compensation, and optimistic compensation. The last represents an asymptotic best case, in that it cannot be reasonably expected to achieve the accuracies shown for the optimistic case. Thus, attainable levels of accuracy will fall between the curves for present and optimistic compensation. The following conclusions are drawn from Fig. 29:

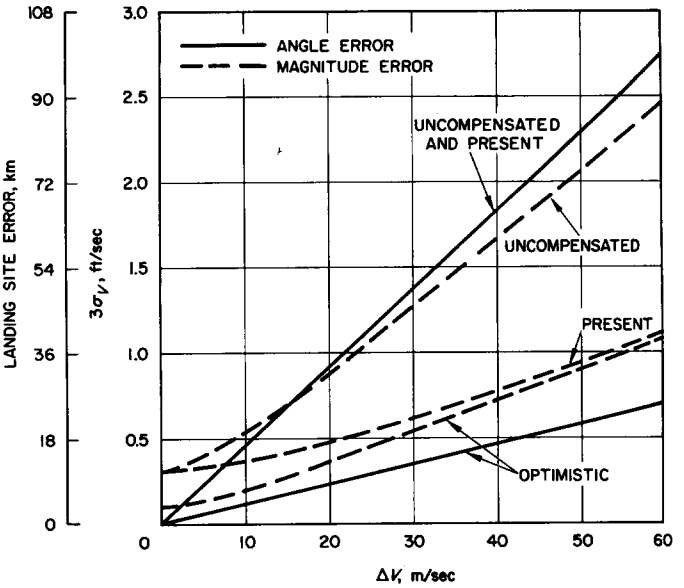

Fig. 29. Midcourse velocity magnitude and angle error vs magnitude of velocity correction

(1) Since the bound on the landing site error is determined by the larger of the two errors, magnitude or angle, compensation of one error does not necessarily reduce the landing errors. This is true for ΔV's greater than a specific value. Fig. 29 shows that for the uncompensated case, compensation of magnitude errors for ΔV's greater than 15 m/sec does not result in any significant reduction in landing site errors if the angular error is uncompensated. Below 15 m/sec this is not true. This is the present status of the expected errors.

(2) If both magnitude and angle errors are optimistically compensated, the magnitude error dominates; therefore, compensation of the angle error beyond the magnitude error, for all ΔV's, is not significant.

(3) A 56% reduction in the landing site error is possible with optimistic compensation.

(4) Only spacecraft mechanization errors were considered. To assess the total landing site error, the tracking uncertainties must be included, for there is no reason to compensate for mechanization errors if the tracking errors are much larger. Fig. 30 shows the total landing site error as a function of ΔV. Also parameterized are the uncompensated (present and optimistically compensated cases for various tracking uncertainties, $3\sigma_T$. If the optimistic compensation could be attained, the total landing

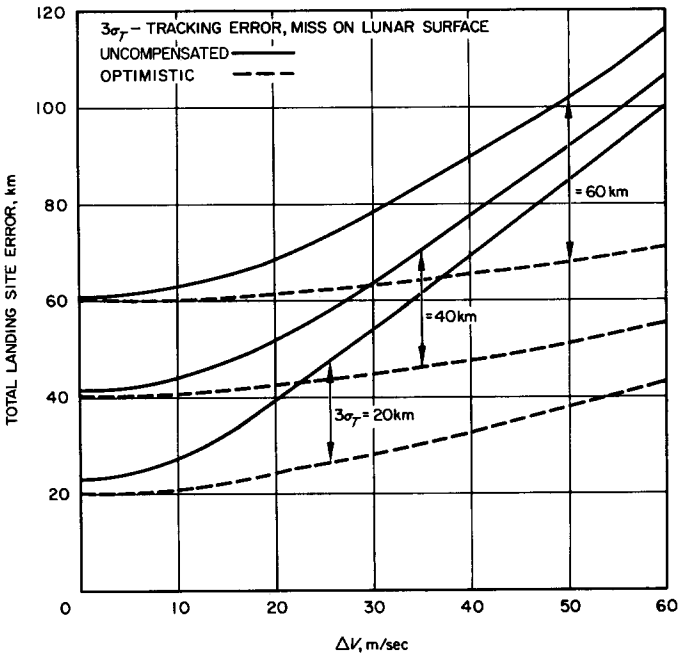

Fig. 30. Total landing site error $3\sigma_T$ vs midcourse velocity $\triangle V$

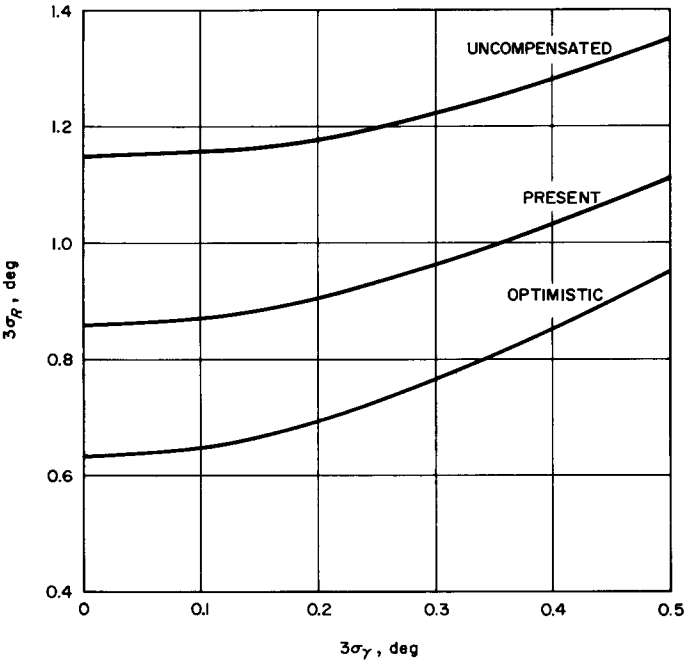

Fig. 31. Main-retro pointing error $3\sigma_R$ vs uncertainty in direction of unbraked impact velocity $3\sigma_\gamma$

site error could be significantly reduced for ΔV's greater than approximately 10 m/sec.

When considering main-retro pointing errors, it should be noted that tracking error is not a spacecraft mechanization error and should be considered in a position similar to the tracking error at midcourse. During a mission this value will be measured and will most likely be less than 0.4 deg. The variations in the total pointing error, $3\sigma_R$, as a function of the tracking error, $3\sigma_\gamma$, are shown in Fig. 31 for the uncompensated, present, and optimistic cases.

The value of compensation with respect to the retro pointing direction is not so clearly defined as it is with respect to midcourse errors, but the following statements indicate it in a general way:

(1) Retro pointing error directly affects burnout flight-path angle; reduction of this dispersion by any significant amount results in an increase of mission success confidence. Since this is a fundamental *Surveyor* terminal descent design problem, such an improvement is of great consequence.

(2) During the terminal phase of a mission, the resultant pointing error could be used to optimize the terminal descent control parameters.

(3) Through the use of compensation, the expected pointing error can be reduced; therefore, future spacecraft designs can be based on this reduction. The key feature is a reduction of the allowable minimum burnout velocity.

The following comments are also applicable to the data used for this study:

(1) The uncertainties associated with the measurements have not been determined; therefore, the value of using these measurements for compensation is questionable.

(2) The signs ($\pm$) corresponding to the measurements were not retained; the latter therefore cannot be used for compensation and new measurements would be required.

(3) Since there will always be uncertainties associated with the measured values, the amount of compensation possible will fall short of the optimistic case.

8. A-21A Terminal Descent Performance and Propellant Requirements Analysis

A comprehensive A-21A terminal descent performance analysis has been completed. The important design constraints were considered fixed, and include: (1) non-zero

midcourse maneuver requirement, (2) maximum unbraked impact angle capability, (3) payload requirements, and (4) maximum injected weight. Because of the inherent uncertainties involved in the analysis of an evolving design, the study has covered a range of injected weights from the specified value of 2450 lb to a maximum of 2500 lb.

In contrast to previous design studies of this type, the major portion of the terminal phase design having a statistical nature has been carried out through use of a terminal phase Monte Carlo simulation program, a portion of a larger mission simulation computer program. Results from this study are only slightly different from those of previous studies utilizing linear transformation variables and graphic techniques; nevertheless, the decrease in the number of simplifying assumptions obtained through use of the more complete simulation serves to validate the results of previous studies, and outweighs any loss of engineering "feel" for the problem usually obtained through the more traditional analytical and graphic techniques.

Computation of nominal parameter values continues to be carried out through use of a numerically integrated terminal descent computer program, since a small percentage error in nominal values would nullify the value of statistical propellant dispersion computations.

a. Summary. At the beginning of this study, several items had not been analyzed to the extent necessary for a design freeze. They were: (1) retro burnout velocity constraints, (2) unbraked impact velocity range, (3) propellant requirements, and (4) a relatively new constraint of maximum terminal phase descent time as dictated by radar altimeter and doppler velocity sensor (RADVS) operating time constraints. Through use of Monte Carlo techniques, the minimum and maximum retro burnout velocity constraints have been fixed at 300 and 410 ft/sec, respectively. This burnout range, in turn, allows an equivalent range on unbraked impact velocities of 38 m/sec. Recent study of the A-21A launch periods shows that the actual unbraked impact velocities for direct ascent trajectories range from a minimum of 2632 to 2649 m/sec. Therefore, the required unbraked impact capability is 17, and the actual capability (assuming a constant midcourse maneuver of 50 m/sec) is 38 m/sec. The additional capability of 21 m/sec is thus available for reducing the minimum permissable midcourse maneuver of 50 m/sec to approximately 37 m/sec for an assumed maximum unbraked impact velocity.

Propellant consumption design points have been fixed as follows: The retro loading requirement is computed for minimum unbraked impact velocity, minimum retro burnout velocity, and maximum midcourse maneuver. Maximum vernier propellant consumption occurs at maximum unbraked impact velocity, maximum midcourse maneuver, and maximum (45-deg) unbraked impact angle. Final propellant weight numbers will be found in Part 8c, below.

The terminal operating time study, although not complete, has progressed sufficiently to indicate that to at least a 0.99 probability level there should be no problem in meeting RADVS operating time constraints.

b. Terminal phase statistical analysis.

Terminal command descent segments. Assuming the possibility of spacecraft injected weights above the specified value of 2450 lb, command descent segment designs have been carried out by Flight Control for injected weights of 2450 and 2500 lb; the latter design (Fig. 32) can be used, with uniformly varying dry weight penalties, for injected weights ranging from 2450 to 2500 lb. Because any differences can be expected to be small over this range, all statistical analysis was carried out using the 2500-lb design, which results in a more conservative design at lesser weights.

Maximum and minimum spacecraft weights at command segment intercept were given for both weight spacecraft. Because of the requirement that the 2500-lb spacecraft design be valid for injected weights down to 2450 lb, minimum weight and therefore minimum acceleration are the same for both spacecraft.

Minimum nominal retro burnout velocity. The minimum nominal retro burnout velocity is fixed by a combination of three major parameters at the beginning of the vernier phase: (1) spacecraft flight-path angle and its effect on touchdown conditions, (2) RADVS operating constraints, and (3) vernier propellant consumption. Considering the above in an approximate order of decreasing importance, the following discussion examines the RADVS operating constraints and their effect on the terminal design philosophy.

The present design of the spacecraft attitude-control system will accommodate the two doppler radar operating states of reliable and conditionally reliable. A reliable state implies that all three doppler radar beams have locked on a return signal, and are giving good information. The conditionally-reliable state implies only that

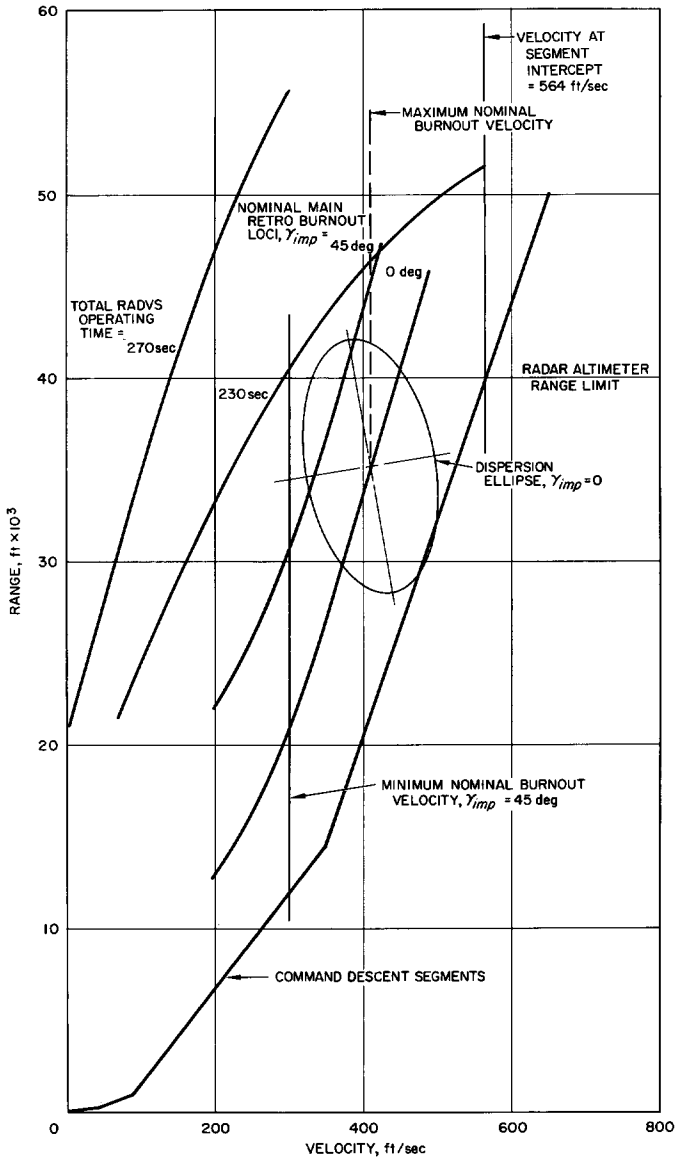

Fig. 32. Main-retro burnout constraints and terminal descent control segments

one or more radar beams have locked on, and are giving good signals. In this latter state, spacecraft steering is based on the assumption that those beams that have not locked on are measuring zero velocity. For low burnout velocities and corresponding low ranges, this assumption is nearly true, since the major cause of a radar beam not locking on is that beam velocities are below the minimum lockup velocity of 30 ft/sec. However, to maintain a conservative design, minimum burnout velocities of the A-21 spacecraft have always been fixed to prevent radar conditionally-reliable operation. Because of a more restrictive burnout velocity range incurred on the A-21A design, this conditionally-reliable philosophy must be re-evaluated.

A second reason for a radar beam not locking on the return signal and remaining locked up is lack of sufficient signal strength. Whereas range along the spacecraft z-axis is relatively small for low burnout velocities, spacecraft flight-path angles of 45 deg can produce beam incident angles of 70 deg. As the spacecraft flight path relative to the local vertical increases above 45 deg, the worst-case radar-beam incident angle increases above 70 deg, with a resultant rapid increase of beam range. Since radar performance analysis becomes uncertain above incident angles of approximately 65 deg, it is prudent to limit spacecraft flight-path angles to 45 deg. In Fig. 33, which is a plot of failure probability versus nominal retro burnout velocity, it will be seen that the probability that the spacecraft flight-path angle will exceed 45 deg is almost identical to the probability that one or more radar beams will have a velocity of less than 30 ft/sec. Given, then, that the maximum spacecraft flight path is constrained to 45 deg because of radar considerations, the conclusion may be drawn that fully reliable radar operation can be maintained with little or no cost to performance. In addition, the maximum spacecraft attitude at touchdown due to initial flight-path conditions will also then remain within tolerable bounds.

Assuming a 45-deg flight-path angle as a design constraint, and including the higher confidence of using a 1%, as opposed to the specified 0.75%, 3σ retro total impulse variation used in Fig. 33, Fig. 34 was used as the basis for fixing minimum and maximum nominal burnout velocity. Noting the rather gradual decrease in the probability of violating the 45-deg design constraint, a minimum nominal burnout velocity at 300 ft/sec was chosen.

Maximum burnout velocity. Excluding parameters such as vernier propellant consumption and descent time, which will be discussed later, RADVS sensitivity is the major constraining factor in determining a maximum nominal burnout velocity. To better examine these constraints, a mathematical model of the doppler velocity radar was incorporated into the terminal phase Monte Carlo program.

The basic continuous wave radar equation for the lunar RADVS is

$$P_r = \frac{P_t G \lambda^2}{32\pi^2 R^2} [\eta F(\theta)]$$

where P_t = power transmitter, G = peak antenna gain, λ = operating wavelength, R = slant range (along beam

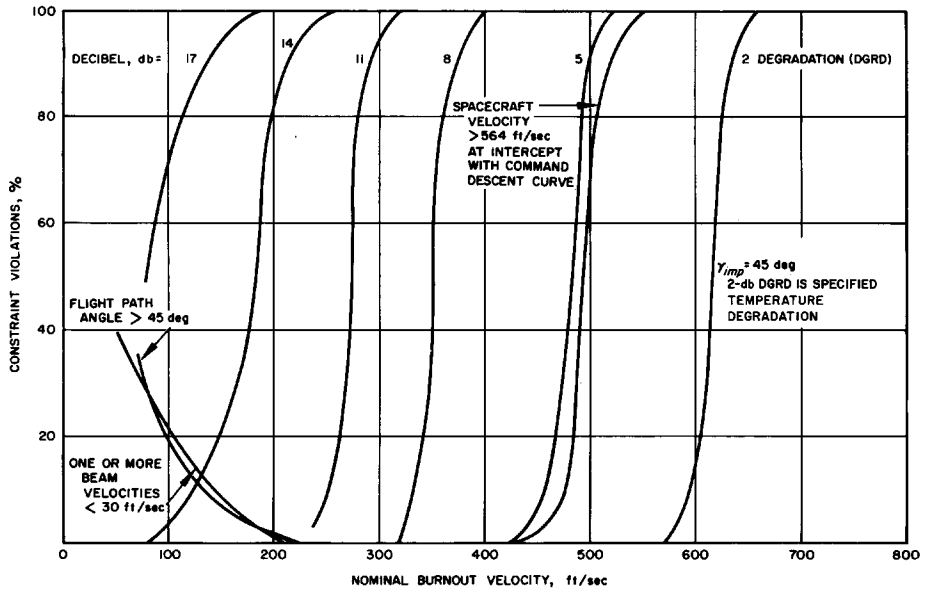

Fig. 33. Terminal phase constraint violations vs nominal burnout velocity (¾ % I_{sp} dispersion)

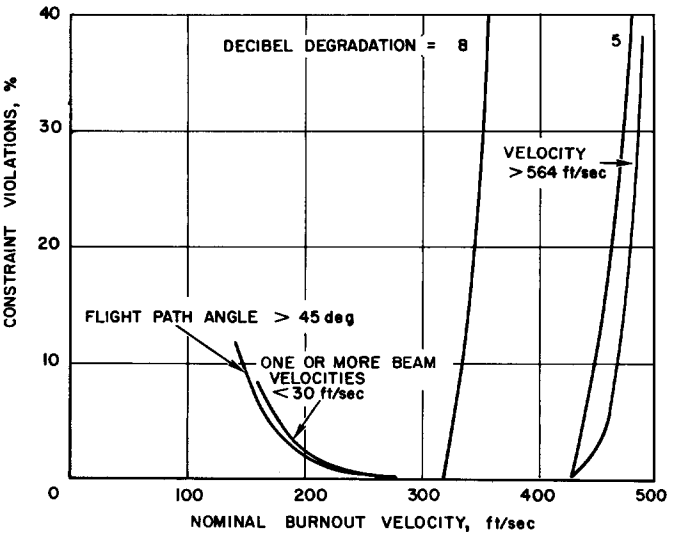
DECIBEL DEGRADATION = 8
5
VELOCITY >564 ft/sec
FLIGHT PATH ANGLE > 45 deg
ONE OR MORE BEAM VELOCITIES <30 ft/sec
CONSTRAINT VIOLATIONS, %
NOMINAL BURNOUT VELOCITY, ft/sec

Fig. 34. A-21A constraint violations at retro burnout vs burnout velocity (γ_{imp} = 45 deg; 1 % I_{sp} dispersion)

axis), θ = incidence angle (of beam axis), and $\eta F(\theta)$ = Muhleman lunar model (as revised). This equation is examined for each of the doppler velocity sensor beams to predict the signal power available on that beam as a function of the operational variables R, θ. Because the signal is itself a spectrum of doppler frequencies, some of this energy may lie outside the fixed bandwidth of each beam's frequency tracker, causing "spectral spreading loss." In addition, a degradation factor is included to account for off-nominal radar performance.

The minimum signal power condition on the ith beam is expressed as

$$(P_{r_i} + L_i) \geq P_{min}(f_i) + DGRD$$

where, as hereafter, db and dbm are used for convenience. In addition, a fixed doppler frequency band is searched by each beam tracker to acquire its lunar reflected signal, and this condition is examined first for satisfaction of $0.8000 < f_i < 18.90$ where, for convenience, all frequencies are in kilocycles per second. The spectral spreading loss is approximated as that for a gaussian spectrum through a rectangular bandwidth. The tracker sensitivity P_{min} has been referred to each beam's receiving feedhorn, for consistency of reference, by modification of basic tracker sensitivity data furnished by Ryan Aeronautical Company, the RADVS supplier.

For ease of reference, the *DGRD* factor has been referred to specified performance at ambient conditions, the conditions for tracker sensitivity test measurements. The Ryan nominal allowance for temperature degradation is 2 db; hence, the 2-db curve noted in Fig. 33 is the nominal in-flight performance for nominal lunar reflectivity as well. The sum of off-nominal radar performance plus lunar terrain variation from average reflectivity is thus accounted for by a single *DGRD* factor shift from the 2-db case. Actual measured sensitivities have been as much as 10 db better than specified, but this cannot be required of the supplier. By *Surveyor* System Functional Requirements (224510 E, 4.6.1), the lunar terrain reflectivity variation below average is −6 db (required), −10 db (desired).

The radar altimeter is temporarily simulated by its acquisition capability as required by specifications. Separate hand calculations have shown adequate gain margin, so this is conservative. Signal power conditions analogous to the doppler velocity sensor simulation are planned for incorporation. They will be generally similar,

except that the radar altimeter signal bandwidth is determined primarily by the variation of range across its beamwidth, and only secondarily by the spread of doppler frequencies involved.

For the specified radar altimeter capability of 40,000-ft range, Fig. 32 shows that this limit crosses the command descent segments at a velocity of 564 ft/sec. If at the time of spacecraft intercept with the command descent segments, the radar altimeter has not acquired its returning signal, the spacecraft acceleration will remain at minimum value, causing it to drop below the command segments, with a resultant possibility of hard landing. Therefore, a definite constraint on maximum burnout velocity is that at command segment intercept the spacecraft velocity must be less than 564 ft/sec. Fig. 34 shows that the probability of spacecraft velocities being above 564 ft/sec rises very sharply for nominal burnout velocities much above 425 ft/sec. For reasonable conservatism, 410 ft/sec would seem to be a suitable maximum nominal velocity from this standpoint.

Returning to the problem of doppler radar signal acquisition, Fig. 34 shows that a 5-db *DGRD* curve for the probability of doppler radar lockon, given the worst-case spacecraft roll-attitude for single beam, is nearly coincident with the 564-ft/sec radar altimeter constraint. Noting again that the specification is -2 db and that allowance must also be made for 6-db degradation due to terrain reflectivity variations, one finds that the 8-db *DGRD* curve is equivalent to the maximum worst-case flight condition. If the maximum burnout velocity were to be fixed based on the -8-db curve, there would be little or no burnout velocity range available to accommodate impact velocity variations, which would result in unacceptable launch window constraints. The relevant question then arises: given a design to a *DGRD* factor of 5 db (-3-db terrain variation), which is coincident with the radar altimeter constraint, what will be the probability of mission success if in reality the terrain variation is -6 db?

Given the worst spacecraft roll-attitude for single-beam lockon, the worst beam would not lock up because of a 3-db deficiency in gain, while the other two beams would have a high probability of lockup because of a 10-db margin. The RADVS would then be in a conditionally reliable mode, assuming that the nonreliable beam is measuring zero velocity. In this condition, the spacecraft would rotate toward the vertical. Since for high burnout velocities the maximum expected flight-path angle is 35 deg, this is the maximum angle for which the nonreliable beam would have to acquire to avoid further complications. Since a spacecraft rotation from 45 to 35 deg produces a 4-db gain increase along this beam, the probability is high that fully reliable operation will occur.

With the combined probability of having a maximum unbraked impact angle, worst-case roll attitude, and maximum terrain reflectivity variation, being very small, and also with a good probability of better-than-specification RADVS performance, the maximum design burnout velocity has been fixed at the radar altimeter constraint at 410 ft/sec, consistent also with the 5-db *DGRD* factor limit.

Maximum descent times. Because of RADVS temperature constraints, the maximum RADVS operation time, including a 0.5-min warmup time, has been set at 4.5 min. The time parameter has not yet been included in the Monte Carlo simulation. Therefore, in order to quickly assess the impact of this constraint on the terminal phase design, a preliminary analysis was completed for the vertical descent case.

Fig. 32 depicts the 4.5-min constraint in the range-velocity plane, which for the vertical case is equivalent to altitude-velocity. Also included is an altitude-velocity dispersion ellipse, as computed from the latest Monte Carlo analysis. For this case the maximum dispersion has a corresponding descent time well within (40 sec) the 4.5-min constraint.

For the 45-deg unbraked impact trajectory, analysis has not been completed. However, since it is estimated that the maximum range dispersion corresponding to the 45-deg case is $\leq \pm 12{,}000$ ft, it is judged that at 45 deg at least 99% of all cases will also fall within the 4.5-min constraint.

Propellant dispersions. Fig. 35 shows vernier propellant dispersions as a function of nominal main retro burnout velocity. Data points on the curve were generated from the latest Monte Carlo runs. For the maximum vernier propellant design point corresponding to maximum unbraked impact velocity and maximum midcourse maneuver, the nominal burnout velocity is 350 ft/sec. Fig. 35 indicates a 3σ propellant dispersion at this point of approximately ± 9.5 lb. However, because of some uncertainty as to the analytical method used in treating mixture ratio dispersions in this particular program, as well as the as yet tentative nature of these newer results, all propellant loading computations have been based on previous results indicating ± 11.5-lb 3σ dispersions.

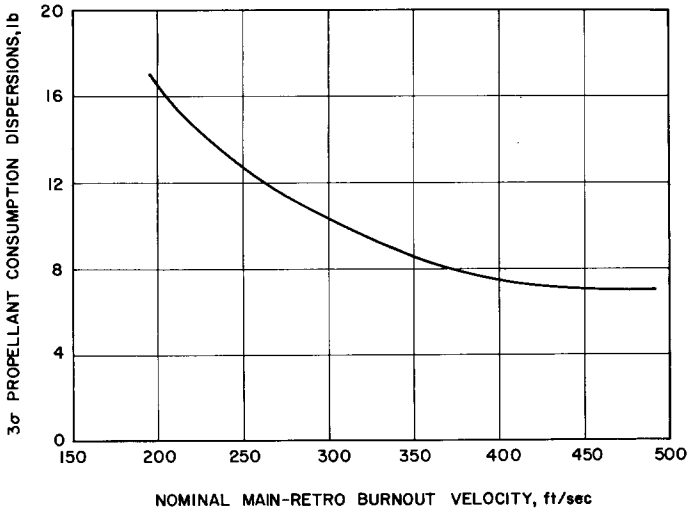

Fig. 35. 3σ vernier propellant dispersions vs nominal main-retro burnout velocity

b. Retro sizing and nominal vernier propellant computations.

Main retro sizing. Because a zero midcourse maneuver is not always possible under present terminal phase constraints, the main retro is sized to give minimum burnout velocity for minimum unbraked impact velocity (2632 m/sec) and maximum midcourse maneuver. This is in contrast to the A-21 spacecraft, which sizes the retro at maximum unbraked impact velocity, maximum burnout velocity, and zero midcourse maneuver. The A-21A is sized at the lower velocity end of the burnout velocity range so that the available range may be used to accommodate either increased impact velocity or midcourse maneuvers less than 50 m/sec. Fig. 36 shows this tradeoff, assuming a maximum burnout velocity of 410 ft/sec.

Vernier propellant loading. Maximum vernier propellant consumption has been found to occur at maximum midcourse maneuver, maximum design unbraked impact velocity (2649 m/sec), and maximum unbraked impact angle. The corresponding nominal burnout velocity is 368 ft/sec. Reduction of the midcourse maneuver to the point of maximum burnout velocity causes a slight decrease in total propellant consumption, approximately 1 lb, compared to the above design point.

Fig. 37 shows the vernier and main-retro propellant requirement as a function of dry landed weight. The data are based on having one terminal phase design (constant command descent segments A_{max} and A_{min}) for a maximum injected weight of 2500 lb.

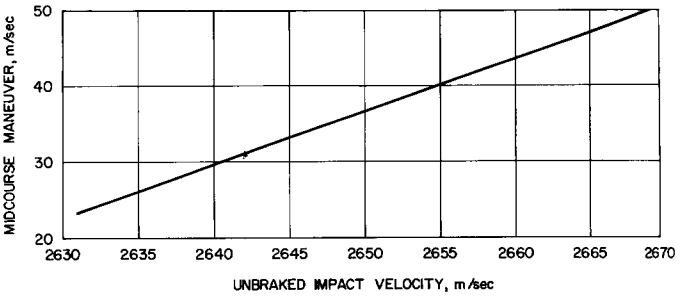

Fig. 36. Midcourse maneuver vs unbraked impact velocity for burnout velocity = 410 ft/sec

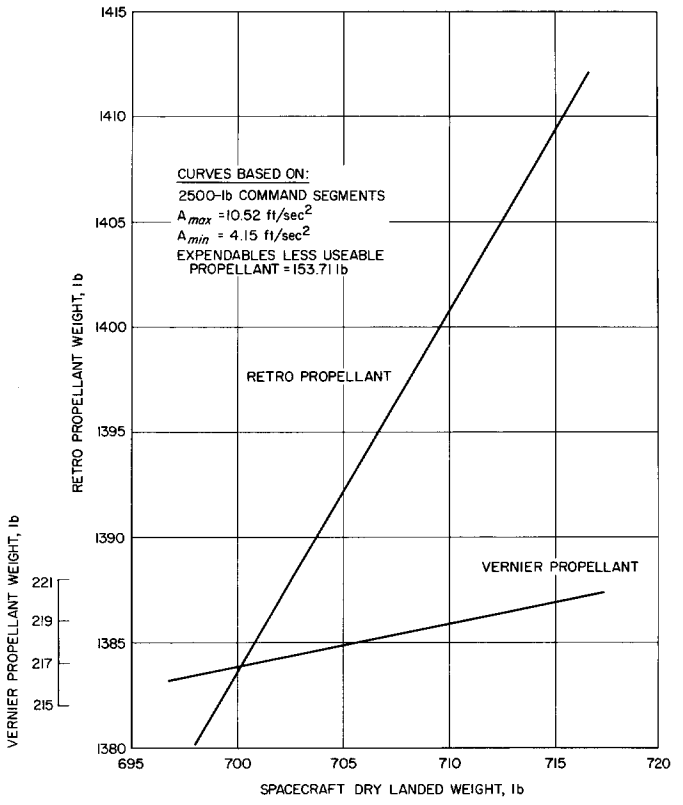

Fig. 37. Main-retro and vernier propellant weight vs dry landed weight

9. A-21A Surveyor Spacecraft Moment Control

a. Introduction and results. Spacecraft moment control is critical during the retro phase of the *Surveyor* mission because of the limited capability of the vernier engine system to generate control moments to react to disturbances produced by the interaction of the retro engine and the spacecraft. Because of the design of the moment control system and the nature of the disturbance torques, the pitch-yaw and roll control problems were analyzed separately.

A conservative calculation of the pitch-yaw disturbance limit at ignition is 1150 lb-in., compared to a worst-case moment capability of 1897 lb-in. in the worst direction with the combined cg at 1.0 in. from the roll axis. If the improvement in retro thrust to combined cg offset due to vernier propellant shifts is ignored, the disturbance limit during the retro period increases to 1820 lb-in.

The roll control problem was analyzed in terms of roll actuator angular margin. The angular travel required for dynamic control in addition to that required for reacting the static disturbances is 0.9 deg. The minimum available range is 1.3 deg at a 99% probability level, which yields a 0.4-deg minimum margin.

b. Pitch-yaw moment control. The worst-case moment capability of the A-21A vernier engine system with total thrust maintained at 201 lb is given in Fig. 38 as a function of moment direction in the pitch-yaw plane. Curves for both 0- and 1.0-in. displacement between the combined retro-spacecraft cg and the roll axis are given. The present value of the displacement for the A-21A spacecraft design is 0.4 in. The lower limit of moment capability as indicated on these curves is 1900 lb-in. for a 1.0-in. displacement.

The moment disturbance during the retro period is the product of the retro thrust and the offset between the thrust vector and the combined cg. The maximum thrust produced by the retro engine as controlled by the engine specification is 11,400 lb at nominal thermal gradient conditions, and 11,500 lb at thermal gradient extremes.

The combined retro-spacecraft cg offset was determined by analysis of the contributing effects that apply at retro ignition and consideration of the changes that occur during the retro period. Because of the importance of this parameter to the success of the *Surveyor* mission, a conservative approach was taken in combining the error sources to obtain the final limit. Thus, the effects of initial alignment, component exchange, and vehicle deformation were categorized as allowances and were directly added to obtain a worst-case result. The effects of dispersion were combined to yield an rss total. The total offset was obtained by taking the sum of the totals of the allowance and dispersion effects.

Since the vernier propellant cg will shift to reduce the offset during burning, the critical time is at retro ignition. To obtain the offset limit at ignition, the results of the above analyses were combined with the effects of retro nozzle centerline to thrust excursions to obtain a value of 0.098 in. If the improvement in offset is not included, a very conservative limit for offset is obtained by combining the effects at ignition and during burning to obtain an overall offset of 0.158 in.

The total disturbance at ignition was calculated as 1150 lb-in. If the offsetting effects of vernier propellant

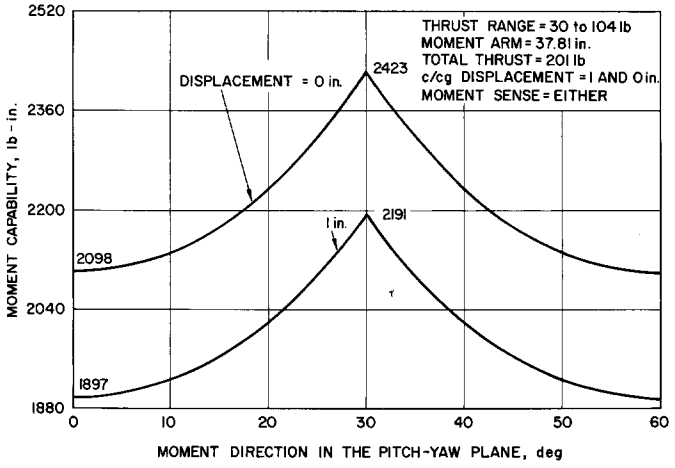

Fig. 38. Maximum guaranteed moment in either direction with thrust fixed at 201 lb

Table 19. Roll moment control analysis parameters

Thrust / Mass	Main-retro vortex torque, in.-lb	Deflection of roll control nozzle
8,000 / 2,400	0	$-0.1 \leq \delta \leq 1.7$
	80	$-2.3 \leq \delta \leq -0.3$
	−80	$1.4 \leq \delta \leq 4.3$
11,800 / 980	0	$-1.2 \leq \delta \leq 0.8$
	80	$-4.2 \leq \delta \leq -1.1$
	−80	$0.7 \leq \delta \leq 3.9$

Main retro disturbance	
cg—retro thrust vector displacement R_z, ft-lb[a]	0, 50
Direction of retro vector R_z, deg	0, 0.08
Magnitude of thrust vector, lb	8,000 and 11,800
Vernier engine system disturbance	
Thrust vector excursion R_z, deg	0, 0.11
Support bracket bending N, deg/lb[b]	5/1,000, 5/30,000
Prelaunch alignment angle N, deg	0.0, 0.017
Vernier engine thrust command N, lb	66.7, 2.22
Weight of spacecraft, lb	2,400 and 980
Weight supported by vernier engine bracket, lb	
Roll control	7.82
Engine 2	6.41
Engine 3	6.46

[a] R_z (m, σ) denotes a Rayleigh probability density function formed from two orthogonal gaussian distributions with mean m, standard deviation σ.

[b] N (m, σ) denotes a normal probability density function with mean m, standard deviation σ.

shift are not included, a very conservative moment disturbance limit of 1820 lb-in. is obtained for the retro thrust limit of 11,500 lb. This value is less than the vernier system lowest capability limit and provides an adequate margin for pitch-yaw moment control design.

c. Roll moment control. A Monte Carlo computer program was used to determine the angular range of roll actuator travel to offset the roll disturbance moments. The 99% probability limits of travel and the parameters included in the analysis are listed in Table 19. The largest actuator angle is 4.3 deg. The required angular travel for dynamic considerations is 0.9 deg. Thus the required minimum stop limit is 5.2 deg. The minimum center-to-stop range for the roll actuator will be controlled to 5.6 deg. The resulting angular range margin is 0.4 deg.

A plot of the probability of exceeding a value of angle between the minimum stop limit and the actuator angle corresponding to the roll disturbance is given in Fig. 39. As indicated, the probability is very high that 2-deg angular travel will be available as dynamic range for the A-21A roll actuator design.

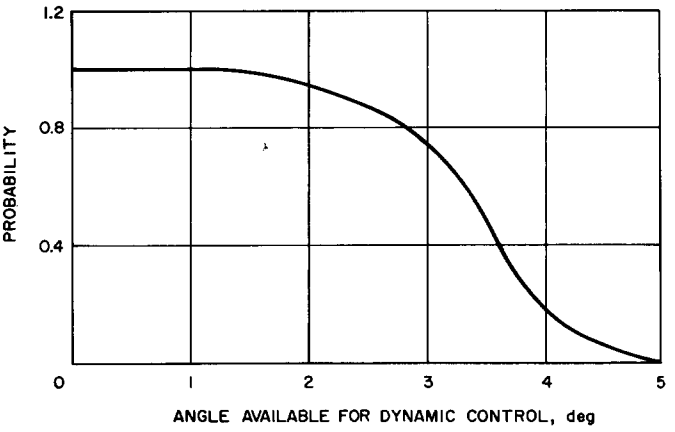

Fig. 39. Probability of exceeding angle available for dynamic control

D. Launch Vehicle Integration[3]

1. Spacecraft/Launch Vehicle Integration Schedule

a. Support of Atlas-Centaur R & D flights. The *Atlas-Centaur* 6/*Surveyor* Dynamic-Model 2 (AC-6/SD-2) vehicle was successfully launched on August 11, 1965 from Launch Pad 36-B, Cape Kennedy, Florida. All flight events occurred at, or very close to, predicted times and the SD-2 was successfully placed in a simulated lunar trajectory as planned. All flight objectives were satisfied. An anomaly in the spacecraft tip-off rate is discussed in Part 3 below.

The statement of work outlining JPL support of *Atlas-Centaur* R & D flights AC-8 and AC-9 has been approved by Lewis Research Center (LeRC) with minor modifications. This statement was transformed into a directive to Hughes Aircraft Company (HAC) to provide the required support for AC-8. November 1, 1965 was established by LeRC as the need date for AC-8 equipment deliveries. Funding and negotiation delays may cause this date to be advanced. A tolerable slippage is presently being determined by LeRC and General Dynamics/Convair (GD/C). AC-9 support requirements are under negotiation between JPL and HAC.

b. System testing and operations. A significant milestone accomplished essentially on schedule during this reporting period was the completion of Air Force Eastern Test Range (AFETR) Launch Pad 36-A and facility checkout with the T-21 prototype *Surveyor* spacecraft on July 31, 1965. Results of this activity are given in Part 6b below. The experience gained during the T-21 AFETR operation was factored into documentation for operational flights, namely SC-1. Such documentation originated or revised to date includes:

Originator	Number	Title	Released
HAC	227651	*Surveyor* Pad Safety Report	Sep 1965
HAC	288350-1, Vol. II	SC-1 Launch Operations Directive—AFETR	Sep 1965
HAC	227391	SC-1 Countdown Test Procedure	Sep 1965
HAC	288443	Abort Procedure for Vernier Propulsion System Propellant Leak	Sep 1965
HAC	288452	Cleanliness Requirements for *Surveyor* Operations at AFETR	Sep 1965
GD/C	UTP Sec. 8.7	*Centaur* Unified Test Plan AC-7/SC-1	Sep 1965

[3]Prepared by JPL Section 291.

The majority of remaining documentation applicable to AC-7/SC-1 operations is scheduled for release by November 1965.

Various problems experienced with the *Surveyor* SC-1 spacecraft during system thermal-vacuum testing have resulted in more complete and thorough test program plans and a delay in the launch. The earliest practical launch is presently anticipated for the first quarter of 1966. Upon establishment of a firm launch date, detailed scheduling will be accomplished.

2. Interface Requirements

a. Surveyor Project Document No. 1 (PD-1). A revised draft of Revision 2, incorporating LeRC-requested changes and additional *Surveyor* Project changes, including provisions for co-signing by the *Surveyor* Project Manager and the Launch Vehicle Project Manager, was forwarded to LeRC during the reporting period. LeRC comments and requested changes have been received. The changes consist primarily of:

(1) Adding a formal change and control procedure.

(2) Precluding LeRC-GD/C contractual difficulties by rewording certain sections.

(3) Deleting several requirements that have not been resolved.

No difficulty is anticipated in obtaining concurrence on these additional changes. However, the additional revisions will delay publication of Revision 2 until November 15, 1965. Requirements which cannot be resolved in time to meet this date will be processed separately by issuance of amendments as concurrence by LeRC and JPL is obtained. Publication by amendment is expected for: (1) Spacecraft Cleanliness Requirements, (2) Spacecraft RFI/EMI Requirements, and (3) the Figure of Merit (FOM) Requirement.

A special FOM review meeting was held between representatives of LeRC, JPL, GD/C, HAC, and Space Technology Laboratories to establish the revised launch vehicle accuracy requirement. JPL defined the worst-case trajectory with a set of U and K matrices. The U matrix is a 3×6 matrix which maps injection errors into a lunar miss; and the K matrix is a 3×3 matrix which maps the midcourse maneuver at a specified guidance point into a lunar miss. Further review by all agencies is required prior to publication of this amendment to PD-1.

3. Surveyor/Centaur Separation System

Spacecraft (T-1 test vehicle) separation tests were performed by LeRC-GD/C since the last reporting period. The new pin pullers and inadvertent separation switch/separation rate potentiometer assemblies did not significantly alter the spacecraft separation and tip-off rates. The inadvertent separation switch/separation rate potentiometer assemblies however did not perform properly as seen in the test films and data. Improper tracking of the separation spring plungers was observed, with the potentiometer plungers seen lagging the main spring plungers.

Additional component evaluation tests indicate some design changes and installation procedure changes are required. These will be reviewed by JPL in detail upon completion of the testing.

The flight data from the AC-6 flight indicated a spacecraft tip-off rate anomaly. The separation rate potentiometer traces indicated a rate of approximately 1.2 deg/sec was experienced. The RF signal strength cycling period indicated, however, a 1.8-deg/sec tumble rate. Further testing and analysis by GD/C indicated a main separation-spring hang-up was experienced rather than the potentiometer shaft improperly tracking. Epoxy which had been applied to a screw holding the separation-spring plunger stop was analyzed and verified by test as having probably spread to the plunger shaft, causing it to bind in its guide. On this basis, further analysis provided a spacecraft tip-off rate estimate quite close to that indicated by the RF signal trace. As a result of the investigation, lubrication, clearances, and procedural changes will be implemented. No further full scale spacecraft separation tests are planned.

Further work on the spacecraft/launch-vehicle separation dynamics analysis was performed at GD/C, JPL, and Lockheed Missiles and Space Company (LMSC). Correlation between the three independent analyses has been achieved. It has been established with a high degree of confidence that with the 3σ worst-case combination of parameters the highest tip-off rate that the *Surveyor* will experience is about 2.5 deg/sec. This rate is well below the 3.0-deg/sec flight control system requirement and well below the rate (approximately 8.5 deg/sec) which would cause collision between the *Surveyor* and *Centaur*. The LMSC analysis report (LMSC No. A 765806, September 14, 1965) contains a parametric study of the individual effects from each parameter on both the *Surveyor* and *Centaur*. This report is quite valuable in determining the effects of slight changes or deviations

from tolerances of all equipment significantly affecting *Surveyor* or *Centaur* motions at separation. Any and all combinations of parameters can be derived from the report, and motions of either body relative to each other and relative to three orthogonal axes fixed in space are also contained in the report.

4. Surveyor Cleanliness and Contamination

Further effort has been expended to obtain a better understanding of the spacecraft sensitivity to contamination in order to define realistic specifications for launch vehicle equipment. The periods and areas of concern are:

(1) The contamination, size and quantity, deposited on the spacecraft during encapsulation.

(2) The contamination, size and quantity, deposited on the spacecraft during air-conditioning after encapsulation.

(3) The contamination, size, quantity and state (smoke, out-gassing, or solids), deposited on the spacecraft during ascent, nose fairing ejection, and functional operation of devices such as pin pullers.

(4) The contamination and effects produced by the *Centaur* retro-maneuver.

The most critical spacecraft areas of concern are:

(1) The thermal-control-switch glass covers on the temperature-controlled Compartments A and B.

(2) The reference Sun sensor for the Canopus tracker.

(3) The Sun acquisition sensor.

(4) The Canopus tracker.

(5) The space-science TV survey-camera instrument.

As a result of several JPL in-house discussions, a tentative specification has been formulated and is being circulated for final in-house concurrence. Upon receipt of approval, the requirements will be forwarded to LeRC for review and assessment of the specifications relative to the pertinent launch vehicle equipment. It is desired that tests be performed to provide information that will establish the degree of contamination that can be experienced. An evaluation can then be made to determine the degree of mission performance degradation the spacecraft could experience and if further design changes, special cleaning procedures, or encapsulation operations are required.

5. Ground Support Equipment (GSE) Schematics

GSE interface system schematics have been developed by GD/C detailing the interconnections between the *Surveyor* umbilical function pins and the Hughes Aircraft Company GSE. Details of shielding, wire size, and the first significant circuit element in the HAC GSE are shown. To date, these schematics have been released for Launch Complex 36-A at AFETR and for the Combined System Test Stand at GD/C, San Diego, with Launch Complex 36-B release scheduled for June 1966.

The purpose of these drawings is to increase reliability and confidence in the interconnection documentation for use during launch complex checkout and trouble shooting circuit analysis.

In order to determine the first significant circuit element in the HAC GSE a supporting system schematic was generated by HAC which also details in simplified form the corresponding significant circuits in the spacecraft. In addition to supporting the GD/C GSE schematics, these drawings have been used during EMI/RFI noise problem analysis.

Additional drawings were generated by LeRC detailing interface circuity between the *Centaur* and *Surveyor* not shown on the GD/C or HAC GSE drawings.

6. AFETR Operations

a. EMI/RFI test program. The EMI/RFI test program was initiated to establish realistic noise specification levels, identify and correct "out of specification" noise sources, and establish test requirements for all *Surveyor* spacecraft. The test program consists of subsystem, system, and combined system tests performed at Hughes Aircraft Company, at the Combined System Test Stand, San Diego, and at AFETR Launch Complex 36-A.

The first EMI combined system test was performed at the Combined System Test Stand using the T-21 spacecraft and the AC-7 vehicle. As a result of this test and subsequent subsystem testing performed at HAC, the proposed spacecraft susceptibility levels were readjusted to more realistic levels.

Although no actual failures were attributed to EMI problems during this testing, several noise problems were uncovered leading to concern for the spacecraft during exposure to the AFETR test environment. GD/C was authorized to conduct a series of 4 EMI tests at AFETR within the existing schedule using simulation where

necessary and designed to uncover and correct noise problems before launch operations.

EMI Test No. 1 was performed using the T-21 spacecraft and the HAC GSE at AFETR. Instrumentation grounding problems prevented obtaining data on several lines. However, as a result of this test, the GSE regulator circuit is being redesigned to reduce its susceptibility.

EMI Test No. 2 is being conducted at Launch Complex 36-A, using the GD/C GSE, the AC-7 vehicle, and a HAC test set as a spacecraft load simulator. This test is expected to take approximately five weeks and involves exercising of *Centaur* and *Atlas* functions while monitoring the spacecraft interface. Preliminary data thus far has disclosed no noise problems not explained by abnormal conditions.

EMI Test No. 3 was performed at Launch Complex 36-A during the preliminary joint flight acceptance composite test (J-FACT) using the HAC test set as a simulated spacecraft load, the AC-7 vehicle, and the HAC and GD/C GSE. Preliminary data on this test also disclosed no noise problems which could cause spacecraft malfunctions. A meeting is scheduled for early November to review the results of this test and evaluate the data to date.

EMI Test No. 4 is scheduled for performance in conjunction with the final J-FACT test using the SC-1 flight spacecraft, the AC-7 vehicle, and the HAC and GD/C GSE at Launch Complex 36-A. This is the only test scheduled to evaluate noise at the spacecraft interface using the flight spacecraft in the prelaunch environment.

While it appears that there may be no catastrophic-type EMI problems indicated by the testing to date, it should be noted that complete detailed testing of the flight equipment and support equipment under actual launch conditions has not been accomplished due to the schedule and technical restraints. It is the intent to accomplish this as far as practical during EMI Test No. 4. A significant side benefit resulting from the RFI/EMI investigation and testing was the creation of the spacecraft and launch vehicle electrical system interface schematic, which proved invaluable in interface circuit analysis.

b. T-21 operations. Major achievements accomplished during the AFETR facility and operational proofing exercises using the T-21 model spacecraft were:

(1) The spacecraft was demonstrated to be compatible with major GSE and AFETR environment.

(2) The spacecraft was checked by the System Test Equipment Assembly (STEA) by means of and through the microwave air link.

(3) The toxic gas detector system for the encapsulated (and fueled) spacecraft was evaluated.

(4) Spacecraft propellant loading and downloading was demonstrated.

(5) Personnel operated in proximity of the fueled spacecraft.

(6) A spacecraft abort capability was demonstrated.

(7) The encapsulated spacecraft was transported to and from the launch pad by caravan without major accident.

A total of 162 individual Trouble/Failure Reports were written during the tests. Each one is being evaluated and appropriate action initiated. Special attention is paid to the effect upon SC-1 operations.

Evaluation of the spacecraft encapsulation, propellant handling, and toxic gas detection operations disclosed requirements for the following:

(1) Development of joint encapsulation procedures to enable GD/C and HAC personnel to operate efficiently, including provisions for accountability of flight equipment and tools through the use of an "accountability rack." Each flight item to be installed during encapsulation together with each required tool will be located on its identified place on a rack prior to the start of encapsulation. Photographic records of the rack in the "before and after" condition will insure that no loose tools or parts will remain within the nose fairing after encapsulation. JPL, HAC, and GD/C are presently developing the joint encapsulation procedure to be published by GD/C.

(2) Refinement of the encapsulated spacecraft abort and safing procedures in the event of a failure or leak in the vernier engine fuel and oxidizer systems. This procedure, approved by JPL, has been published (HAC Document No. 288443).

(3) Additional toxic gas detection tests to establish confidence in the detection system.

(4) Additional testing to determine the ability of the air conditioning system to maintain a proper degree of cleanliness within the nose fairing.

The toxic gas detection and cleanliness tests are presently in process at AFETR.

7. Launch Vehicle Payload Capability

A summary of current launch vehicle payload capability for the *Surveyor* missions as of approximately September 1, 1965 is presented in Table 20. Values for parking orbit as well as direct ascent modes are given for Flights AC-13 thru AC-15. A loss in performance of 206 lb is currently indicated for the use of parking orbit in place of direct ascent on Flights AC-13 thru AC-15; and the current margin for parking orbit ascent on these missions is about −140 lb for a 2450-lb spacecraft. The current status shown in Table 20 reflects the loss in payload capability (approximately −11 lb for direct ascent and −33 lb for parking orbit) which resulted from the implementation of the "dual-ascent" pitch program. The dual-ascent pitch program permits the use of a single compromise pitch program for both direct ascent and parking orbit missions. The *Centaur* Project Manager has approved an increase of 2 sec in the *Centaur*-stage engine specific impulse value used to determine performance of Vehicles AC-12 thru AC-15. This increase in specific impulse has resulted from improvements made to the RL 10A-3-3 engine systems which will be used in Vehicles AC-12 thru AC-15, as well as development Vehicles AC-8 and AC-9. The net gain in payload capability due to increased specific impulse should be approximately 56 lb and is expected to be included in the payload capability status summary of the next reporting period.

E. Launch Operations

1. Air Force Eastern Test Range (AFETR)

a. Surveyor Dynamic Model SD-2 Joint Flight Acceptance Composite Tests. Early in the reporting period, SD-2 was in the *Atlas–Centaur 6* (AC-6) mated condition undergoing daily transponder checks while awaiting joint flight acceptance composite tests (J-FACT), which were initiated and accomplished in 1 day.

During J-FACT, the SD-2 transponder would not go to high power on command from the *Surveyor* operations

Table 20. Summary of current launch vehicle performance[a]

Flight	Payload	Ascent mode	Minimum burnout weight, lb[b]	Centaur jettison weight, lb	Payload capability, lb	Spacecraft weight, lb	Margin, lb
AC-7	SC-1 (engineering)	Direct	6294	3909	2385	2176	+209
AC-10	SC-2 (engineering)	Direct	6299	3956	2343	2165	+178
AC-11	SC-3 (engineering)	Direct	6297	3943	2354	2178	+176
AC-12	SC-4 (engineering)	Parking orbit	6439	4135	2304	2178	+126
AC-13	SC-6 (scientific)	Direct	6491	3978	2513	2450	+ 63
		Parking orbit	6439	4132	2307	2450	−143
AC-14	SC-7 (scientific)	Direct	6491	3975	2516	2450	+ 66
		Parking orbit	6439	4129	2310	2450	−140
AC-15	SC-8 (scientific)	Direct	6491	3975	2516	2450	+ 66
		Parking orbit	6439	4129	2310	2450	−140

[a]As reported in GD-C/63-0495-28, "*Centaur* Monthly Configuration, Performance, and Weight Status Report," (U), General Dynamics/Convair, San Diego, California, September 21, 1965 (Confidential).

[b]"Minimum burnout weight" equals "nominal burnout weight" less the "performance reserve" of 180 lb.

console in the blockhouse; however, it did go to high power on command by the *Centaur* programmer. Examination revealed that the command pulse amplitude required was slightly greater than the output of the *Surveyor* operations console monitor and control panel. The panel function was modified, and recheck of the command function showed proper operation. The spacecraft was then demated and returned to the explosive safe facility for flight preparation.

b. SD-2 flight preparation. Flight preparation of SD-2 was started on July 28 and completed on July 31. The spacecraft was then moved to Launch Pad 36B for remating to AC-6. Mating was accomplished on August 1 with all operations proceeding normally and on schedule.

c. Transponder readiness tests. After mating, daily transponder checks were performed and frequency data for Deep Space Instrumentation Facility (DSIF) use were transmitted to JPL. During the transponder checks, lockup could not be acquired properly because the DSIF-71 S-band transmitter had been inadvertently left in operation. Retest established that this malfunction condition could be simulated. Daily transponder checks continued until completion of a GD/C flight acceptance composite test of AC-6.

d. F − 1 day countdown. F − 1 day countdown was performed on August 9, with SD-2 transponder operations normal. Participation on SD-2 consisted of transponder frequency measurements and system end-to-end calibration of all instrumentation.

e. AC-6/SD-2 Launch Countdown 1. Launch countdown was initiated on August 10 and proceeded with three unscheduled holds until approximately T−90 sec when the launch attempt was aborted because of failure to obtain an ARM indication on the range safety destruct mechanism on the *Centaur*.

The holds were caused by the following factors:

(1) Difficulty in removing gantry.

(2) DSIF-51 time-code generator giving unreliable data which was rejected by the JPL Pasadena computer.

(3) Difficulties in teletype transmission of antenna pointing information for Antigua.

(4) Failure to obtain an ARM indication on the *Centaur* destruct system.

The destruct problem was cleared by replacing the *Centaur* destruct package, and launch was rescheduled for August 11.

f. SD-2 launch (Launch Countdown 2). The *Atlas–Centaur 6/Surveyor* Dynamic Model 2 (AC-6/SD-2) vehicle was successfully launched at approximately 14:31 GMT on August 11, 1965. Launch Countdown 2 was initiated at T − 280 min, at 08:11 on August 11, 1965. Liftoff was planned for 14:31 GMT, the opening of the Day 2, Plan 1 launch window. The window extended to 15:29 GMT, giving a duration of 58 min. Two planned built-in holds had been incorporated in the countdown: the first of 60-min duration, beginning at T − 90 min, and the second of 40-min duration, starting at T−5 min.

Spacecraft countdown operations began at 07:36, GMT, 35 min prior to start of the range countdown, with RF tests of the S-band transponder. The countdown proceeded normally, with most spacecraft and launch vehicle operations being performed on or ahead of schedule. The only difficulties experienced were with the *Atlas* battery and the range safety 7-v battery, both of which required replacement because of voltage variations.

The T−90 min built-in hold began at 11:21 GMT, with the count being resumed at 12:21 as scheduled. Operations then continued without incident down to the T−5 min built-in hold, which was entered at 13:46. The countdown was resumed at T−5 min at 14:26, as scheduled. An azimuth of 94.539 deg was established for a planned liftoff at 14:31. Ignition occurred at T−3 sec, and liftoff was recorded at 14:31:04.430 GMT.

The spacecraft and launch vehicle systems performed normally during the launch-to-injection phase. The powered flight trajectory was close to nominal, and the spacecraft was successfully injected into the simulated lunar transfer trajectory. The injection parameters were well within the established limits. Fig. 40 illustrates the liftoff of AC-6/SD-2 from the pad.

All tracking stations were able to lock on and track the spacecraft. SD-2 separation tumble rate was well below the maximum. The flight path was such that the "paper Moon" landing was only 150 nm off the planned target area.

At launch + 16 hr the SD-2 signal cut off abruptly. Up to that point, signal levels had compared favorably with predicted levels. An investigation of possible

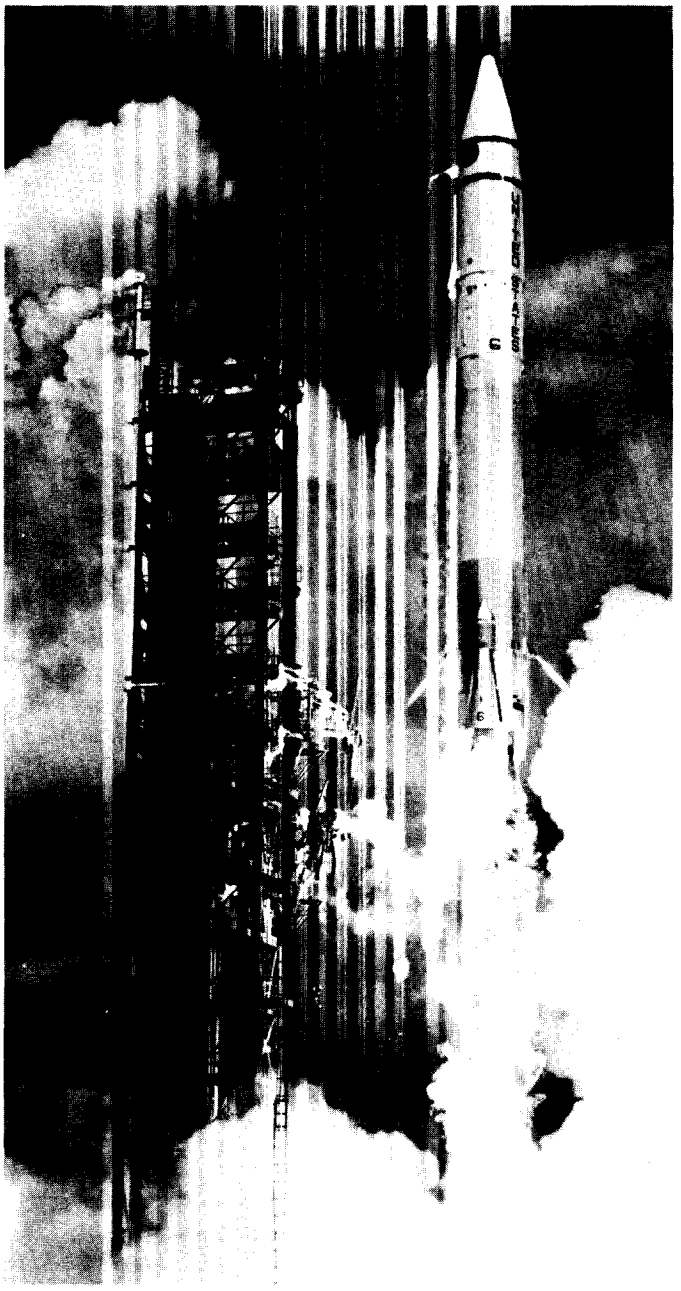

Fig. 40. AC-6/SD-2 liftoff from Launch Pad 36B

causes for signal loss resolved to the large increase in transmitter frequency noted during one-way lock. At L + 11:38:56, a total increase of 52.1 kc had been observed. This increase, if caused by temperature effects, would be indicative of a very high magnitude temperature rise. All other probable causes were reasonably eliminated, and the problem is considered readily resolvable. In addition, the existence of a thermal-vacuum problem was disclosed during the investigation. The problem was associated with the high-power switching transistors in the electrical conversion unit. These transistors are mounted close to the transmitter voltage-controlled crystal oscillator which controls the transmitter frequency in one-way lock. Appropriate corrective action is in process.

The SD-2 launch and flight were successful in meeting program objectives. The mission yielded factual information on spacecraft physical environment during launch, enabled all tracking stations to obtain actual flight tracking experience, and verified *Atlas–Centaur* boost vehicle capability for placing *Surveyor* in the proper flight path to the Moon.

g. SD-2 transponder signal-loss investigation. An extensive test program was initiated at AFETR to determine the status of the SD-2 transponder battery at launch as a possible contribution to S-band transponder signal loss.

A test circuit was set up at Launch Complex 36 to simulate the SD-2 on-pad operation as closely as possible. A series of tests was performed to determine if the battery simulator would supply the spacecraft load as operated during SD-2 tests on pad in the days prior to launch, and still provide a properly charged spacecraft battery at launch. These tests also provided information for determining the status or capacity of a spacecraft battery while on pad and in the launch configuration condition.

Test Series I. During the initial tests, conducted with both a fully charged and a partially discharged battery, access to the blockhouse and spacecraft location on the service tower was restricted; accordingly, the test circuit was set up in the transfer room and the test was performed from the launch control rack.

Battery pressure transducer readings at the blockhouse console are meaningless because the reference line is the same as the 22-v return for the battery simulator. If the battery simulator is turned on, the pressure transducer reading at the console will vary with battery simulator current due to line drop. This return line is also common with the *Atlas–Centaur* missile ground, and the measurement shows some dependence on *Atlas* and *Centaur* loads.

Test Series II. Later tests, run with a battery discharged to 66% capacity, were conducted with the spacecraft simulated in the service tower, utilizing the long line runs on the umbilical tower. This simulated the actual spacecraft on-pad launch configuration.

With the battery in the 66% state of charge and because the battery simulator is a constant voltage source, the minimum setting of the battery simulator resulted in a no-load output reading at the console of 1.7-amp charge into the battery. With a 1-amp load, the minimum output read 1.94 amp, indicating both supply of the load and charging of the battery.

These results indicate that the battery on SD-2 at launch was fully charged because it was possible to set the battery simulator to an output of only 1 amp to supply the spacecraft load to low power; a low battery would have resulted in a high current output of the battery simulator even at a minimum setting. The latter condition was not experienced during the SD-2 countdown.

Test Series III. The final tests were conducted with two batteries, one fully charged and the other discharged to 60% capacity. The battery simulator was controlled from the blockhouse console to duplicate SD-2 on-pad operations.

These tests provided a good insight into determining the approximate status of the spacecraft battery in the launch configuration. It was noted that the battery simulator output current under each condition of the simulator is a function of the battery capacity. Thus, considering only the Test Series III results, it is indicated that the SD-2 battery was somewhat near full charge at launch as evidenced from the performance of the battery simulator during the countdown; Test Series III results with the battery fully charged closely approach SD-2 readings during the countdown.

Main-battery discharge test. As a followup to the test series, a main-battery discharge test was performed to discharge the test main battery used in the J-FACT tests and to determine its voltage characteristics and capacity. SN 19, the test battery, and SN 20, the SD-2 flight battery, had undergone the AFETR flight acceptance tests at the same time and had received identical handling.

Having already served as a test battery for the launch complex and with its specified life having expired 10 days prior to beginning of this test, the main battery was loaded with a resistive load adjusted to draw a continuous current of 3 amp. The following parameters were monitored at appropriate intervals during the discharge:

(1) Load current.

(2) Load voltage.

(3) Open-circuit battery voltage measured first with the load current at 0 amp and, after a short time, allowing the battery terminal voltage to rise to a stable value.

(4) Battery pressure measured using the battery transducer.

(5) Battery case temperature measured using an external thermometer.

The net effect of the Series I, II, and III tests was assumed to be negligible compared to the discharge test. The battery proved to be in good condition in every respect. Battery voltage reached the 22-v plateau at approximately 20-amp-hr discharge and reached the 17.5-v specified battery limit after 170 amp-hr were dissipated. The parameters monitored during the test were evaluated as plots of voltage, pressure, and temperature versus amp-hr.

Parameter evaluation showed that the main battery (SN 19), after AFETR flight acceptance testing, storage, use as a standby, use as a backup for the SD-2 flight battery (SN 20), and launch complex tests, had maintained more than 170-amp-hr capacity with normal discharge-voltage characteristics. It was concluded that the flight battery could safely be assumed to have been in the same proper charge condition at time of launch.

h. Real-time telemetry. Both the range and Hughes/JPL portions of the S-band real-time telemetry system underwent extensive testing during the past 2 mo. Tests are summarized as follows:

Range testing. The range has conducted receiver tests utilizing a JPL-supplied test transponder (Tel-2) and data transmission from ships at sea. Currently, downrange stations are being equipped. The system was exercised on a test basis during the AC-6/SD-2 flight with satisfactory results.

Hughes/JPL testing. The JPL-supplied switch matrix and model were installed in the command and data handling console (CDC). The model had to be placed in the programmed automatic telemetry evaluator rack because it was too deep to fit into CDC Bay 12. Connections were made to the JPL communications center, and the system was checked by feeding the pulse code modulation (PCM) simulator output to the communications center and back through the Tel-2 and downrange inputs. The system performed all modes as designed.

During the early portion of the T-21 EMI/RFI test, Tel-2 was to receive spacecraft S-band and transmit PCM data to Building AO. Tel-2 received the S-band successfully (even though they were looking at the spacecraft through the service tower) and PCM data were observed on an oscilloscope at AO. However, when these data were patched to the CDC, they were unusable. Later investigation revealed a lead pair reversal between Tel-2 and AO. Thus, as soon as the data were supplied to the CDC, they were shorted to ground. After this pair reversal was corrected, data from a test tape were fed from Tel-2 to AO, and the CDC successfully locked to this signal.

Further testing with T-21 transmitting from AO to Tel-2, and Tel-2 feeding PCM data back to the CDC in AO, was planned; however, because of a failure in the Tel-2 decommutator, the test was limited to Tel-2 receiving data from T-21 and transmitting taped data back to AO. This test demonstrated that the system is feasible and will work satisfactorily.

Combined testing. A test of the Tel-2–CDC–Space Flight Operations Facility (SFOF) interfaces was performed on September 14. A test tape utilizing the *Surveyor* launch PCM format was played from Tel-2 to the CDC in Building AO and on to the SFOF in Pasadena. Satisfactory data were obtained at the SFOF in the normal configuration, where the data is played through the CDC, and in the backup CDC bypass configuration. Only a failure of the switch matrix timing signal conditioner in the bypass mode prevented this test from being completely successful.

i. Flight control sensor group laboratory activation. Setup, calibration, checkout, and validation of the Flight Control Sensor Group (FCSG) Laboratory at AFETR was completed during the reporting period. Because the Building AO addition which is to house the FCSG Laboratory will not be completed in time, the laboratory has been temporarily located in Building AM for *Surveyor* Mission A only. Necessary facility alterations for Building AM operations were completed by the range contractor on September 17.

The FCSG console and necessary tooling were received at AFETR, and inspection, preparation, and calibration of commercial items were completed by September 17. The divider head, rate table, electronics, and tooling were installed in the laboratory. The JPL-provided carbon arc solar simulator was reinstalled and restored to operating condition.

Verification of the laboratory was performed utilizing a test FCSG flown to AFETR from Hughes Aircraft Company, El Segundo. Fig. 41 shows the FCSG in the as-received configuration installed in its shipping container. Laboratory verification required 3 days and was completed on September 24. Fig. 42 shows the laboratory verification test setup.

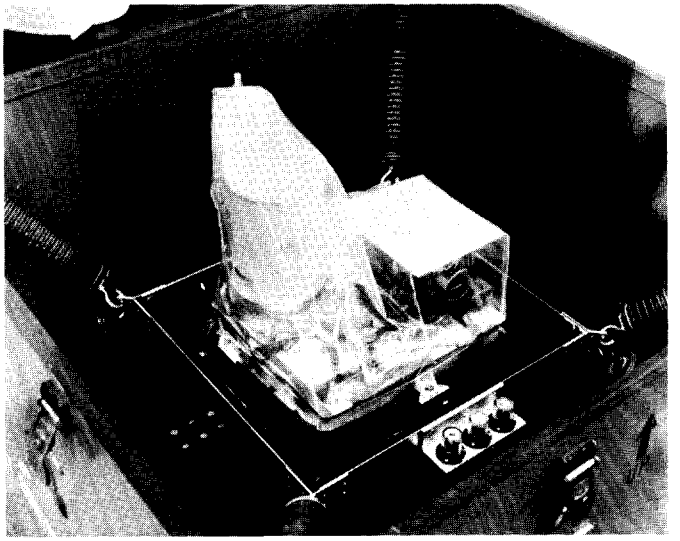

Fig. 41. Flight control sensor group

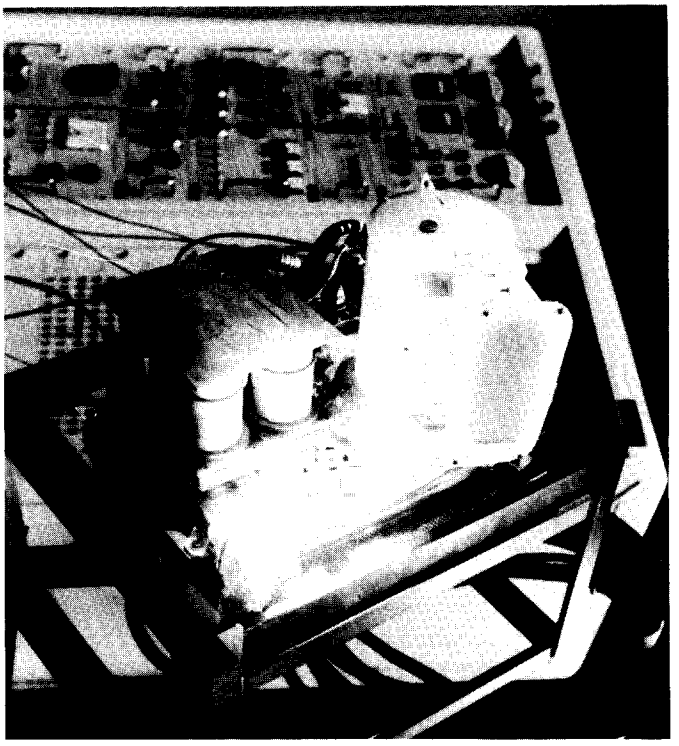

Fig. 42. Flight control sensor group verification test setup

A need for modification of the carbon arc solar simulator optics to provide both greater uniformity of intensity across the beam and better collimation was revealed by the laboratory checkout. This task is presently underway. As a result of the laboratory checkout and the dry run with the test FCSG, it was concluded that the scheduled 3 days is sufficient time to validate the SC-1 FCSG and that the existing equipment is adequate for the task.

2. T-21 Spacecraft Operations at Goldstone

a. T-21 spacecraft arrival at Goldstone. The A-21 prototype spacecraft, T-21, was shipped from AFETR on July 31 by van and arrived at Goldstone, California on August 3. Activation of the temporary spacecraft facility at Goldstone, consisting of three trailers and a screen room, had been completed on August 2 in time for necessary spacecraft support. Fig. 43 shows the T-21 on the ground transport vehicle (GTV-1) being moved into the screen room.

b. T-21 spacecraft test preparation. Preparation of the spacecraft for DSIF testing was comprised chiefly of running Performance Verification Test 1 and the system readiness test. In addition, several special operations were performed to render the spacecraft compatible with DSIF test requirements, such as the exchange of transmitters, the checkout of TV Cameras 3 and 4, and the calibration of receivers.

Fig. 43. Removal of T-21 spacecraft from GTV-1 to screen room

c. DSIF/DSN/spacecraft compatibility tests. The DSIF/DSN/spacecraft compatibility tests were started on August 14. Initial progress was slow because of considerable difficulties in obtaining repeatable measurements of spacecraft–DSIF RF link losses. The solution to this problem was replacement of one of the two parabolic dishes on the collimating tower with a larger antenna. This corrective action, performed by Goldstone facilities personnel, proved satisfactory, and the compatibility tests proceeded. Operations included:

RF compatibility tests
- Calibration spacecraft–DSIF RF link
- DSIF/CDC/spacecraft verification
- One-way acquisition
- Two-way acquisition

Command compatibility tests
- Automatic phase control command mode test
- Automatic frequency control command mode test
- Command verification

Telemetry compatibility tests
- PCM/FM/PM telemetry
- PCM/FM/FM telemetry
- PCM/FM/FM telemetry (high power)
- Multiplexer telemetry PCM/FM/PM
- Multiplexer telemetry PCM/FM/FM
- Telemetry verification

Television compatibility tests
- TV emergency mode engineering test
- TV emergency mode function test
- TV normal mode engineering test
- TV normal mode function test

Spaceflight operations compatibility tests
- Phasing and polarity tests
- Command mode/bit rate tests
- Study mission sequence
- Television sequence

Miscellaneous
- Operator training
- On-site data processing
- Solar panel preparation and test

Testing on the last day of operations involved the simulation of various spacecraft malfunctions unannounced to the DSIF operations personnel. The purpose was to exercise operations personnel in the analysis of spacecraft failure symptoms. Evaluation of results of this special test is still in process.

d. Operations support summary. The T-21 spacecraft System Test Equipment Assembly 3 equipment performed satisfactorily throughout the DSIF tests, with only 36 minor perturbations reported. T-21 will leave Goldstone by van in mid-October for Hughes Aircraft Company, El Segundo where it will undergo preparation for drop testing.

F. System Testing

1. T-21 Prototype Vehicle Tests

a. Lunar landing shock tests. A landing loads parametric study of T-21 is being conducted to determine the dynamic conditions at impact. This study will establish the level of the most severe loading of selected spacecraft components under assumed boundary conditions of approach velocity, surface slope, and friction. The components selected for study are thermal compartments, survey television camera, antenna solar panel positioner, and Omni-antennas A and B. In three of these cases, analysis assumes the limiting vertical velocity to be 15 ft/sec and the horizontal velocity to be 5 ft/sec. In the fourth case, these limits are assumed to be 20 and 7 ft/sec, respectively. Parameters to be varied in the study are: lateral velocity, spacecraft inclination, and spacecraft orientation about the roll axis.

The first part of this study will determine the most adverse combined-parameter conditions (within 3σ probability) for component loading under the assumed lunar impact boundary conditions. The second part discusses the combination of parameters in an Earth g field to generate the equivalent peak loading. The results of the study will establish values to be tabulated in the landing shock system test specification table of environmental conditions. Final release of this specification is therefore pending the completion of the parametric study.

Changes in the instrumentation schedule, plus the change from a three to a four drop test program, have required revisions to the test plan. Other changes result from the increased interval between the T-21 vibration system test and the lunar landing shock tests.

2. SC-1 Spacecraft Flight Acceptance Tests

a. Mission sequence — electromagnetic interference tests. A Survey of the Merritt Island Launch Area Electromagnetic Compatability Control, Boeing report DS-13088-1, dated March 1, 1965, has been reviewed. This survey indicates that measured field strength levels at Launch Pad 39 are 10 to 15 db lower than calculated values used in designing the A-21 electromagnetic interference tests. This difference in field strength levels is ascribed to reflections, reradiations, and absorptions.

b. Vibration tests. The SC-1 vibration test phase report is ready for publication with the exception of three sections containing functional test results, conclusions, and recommendations. Analysis presently completed includes tabulations of the results obtained from TV alignment checks, and the post-vibration short system confidence check, and phase jitter and frequency stability test results obtained during the flight-acceptance-test-level vibration test runs.

The summary of total SC-1 vibration test time is given in Table 21. The time durations are categorized in four groups. The first two groups represent actual test durations as defined by the A-21 flight-acceptance vibration test specification. The third category relates the time of vehicle exposure to random vibration equalization occurring at 3.18 g rms or 3 db down in level from the specified amount of 4.5 g rms. The last category of dwell time refers to the time of exposure attributed to the dwell period at 0.25 g (5 cps) for instrumentation checkout conducted before each run. Thus, the SC-1 spacecraft was exposed to vibration for 77 min 8.4 sec, of which 31½ min were to satisfy the specification.

c. Vibration retests. The test and operation plan supplement, and the test plan have been prepared and issued for the vibration retest of the SC-1 spacecraft made necessary by the replacement of several components damaged during special tests (following original SC-1 vibration flight acceptance tests). The retest, however, will be limited to testing only the z-axis thrust direction in order to conserve spacecraft fatigue life. The test levels will remain the same as in the initial flight-acceptance-test vibration phase. A sequence summary for this test is presented in Table 22. The parameters of the retest differ from the initial vibration in frequency range only. The initial frequency was set at 15 cps instead of the 5 cps called for in the vibration test phase because of the need to conserve fatigue life of components having lower resonant frequencies, but which are not involved in the replacement schedule.

Table 21. Summary of total vibration test time (SC-1 flight acceptance test)

Run number	Type of test	Axis	0.25-g test	Flight acceptance test	Equalization test	Dwell period	Total time
1A	Low-level sine sweep	Vertical	4:20			1:51.4	6:11.4
2A	Flight-acceptance-test level sine sweep	Vertical		2:10		3:54.4	6:04.4
2B	Equalization 1	Vertical			0:30	0:12.4	0:42.4
2B	Equalization 2	Vertical			0:30	0:29.4	0:59.4
2B	Equalization 3	Vertical			0:30	0:15.4	0:45.4
2B	Flight-acceptance-test sine-random	Vertical		4:00		3:12.0	7:12.0
3A	Low-level sine sweep	Lateral 1	4:20			1:49.2	6:09.2
4A	Flight-acceptance-test level sine sweep	Lateral 1		2:10		3:04.2	5:14.2
4B	Equalization 1	Lateral 1			0:15	0:30.6	0:45.6
4B	Equalization 2	Lateral 1			0:15	0:24.5	0:39.5
4B	Equalization 3	Lateral 1			0:15	0:17.0	0:32.0
4B	Equalization 4	Lateral 1			0:15	1:02.0	1:17.0
4B	Equalization 5	Lateral 1			0:15	0:13.8	0:28.8
4B	Equalization 6	Lateral 1			0:15	0:20.6	0:35.6
4B	Flight-acceptance-test sine-random	Lateral 1		4:00		3:23.1	7:23.1
5A	Low-level sine sweep	Lateral 2	4:20			4:42.0	9:02.0
6A	Flight-acceptance-test level sine sweep	Lateral 2		2:10		12:50.0	15:00
6B	Equalization 1	Lateral 2			0:15	1:41.0	1:56.0
6B	Equalization 2	Lateral 2			0:15	0:54.2	1:09.2
6B	Flight-acceptance-test sine-random	Lateral 2		4:00		1:11.2	5:11.2
Totals			13:00	18:30	3:30	42:08.4	77:08.4

Table 22. SC-1 vibration retest sequence

Pre-vibration alignment of TV cameras performed with spacecraft mounted on vibration test fixture: approach camera; survey camera

Squib circuit verification: replace simulators

Mechanisms verification

Mechanical integrity check

Systems readiness test

Propulsion system leakage and contamination check

z-axis vibration (pre-launch configuration established[a]): low- and high-level sinusoidal vibration above 15 cps and high-level combined sine-random vibration imposed on spacecraft

Functional tests performed during vibration: FM mode engineering interrogation during upsweep for the flight-acceptance test sine run and the upsweep for the flight-acceptance-test combined sine-random run; PM mode interrogation, phase jitter, and frequency stability during the low-level survey and the flight-acceptance-test combined sine-random downsweep run

System readiness test

Post-vibration alignment checks of TV cameras: approach camera; survey camera

Post-vibration leakage and contamination check of propulsion system

Addendum tests of short-system confidence check

[a]Flight compartment covers installed, squibs installed (except as noted), and test access provided on Omnidirectional Antenna B and on auxiliary battery.

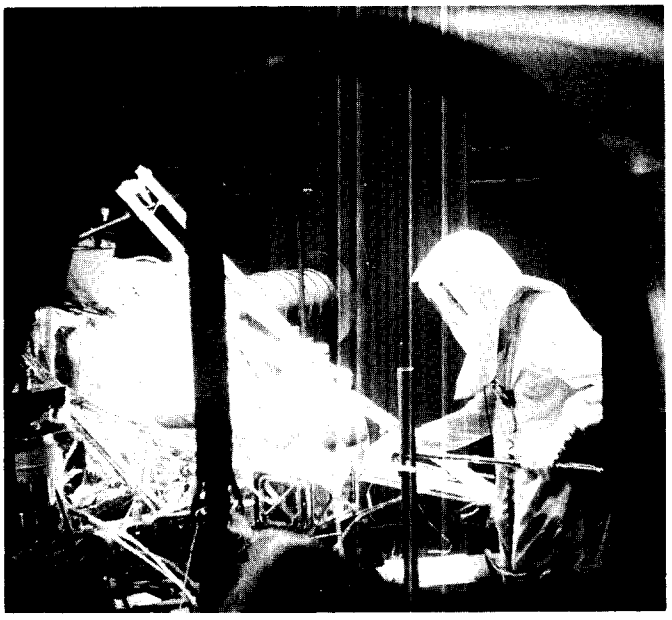

Fig. 44. Solar mapping with the SC-1 spacecraft

d. Solar-thermal-vacuum tests. Solar mapping with the SC-1 vehicle in place was accomplished as shown in Fig. 44. On September 9, prelaunch countdown was begun. Because of spacecraft/system-test-equipment-assembly difficulties, the Phase A test was aborted after an unsuccessful terminal descent. The second terminal descent was successful. Special troubleshooting tests were continued on the spacecraft after shutdown on September 10. The test as finally defined was a single 66-hr mission sequence with equal periods of nominal and high solar conditions prevailing. A second eclipse for testing "star mode" of the redesigned TV-3 survey camera was incorporated. A black-white plate radiometer was added as a backup intensity monitoring device for the Epply radiometers. External thermocouples were added to the spacecraft and test equipment for real-time monitoring utilizing the temperature-identification data-acquisition-system/advance-data-monitoring-system thermal instrumentation.

The computer data system providing "delta" parameter measurements of the telemetry functionals in real time has been installed and was operational for this test phase. A line printer and several character printers provided necessary output information. Various power shunts were installed in the spacecraft for real-time power management monitoring as displayed on a digital printer. Test tees allowing full exercise of the spacecraft in conformance with the test specification have been installed. Instrumentation for continuous monitoring of the chamber pressure was installed and operable.

3. SC-2 Spacecraft Flight Acceptance Tests

a. Test operations. The SC-2 vehicle started system test with initial system checkout on September 13. The harness power and grounding tests had been accomplished previously. The vehicle was delivered with all major control items installed except the planar antenna and solar panel positioner.

Telecommunications intergroup integration testing was started September 15. Some delay was encountered and certain items required retest because of transmitter changes required to support SC-1 testing. Television-telecommunications testing was completed and radar altimeter doppler velocity sensor (RADVS) group test was accomplished prior to harness upgrade. The spacecraft was shut down for 4 days to incorporate harness changes to the flight control telemetry circuitry. Upon application of power, telecommunications intergroup integration retest was accomplished and flight control telecommunications testing was started. Initial system checkout mission-sequence/electromagnetic-interference, and vernier shake tests are scheduled for the next reporting period.

b. Vernier engine vibration tests. This new A-21 flight acceptance test is designed to accomplish the following goals:

(1) Verify the capability of the flight control sensor group and RADVS to function properly while subjected to random vibration of type anticipated during operation of vernier engines.

(2) Verify that vibration transfer characteristics between vernier engines and the flight control sensor group are within design specifications.

Random vibration will be applied to the spacecraft at the dummy vernier engines during a simulated closed-loop midcourse correction and a simulated closed-loop terminal descent. In the transmissibility test, sinusoidal vibration will be applied to the dummy vernier engines and the response of the flight control accelerometer located in the flight control sensor group will be recorded. Rough drafts of both the vernier engine vibration test specification and test plan have been prepared. Vibration equipment operating procedures written for the consent-to-ship test are directly applicable to the vernier engine vibration test.

The shaker support structure, system test stand adapter, airmount suspension system, shakers, and the shaker-to-vernier engine adapters were assembled around the

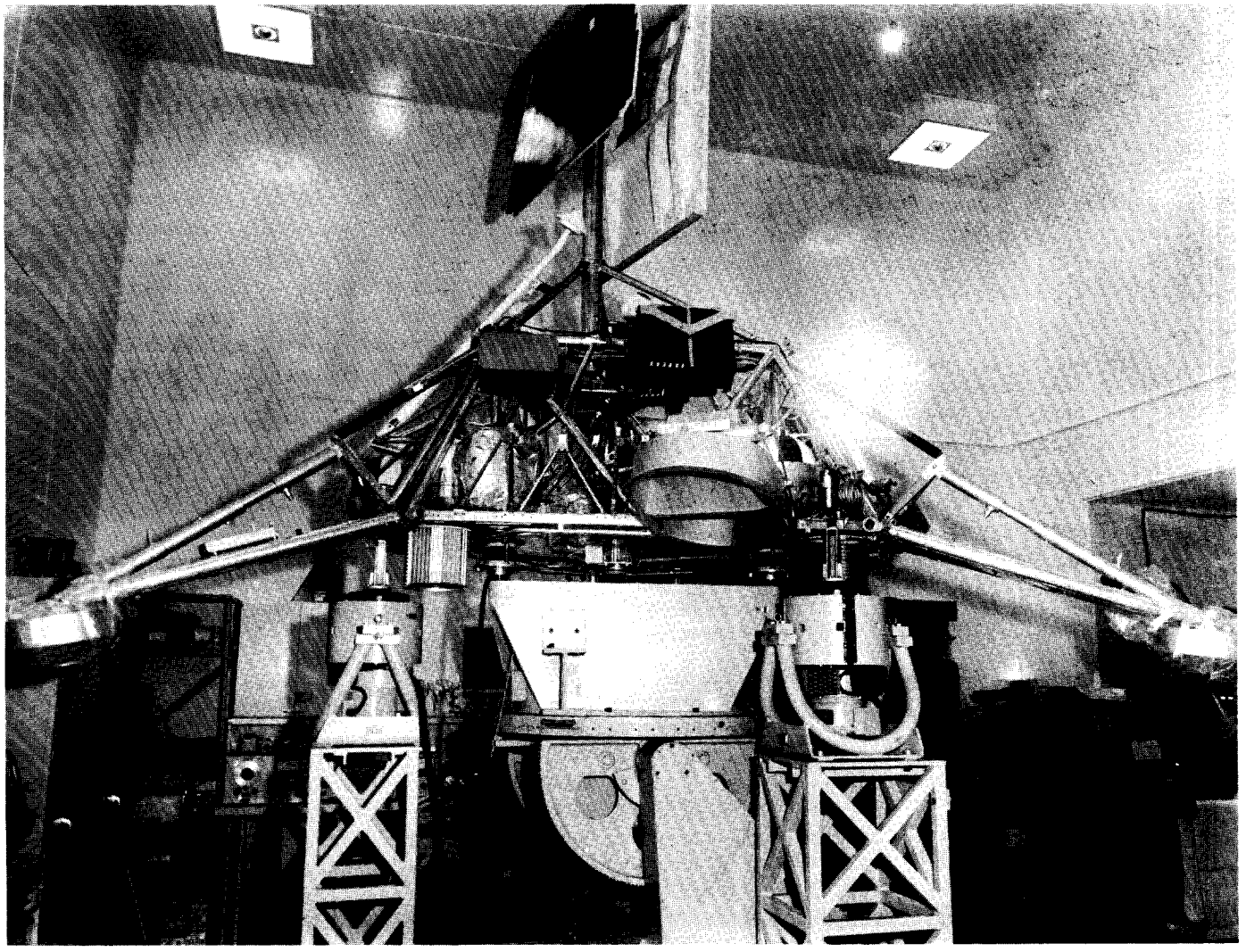

Fig. 45. M-12 engineering spacecraft mockup installation on vernier-engine vibration test apparatus

system test stand in the Space Systems Environment Simulation Laboratory to verify the fit and function of these units using the M-12 engineering spacecraft mockup. Fig. 45 shows the installation of the three shakers around the system test stand and the installation of the M-12 on the special airmount suspension systems.

The procedure used for the RADVS closed-loop operation in this test will differ from the closed-loop procedure presently used in the short system confidence check. Hence, modifications will be made to update existing closed-loop procedures to make them applicable to the vernier engine vibration test phase.

4. Group Test Vehicle (GT-1) Flight Acceptance Tests

a. Test operation. The GT-1 vehicle entered an upgrade period during which the new NAS 703 harnesses were installed along with television, RADVS, and the antenna solar panel positioner. On return to test, the SC-2 survey camera and some SP-1 (spare) and SC-3 power units were group-tested. The SC-2 engineering signal processor and auxiliary engineering signal processor were retested after modification in the unit area in preparation for installation on SC-2. Although not physically installed on GT-1, the SC-2 altitude marking radar unit was group-tested. Group-testing of SC-3 and SP-1 units continued.

UNCLASSIFIED [redacted]ENTIAL

5. T-2N Descent Test Program

a. T-2N-R recovery system test vehicle. The T-2N-R test program was completed during this reporting period, and all test objectives were satisfactorily met. High pitch, yaw, and roll moments were exhibited during Tests 1 through 4, resulting in an increase in the area of the aerodynamic balance plate Results of Tests 5 and 6 indicated that pitch and roll moments were marginal. The aerodynamic balance plate area was again increased and three airfoils were added Results of Test 7 demonstrated acceptable aerodynamic moments.

Satisfactory operation of the tether-winch system at 1500 ft was verified. The parachute recovery systems for both the gondola and the RADVS test fixture were also demonstrated to operate satisfactorily.

A summary of the T-2N R test results by planned test objective follows:

(1) Parachute deployment time and effective recovery distance were in tolerance.

(2) Recovery electronics assembly and telemetry conditioning operated satisfactorily.

(3) Solenoid release mechanism and safety lock operated satisfactorily. Release delay was 53 msec maximum.

(4) Maximum kappa angle of 30 to 40 deg at chute deployment reduced to an in-tolerance angle at touchdown to indicate satisfactory descent stability.

(5) Vehicle exhibited no rebound nor evidence of toppling, indicating satisfactory touchdown stability.

(6) Site facilities and ground equipment were satisfactory.

(7) Average sink rate of all tests was within 20 ft/sec tolerance. Average sink for Tests 6 and 7 was measured at 21.5 and 20.5 ft/sec.

(8) Vehicle safety requirements precluded use of a strain gage, but accelerometers indicating chute deployment caused an in-tolerance force with no structural damage.

(9) Vehicle was at full fuel weight (greater than normal) for Tests 5, 6, and 7. Impact forces exceeded specifications in Test 6, but absence of structural deformation proved adequacy of recovery system.

(10) Aerodynamic parameters were determined from test data.

A complete summary of T-2N-R data from Tests 1 through 7 is given in Table 23.

b. T-2N-1 descent test vehicle. Tethered tests were conducted on the T-2N-1 vehicle. The first tethered terminal countdown was completed to $T-10$ hr, at which time a RADVS klystron power supply modulator failure precluded completion. The malfunction was corrected, and Tethered Test 1 was completed on September 10. Problems revealed during Tethered Test 1 include:

(1) RADVS D_1 tracker locked up on the altimeter flyback.

(2) RADVS D_2 and D_3 trackers locked up on noise during low thrust.

(3) Flight control system exhibited an apparent attitude instability.

(4) High thrust could not be commanded.

The D_1 tracker lockup problem was corrected by adding microwave DVS isolators, and acoustic protection to an overall sound pressure level of 142 db was added in an attempt to correct the D_2 and D_3 tracker lockup problem. The apparent flight control attitude instability was completely analyzed through analog simulation, and it is concluded that attitude oscillation is the result of attempts by the vehicle control system to stabilize a complex pendulum made up of the balloon, gondola, and vehicle. Since the system was not designed to control this complex system, this is not a problem. The inability to command high thrust was a vehicle telemetry/console compatibility problem and has been corrected by lowering the "engines on" signal threshold level in the operations display system equipment.

Tethered Test 2 was completed September 23 with the following problems:

(1) RADVS test fixture failed to jettison.

(2) RADVS D_3 tracker locked up on noise in low and high thrust

(3) RADVS D_2 tracker locked up on noise during high thrust.

(4) RADVS D_4 tracker broke lock before and during the engine run.

UNCLASSIFIED [redacted]AL

Table 23. T-2N-R test data

Item	Test 1	Test 2	Test 3	Test 4	Test 5	Test 6	Test 7
Release altitude, ft	1165	1186	1154	1192	1271	1328	1289
Velocity at recovery, ft/sec	90	90	90	92	No data	100	102
Recovery distance (within 275 ft), ft	220	245	245	210	No data	245	232
Recovery chute deployment time (< 3.5 sec), sec	3.4	3.5	3.5	3.4	No data	3.4	3.3
Stab sink rate (< 20 ft/sec), ft/sec	19.0	19.8	19.8	18.5	19.9	21.7	20.5
Impact shock, first-second[a], g							
Platform 1	10–6	9–10	9–7	9–7	10–11	9–10	10–8
Platform 2	12–11	12–12	8–10	10–5	No data	11–16	10–12
Platform 3	10–7	10–6	8–8	7–3	8–12	8–15	8–11
Center-of-gravity accelerometer	11–7	9–8	9–10	9–	10–8	10–15	12–10
Chute opening shock (< 1500 lb)[b], lb	840	1040	940	920	1100	1100	1000
Chute stability (5-deg maximum impact kappa angle), deg	2.5	2.5	5.5[c]	4.0	No data	No data	1.0
Effective vehicle drag area, ft^2	26	26	26	26	No data	25.5	26.5
Aerodynamic roll moment (computed using $SC_D = 26$), ft-lb	14	12	13	13	No data	9	5[d]
Kappa angle (computed at $V_z = 70$ ft/sec)[e], deg	15	14	16	22	No data	17	10

[a]First shock, 10 g; second shock, 12 g; 14 g once in five touchdowns.
[b]Approximate readings from accelerometers.
[c]Data accurate to ±1%.
[d]Opposite roll direction from first six tests.
[e]Pitch and yaw moments in Tests 1 through 4; essentially only pitch in Tests 6 and 7.

(5) Oxidizer manifold pressure and Thrust Chamber 3 pressure exhibited low-magnitude 4- to 5-cps oscillations.

(6) Constant vehicle roll rates were exhibited during low- and high-thrust engine run.

(7) Gyro heaters switched synchronously for short periods while on external power.

The RADVS test fixture release mechanism has been redesigned to correct the first problem. Corrective action for the RADVS tracker lock-up problems consisted of a complete re-examination, factory upgrade, and the addition of acoustic protection accomplished at Ryan Aeronautical Company, San Diego. The overall sound pressure level against which the system is now protected is 148 to 150 db. The susceptibility of the range tracker to break lock has been lessened by reducing the sensitivity on the tracker blanking line. The oxidizer manifold and chamber pressure oscillations are not considered to be problems since the propulsion system data and subsequent flow check data demonstate satisfactory performance within the required limits during the test. Vehicle roll rates are attributed to vernier-engine bracket bending as demonstrated by force application and angle measurement conducted subsequent to the tethered test. A new alignment position for the engines will be used to minimize this effect. Synchronous gyro heater switching is anticipated when the bus voltage at the input to the inertial reference unit is below approximately 17.5 v and the line impedance is in excess of 1 Ω.

The present status of test results is summarized by planned test objective:

(1) Acoustic isolation between the vernier engines and RADVS subsystem was inadequate for both tethered tests.

(2) Pitch, yaw, and roll attitude stability have been satisfactorily demonstrated on both tethered firings; however, roll rates have been present due to engine bracket bending.

(3) All subsystems except RADVS have exhibited satisfactory performance in the engine noise environment.

(4) Ground control facilities and ground handling procedures have been adequate for mission accomplishment.

(5) Pre-release checkout of all subsystems except RADVS test fixture jettison on Tethered Test 2 was satisfactory.

(6) Countdown procedures, abort sequence, and postmission downloading were satisfactorily demonstrated.

(7) Compatibility of operation display system and crew was satisfactorily demonstrated except for recurrent communication system problems.

c. T-2N-2 second descent test vehicle. Phases 1, 2, and 3 of T-2N-2 system functional testing were completed on September 24. During all phases of this environmental testing, an erratic intermittent RADVS Beam 2 lockup was observed, but it had no effect on the closed-loop mission sequence, which is the criterion for a successful test; therefore, the test results were valid. These items are all on the RADVS system, which will undergo retesting on its return from Ryan Aeronautical Company where it is currently being upgraded. No major functional problems were encountered with any of the other electronic systems.

Vehicle flight-acceptance testing, consisting of RFI, static discharge, vibration, thermal and humidity, and landing shock phases, was completed on October 5. All phases of environmental testing were completed on October 5. The major problem encountered was the failure of the air bag system to inflate properly during the high temperature and landing shock phases. The problem was traced to an intermittent heater wire in the CO_2 system. Retesting verified the system operation under environmental conditions.

When the RADVS system is returned by Ryan Aeronautical Company, RADVS functional tests will be performed, and the vehicle will go through one more vibration phase before shipment to the Air Force Missile Development Center, Holloman Air Force Base, New Mexico.

G. Scientific Payload

1. Scientific Payload Engineering

A detailed presentation summarizing the plans and status of the Hughes Aircraft Company Payload System Laboratory was made to JPL personnel on August 17.

Direct support of and participation in the A-21A design freeze and definition activities were provided by finalizing the specifications covering the details of all Hughes-designed portions of the scientific payload, except for the touchdown dynamics instrumentation subsystem. Specifications covering all scientific instruments were released.

2. Television

An assessment was made of *Surveyor* survey television photogrammetric performance for missions E, F, and G in comparison to proposed noncontractual requirements. The results of the assessment are:

(1) Ranging errors (rms) predicted for 30 m are from 30% (1σ) with no camera calibration to 9% (1σ) with camera/spacecraft calibration.

(2) All viewability requirements will be met. At 0-deg elevation angle, performance is 13% better than required, and at 45 deg it is 9% better than required.

(3) Calculation of the positions of two points on the TV image format may be possible to a 1% accuracy. Data indicating achievement of a positional accuracy near 1% of the total angle subtended by one side of the format have been observed. It is not certain at this time that this requirement can be achieved to the desired tolerance.

(4) Reseau and reference marking accuracies are met by existing vidicon tubes.

(5) Requirements for calibration of magnification and distortion are met in terms of the required physical dimensions, with one exception. Additional measurement and analysis are required to predict if the electrical aspects of this requirement will be met in all cases.

(6) Mirror stepping size and accuracy requirements are being met.

(7) The proposed mirror fiducial mark provisions can be met, but are not currently planned since they are not contractually required.

(8) The present camera internal alignment tolerances, assembly methods, and calibrations must be modified to meet the precision mechanical relationships implicit in a quantitative photogrammetric application.

(9) Survey cameras are installed and aligned with respect to the spacecraft z-axis but to different tolerances than required for precision photogrammetric performance.

a. Ranging errors.

Estimate of range errors. In a simple stereo ranging situation, with the object lying in the horizontal plane near the perpendicular bisector of the camera baseline, and at a distance large compared to the baseline, the fractional error in range is approximately

$$\frac{dy}{y} = \frac{1.4y}{b}\, d\alpha$$

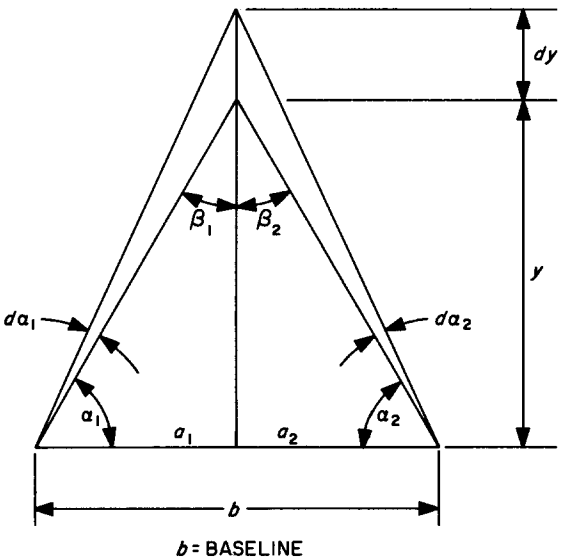

This can be obtained as follows:

$$\beta_1 = \frac{a_1}{y}$$

$$\beta_2 = \frac{a_2}{y}$$

$$\beta_1 + \beta_2 = \frac{a_1 + a_2}{y} = \frac{b}{y}\left(\frac{\pi}{2} - \alpha_1\right) + \left(\frac{\pi}{2} - \alpha_2\right) = \frac{b}{y}$$

$$-d\alpha_1 - d\alpha_2 = -\frac{b}{y^2}\, dy$$

$$\frac{dy}{y} = \frac{y}{b}\,(d\alpha_1 + d\alpha_2)$$

For independent errors $d\alpha_1$ and $d\alpha_2$

$$\frac{dy}{y} = \frac{y}{b}\sqrt{d\alpha_1^2 + d\alpha_2^2}$$

If the variances of α_1 and α_2 are equal, $d\alpha_1 = d\alpha_2 = d\alpha$.

$$\frac{dy}{y} = \frac{y}{b}\sqrt{2d\alpha^2}$$

$$\frac{dy}{y} = \frac{1.4y}{b}\, d\alpha$$

Range error with no calibration after camera assembly. If each camera is mounted on the spacecraft, its mounted orientation known to within 15 min of arc, and no further optical calibrations are performed, the errors in it would be composed chiefly of the square root of the sum of the squares of the following:

	Error, in.
Vidicon position	0.0194
Lens axis alignment	0.0146
Reseau position on vidicon	0.0150
Intersection of mirror azimuth axis and vidicon faceplate	~0.0150 (estimated)
Camera line of sight	0.015
rss total	~0.034

On the vidicon face, one TV line equals 0.00073 in., and one TV line equals 0.188 mrad (for the 100-mm lens), which equals 0.64 min of arc. So

$$0.034 \text{ in.} = 46.5 \text{ TV lines} = 0.0087 \text{ rad}$$

and the ranging error at 30 m, for a base of 1.26 m is

$$\frac{dy}{y} = \frac{1.4y}{b}\, d\alpha$$

$$= \frac{1.4 \times 30}{1.26} \times 0.0087 = 0.29$$

$$\frac{dy}{y} \approx 30\% \ (1\sigma) \text{ error at } 30 \text{ m}$$

Range error with calibration after camera assembly. If each camera is fully calibrated before launch by photographing known test objects whose geometrical relations

to the cameras are accurately known and there is complete calibration of linearity and distortion via the reseau pattern and the necessary computer program, essentially all fixed errors can be eliminated, leaving only errors due to mirror repeatability and data readout (including residual effects of distortions and nonlinearities after appropriate processing of the reseau data). These errors, which were neglected as small in the previous uncalibrated case, include

	Error, min of arc
Mirrors	6
Calibration	4
Readout	4
Miscellaneous, including calibration chart errors	4
rss total	~9(0.0026 rad)

The resulting fractional error at 30 m is

$$\frac{dy}{y} = \frac{1.4\,y}{b}\,d\alpha$$

$$= \frac{1.4 \times 30}{1.26} \times 2.6 \times 10^{-3} = 0.088$$

$$\frac{dy}{y} \approx 9\%\ (1\sigma) \text{ error at 30 m}$$

b. Viewability expected for A-21A survey television. The predicted viewing capability of the A-21A survey television subsystem is compared with presently specified viewability criteria. Viewability predicted for the A-21A survey television agrees with the design goals and specific requirements set forth for this spacecraft. Attainment of these viewing objectives represents the best compromise between the following conflicting requirements:

(1) Unobstructed view of surrounding lunar landscape.

Table 24. A-21A spacecraft viewability summary

Requirement	Fulfillment of requirement	Predicted capability
Survey camera capability		
360-deg azimuth view from camera	Full 360-deg view possible (as required)	Mirror unit rotates 354 deg; 6.4-deg narrow-angle view allows opposite azimuth end steps (3.0-deg steps) to produce 0.4-deg view overlap for near-horizon elevation angles, less overlap for other elevation angles (25.2-deg wide-angle view allows greater overlap)
20- to −45-deg elevation view from camera	Elevation range view better than required	49.7- to 64-deg view possible
Survey television subsystem capability		
360-deg azimuth view for 0- to −30-deg elevations	Full 360-deg view requirement met at horizon and −15-deg elevation angles; 325 deg at −30-deg elevation	View will be approximately 325 deg (90%) at −30-deg elevation angle
Two-camera stereo observations of horizon (80%), −15-deg elevation (60%), −30-deg elevation (25%), −45-deg elevation (10%)	All requirements bettered	Horizon (93%), −15-deg elevation (89%), −30-deg elevation (40%), −45-deg elevation (19%)
Soil-mechanics/surface-sampler observable during and after emplacement on lunar surface; stereo desirable	Requirements generally met; desired performance partially met	Sampler scoop observable in stereo in 68.5-deg portion of spacecraft Sector 2; approximately 85% of sampling area viewable by one camera; TV Camera 3 view of sampling operation by Leg 2 footpad. Note: TV Camera 2 (preferable) view of Leg 2 footpad obscured by touchdown dynamics instrumentation subsystem thermal compartment
Alpha scattering experiment within unobstructed view of at least one survey television camera for all possible deployed positions	"Deployed" sensor viewable in stereo, which is better performance than required	Sensor viewable by TV Camera 2 in stowed position; sensor viewable by both cameras, in background count and initial deployed positions; redeployment of sensor within its minimum viewing range to TV Camera 3 permits single-camera observation—TV Camera 2 view obscured by helium tank

(2) Views of several different scientific experiments.

(3) Location of survey TV cameras on spacecraft to meet needs imposed by thermal control, structural, cg, and *Centaur* shroud requirements.

(4) Location of scientific experiment instruments on spacecraft to meet needs imposed by thermal control, structural, cg, instrument operation, and instrument deployment requirements.

The A-21A spacecraft viewing capabilities are summarized in Table 24. Spacecraft azimuth viewing capabilities predicted from this study are shown in Fig. 46.

c. Viewing capability inherent in present A-21A spacecraft general arrangement. Present A-21A viewability attained through optimum employment of the features of the present spacecraft television generally agrees with the specified viewability. Viewing capabilities have been derived by evaluation of changes between the earlier

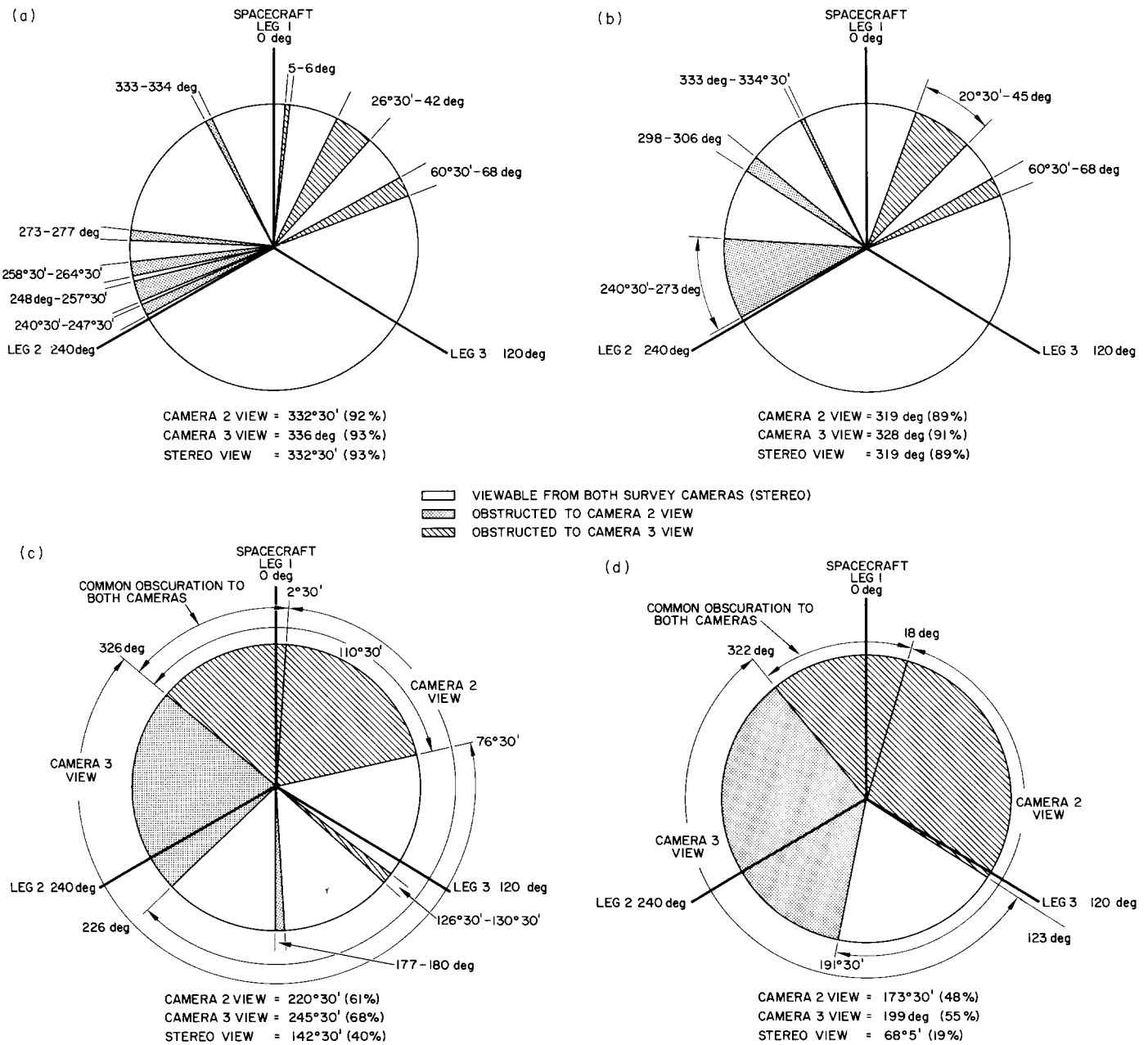

Fig. 46. A-21A spacecraft visibility of lunar surface: (a) 0-deg depression angle; (b) 15-deg; (c) 30-deg; (d) 45-deg

A-21A spacecraft configuration and the present A-21A design, which was then used to predict corresponding changes in spacecraft viewability. Changes in the A-21A spacecraft general arrangement are given in Table 25.

d. Factors contributing to viewing changes. Changes that have evolved from the earlier A-21A spacecraft configuration, and that have correspondingly affected present survey television viewability, are categorized as follows according to their effects on types of viewing requirements:

(1) Changes shifting camera azimuth and elevation view limits, when on the spacecraft:

(a) Addition of azimuth stop pin to mirror unit.

(b) Uprighting of TV Camera 3 in mount to have major axis parallel to spacecraft *z*-axis.

Table 25. A-21A spacecraft unit position/location changes

Item	New constraints	
	Spacecraft coordinates[a]	Spacecraft-mounted attitude or size change
Camera system Survey TV Camera 3	*x* 15.00 (to center of camera mounting ring on spacecraft) *y* −25.957 *z* S83.23	Camera uprighted to align major axis parallel to spacecraft *z*-axis
Survey TV Camera 2	*x* −29.75 (to center of camera mounting ring on spacecraft) *y* −4.96 *z* S80.18	Unchanged
Approach TV Camera 4	*x* 24.00 (to center of camera mounting ring on spacecraft) *y* −26.50 *z* S60.00	Unchanged
Scientific experiments[b] Soil-mechanics/surface-sampler subsystem	*x* 24.37 (to instrument elevation axis) *y* −35.00 *z* S52.00	Unchanged
Alpha scattering subsystem	*x* 4.20 (to center of sensor supporting knob) *y* −39.50 *z* S62.60	Stowed position
	x −15.50 (to center of sensor supporting knob) *y* −66.50 *z* S51.70	Background-count position
	x −15.50 (to center of sensor supporting knob) *y* −66.50 *z* S36.22	Lunar-surface-count position
Viewing obstructions Helium tank	*x* −12.00 (to geometric center of tank) *y* −34.00 *z* S55.48	Nominal diameter of tank increased from 14.2 to 15.7 in.
Nitrogen tank	*x* 0.00 (to geometric center of tank) *y* −27.58 *z* S55.00	
Touchdown dynamics instrumentation subsystem	*x* −3.12 (cover corner nearest Leg 3) *y* −25.30 *z* S74.50 (edge of cover away from spacecraft *z*-axis) S76.50 (inboard edge of above cover)	Newly added to spacecraft; cover portion of compartment obstructs Survey Camera 2 view of experiment area
Signal data converter	*x* −19.24 (upper corner nearest Leg 3) *y* −8.03 (top surface of unit) *z* S82.25	Unit has been relocated on top of Leg 3 corner of spaceframe

[a]*z*-axis coordinate shown as spacecraft station plane.

[b]No specific TV viewing requirement for experiments not listed here.

(2) Television changes reducing unobstructed view and stereo three-dimensional effect:
   (a) Relocation of TV Camera 2 farther in toward spacecraft z-axis, closed to TV Camera 3.

(3) Changes reducing television coverage of scientific experiments:
   (a) Relocation of alpha scattering experiment below and in front of TV Camera 3.
   (b) Change of alpha scattering sensor deployment device to one remaining extended, partially obscuring TV Camera 2's view of soil-mechanics/surface-sampler experiment.
   (c) Uprighting of TV Camera 3, relocation of TV Camera 2 farther in toward spacecraft z-axis.
   (d) Increase in size of helium tank.
   (e) Addition of touchdown dynamics instrumentation subsystem thermal compartment, obscuring the TV Camera 2 view of this area.

(4) Changes improving television coverage of scientific experiments:
   (a) Rotation of soil-mechanics/surface-sampler operating area clockwise to include Sector 2 half of spacecraft Leg 2 footpad.
   (b) Redesign of camera mirror hood to sunbonnet form; annoying or veiling side glare to the mirror is eliminated, permitting use within wider Sun angles.
   (c) Addition of a sensor repositioning knob on the alpha scattering sensor.

e. Accuracy of position readout and distortion correction. The errors associated with the location of a point in the frame and correction of the distortions introduced by the lens and sweep circuits are of fundamental importance in estimating the photogrammetric capability of the system. The presently specified requirement (*Surveyor* System Functional Requirements) is that the error in determining the angle between any two defined points in a TV picture should be less than 1% of the frame side (6.4 deg) at the 95% confidence level after corrections employing the vidicon reseau. The location error is thus about ±4 min of arc. The following discussion presents data demonstrating compliance with this requirement. The test performed at the system level consists of photorecording a precise grid test chart viewed by the camera. The locations of grid intersections and the reseau marks are measured with a precision photo reader and input to a computer program for distortion correction.

Table 26. Results of linearity tests on SC-1 cameras (nominal scale factor)

Test phase	Camera	Scale factor	2σ error, arc min
Group	Survey	3.731	3.1
Group	Approach	3.785	1.84
TCM	Approach	3.785	2.0

The resultant position errors are summarized in Table 26 for several tests on SC-1 approach and survey cameras. These results are based on the locations of 20 grid points, which yield 190 combinations of distances throughout the format within the reseau pattern. Test chart to vidicon faceplate scale factors are calculated from lens and test chart collimator data.

$$\text{Scale factor} = \frac{\text{collimator focal length}}{\text{camera/lens focal length}}$$

The data in Table 27 also show the effect of using the optimum scale factor as determined in the computer run. The significant reduction in error in Table 27 for the survey camera indicates that scale factor errors are a major contribution to readout inaccuracy. The two cases for the approach camera in the group test are for different cameras with an extended time period between tests.

Table 27. Results of linearity tests on SC-1 cameras (optimum scale factor)

Test phase	Camera	Scale factor	2σ error, arc min
Group	Survey	3.750	1.8
Group	Approach	3.787	1.82
Group	Approach	3.795	1.47
TCM	Approach	3.791	1.84

It appears that the survey camera failed to meet the 1% criterion in one case and passed in the other. These results are based on relatively limited test experience and test techniques may contribute some error. Known sources of error which are believed to contribute less than 0.1% error arise from the use of nominal rather than measured reseau point locations, which are not available for this vidicon, and the use of the center reseau point rather than the true center of distortion for the lens distortion correction.

The data in Table 27 are of interest in connection with the capability that can be expected if calibration on the Moon can be performed to reduce scale factor errors.

Inherent sensitivity of the camera with the "star mode" modification is sufficient to see more than one star in the field of view. If veiling glare and diffuse reflections from the mirror are small enough, this will provide a powerful calibration capability.

f. TV mirror fiducial mark. The results of an experiment that demonstrated the ability of the *Surveyor* survey camera to record images of crossline targets are presented in the following paragraphs. This experiment evaluates the use of a dark crossline placed on the *Surveyor* camera mirror face so that the center of the cross lies on the elevation and azimuth axes of the mirror assembly. Such a cross simplifies the alignment of the camera on the spacecraft. When two survey cameras are used, the cross on each mirror also provides a simple means of establishing the angular coordinate system for each camera with respect to the baseline. The latter function requires that each camera photograph the cross on the other camera. The tests described below simulated this photography of the crossline.

Experimental procedure. The *Surveyor* survey camera was positioned so that its azimuth axis was greater than 1.24 m from a target transparency. The transparency was illuminated from behind with diffuse uniform light, providing a target of black lines of various widths with a bright background (Fig. 47). The luminance of the background was 140 ft-L for the pictures taken at f/4 and 3100 ft-L for the pictures taken at f/22; these luminance values were chosen as representative for normal photography with the survey camera.

The camera was operated in the "shutter mode" with a V_0 of 3 v. A single scan line crossing the target was presented on the A-scope with a horizontal scale of 40 μsec/cm and a vertical scale of 1 v/cm. The A-scope trace was photographed with a Polaroid camera.

Results. Fig. 47 shows the A-scope photographs and a schematic drawing of the test target to identify the signals from the individual lines. Photographs were taken at the best focus and one step inside and one step beyond best focus to show that the object position is not critical. The original photographs show that at f/4 the 0.003-in. wide line is clearly resolved at all three focus settings; at f/22 the 0.0025-in. wide line is clearly resolved at all three focus settings. All the wider lines are clearly resolved at all three focus settings at both aperture settings.

Conclusions. The survey camera is capable of resolving 0.003-in. wide black lines at a distance of 1.24 in. so the method of using the crossline on the mirror is practical. A line width specification of 0.005 $\pm$ 0.001 in. can be used

g. TV camera internal axial alignment. Photogrammetric requirements necessitate knowing the maximum and rms tolerance deviations that could exist between the mechanical axis and the theoretical optical reference centerline. For present purposes, these possible misalignments are analyzed in two parts: (1) all misalignments except those that might result from the variable focal length lens assembly, and (2) variable focal length lens

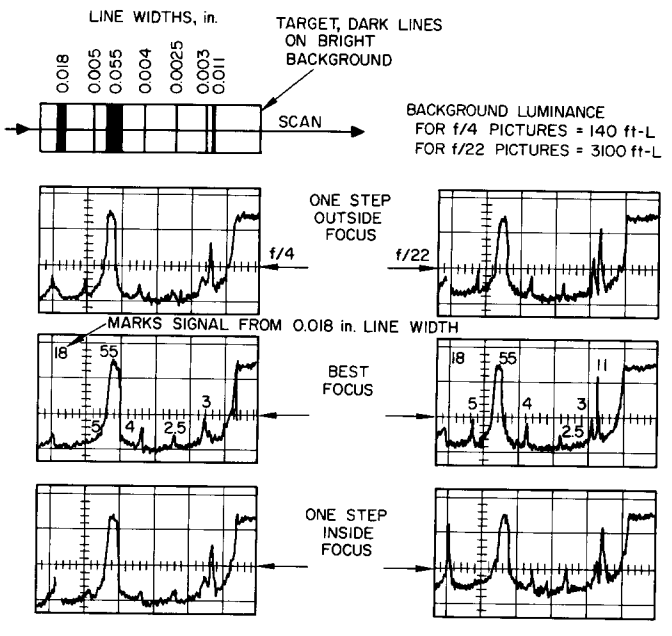

Fig. 47. A-scope photographs of vidicon signal scanning across image of line target

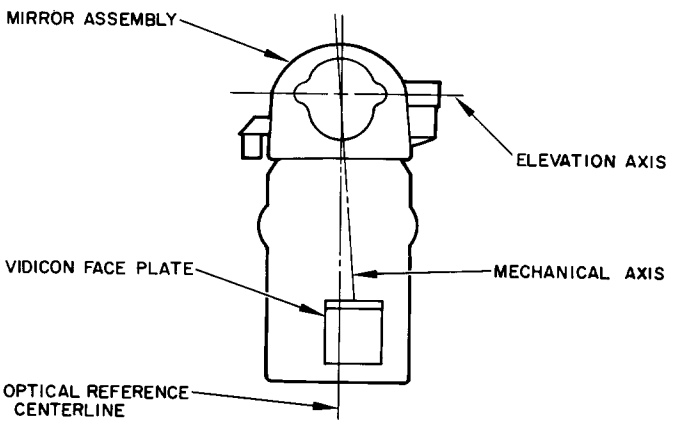

Fig. 48. TV camera axis orientation

assembly tolerance deviations. The results of the two parts are then added, and the summation indicates the total possible TV camera misalignment.

Part I. This analysis determines the maximum misalignment of the mechanical axis from the optical reference centerline resulting from eccentricity, hole spacings, and allowable tolerances. The mechanical axis may be defined as the axis originating at the center reseau mark on the vidicon faceplate and passing through the intersection of the azimuth and elevation axes of the mirror assembly (Fig. 48). The optical reference centerline is defined as the axis that would exist if the camera were structurally perfect.

Table 28 summarizes the results of the analysis.

All mechanical parts that affect the actual axis alignment are shown in Fig. 49. There are no provisions for lateral or transverse adjustments; therefore, the concentricity and tolerance allowances between parts determine the possible misalignment. The parts in Fig. 49 are shown assembled in Fig. 50

Table 28. Results of TV camera misalignment analysis (Part I)

Location point	Mechanical tolerance, in. diameter	Concentricity factor	Maximum tolerance, in.	rms tolerance, in.
Azimuth axis center on mirror surface	–	Starting point, maximum mirror elevation axis deviation 0.006 in.	0.0060	$(0.0060)^2$
Mirror baseplate bearing surface interdimension	2.3758–2.3754	Tolerance difference 0.0028	0.0014	$(0.0014)^2$
Support structure hub bearing surface	2.3734–2.3730	Concentricity 0.001 TIR[a]	0.0005	$(0.0005)^2$
Footing of support structure	5.302–5.300	Tolerance difference 0.005	0.0025	$(0.0025)^2$
Recessed diameter of deck structure, lower housing	5.305–5.302	Concentricity 0.006 TIR	0.0030	$(0.0030)^2$
Deck structure stud centers for vidicon housing	4.250–4.240	Centered on stud bell	–	–
Bore on vidicon housing for studs	4.250–4.245	Concentricity 0.003 TIR	0.0015	$(0.0015)^2$
Bore in vidicon housing	1.752–1.750	Centered by O-ring	–	
Support ring outer diameter	1.740–1.735	Concentricity 0.002 TIR	0.0010	$(0.0010)^2$
Support ring inner diameter	1.252–1.250	Tolerance difference 0.004	0.0020	$(0.0020)^2$
Thermal collar outer diameter	1.250–1.248	Concentricity 0.001 TIR	0.0005	$(0.0005)^2$
Thermal collar inner diameter	0.968	Match bore to within 0.002 in	0.0010	$(0.0010)^2$
Vidicon tube	1.050–0.985		0.194	0.0078

[a]TIR = total indicator reading

Total angle: maximum mirror to faceplate distance:

$$\tan = \frac{0.0194}{9.650} = 0.00201 = 6.891$$

Total angle: minimum mirror to faceplate distance:

$$\tan = \frac{0.0194}{9.372} = 0.00207 = 7.10$$

Maximum deviation = 0.492 mm

rms deviation = 0.198 mm (maximum)

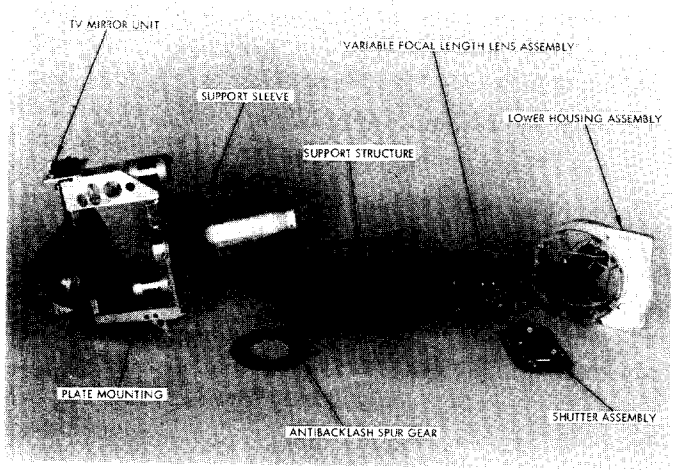

Fig. 49. TV camera parts involved in axis alignment

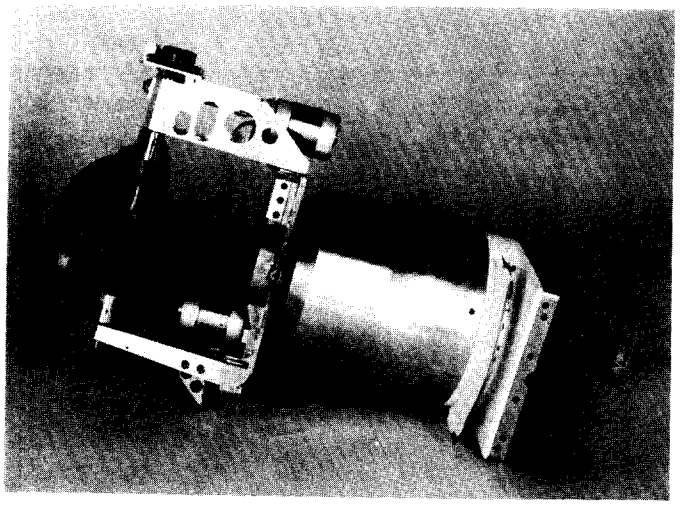

Fig. 50. TV camera parts assembled

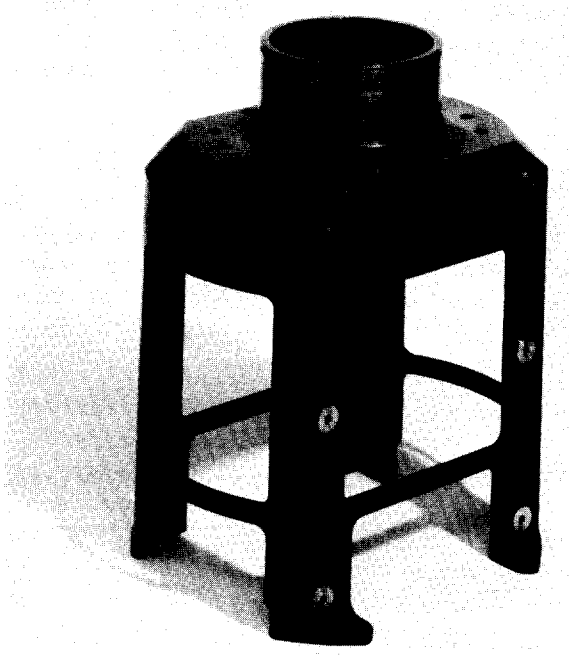

Fig. 51. TV camera support structure

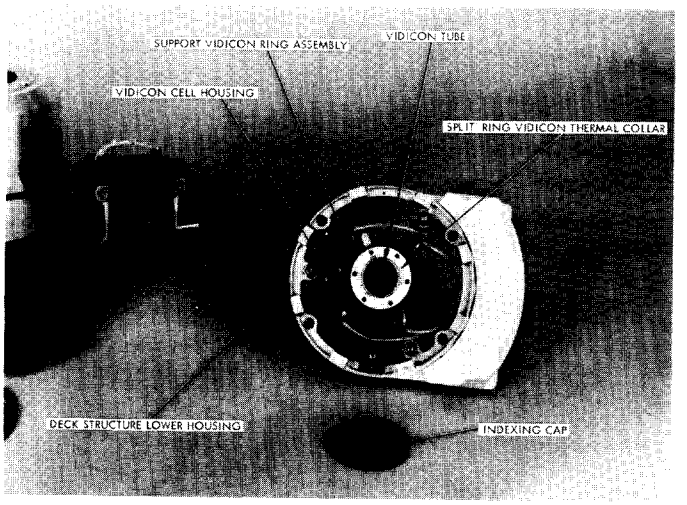

Fig. 52. TV camera lower housing assembly

Fig. 51 is a full view of the support structure, which constitutes the center about which the assemblies involved in alignment are mounted. The variable focal length lens assembly (Fig. 49) is positioned inside the support structure with the lens extending up through the hub.

The support structure is designed as a series of concentric circles. The smallest circle (the inner dimension of the hub) contains the focus cell portion of the variable focal length lens assembly. The outer dimension of the hub describes the bearing surface for the mirror assembly.

The lower housing assembly consists of the deck structure to which is attached the vidicon cell housing assembly (Fig. 52). Three arms extend out from the vidicon cell housing for mounting to the lower housing assembly, thereby assuring that the assemblies are centered under the hub of the support structure. The vidicon tube is centered in the vidicon cell housing by utilizing two separate round parts. First, the vidicon thermal collar encompasses the vidicon faceplate, and second, the support ring surrounds the collar and centers the faceplate and collar with respect to the cell housing. Thus, as in

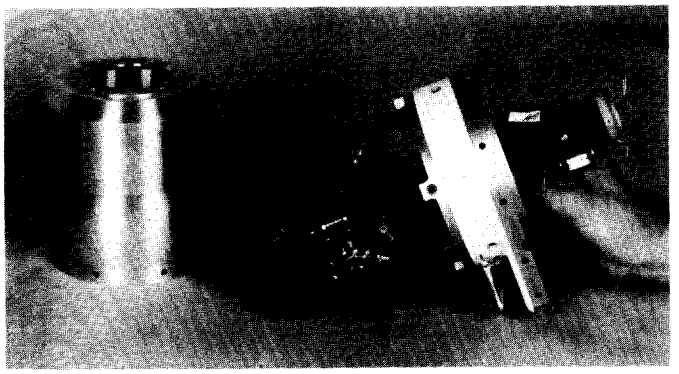

Fig. 53. TV camera support structure joined with lower housing assembly

the support structure, the lower housing assembly consists of a series of concentric circles.

Fig. 53 shows the way that the support structure, with the lens and shutter assembly enclosed, is mounted into the lower housing assembly.

The mirror assembly is shown in Fig. 49. The mounting plate that supports the mirror assembly contains a bore hole mounted over the outside diameter of the hub of the support structure. These two surfaces act as bearings during periods of mirror assembly azimuth rotation. The antibacklash gear is bolted through the topside of the support sleeve. A small spur gear projects from the mounting plate and rotates the mirror assembly around the antibacklash gear. Fig. 54 shows the gears mounted to their respective assemblies; Fig. 50 shows the assemblies connected.

The mirror assembly is designed and assembled in such a manner that the mirror elevation axis coincides with the surface of the reflecting mirror. Also, the mirror is assembled with a special tool to ensure that the elevation axis intersects the azimuth axis within ±0.010 in.

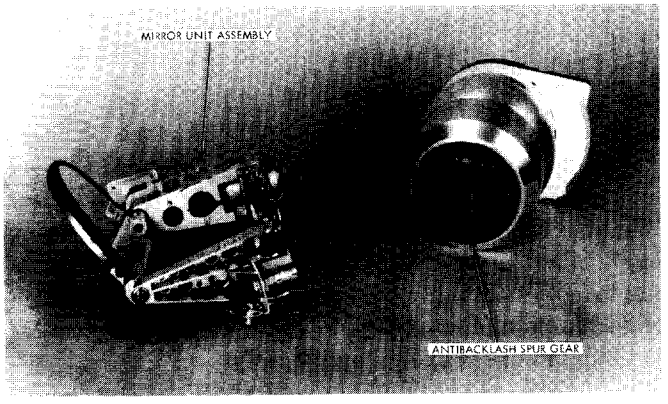

Fig. 54. TV camera antibacklash and spur gears, mounted

Part II. The second part of the analysis determines the maximum deviation that could occur between the mechanical axis and the optical reference centerline, considering only the variable focal length lens assembly.

The variable focal length lens assembly is shown in Fig. 49. In Fig. 53 the assembly is mounted inside the support structure. It is positioned and secured by four screws which extend through bore holes in the support structure. These screws are threaded to the lens assembly. Possible misalignment could occur as a result of the difference between the screw outside diameter and bore hole inside diameter.

Misalignment resulting from a canted lens assembly may also occur because the plane to which the two lens assembly support brackets are aligned may deviate by 0.002 in. (Fig. 55).

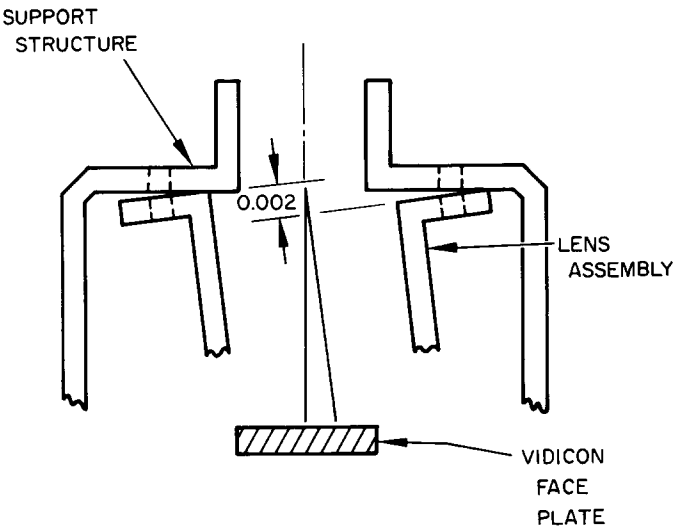

Fig. 55. Canted lens assembly misalignment (TV camera)

The results of Part II are summarized in Table 29. The maximum allowable mirror elevation axis deviation of 0.006 in. will not be considered here, since the results of the two parts are added together, and the elevation axis deviation was included in the first part. Table 30 is the summation of Parts I and II, giving the total possible misalignment.

Table 29. Results of TV camera maximum deviation analysis (Part II)

Location point	Mechanical tolerance, in. diameter	Concentricity factor	Maximum tolerance, in.	rms tolerance, in.
Azimuth axis center on mirror surface	—	Starting point	—	—
Maximum bore holes on support structure	1.4665–1.2875 in.	Included in Part I (Table 29)	—	—
Minimum screw distance on lens assembly	1.4558–1.2918 in.	Tolerance difference 0.0043	0.0043	$(0.0043)^2$
Canted lens assembly	tan = 0.00076	—	—	—
Lens concentricity	0.010	Tolerance difference 0.0006	0.0006	$(0.0016)^2$
		Concentricity 0.010	0.0100	$(0.0016)^2$
			0.0149	0.0108

Total angle: maximum mirror to faceplate distance:

$$\tan = \frac{0.0343}{9.650} = 0.00355 = 12.20$$

Total angle: minimum mirror to faceplate distance:

$$\tan = \frac{0.0343}{9.372} = 0.00366 = 12.59$$

Table 30. Total possible TV camera misalignment

Angle	Value
Maximum mirror-to-faceplate distance	12.20 min
Minimum mirror-to-faceplate distance	12.59 min 0.0343 in.
Distance	0.8713 mm 0.0187 in. (rms) 0.4750 mm (rms)

h. Survey camera alignment and mounting on spacecraft.

Alignment in spacecraft coordinates. Gimbal angles on the antenna/solar panel positioning mechanism are calibrated in spacecraft coordinates. Survey cameras are placed on the spacecraft and aligned with respect to the spacecraft z-axis. Neither the location of the intersection of the azimuth and elevation axes nor the mirror positions with respect to the gimbal angles on the antenna/solar panel positioning mechanism are calibrated. Additional tests could be implemented to provide these data.

Present plans are to align the z-axis of the survey cameras to within ± 0.5 deg with respect to the spacecraft z-axis and calibrate the alignment to within ± 0.25 deg.

The 0-deg line of sight of each camera is not calibrated. The ± 6-min-of-arc mirror position repeatability would prevent this parallelism between the two survey cameras from exceeding ± 12 min of arc.

Baseline measurement. Baseline distance is 1.24 m nominal for A-21A survey cameras. Calibration is not performed.

Alignment in camera coordinates. The intersection of the azimuth and elevation axes of each camera is not calibrated in spacecraft or camera coordinates.

Raster alignment. The rows of reseau marks are aligned parallel to the raster scan to ± 0.7 deg. Parallelism of the reseau and raster of each survey camera with respect to the spacecraft x-axis is not calibrated.

H. Flight Control

1. Effects of Degraded Vernier Engines on Flight Control System Stability

The influence of degraded vernier engine dynamic performance, because of helium-saturated propellants, on flight control system stability and performance is

being investigated by means of analog computer simulation. A "small signal" transfer function, based on analysis of propulsion system dynamics and correlation with latest test results, is used to represent each vernier engine. The transfer function has the form

$$\frac{\Delta F}{\Delta F_c} = \frac{0.316\tau S + 1}{(\tau S + 1)\left[\frac{(S)^2}{264} + \frac{2(0.3)}{264} S + 1\right]}$$

where the parameter τ is related to steady-state engine thrust as indicated in Table 31. Both the retro phase and the vernier descent phase, including interaction with radar noise, are being investigated in this study. Preliminary results verify that flight control system response to retro disturbances and noise inputs becomes less well damped with this engine model, particularly for the low steady-state thrust levels. The analysis to date has been done with the simplifying assumption that the linear model for a particular thrust level is valid over the entire thrust range. For a true assessment of the system stability, however, it appears that it will be necessary to incorporate the thrust-variable and time-variable aspects of the engine dynamics. This will be approached from two aspects: (1) development of the necessary refinements to the engine model, and (2) tie-in of the actual engines with a closed-loop system simulation at Placerita Canyon during the S-6 margin limit tests.

Table 31. Vernier engine steady-state thrust values

Vernier engine thrust level, lb	Vernier engine time constant τ, sec
33	0.16
67	0.048
101	0.02

2. Flight Control Sensor Group Testing

The third flight model (235000-4 SN-2) was delivered to the SC-1 spacecraft on August 20, replacing the second model of the -6 configuration, which was on the spacecraft, and providing SC-1 with the fully automatic Sun acquisition capability. The 235000-4 SN-1 unit was subsequently delivered to the SC-2 spacecraft. Flight acceptance testing was initiated on the SP-1 (spare) unit (235000-7 SN-1) with delivery to the systems area scheduled for mid-November. The flight control sensor group test position was delivered to the Air Force Eastern Test Range and checked out using a Class IV-T flight control sensor group.

3. T-2N Design Review, Analysis, and Testing

a. Design review. An informal design review of the T-2N descent control system was conducted and a detailed listing of operational and design constraints was presented. One critical constraint was the lack of adequate aerodynamic drag data for T-2N vehicles; this data was obtained from subsequent T-2N-R tests.

b. Drag determination. In the equation for drag D,

$$D = 1/2\,\rho\, SC_D\, V^2$$

the term $SC_D/2$ should be a constant, where ρ = air density, S = area, C_D = drag coefficient, and V = velocity. Results of T-2N-R Tests 6 and 7 showed a difference of approximately 3% for this term with the results of Test 7 slightly higher than those of Test 6. This increase is attributed to a modification in the aerodynamics configuration to obtain a gain in roll damping. These test results are adequate to remove any further uncertainties about the drag coefficient C_D.

c. Analog studies. Some of the analog studies that were outlined during the design review have been completed. These studies were required to determine the best operational conditions for the actual descent test. These operational conditions must be consistent with the actual operational capabilities and with the design constraints. The analog descent runs were conducted with specification allowable errors (errors that are within the normal allowable tolerances) for such items as radar, propulsion, flight controls, and field equipment. From these runs the actual descent flight time (35 sec), initial launch mass (7.1 slug), and launch altitude (1450 ft) were determined.

Additional analog studies will be conducted prior to the actual descent test, utilizing the error values determined from actual hardware measurements, and thus will be as close as possible a prediction of the expected test performance.

d. Tethered tests. Two tethered tests have been conducted and the data analyzed. Both tests showed that the flight control system performed its control function very well, thus adding confidence to the expectation of successful descent tests.

4. Canopus Sensor

A production model of the new configuration sunshade, which is longer and includes a greater number of baffles,

has been subjected to stray light and moonlight interference tests such as were performed on the developmental model. A comparison of production model data and developmental model data indicated no significant differences.

The susceptibility of the Canopus sensor to free particles that may enter the sensor field of view has been investigated. No significant degradation of mission success is expected to result from this source.

5. Inertial Sensors

a. Gyros. Repeated testing of a number of gyros over the last 2 yr has revealed a trend, in some gyros, of decreasing transfer function with time. Several gyros were returned to the manufacturer where the low transfer function values were verified. Subsequent to various diagnostic tests, the manufacturer disassembled Gyro 55 for an evaluation of internal parameters. There are five parameters that affect transfer function; namely, wheel speed, signal generator scale factor, fluid temperature, fluid viscosity, and fluid gap dimensions. Of these five parameters, wheel speed, signal generator scale factor, and fluid temperature were found unchanged. However, the lack of absolute measurements (only go, no-go gages were used) of some gap dimensions and a lack of fluid viscosity measurements at the time of gyro sealing suggest that changes in gap dimensions and fluid viscosity could have caused the transfer function shift. After discussions with representatives of both gyro manufacturers and the fluid manufacturer, the possibility has developed that a polymerization reaction may continue after a fluid is sealed in a gyro, thus causing a viscosity increase. Time and temperature gyro time histories are being analyzed to determine if some correlation does exist between transfer function decreases and chemical reaction time, thus supporting the polymerization reaction possibility.

The practice of returning out-of-specification, in-warranty gyros to the manufacturer for rework will continue. The knowledge that transfer function decreases with time may be utilized to retrim the transfer function to the high side of its tolerance.

b. Accelerometer. An analysis of the two type-approval-test ± 0.75-g accelerometers revealed that one of the accelerometers had a discrepancy in scale factor; a pivot bearing holding screw was not staked with cement, allowing the preload to be lost during vibration. Although staking cement was present in the other unit, it was decided that too low a preload was being used and that all ± 0.75-g units would be reworked to incorporate a higher preload. Since the accelerometer is excited some time before launch, any increased turn-on friction due to the increased preload would not be present after launch.

Based on additional vibration data it was determined that the previously prescribed type-approval vibration level of 30-g sine-wave plus 4.5-g random was too high, and the level has been below load to 18-g sine-wave plus 4.5-g random. Two additional accelerometers with the higher bearing preload are being subjected to type-approval testing at revised vibration levels. Preliminary results indicate that one sample is slightly out of specification after vibration, and it is suspected that the actual bearing preload is lower than the manufacturer's specified value. Also it is suspected that the actual vibration levels seen by the accelerometers were higher than the prescribed levels due to test fixture resonances. Further testing and an analysis by the manufacturer are under way.

c. Inertial reference unit. Inertial reference unit was delivered and is undergoing group-level flight acceptance tests with the SP-1 flight control sensor group. Data from partial solar-thermal-vacuum testing on the SC-1 spacecraft indicates that the pitch, roll, and yaw gyro heaters were cycling at 12, 16, and 25%, respectively. Thus it appears that the addition of the side thermal radiator has resulted in an adequate gyro heater control margin; but, as predicted, the thermal unbalance between gyros has not been significantly changed.

Additional low-voltage tests on the 22-vdc bus have been conducted at the inertial reference unit and flight control sensor group testing levels in an effort to duplicate a temperature controller oscillation first observed in T-21 solar-thermal-vacuum low (18 vdc) voltage tests. To date duplication of the oscillation has not been achieved, although different modes of oscillation have been observed at voltages lower (16.5 vdc) than the lowest (18 vdc) expected on the spacecraft. Investigations are continuing to obtain the oscillation, determine if gyro temperatures are affected, and determine the cause of and remedy for the oscillations, if the temperatures are grossly affected.

6. Electronics Unit

To provide a spare (SP-1) flight control sensor group (FCSG) as a backup for SC-1 and SC-2, it was decided to install Electronic Unit 12, the first of the -5 configurations having quasi-square wave power, in a FCSG-4 housing that can be mated to SC-1 or SC-2. A new internal

harness for the electronics unit has been fabricated which mates the -5 electronics unit to the FCSG-4 housing and creates a -7 configuration of the electronics unit and the FCSG. This unit has been delivered to the subsystem test area.

Electronics Unit 16, as part of FCSG-5(SN 1), has been delivered for use on SC-3. Electronics Unit 17 is undergoing subassembly testing as part of FCSG-5(SN 2). Partial redesign is in process for the electronics units for model A-21A spacecraft (SC-5 through SC-8). The redesign, which creates a -8 configuration, affects the midcourse acceleration level and the descent segment networks because of the heavier spacecraft. It is expected that Electronics Unit 13, part of FCSG-6(SN 1) subjected to an overvoltage application during SC-1 system testing, will be modified to the -8 configuration as a Class IV-T unit for use on the A-21A proof test model (SC-5).

7. Gas Jet System

a. Gas supply. During flight-acceptance testing of the gas supplies for SC-1 and SC-2, the gas tank was pressurized to 125 psig, which is sufficient to maintain the regulator valve in a closed position. Higher pressures are not permitted because of safety limitations. It was decided that unit flight-acceptance vibration testing should be accomplished with the gas tank pressurized to flight limits; therefore, future vibration testing will be done at the Hughes Aircraft Company Tucson facility, which has the required safe area.

Normal flight-acceptance testing of the gas supply does not include a test of the tank charging valve since unit flight-acceptance testing is done in an area where flight pressures cannot be used. To demonstrate the reliability of the tank charging valve, including removal of the charging line, a test program is planned to test two tanks at flight pressure at a remote safe area. A preliminary test has been made on a portion of a tank with charging valve and fitting attached. In this test the valve was operated 27 times at 4600 psig and 4 times at 6000 psig by closing the valve with the specified torque of 55 to 60 in.-lb. It was observed that shutoff (i.e., no leakage) occurred between 25 and 30 in.-lb torque, which indicates an adequate safety margin against leaks.

b. Attitude jets. The SC-1 attitude jets were re-leak-tested after the six individual jets had been operated from 5,460 to 34,200 cycles. All jet valves were leaking less than 2 cm^3/hr, at standard temperature and pressure (STP), well within the allowable limits, 18 cm^3/hr STP. Also, jet valve discharge cleanliness was within allowable limits.

The probable operating life of a jet valve has been demonstrated by testing five valves over 100,000 cycles, the type-approval-test valve over 250,000 cycles, and another valve over 500,000 cycles, all without exceeding allowable leakage limits. The last valve has now been tested over 900,000 cycles and is still operating, but outside allowable leakage limits. Based on these tests, it appears that a nominal jet valve life before wearout begins is 100,000 cycles and at least 65% life remains on the most exercised jet valve on SC-1.

c. System installation. Manifold line material has been changed from 6061-T6, 0.025-in.-wall, 3/16-in.-diameter aluminum tubing to 5052-0, 0.028-in.-wall, 3/16-in.-diameter aluminum tubing to obtain a better tubing flare. Based on manifold pressure drop tests this small decrease in tube inside diameter will not measurably affect system operation.

The attitude control system installation and test procedure has been revised to specify in detail the installation sequence, fitting torques, leak tests, and cleanliness tests required to assure a satisfactory system. The SC-2 installation has been completed to this revised procedure and checkout tests are under way.

8. Roll Actuator

Additional vibration exposures were performed on the former type-approval-test roll actuator unit modified to the latest configuration. The survival of the unit through an additional 54 min of type-approval-test level and 90 min of flight-acceptance-test level vibration has demonstrated that the fatigue life is sufficient to allow 12 complete flight-acceptance-test vibration exposures at the unit level prior to subsequent vehicle vibrations from transportation and handling and the actual mission. Since the unit was subjected to the equivalent of 6 complete flight-acceptance-test level vibrations during the actual type-approval test program, the total number of complete flight-acceptance-test level vibrations survived is 18. Based on these data and allowing a large margin of safety, the specifications for flight-acceptance-test vibration exposures at the unit level now limit the number of such exposures to 5.

Because of a high probability that the squib in the pin puller may exhibit, after ignition, an electrical short circuit between squib firing circuitry and spacecraft

ground, it was decided to provide electrical insulation between the squib and spacecraft ground. This modification consists of various teflon insulators and has been accomplished on SC-1 and SC-2.

An operating roll actuator was installed on the S-7 vehicle for the purpose of exercising the roll actuator and Vernier Engine 1 during the type-approval vibration testing of the vernier propulsion system at the JPL Edwards Test facility. The roll actuator was commanded through a series of plus and minus roll positions during simulated midcourse firings and vernier descent firings. Preliminary test results indicate that all roll actuator responses were satisfactory and no failures occurred. Data from a post-type-approval functional test will be analyzed to ascertain if any significant change occurred in the roll actuator.

I. Electronics

1. Diplexer and Transmitter

a. Voltage breakdown in low air pressure. Efforts to make the transmitters insensitive to the critical air pressure region are continuing. Some success was achieved during high voltage tests conducted on the spacecraft compartment. The present fix utilizing high density foam can only be considered as a temporary solution. Work is continuing to find an acceptable solution. Test results showed that the compartment is not well vented as evidenced by an internal pressure lag over external pressure; therefore, the compartment will be at critical pressure at the time of high power turn-on, approximately 11 min after launch.

Since the transmitter contains high voltage in the electrical conversion unit and high RF voltage, when operated through the diplexer, several modifications were necessary: (1) in the electrical conversion unit, the high-voltage wires were rerouted, (2) high-voltage areas were foamed, (3) the diplexer was arc-proofed by connecting a tube from a hole in the diplexer wall to the outside of the compartment so that this unit will not be subject to the pressure lag. Three transmitters have been upgraded on the high-voltage configuration and have passed portions of the critical pressure high-voltage test. The test consisted of the following steps: (1) turn high power on while at sea level and pump vacuum chamber to 1×10^{-4} mm of Hg, (the critical pressure zone is from 38 mm of Hg to about 5×10^{-4} mm of Hg), (2) dwell at 1×10^{-4} mm of Hg for 15 min, (3) bring vacuum chamber back to sea level, and (4) pump vacuum chamber to 1×10^{-5} mm of Hg.

b. Electrical conversion unit turnoff problem. While performing the thermal vacuum test on transmitters, it was discovered that after 1 hr of high power operation in vacuum and +125°F mounting tray temperature, the high-voltage converter on several of the units would not turn off. Investigation revealed that the converter transistor temperatures were too high and circuit deficiencies existed in the converter. "Sneak paths" in the converter base drive circuit apparently caused the problem, since removal of such paths led to proper operation. High temperature effects on the malfunction have not been precisely determined. Temperature-dependent parameters, such as current gains, diode drops, and leakage currents, however, were so affected as to contribute to the malfunction. Circuit and heatsinking changes have been completed on four transmitters. These transmitters have been thoroughly tested and delivered for spacecraft installation. In several cases, however, these transmitters have, for schedule reasons, been delivered with an out-of-specification power drop in the low power mode after high power operation.

2. Altitude Marking Radar

a. Magnetron tuner problem. A joint program was undertaken between Hughes Aircraft Company and the tube vendor (METCOM) to make design improvements necessary to improve the magnetron tuner locking mechanism in order to assure frequency stability. Problems related to the tuner found to cause frequency changes beyond ±1.5 Mc are:

(1) Changes of frequency due to vibration.

(2) Temperature coefficient repeatability.

(3) Frequency repeatability after cycling.

Analysis of these problems led to the following design efforts:

(1) Internal tuner redesign to eliminate radial play was accomplished by the design of an expanding slotted stainless steel bearing collar in the vicinity of the electrical tuning ring.

(2) External tuner redesign to improve the stability under conditions of vibration and temperature

cycling was accomplished by providing a compression-controlled axial spring at the outside end of the tuner shaft. This established a positive axial seat.

b. External tuner redesign. The old design of the tuner depended on the pull of the vacuum on the bellows, the fit of the No. 4-40-NC3 threads between the vertical shaft and helical gear, and a spring washer between a shoulder on the aluminum housing and top of the helical gear. This combination showed frequency repeatability problems with temperature cycling and vibration and a varying temperature coefficient slope from tube to tube. Investigation showed this to be a problem because the longitudinal members of the tuner did not have a dependable established axial position. A positive locking mechanism was designed and installed on several RF assemblies. This mechanism used a 0.0625-in.-diameter ball nestled between sockets in the tuning shaft and the lock nut.

On some tuners, change in frequency, after temperature cycling, was found to occur with this design. It was found to be related to the mating surfaces of the top of the tuning shaft and the locking socket. There was also the danger of having the ball fall out of the socket when the locking nut was backed off. The next design modification was to eliminate the ball and use a rounded section on the locking shaft. Some RF assemblies were originally produced in this way.

Testing indicated that this solution was inadequate for the temperature cycling problem. The point of contact with the socket in the tuning shaft could shift, causing a change in axial force, resulting in a frequency jump.

The final design installed a flat-to-flat mating surface to eliminate the problems of a new set taking place after temperature cycling. Tests with this design indicate worst-case shifts after temperature cycling of less than 1 Mc. This is well within the acceptable limits for proper altitude marking radar performance.

c. Present status. Four RF assemblies were delivered with the ball and socket locking mechanism. Three of these have been downgraded and are no longer flight hardware. Although this design has shown greater frequency shifts in temperature cycling than the latest design, tests indicate that the frequency stability is within 1.5 Mc, which is within specification requirements for system performance.

Three RF assemblies were delivered with the locking mechanism using a rounded section. Several RF assemblies were reworked by the vendor to incorporate the locking mechanism employing flat surfaces. During acceptance tests all RF assemblies are now subjected to temperature cycling and a vibration test. A continuing test program is being conducted in cooperation with METCOM to ensure the quality of the RF assemblies.

3. Radar Altimeter and Doppler Velocity Sensor

a. Klystron power supply modulator (KPSM) altimeter. Altimeter klystron problems caused by noise generated by klystron mechanical resonances and excited by mechanical noise in the KPSM were detected during testing. The KPSM mechanical noise which changes as a function of input voltage and temperature must be coincident with the klystron mechanical resonances to cause the problem. The klystron noises have peaks which rise as a function of time and input and reach amplitudes far above that of the tracker lockon level.

It was first thought that the problems were electrical, and that to reduce the noise output a decrease in the electrical noise on each of the klystron critical lines (reflector and cathode) would have to be made. When measurements were made of these lines on two KPSMs (AM-3 and AM-4) and extrapolated, good correlation could not be obtained with RF output noise at the various frequencies. Tuning the reflector voltage for minimum amplitude modulation (AM) output at 3.5 or 7.0 kc yielded similar results. No correlation could be made at several points nor could the noise be minimized when the reflector voltage was varied for minimum AM at these points. When the tube and corner section were separated from the structure, the general noise level dropped and the noise problems disappeared entirely. Replacing the tube and corner section on the structure again yielded the same results.

A dynamic vibrator was then pressed against the klystron corner section, which was removed from the structure and the frequency varied. It was discovered that a great number of resonances appeared; resonances with large Q factors appeared at 10, 18, 31, 44, and 49 kc. Q factors of approximately 5000 were measured with the frequency difference method.

Measurements of the mechanical noise on the KPSM were made in three planes using an accelerometer. Large incident noise around 18 kc was noticeable with noise

occurring at 8, 11, 31, and 35 kc in varying degrees. One plane showed a greater level of 18-kc incident noise, this plane being in the longitudinal direction of the switching reactor. The switching reactor was removed from the KPSM and, again, the mechanical noise was measured in three planes on the KPSM structure. Very little noise was measured at any frequency and none appeared at 18 kc. Mechanical noise was then measured on the switching reactor core. The 18-kc noise was extremely high, greater than 20 db higher than that measured on the structure when the reactor was mounted in the unit.

It was concluded that the isolated corner section presented the best solution. This correction was made and put through type approval testing. Subsequently the KPSMs for the SC-1, SC-2, and the thermal control model spacecraft were so isolated. All flight models now have isolated corner sections. Test results demonstrate that this modification has helped to solve the problem.

b. Mixer diode problem. Ryan Aeronautical Corporation has determined that the mixer diodes that have been delivered thus far can be grouped into three general categories with regard to case construction:

(1) Older diodes with rugged cases.

(2) New diodes with rugged cases.

(3) Interim diodes, which exhibited an unacceptable failure mechanism in that the terminals separated from the ceramic body.

All of the latter have been removed from Class IV stocks and will be used only in test equipment.

Those diodes that are in SC-1 and SC-2 units have been identified as being from the first category. Positive assurance will be obtained on future systems to preclude the possibility of receiving diodes that exhibit the failure mechanism of the third category. Ryan is continuing to develop acceptance criteria that can be used on future deliveries.

4. Antenna Radiation Measurements[4]

The need for a remeasurement of the *Surveyor* spacecraft omnidirectional antenna patterns has been established (Ref. 7). It has also been established (Ref. 7) that in order to realize an increase in antenna pattern accuracy by use of the JPL spacecraft antenna range, a spacecraft model of higher quality than that originally used for antenna pattern evaluation will be necessary. This article illustrates one of the problems of modeling a full-scale model spacecraft for duplicating the RF radiation patterns of the flight spacecraft. For proper modeling, the problems associated with electrically-grounded dielectric slabs were investigated.

a. Grounded dielectric slabs. Dielectric materials of various electrical properties, surface area, and thicknesses are used on the current *Surveyor* spacecraft for functions such as thermal control and energy conversion. One example of a thermal-control structure is a system of vicor mirrors (Fig. 56) which make up the major portion of the top surfaces of electronic Compartments A and B. These mirrors are the radiating part of a thermal switching system which varies, as needed, the thermal conductance between the inner and outer portions of the compartments. When viewed from an RF standpoint these surfaces have the potential of supporting surface waves and creating surface-wave radiation, to be presently discussed. The solar panel (Fig. 56) consists of a series of solar cells bonded to an aluminum substrate. This solar panel constitutes a grounded dielectric surface which is also subject to RF surface-wave excitation and radiation, similar to the mirror surface. In both of these situations,

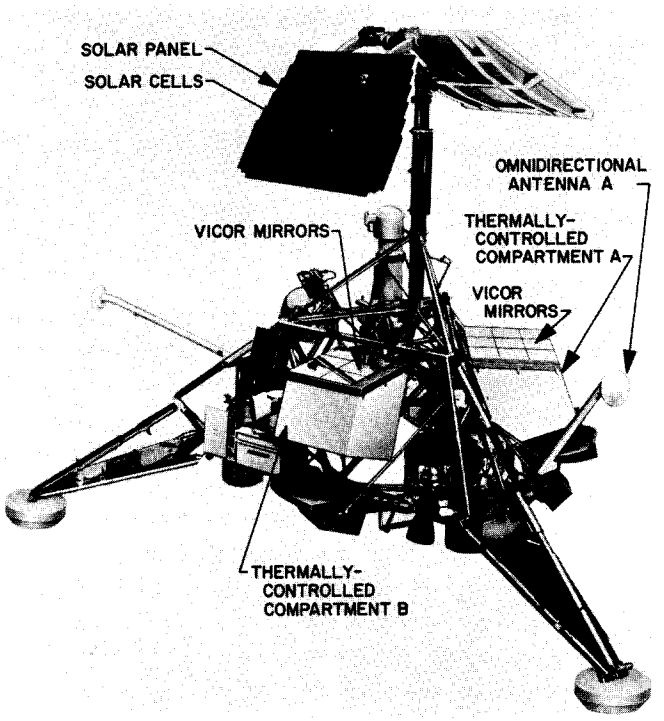

Fig. 56. *Surveyor* A-21 spacecraft—solar panel and thermal-controlled compartments

[4]Prepared by JPL Technical Section 336.

the question arises as to what the effect of the dielectric surfaces is, and whether the dielectric surfaces must be incorporated in the RF model for accurate external reflective simulation.

A decision concerning use of a particular dielectric in the model depends on the following factors:

(1) Relative location of the dielectric surface on the spacecraft.

(2) Physical dimensions of grounded dielectric slab.

(3) Electrical properties of the dielectric material.

The discussion which follows is relative to the thermal-control vicor mirrors (but applicable to the solar panel) and is to show the necessity for mocking-up the mirror dielectric surface in the RF spacecraft model.

b. Analysis. The vicor mirrors used on Compartments A and B (Fig. 56) constitute a grounded dielectric surface of 0.020-in. thickness, having a relative dielectric constant of $E_r = 3.80$. Fig. 57a shows the relative position between the edge of the top surface of Compartment A and Omni-antenna A to be approximately 30 deg in elevation.

At the air-dielectric interface of this surface there exists the possibility of surface-wave excitation (Ref. 8, Chapter 11) along the top surface of the compartment for angles of incident radiation which are near grazing with respect to the compartment surface. Two consequences of surface-wave excitation are of concern:

(1) The amount of power carried by the dielectric surface.

(2) The effective surface-wave antenna created and its corresponding gain and directional characteristics.

Collin (Ref. 8, pp. 476–477) has shown that a complete solution for the fields which may propagate along a dielectric surface consists of:

(1) One or more modal solutions.

(2) A continuous spectrum solution.

(3) A continuous spectrum solution of waves which are evanescent in the direction of propagation.

The modal solutions for a grounded dielectric slab have a low-frequency cutoff for the case of perpendicular or TE polarization and hence this polarization is of no interest with a dielectric 0.020-in. thick. Parallel or TM polarization however, has no low-frequency cutoff and constitutes the continuous spectrum solution for dielectric thicknesses approaching zero.

Focusing attention on the case of TM polarization, we wish to calculate the ratio of power carried in the dielectric to that outside the dielectric. Atwood (Ref. 9) has derived expressions for power for the case of a grounded thin dielectric slab of infinite surface area as shown in Fig. 58. From Atwood's paper,

$$\bar{P}_{z2} = K_z^2 \frac{\beta}{4\, k_2\, \omega \epsilon_2} \left[k_2 a + \frac{1}{2} \sin (2\, k_2 a) \right] \tag{1}$$

$$\bar{P}_{z3} = K_z^2 \frac{\epsilon_3\, k_2^2 \beta}{4\, \epsilon_2\, k_3^3 \omega \epsilon_2} \sin^2 (k_2 a) \tag{2}$$

where $\bar{P}_{z2}$ = the z-directed power carried inside the dielectric, medium 2; and $\bar{P}_{z3}$ = the z-directed power carried outside the dielectric, medium 3.

Forming the ratio $\bar{P}_{z2}/\bar{P}_{z3}$ and making the approximation $\sin (2k_2 a) \simeq 2\, k_2 a$ since $2\, k_2 a \ll 1$, we have

$$\frac{\bar{P}_{z2}}{\bar{P}_{z3}} = \frac{\epsilon_2\, k_3^3}{\epsilon_3\, k_2^3} \left[\frac{k_2 a + k_2 a}{(k_2 a)^2} \right] \tag{3}$$

$$\frac{\bar{P}_{z2}}{\bar{P}_{z3}} = \left[\frac{2\, \epsilon_r\, k_3^3}{k_2^4 a} \right]; 2\, k_2 a \ll 1 \tag{4}$$

where a = thickness of dielectric slab, ϵ_r = relative dielectric constant of dielectric, k_2 = transverse propagation constant inside dielectric, and k_3 = transverse propagation constant in air.

For $\epsilon_r = 4.0$ and k_2, k_3 selected at $f \sim 2.3$ Gc from data supplied by Atwood, Eq. (4) has been plotted (Fig. 58) and relates the percentage of power carried by the dielectric relative to that outside the dielectric. For a dielectric thickness of 0.020 in. (thickness of vicor mirrors), this power ratio is 0.020% or −37 db. With the power carried by the dielectric surface known, we wish now to determine the characteristics of the effective surface-wave antenna.

c. Compartment A as a surface-wave antenna. Referring again to Fig. 56, the dielectric-clad top surface of the compartments have the potential of radiating that portion of energy carried in the surface, as an endfire antenna.

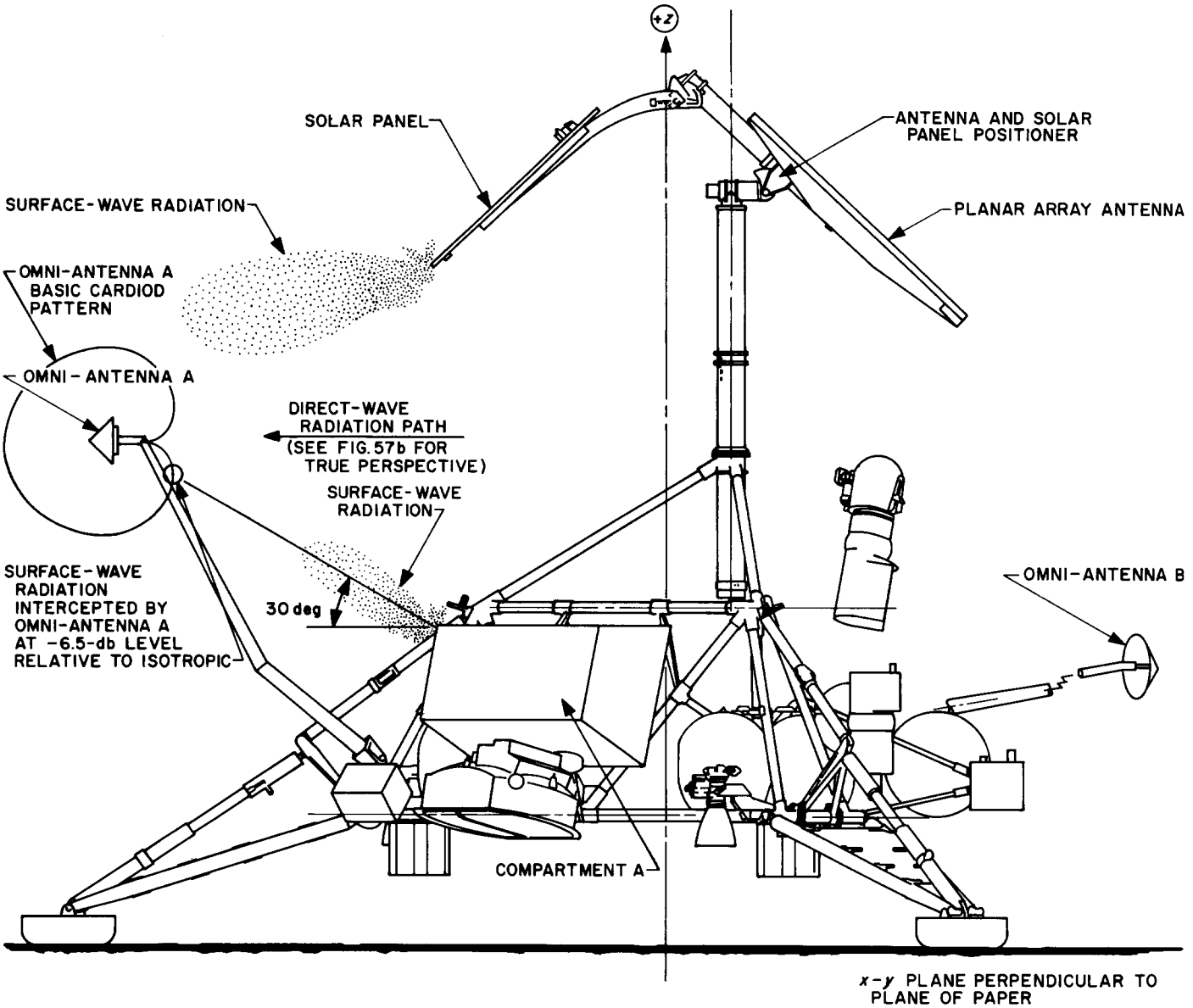
+z
SOLAR PANEL
ANTENNA AND SOLAR PANEL POSITIONER
SURFACE-WAVE RADIATION
PLANAR ARRAY ANTENNA
OMNI-ANTENNA A BASIC CARDIOD PATTERN
OMNI-ANTENNA A
DIRECT-WAVE RADIATION PATH (SEE FIG. 57b FOR TRUE PERSPECTIVE)
SURFACE-WAVE RADIATION
SURFACE-WAVE RADIATION INTERCEPTED BY OMNI-ANTENNA A AT -6.5-db LEVEL RELATIVE TO ISOTROPIC
30 deg
OMNI-ANTENNA B
COMPARTMENT A
x-y PLANE PERPENDICULAR TO PLANE OF PAPER

Fig. 57a. *Surveyor* A-21 spacecraft—relative location between Compartment A and Omni-antenna A

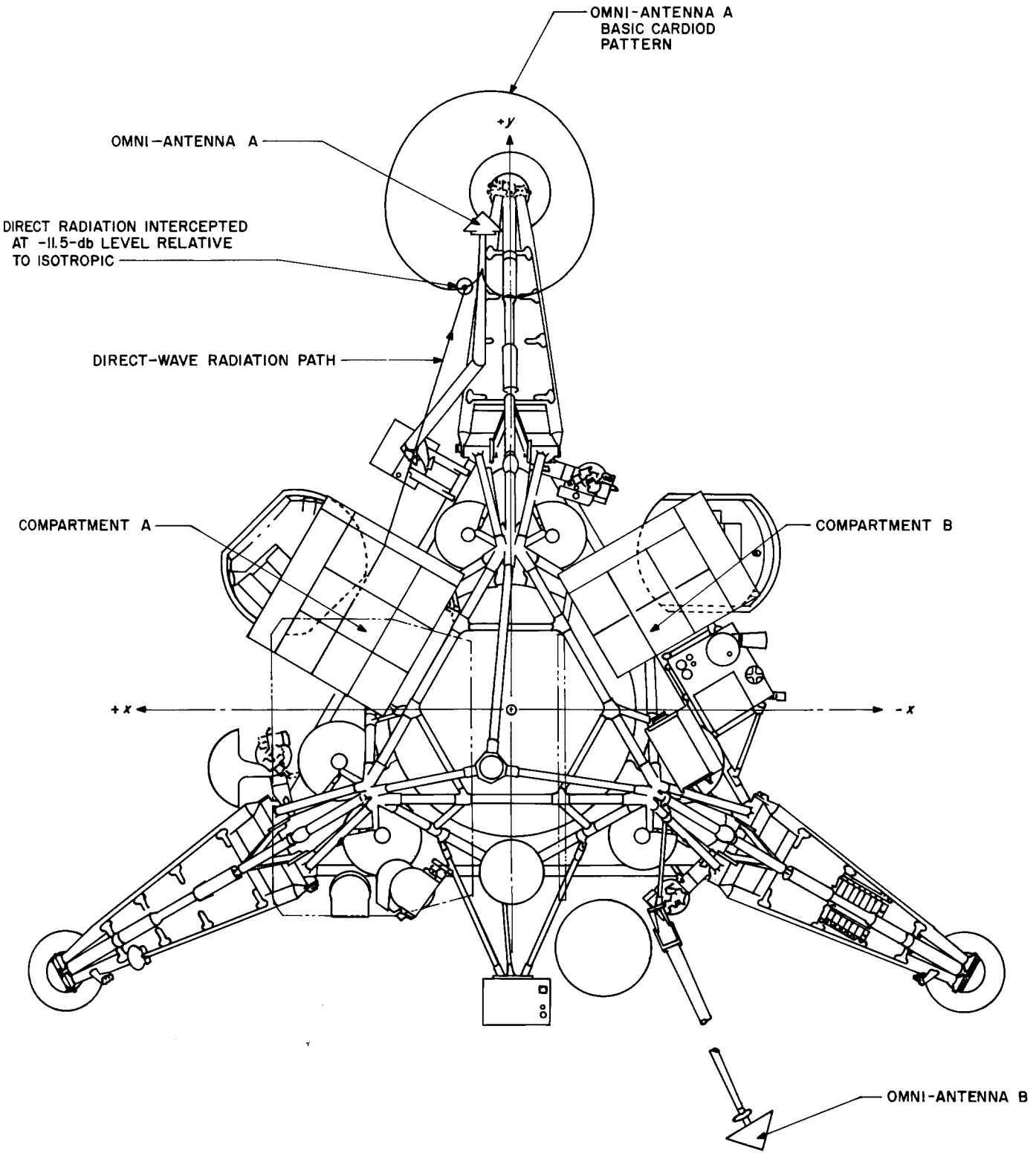

Fig. 57b. *Surveyor* spacecraft—plan view of direct path radiation

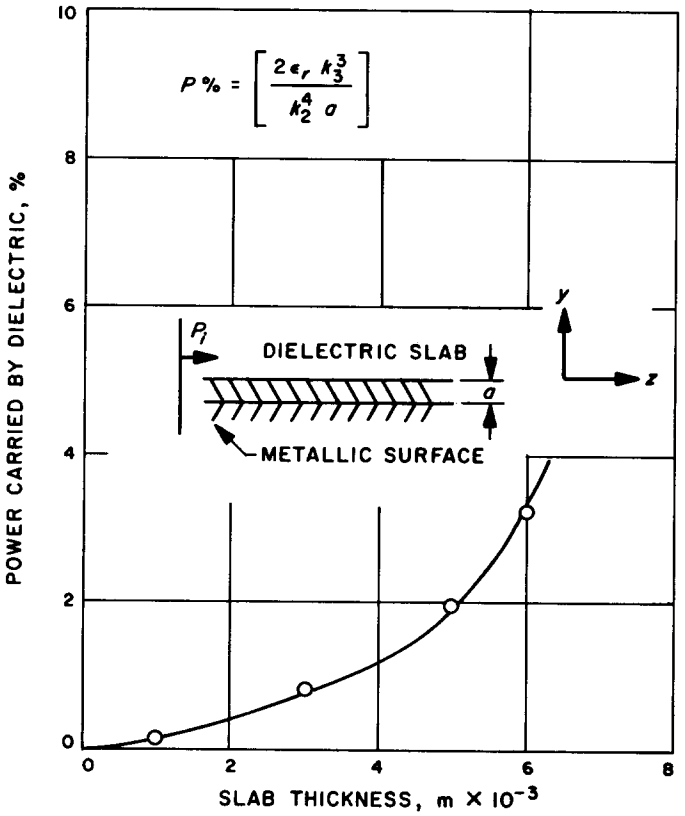

Fig. 58. Relative power carried in dielectric surface

The gain (Ref. 10) of this effective surface-wave antenna is

$$G = 10 \log_{10} \left[12 \frac{w}{\lambda} \sqrt{\frac{L}{\lambda}} \right] = 19.7 \text{ db} \qquad (5)$$

where w = surface width = 18.5 in., L = surface length = 22.0 in., λ = wavelength = 5.14 in., and the main lobe is tilted (Ref. 10) from a true endfire direction through an angle in an upward direction of

$$\psi = 60 \sqrt{\frac{\lambda}{L}} = 29.0 \text{ deg} \qquad (6)$$

It is noted from Fig. 57a that the Omni-antenna A is approximately 30 deg from the edge of the compartment surface. Eq. (6) reveals that the main lobe of the resultant surface-wave antenna is pointing right at Omni-antenna A, indicating a direct influence on Omni-antenna A by the surface antenna.

Figs. 57a and 57b depict graphically the case where the incident and re-radiated surface-wave energy intercepts the Omni-antenna A in the rear hemisphere of its radiation pattern. The influence of this re-radiated surface-wave energy on the amplitude of the antenna pattern at this location can be determined in the following manner (it is assumed for simplicity that the energy incident on the omni-antenna is from the two directions only).

Consider first, the relative levels between the surface-wave and direct-wave radiation.

$$\Delta\text{db} = G_s + P_d + P_p = -20.3 \text{ db} \qquad (7)$$

where Δdb = difference between direct and surface-wave signal levels, G_s = gain of surafce-wave antenna = 19.7 db, P_d = relative power carried inside dielectric = −37 db, and P_p = polarization loss, considering TM wave only = −3 db.

Now the surface-wave radiation is intercepted by the omni-antenna at a point corresponding to a level of −6.5 db relative to isotropic. The direct radiation is intercepted by the omni-antenna at a point corresponding to a gain level of −11.5 db relative to isotropic. The surface-wave radiation has, therefore, a 5.0-db gain over the direct radiation when viewed from the omni-antenna terminals.

We add the 5.0 db of surface-wave radiation gain to Eq. (7) to determine the resultant relative levels between the surface-wave and direct-wave radiation at the antenna terminals.

$$\delta\text{db} = \Delta\text{db} + G_A = -15.3 \text{ db} \qquad (8)$$

where δdb = relative levels between the direct and surface-wave radiation at the terminals, Δdb = same as in Eq. (7), and G_A = gain of surface-wave radiation over direct radiation due to omni-antenna pattern shape and angle of arrival.

The relative signal level of −15.3 db at the antenna terminals could add in phase to yield a maximum or out of phase to yield a minimum resulting in an amplitude level which lies within a maximum possible peak-to-peak uncertainty of

$$\delta'\text{db} = 10 \log_{10} \left[\frac{V_i + V_s}{V_i - V_s} \right]^2 = 2.94 \text{ db} \qquad (9)$$

where δ'db = maximum possible peak-to-peak pattern variation of Omni-antenna A at the grazing angle of incidence, V_i = voltage due to direct path radiation, and V_s = voltage due to surface-wave antenna.

The magnitude of this amplitude variation suggests that the surface if not mocked up could produce an uncertainty of 2.94 db worst case in the amplitude of the

omni-antenna pattern. It is believed however, that the level of uncertainty will be less than worst case since random effects such as small discontinuities in the dielectric and a small effective ground plane at the edge of the surface will tend to decrease the level of surface-wave radiation at the omni-antenna terminals. For angles of incidence other than the critical grazing angle, surface-wave radiation is expected to exist, but of decreased influence due to the decreased amplitude of surface-wave excitation. To eliminate any doubt as to the actual pattern amplitude perturbations caused by the surfaces of the electronic compartments, these surfaces will be mocked up.

The solar panel dielectric, under similar analysis, should also be mocked up. The solar panel has a larger surface area, which provides an effective surface antenna of higher gain. It also has a number of degrees of freedom, which provide the capability of illuminating the omni-antennas directly as well as indirectly by illumination of different parts of the spacecraft.

d. Summary. It has been shown that the influence of thin dielectric surfaces, such as used in thermal-control mirrors and solar panels on a spacecraft, can theoretically cause perturbations on spacecraft antenna patterns, depending on such conditions as the relative location of the surface on the spacecraft with respect to the antennas and the physical dimensions and electrical properties of the dielectric. Although the example cited does not yield values of perturbations which are too large, the benefit of the doubt is given to mocking up the dielectric surfaces.

J. Electrical Power Supply

Fabrication of solar panels SN 1 through 4 has been completed. Solar cell module installation is underway on solar panel SN 5. Type approval qualification of the revised solar panel diode installation was completed and the revised installation has been incorporated in all flight solar panel hardware. Sunlight electrical performance test procedures have been published for solar panel testing at the Air Force Eastern Test Range (AFETR). The construction of the high-temperature test container has been completed.

Investigation of performance data of the main battery used on the *Surveyor* SD-2 dynamic model indicated vehicle failure was not caused by a defective battery. Recently delivered main batteries have shown abnormal pressure increases during charge. The investigation and analysis are continuing.

Corrective action has been initiated to eliminate the occurrence of excess epoxy in the auxiliary battery receptacle. An auxiliary battery failure on the SC-1 vehicle was caused by inadequate quality control in the manufacturing process. Corrective measures have been taken. The separator wrapping technique has been improved for use on the T-2 main battery. Changes have been incorporated to provide additional support and facilitate vehicle installation.

1. Solar Panel

a. Flight hardware. The status of flight panels is:

(1) Solar panel 1: diode retrofit completed September 1965; temperature sensor relocation retrofit underway.

(2) Solar panel 2: removal from SC-1 spacecraft following pre-solar-thermal-vacuum testing; temperature sensor relocation retrofit completed September 1965; the panel is presently being prepared for continued SC-1 flight acceptance vibration.

(3) Solar panel 3: repeat flight-acceptance vibration test completed (following diode retrofit); the panel is presently being prepared for repeat flight-acceptance thermal-vacuum testing.

(4) Solar panel 4: fabrication completed; flight-acceptance testing to be initiated following temperature sensor relocation retrofit.

(5) Solar panel 5: installation of solar cell modules underway.

b. Diodes. Type-approval vibration testing of the S-2 dummy solar panel with proposed diode installations was completed. All specimens, except the original diode installations which had already failed during the type-approval thermal-vacuum exposure, successfully passed the vibration test. Completion of the vibration test concluded the diode installation type-approval-test program.

c. High-temperature test program. The installation of a radiant heating system and an insulation blanket completed the construction of the high-temperature container.

The radiant heating system provides a self-contained unit which is easily controlled and makes the high-temperature container completely mobile.

A test was run at Table Mountain to determine the temperature gradients in a solar panel when raised to 110°C in the high-temperature container. The type-approval-test panel was instrumented with thermocouples and placed in the container. Test conditions were as follows: clear sky, 75°F ambient temperature, 5 to 10 mph wind, and 101 mw/cm² normally incident solar intensity.

Steady-state was reached after a total exposure of approximately 2 hr. Average temperature on the solar cell side was 105°C with a maximum of 109°C and a minimum of 101°C. Average backside temperature was 103°C with a maximum of 107°C and a minimum of 100°C. No serious hot spots were evident and it may be concluded that the container, utilizing only the greenhouse effect, raises the panel uniformly in temperature. The test will have to be run under a colder environment to evaluate the use of the heaters.

2. Batteries

a. Main battery. Battery SN-20 was installed on the *Surveyor* SD-2 dynamic model spacecraft that was launched from Cape Kennedy on the *Atlas Centaur-6* (AC-6) in early August. Normal operation occurred until launch plus 16.5 hr, at which time the transponder went off. To determine the probable cause of this premature shutdown, battery performance data and preflight history were analyzed.

On the premise that the spacecraft experienced higher than expected temperatures, which might degrade battery performance, Fig. 59 indicates the effects of discharge rate and temperature on amp-hr discharge capacity. The highest ambient temperature to which any main battery has been laboratory-tested is 125°F. For a 7.0-amp discharge at this temperature ambient, the battery itself reaches approximately 140°F. Although there is a decrease in capacity of between 8 to 10%, no failures have occurred under these conditions. At a temperature of 165 to 170°F, the polystyrene cell jars and manifold cover begin to soften. Further increase in temperature will cause melting, distortion of cases, and ultimate shorting of the battery.

There were approximately 5 mo between battery activation and the SD-2 launch, during which the battery had undergone flight acceptance testing. All testing was performed at laboratory ambient temperatures and, when not in test, the battery was stored in a 35 ± 5°F environment. Fig. 60 shows the battery capacity loss rate as a function of storage temperature. SN 20 was at 70 ± 5°F for approximately 3½ mo prior to launch, indicating a degradation in capacity of less than 2%. Fig. 61 is a plot of discharge capacity as a function of charge-discharge

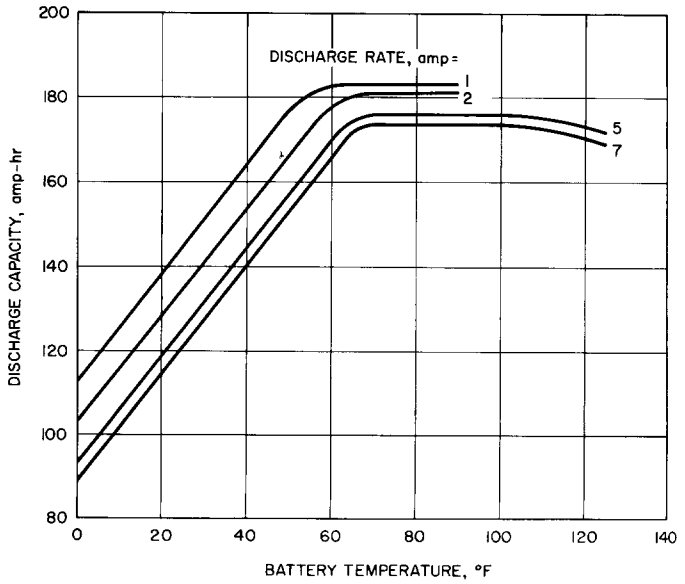

Fig. 59. Main battery capacity as a function of discharge rate and temperature

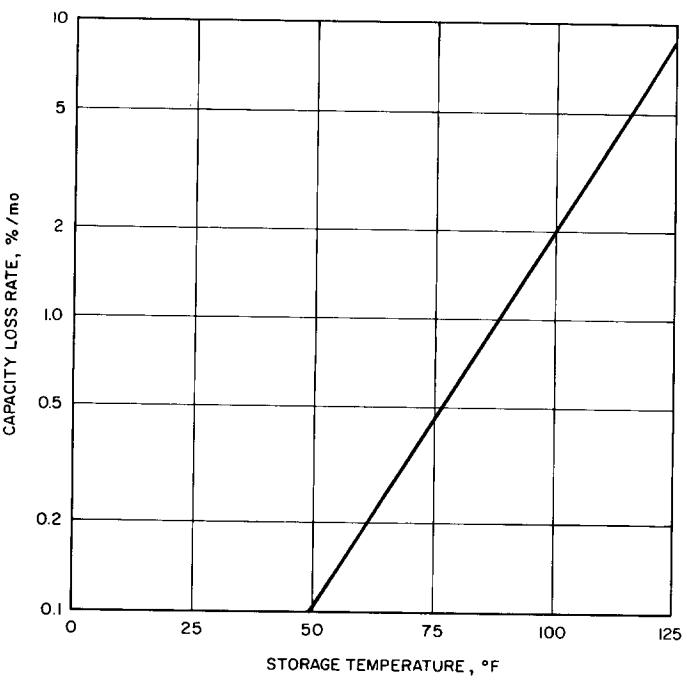

Fig. 60. Main battery capacity loss rate vs storage temperature

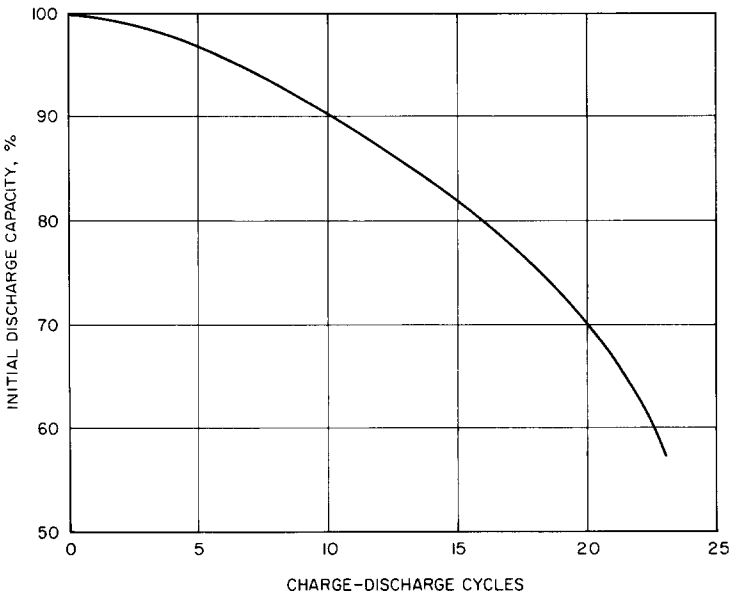

Fig. 61. Main battery discharge capacity as a function of charge-discharge cycle

cycles. Only one cycle was performed on the battery; therefore nearly 100% of the initial capacity was retained.

Based upon typical battery performance and the preflight history of SN 20, sufficient capacity was available to satisfactorily complete a dynamic vehicle mission. It is also difficult to conceive how a defective battery could have caused the abrupt failure of the SD-2.

An additional problem has arisen with the last two lots of batteries received from the Electric Storage Battery Company; these batteries have exhibited a higher than normal pressure increase during the float portion of the Hughes Aircraft Company charging cycle. The potential problem sources under investigation are:

(1) Manufacturing differences.

(2) Electric Storage Battery charging differences.

(3) Hughes testing differences.

(4) Cell unbalance.

(5) Silver impurities.

Investigation and corrective actions taken to date include:

(1) Manufacturing and operational sheets were studied by the Hughes resident inspector and Electric Storage Battery engineering. No differences in the manufacturing between those batteries exhibiting the pressure increase and the previously accepted batteries had occurred.

(2) Battery charging equipment was checked for cutoff voltage and accuracy. All equipment was functioning well and within its tolerance limits.

(3) The Hughes flight-acceptance-test specification was examined. No changes were made in requirement or testing methods that would have an effect on pressure rise during charge.

(4) Cell balance is being improved at Hughes as part of the flight-acceptance-test program. A change was incorporated that involved an 85-hr charge and float period when the batteries were received at Hughes. This method was used on the last four batteries, SN 29, 30, 31, and 32. The pressures reached were 39.2, 43.8, 40.6, and 38.9 psia, respectively. Any pressure improvement will be noted during the discharge-charge cycle later in the flight-acceptance-test program.

(5) The Electric Storage Battery Research Center has not found any silver impurities that might contribute to the problem. One sample revealed approximately ten times the amount (in parts per million) of iron as that in other samples, but the iron content bears no relation to pressure rise.

Although the investigations to localize the cause of the problem will be continued, no effect on spacecraft performance is anticipated. The present spacecraft power profile indicates the battery will be in a state of discharge during transit; no pressure rise occurs under this condition. During installation on SC-1 the initial pressure will be 1 atm. With respect to lunar surface operation, the battery will be in a state of charge during lunar day. The pressure problem could cause a premature charge cutoff, resulting in only a 3% loss in battery capacity.

Discharge of the SN 23 battery was continued to determine the number of amp-hr to be removed during the SC-1 mission. A total of 50 amp-hr remained, indicating the SC-1 test used approximately 135 amp-hr.

The reliability program conducted at Electric Storage Battery has completed its first phase. Batteries SN R-9 through R-13 finished testing on the third lunar day. The batteries performed as predicted and generally within the specification requirements. Some minor exceptions to the specified limits on battery performance were noted and remain to be analyzed. Four additional batteries have begun the lunar load sequence charge-discharge tests after successful completion of flight acceptance vibration.

b. Auxiliary battery. Auxiliary batteries SN 18 through 29 have completed flight acceptance testing. One minor problem arose during the tests; difficulty was encountered in mating a plug with the battery receptacle. It was found that the epoxy used to seal the wiring side of the receptacle leaked down and around the female inserts during the sealing operation. The excess epoxy was removed and retest indicated proper mating of connectors. Corrective action was initiated to preclude the possibility of a recurrence.

Auxiliary battery SN 14 was used on the SC-1 vehicle during the solar-thermal-vacuum test phase. Lower than normal voltage readings were obtained from the battery throughout the mission sequence. Although the voltage remained within the specified limits until late in the test, indications were that at least one cell was shorted. Examination of the battery, after its removal from the spacecraft, revealed that three cells were shorted. The battery was disassembled and the three cells dissected for examination of the plates and generator system.

The analysis revealed that the failure mode was the same for all three cells. Poor edging of the negative plates left high spots of zinc on the corners and sides. These high areas caused pressure points on the separator which ultimately broke through to the positive plate, resulting in low-rate shorts.

Since this problem 100% quality control has been initiated. One of the inspection points is the examination of all plates prior to the addition of the separator material. Flaws in the finished plate are therefore discovered before the plates become part of a cell.

c. T-2 batteries. T-2 main battery SN 104 had two cells exhibiting low voltages at the completion of flight acceptance testing. After disassembly, workmanship deficiency was noted in the method of wrapping the separators in each cell. The cells are constructed by hand wrapping a cellophane layer over every other plate. A second wrapping consists of a layer of fiber sausage casing that is overlapped by ⅛ in. In the defective cells, this outer layer did not overlap, allowing potassium hydroxide to contact the inner cellophane layer. This condition, coupled with the severe temperature exposures that the cells are subjected to during flight acceptance testing, reduced the life of the cells considerably. The problem was resolved by providing an additional layer of fibrous sausage casing beneath the overlap and extending the outer layer overlap to ⅜ in. An insulating carrying case has been constructed to protect against high temperatures while the battery is in transit.

Changes have been incorporated into the T-2 main battery to provide additional support and facilitate vehicle installation. A connector has also been added. The new configuration is shown in Fig. 62.

T-2 main batteries SN 115 through 121 have successfully completed flight acceptance testing. Twenty additional batteries have been ordered from Electric Storage Battery. The modifications described above will be incorporated in these batteries.

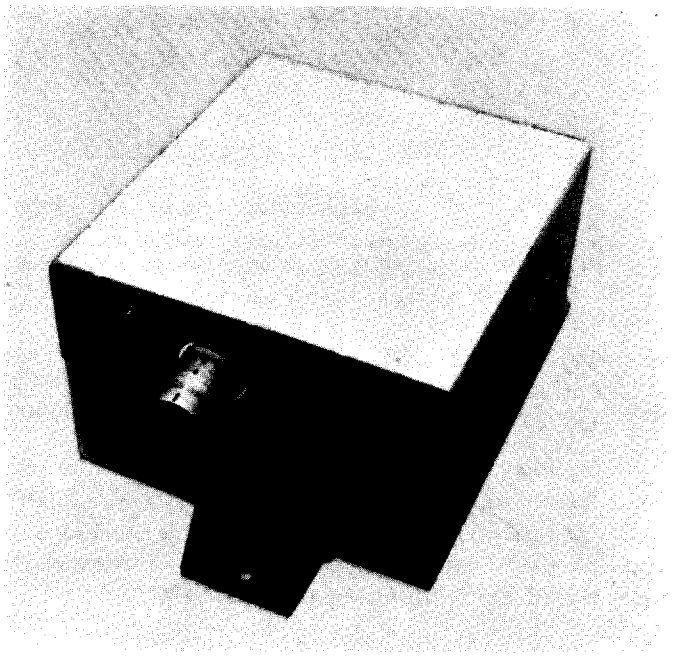

Fig. 62. T-2 main battery

Twenty-five T-2 recovery batteries have been received from Eagle Picher Company. Tests performed on the recovery battery to determine battery life under expected use show the battery should be used as soon as possible after activation and not later than 5 days following activation. The watt-hour capacity of the battery begins to degrade after the fifth day. In addition, the battery should not be used at temperatures below 60°F. Tests are being conducted to determine performance of the T-2 recovery battery utilizing a heater blanket.

3. Main Power Switch

The investigation of the SN 3 switch, which failed to operate after vibration, was concluded. The vendor, Kinetics Corporation, suggested that the failure was caused by a low-voltage condition at the switch terminals.

This conclusion was reached after the unit was opened and an over-heated motor found. Therefore, failure was attributed to operator error. The testing, procurement, and delivery of all units is complete.

4. Boost Regulator

A change to provide protection for the overload trip circuit when the nonessential bus is short-circuited was incorporated in all boost regulator units. The initial design of the overload trip circuit restored the nonessential bus voltage automatically within 20 to 1000 msec after a trip function had occurred. Subsequently the recycle feature was removed from the overload trip circuit but power for the "Remove Nonessential Loads" logic circuit continued to be supplied from the 29-v essential bus.

An overload trip circuit failure which involved a short circuit on the spacecraft 29-v nonessential cable was reported on August 2. The cause of the overload trip circuit failure was traced to the "Remove Nonessential Loads" logic. The logic circuit was not disabled after tripout and therefore provided a leakage path which caused the voltage sensing circuit to block complete turnoff of the overload trip circuit transistor switch Q-1. The problem was corrected by transferring the power source for the logic circuitry from the essential bus to the nonessential bus. Extensive testing of the overload trip circuit under overload conditions ranging from 10 amp to short-circuited output proves reliable operation without damage to the overload trip circuit.

5. Special Tests

A number of special tests were conducted on the boost regulator, battery charge regulator, and engineering mechanism auxiliary to verify performance or increase confidence level in these units. Margin tests were performed on the battery regulator and battery charge regulator in the unit areas to determine any malfunctions that may occur as a result of the worst-case analysis. These tests consisted of a thermal-vacuum test to assure dissipation capability and observe any arc-overs as the pressure was being reduced. Another portion of the margin test on the battery charge regulator checked for maximum power transfer over the thermal range and battery voltage range. All units passed these tests except the SN 12 battery charge regulator, which dropped in efficiency approximately 3% when operating into an 18-v battery at less than +40°F. This condition does not normally occur in the compartment.

Special verification tests were conducted on the SC-1 spacecraft to establish that incorporated modifications performed satisfactorily. These tests consisted of verification of the optimum charge regulator noise filter to prevent improper hunting, and the overload trip circuit oscillation in a bypass mode, and establishment of the actual squib firing current without System Test Equipment Assembly harnessing interposed on the spacecraft.

The optimum charge regulator filter consisted of an L-C network on the output of the regulator. Its purpose was to desensitize the current sensing resistor and prevent noise from forcing the optimum charge regulator to hunt over too wide a voltage range. The verification test consisted of running the optimum charge regulator in a high noise environment established by operating the flight control electronics and the high-power transmitter. In all noise load configurations, the optimum charge regulator maintained correct operation without shifting its operating point. Brush recorder data confirmed the hunting waveform relationships for proper hunting.

In the overload trip circuit bypass test, verification was required to assure no oscillations occurred when the bypass was commanded on. The tests verified that the modification to increase drive to hold the by-pass silicon-controlled rectifier does perform satisfactorily. Another squib firing test was conducted to verify previous data. The spacecraft was stripped of all unnecessary System Test Equipment Assembly cables, squib simulators were installed, and data were collected as squib firing commands were transmitted. All squibs indicated a sure-fire current of 4.5 amp or higher.

K. Thermal Control

SC-1 solar-thermal-vacuum testing began in early September. Participating in this test was a thermal control team whose primary duties consisted of spacecraft preconditioning and the monitoring and assessing of thermocouple and flight temperature sensor data to ensure vehicle safety throughout the test. Evaluation of thermal control systems in near real-time was facilitated by the computer data system and thermal instrumentation data acquisition system which simultaneously displayed flight sensor and thermocouple data. The first test, an abbreviated version of the total solar-thermal-vacuum test, was approximately

12 hr into the mission sequence when spacecraft electrical problems necessitated deviating from the planned test sequence. The original plan called for two complete missions, one at a low, the other at a high intensity, to obtain margin performance data. The first part of the mission was conducted at an average solar intensity of 82% according to the test plan. When the test plan was abandoned, it was decided that the remainder of the abbreviated test should be conducted at 100% solar intensity to obtain nominal thermal performance data. Post-test intensity studies indicated that the actual average intensity during the last phase was 94 to 95%, with localized intensities of 90 to 91% on most units. Two eclipses (15 and 30 min) and several terminal descent tests were performed during the high (95%) intensity phase. A total of 37 hr of the test was completed prior to shutdown.

Post-test data reduction was completed within 24 hr of shutdown. Thermocouple and flight sensor data were tabulated and plotted in groups corresponding to each subsystem. A comparison of pre-test predictions with test results was provided.

The limited test data were sufficient to permit a preliminary evaluation of the thermal performance of the various spacecraft subsystems. Compartment A operated satisfactorily, but tray temperatures were about 15°F above the design upper limit of 125°F. This condition is attributed to warm shadow shroud effects. Compartment B tray temperatures were lower than expected; however, at the traveling wave tube/tray interface, temperatures were higher. It is felt that the high temperatures were caused by low contact conductance; they did not appear to affect compartment performance. A revised installation procedure to maximize conductance has been developed.

Temperature levels exhibited by the auxiliary battery indicate that it would remain operational throughout the planned intensity ranges. The test provided the data necessary to complete the upgrading of the analytical model.

Thrust chamber assemblies (TCA) 1 and 3 performed as expected. TCA 2, located in the warm shroud region, operated cooler than predicted. The reflector size was increased on this TCA in an attempt to raise barrel temperatures by 12°F. Propellant tank cooldown rates were close to those predicted. Since heater power dissipation on the propellant lines was not monitored during test, a comparison with predictions is somewhat difficult. In general, these lines performed satisfactorily, but additional test data are necessary for a thorough evaluation. Helium tank temperatures were essentially as predicted. Nitrogen tank temperatures were lower than predicted because of lower than expected spaceframe temperatures; however, temperatures were within the specified limits.

All radar altimeter and doppler velocity sensor (RADVS) units were within the allowable temperature limits. The test verified that the solar diffusing glass cloth will provide adequate protection from solar focusing. The altitude marking radar magnetron stabilized at 0°F during the solar-thermal-vacuum test, but as in the case of the line heaters no duty cycle data were obtained.

The program certification test, conducted on the thermal management program, successfully performed all criteria but one. The option to store computed temperatures for use as initial conditions was not verified. Temperature profiles obtained with this program have been submitted for incorporation in a mission sequence tape.

Assembly of the S-10 vehicle has been completed with instrumentation about 90% complete. The vehicle is ready for shipment to the Space Environment Simulation Laboratory for retrorocket installation and mounting on the end bell. All cold shrouds and vehicle support hardware have been fabricated. The hot vernier engine cone simulators have completed their development tests and three such cones are available for the vehicle.

A preliminary definition of thermal design requirements, temperature control techniques, and anticipated thermal performance of the A-21A model subsystems has been completed.

1. SC-1 System Test Support

This discussion includes a review of the SC-1 solar-thermal-vacuum test operations, test plan, and test results.

a. Operational aspects. A thermal control team participated in the SC-1 solar-thermal-vacuum operations and real-time data evaluation on a continuing basis. The overall group responsibilities were to: (1) monitor the near-real-time thermocouple and flight sensor temperature data obtained from the auxiliary data monitoring system and the computer data system, (2) monitor preconditioning and blocking heater operations, (3) make periodic temperature assessments and recommend appropriate operating modes to ensure vehicle safety, (4) perform real-time evaluation of the thermal control systems, and (5) plot selected thermocouple data for real-time display purposes.

The addition of the computer data system since the T-21 solar-thermal-vacuum test was a valuable complement to the thermal instrumentation data acquisition system, allowing both spacecraft temperature sensor data and thermocouple data to be displayed, monitored, and hensive real-time assessment of temperature performance.

An operational problem was encountered when it became impossible to chilldown the cold shrouds because of an error in plumbing. The warm shrouds resulted in a degradation to the thermal performance of Compartment A and Engine 2 propellant tanks, the significance of which is presented in the discussion of thermal analysis and design (Part 2, below). The problem has been corrected by improving procedures and coding plumbing.

Another problem was discovered during chamber chilldown when it was necessary to turn on the solar simulator because critical spacecraft temperatures approached the design lower limits before the liquid nitrogen phase of the chilldown had been achieved. This additional heat load in the chamber delayed chilldown. Modification of chamber operating procedures will permit a rapid chilldown for subsequent operations.

Post-test data reduction was performed at the conclusion of the solar-thermal-vacuum operations. Plots and tabulations of all thermocouple and spacecraft temperature sensor data have been prepared for the first phase of SC-1 solar-thermal-vacuum testing. Most of the data reduction was completed within the 24-hr period immediately following the test, permitting rapid evaluation of the test results by the thermal analysts. Comparisons between thermocouple data and spacecraft temperature sensor data were made and good compatibility was obtained.

b. Test plan. The original plan was to perform two complete mission sequences, one at low and one at high solar intensity, but difficulties with electronics forced the planned test sequence to be aborted. It was decided to continue testing at a one solar constant intensity to determine nominal thermal performance and also to perform spacecraft terminal descent tests.

The resulting test environment was 12 hr at 82% solar constant and 14 hr at 94 to 95% solar constant. Two eclipses of the solar simulation of 15- and 30-min durations were performed. These solar intensity levels are average values within a 6-ft circle at the test plane and are relative to a blackplate standard, which is approximately 7% higher than the intensity recorded by Eppley radiometers. An incorrect reading of the Eppley instrument tare resulted in the intensity being 3% lower than was intended during the test. The test results for the 94% solar constant average within the 6-ft test circle indicate that many spacecraft units are located at the fringes of the 6-ft diameter, where the local intensity is 4 to 5% lower than the average.

2. A-21 Model Subsystem Thermal Analysis and Design

An abbreviated portion of the SC-1 solar-thermal-vacuum flight-acceptance test was conducted on September 9 and 10. Approximately 24 hr of transit coast-phase environmental conditions were simulated at two intensity levels. The actual average intensity prevailing within the 6-ft test circle in the control test plane during the last 14 hr was approximately 94% of one solar constant as measured by a blackplate radiometer. Local intensities in the 4- to 8-ft annular zone at the test plane were approximately 3 to 4% less than the average within the central zone; therefore, the majority of the spacecraft remote subsystems were exposed to 90 to 91% of a solar constant during the final portion of the test. Because of the abbreviated nature of the test, a limited amount of thermal data were obtained; hence, only a preliminary evaluation of test data was made and is discussed within the context of these limitations in the following paragraphs. Continuing emphasis on the solution of remaining thermal control problems on the SC-1 spacecraft (e.g., RADVS antenna solar focusing) are discussed in terms of the nature of the solution and the expected effect.

a. Vehicle.

Compartment system. Preliminary analysis of the compartment system thermal data obtained in the abbreviated SC-1 solar-thermal-vacuum test indicates:

(1) All thermal switches on Compartment A appeared to function satisfactorily.

(2) An outboard thermal switch on Compartment B indicated a conductance lower than any of the others; however, it was found to be functioning adequately.

(3) The shadow shroud over Compartment A was incorrectly plumbed and was not cooled to cryogenic temperatures (temperatures of up to 160°F were recorded on the shroud). The hot shroud produced high temperatures in Compartment A, causing the

thermal tray to exceed the 125°F design limit during high-power modes (tray temperatures of up to 139°F were recorded).

(4) Transmitter A traveling-wave-tube thermal performance was satisfactory and was better than the Transmitter A traveling-wave-tube performance during all T-21 solar-thermal-vacuum testing. The Transmitter B traveling-wave-tube thermal performance was not as good as that observed during the T-21 solar-thermal-vacuum test because of an apparent 50% lower contact conductance at the traveling-wave-tube/thermal-tray interface. Although temperatures on the traveling wave tubes were higher than desired, there is no evidence that they will overheat during high-power operation when the tray temperatures are in the range expected with the cold shrouds functioning properly. A new traveling-wave-tube installation procedure using indium foil has been introduced to assure maximum contact conductances at the traveling-wave-tube/thermal-tray interface.

(5) Compartment B temperatures were not significantly affected by the hot shadow shroud over Compartment A. Compartment B thermal-tray temperatures appeared to be approximately 10°F cooler than anticipated. Accurate power data are not available; however, it is believed that a nominal coast-mode power dissipation existed during the steady-state periods. All Compartment B thermal performance aspects appeared to be satisfactory.

Auxiliary battery. Predictions of the thermal performance of this unit during the SC-1 solar-thermal-vacuum test were not completed in time for publication. However, predictions were obtained by means of the partially-revised analytical model. The test provided the necessary steady-state temperature data for completion of the analytical mode. This test also demonstrated that the thermal performance of the auxiliary battery during the actual mission will be within specified limits.

b. Vernier propulsion subsystem.

Thrust chamber assemblies. A comparison of test data and test predictions indicates that TCA 1 (SN 536) and TCA 3 (SN 539) performed as predicted during Phase 1 of the SC-1 solar-thermal-vacuum flight-acceptance test. The solar intensity at the TCA level was determined to be 90% of a true solar constant (130 w/ft^2). Test results indicate that the temperature of the head end and barrel bottom of TCA 1 dropped 24 and 8°F, respectively, during a 15-min solar eclipse period. The head end and barrel bottom of TCA 3 dropped 46 and 14°F, respectively, for the same period. Temperatures of the thrust chamber body (excluding the nozzle extension cone) of TCA 2 (SN 541) were substantially cooler in test than predicted. However, test results indicate that TCA 2 would undergo a 30-min solar eclipse without exceeding its lower temperature limit of 0°F. The steady-state temperature of the barrel bottom at 90% of a solar constant was 50°F. During a 15-min solar eclipse the barrel bottom experienced a 19°F temperature drop. A larger solar reflector is being installed on TCA 2 to increase TCA temperatures by 12°F. No other thermal design changes are contemplated for the TCA.

Propellant tanks. Pre-test predictions compared with test results indicate that the propellant tanks performed as predicted.

Propellant lines. Pre-test predictions could not be readily interpolated because heater dissipation (duty cycle) during test was unknown. Therefore, comparison of pre-test predictions with test results has not been completed. Correlation must include heater duty cycles and adjusting temperature prediction and duty cycles to the appropriate solar intensity. Thermal performance was satisfactory. Test cooldown rate approached theoretical maximum.

Helium tank and lines. A comparison of test data and test predictions indicates that the helium tank performed as predicted during Phase I of the SC-1 solar-thermal-vacuum flight-acceptance test. In general, temperatures were cooler in test than predicted; however, observations and analyses have disclosed that temperature sensors are shadowed by the tank upper support tubes and should read 4 to 10°F cooler than the average calculated temperature. The solar constant at the helium tank level was determined to be 90% of a true solar constant. Test results indicate that the helium valve and tank temperatures will not drop below the lower temperature limit of 0°F during a 30-min solar eclipse; hence, no thermal design changes are contemplated. Helium tank thermal finish optimization studies are continuing; results to date have not disclosed a suitable thermal finish material and/or process to replace the vapor-deposited aluminum on the lower hemisphere of the tank.

No test predictions were made for the helium lines. During test, two line locations were monitored. The shaded region ran at −60°F, while an illuminated segment was +65°F.

c. Flight control.

Flight control sensor group. Although no pre-test predictions for this system were generated, only one irregularity, a low radiator temperature (140°F) appeared during the SC-1 solar-thermal-vacuum test. Investigation revealed a loose thermocouple was not providing true radiator temperatures.

Roll actuator. A comparison of test data and pre-test predictions indicates that the roll actuator performed as predicted during Phase 1 of the SC-1 solar-thermal-vacuum flight-acceptance test. The solar constant at the roll actuator level was determined to be 90% of a true solar constant. Calculations have shown that the maximum temperature rise experienced by the roll actuator, for a 240-sec engine operational period, is 44°F. The maximum temperature of the roll actuator during transit will be 164°F, compared to the maximum allowable limit of 200°F.

Attitude control system. The nitrogen tank temperatures observed in the abbreviated SC-1 solar-thermal-vacuum test were approximately 15°F colder than predicted. About 9°F of this discrepancy is attributed to the spaceframe being 44°F cooler than assumed for the predictions. The regulator was 21°F cooler than predicted. Again, 9°F of this increment is because of the cooler spaceframe. The cooldown rates were consistent with the T-21 solar-thermal-vacuum results and no thermal design problems were apparent. No changes are being made on flight temperature predictions as a result of the test.

d. Radar.

RADVS. All RADVS units were within allowable limits at 1 solar constant. Consequently, no thermal finish changes are necessary. RADVS test results were compared to the test predictions. The temperatures observed on the preamplifier portions of the two receiver transmitter assemblies were for an antenna configuration with the solar diffusing glass cloth covers installed. The thermal performance met RADVS start-temperature requirements satisfactorily.

The use of covers reduces thermal radiation losses from the high emittance microwave absorber located on the inside of the antenna, thereby producing increased antenna temperatures during transit coast flight. Therefore, to prevent the present antenna temperature spread at the start of RADVS warmup from changing when these covers were emplaced, previously used black paint finishing on local areas of the antenna was removed. It was determined that this action not only maintains the present predicted temperature spread at the start of RADVS warmup (−125°F to +235°F), but also reduces the high-temperature gradients that were present in the area of the black paint patterns.

Altitude marking radar. The altitude marking radar magnetron chassis exhibited a mean temperature of 0°F during the mission phase of the SC-1 solar-thermal-vacuum test. Although the desired control point on this unit is +20°F, the minimum operating temperature is −20°F, indicating that the altitude marking radar was within its operational temperature range when the mean solar intensity was 94.5% of a solar constant. Pre-test temperature predictions were not available for this unit. Heater power dissipation was not monitored during test; thus the duty cycle of the altitude marking radar heater was not determined.

e. Television systems. The survey and approach cameras reached equilibrium temperatures which were as much as 40°F higher than anticipated. Although no test predictions were prepared, previous tests, namely T-21, provided sufficient data to permit temperature estimates based on engineering judgment. These higher steady-state temperatures are caused by the shadow shroud temperature being too high, elevating the temperature levels of the cameras.

3. A-21A Subsystem Thermal Analysis and Design

A broad examination of the *Surveyor* A-21A vehicle system was conducted to evaluate the status of the A-21A spacecraft thermal design definition. Intensive analysis was directed at those portions of the system that lacked fundamental technical definition as to the method of controlling the temperature of system elements. The thermal instrumentation data acquisition system and the lunar vent system are notable examples. Conclusions were provided in the form of method of temperature control, preliminary definition of thermal design requirements, and expected thermal performance.

The touchdown instrumentation data acquisition system will be temperature-controlled by passive means, utilizing solar illumination in the transit phase to establish an optimum thermal state within the insulated electronics compartment. Thermal control of the inertial measurement unit portion of the touchdown instrumentation data acquisition system has progressed to the selection of a mounting location for the package on the lower spaceframe members on the Leg 1 side of Compartment B. This

location was selected because the local thermal environment permits the use of passive techniques to satisfy the temperature requirements associated with pre-touchdown operation and post-touchdown data playback.

The lunar vent system will require active temperature control throughout transit to prevent freezing of fluids in the manifolded portion of the lines. It has been estimated that 3.0 w of electrical energy are needed to maintain temperatures above 0°F on heated portions of the line. Conventional heater elements, thermostatic control, and the commanded power switching mechanization will be used. It has been further concluded that the optimum routing of lines is along the lower square tube member of the spaceframe and that strip metal sunshades are needed to prevent overheating of direct illuminated portions of the lines. Even with this design aid, local portions of the line will exceed 100°F. Including engineering estimates of temperature uncertainties, a maximum temperature of 150°F can be reached.

A substantial number of passively controlled subsystem thermal designs will require redefinition because of external thermal environment changes brought about by the addition of the scientific payload and deletion of the engineering payload and other spacecraft configuration changes where units were relocated. Although the thermal designs of some spacecraft subsystems have remained unchanged (i.e., Compartments A and B and the main retrorocket), extensive analyses will be required to define the thermal performance of the subsystem to fulfill design contingencies.

Classification of problem definition from a thermal control point of view is presented in the form of two categories: (1) changes that affect spacecraft weight, electrical power, and performance; and (2) changes where solutions can be derived within a fixed weight, power, and outline and mounting budget after the completion of the necessary engineering analysis effort required to reach a design definition. Table 32 identifies the changes by category.

Table 32. Types of thermal control changes on A-21A configuration

Subsystem	Category 1 (major)	Category 2 (minor)
Vehicle and mechanism		Compartments A and B
		Spaceframe and substructure
		Crushable block thermal protection
Propulsion	Lunar vent system	Vernier propellant tanks
	Helium relief and check valves	Helium tank
	Helium lines	
	Main retro-engine	
Flight control	RADVS–SDC and velocity–sensor antenna preamplifer[a]	Flight control sensor group
	Nitrogen tank	Alitude marking radar
		RADVS–KPSM and altimeter–velocity–sensor receiver–transmitter assembly[a]
Television	TV Camera 2	TV Camera 3 and 4
Scientific payload	Touchdown instrumentation data acquisition system	Soil-mechanics/surface-sampler
		Alpha particle scattering experiment
		Micrometeorite ejecta detector
		Single-axis seismometer

[a]RADVS = radar altimeter and doppler velocity sensor; SDC = signal data converter; KPSM = klystron power supply modulator.

4. S-10 Test Program

S-10 vehicle assembly has been completed. Instrumentation of the vehicle is approximately 90% complete. Forty-seven of the 50 test heaters have been installed.

A leak check was performed on the vernier system, and the bladders in the three oxidizer tanks were found to have leaks. A decision was made to seal off all tanks at the helium line inlet to assure that no propellant can escape through the helium system, which is not pressure-tight. The vehicle is currently ready for shipment to the Space Environment Simulation Laboratory for retrorocket installation and mounting on the end bell (Fig. 63).

All cold shroud and vehicle support hardware fabrication has been completed. Fabrication of the second end bell has been completed, and the second end bell is currently available for an evaluation test with the end bell mated to the C-4 simulator. A contamination plate has been fabricated and is available for installation on the end bell.

Developmental tests on the hot vernier engine cone simulators have been successfully completed and three ceramic cones are now available for the temperature control model (TCM-2) Phase I test. Fabrication of the hot cone simulator support system is in progress.

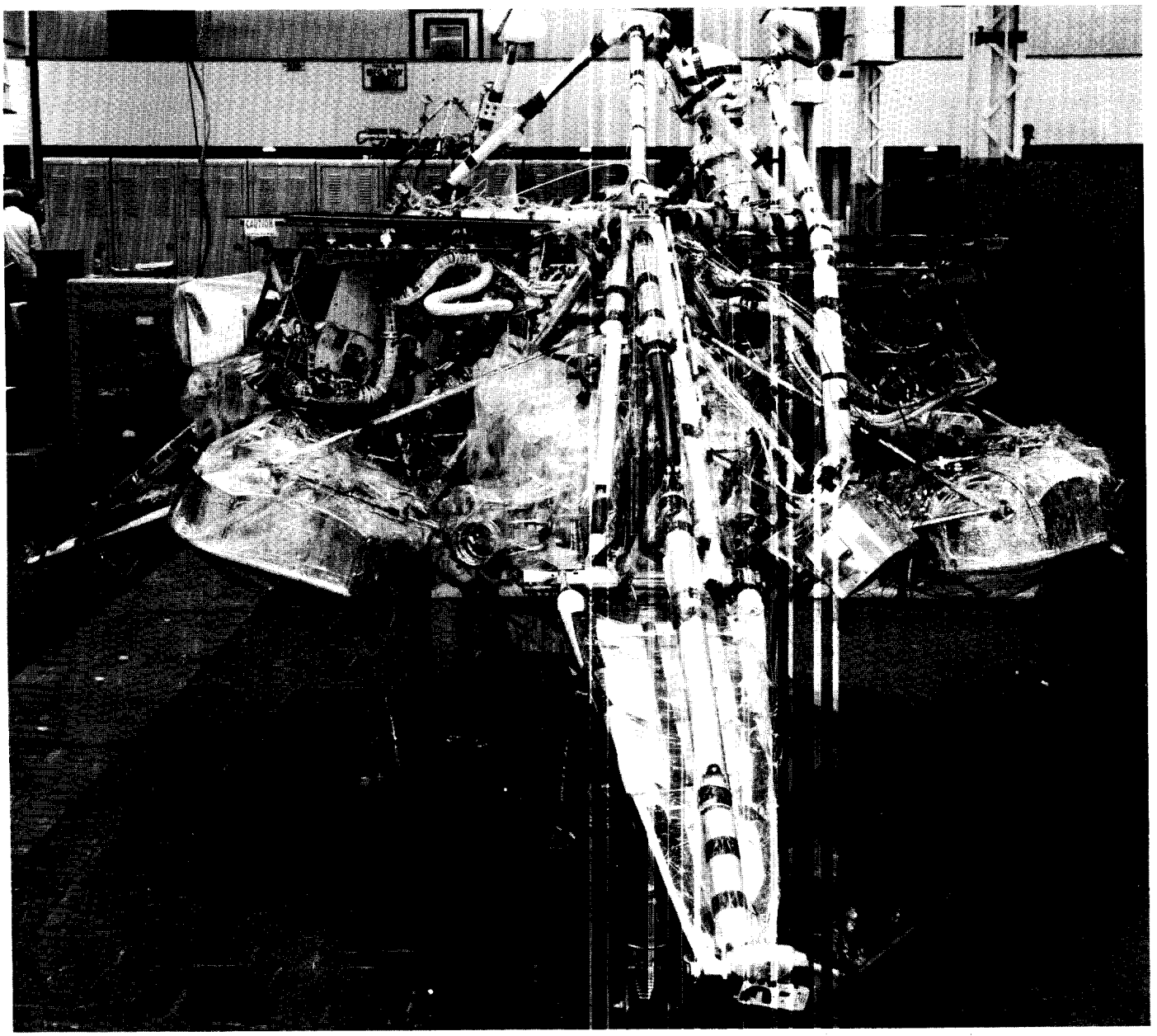

Fig. 63. S-10 thermal control model

5. Spacecraft Performance Analysis and Command Support

The program certification test for the thermal management program, which will be used in conjunction with the power management program to predict spacecraft temperatures and mission power requirements, was conducted during the reporting period. The program successfully met the requirements of test cases for four thermal models with a single exception. The program feature that permits the storage of temperature results computed for initial conditions for subsequent performances was not verified in the test. Until additional testing verifies successful operation of this feature or correction is made, if necessary, to the program, manual input of initial temperatures will be required.

Temperature predictions have been supplied for use in preparing a simulation-tape based on the mission

UNCLASSIFIED [redacted]

sequence given in Revision 4 of EPD 180 (Spacecraft Flight Operation Plan, *Surveyor* Mission A). The temperature profiles were predicted with the thermal management program, using power input data provided from the power management program.

L. Engineering Mechanics

A conceptual design review was held for the A-21A shock absorber. Several areas appear to offer major improvement in ease of manufacture and in improved performance over the current design. One A-21 shock absorber has been subjected to drop tests at low temperature, with loads ranging to over 10,000 lb, without failure. Two units have been burst-tested, and the results are being analyzed. A stress analysis for the annealing problem is in the final stages and indicates that a positive margin still exists in the gas cylinder.

Planning continues for drop tests of the S-15 A-21 drop test vehicle. The gyros to measure vehicle attitude have been received, the load measuring device has been designed, and varied methods are still being considered to measure velocity at the instant of touchdown. The scaffold for the drop tower is being modified, and the new platform has been designed.

Comparisons showing close agreement are presented for predicted and measured values associated with S-2A touchdown conditions in tests of the S-2A structural test vehicle. Additional reduced velocity cases have been studied; the latest calculations were for a polar angle of 0 deg. S-2A drop tests are now complete, and the only malfunction noted was that the elevation axis of the antenna solar panel positioner failed to function for two drops wherein the polar angle was 0 deg.

Assembly of S-9, an upgraded A-21 structural test vehicle, was completed September 1, and the vehicle was delivered to JPL on September 7 for torsion tests. Static tests completed on the surface sampler have shown the need for some redesign. Torque versus load measurements for titanium bolts fitting into titanium threads has been completed. Several typical parts of the *Surveyor* vernier engine have been tested and show the design to be satisfactory.

1. Shock Absorbers

The conceptual design review meeting for the A-21A shock absorber was conducted on September 23. National Water Lift Company (NWL) presented a general description of the shock absorber and its functions. Major items discussed for the new design included 6AL-4V titanium procurement and property verification, redesign of welded areas and improvement of overall titanium welding, static and dynamic seal design, removal of lock fingers, changes in squib energy and squib housing, and piston and metering rod orifice design. Compared with the A-21 unit, the A-21A shock absorber will have increased pneumatic preload force, increased hydraulic spring rate, and a less complex hydraulic circuit.

The A-21 shock absorber MS 27 was drop-tested at reduced temperature on September 1 in preparation for the low-temperature qualification drop tests. Six drops were made with peak load values of 4970, 6975, 8020, 8670, 8310, and 10,060 lb. At completion of the tests, an inspection of the shock absorber showed two ripples in one side of the aluminum housing and a 0.060-in. bow in the length of the tube assembly. No other variation was noted. These results demonstrated a readiness to test so that preparation of hardware for the three qualification drops is underway at NWL.

Gas Tube Assembly 30 was burst-tested on September 9, and the gas tube assembly from MS 27 was burst-tested on September 28. MS 27 was formally used in the drop test and was not considered as part of the qualification burst program. The burst pressure of Gas Tube Assembly 30 was 5050 psi and that of Gas Tube Assembly 27 was 5450 psi. A report with the corrected burst pressures will be available at a later date. Fabrication of hardware for the burst test program is expected to be complete in late October.

Sixteen cylinder and tube assemblies rewelded at Airtek Dynamics resulted in an annealing of the titanium in the weld area. The titanium in the area adjacent to the weld indicated that the units had experienced a maximum decrease of 5 points on the Rockwell 15N superficial scale. Preliminary stress analyses of the area utilizing reduced material properties indicate an adequate design margin. Type-approval units MS20, 21, and 22 have completed their thermal finish cycle at Hughes and have been returned to NWL for the completion of type-approval tests.

UNCLASSIFIED [redacted]

2. Landing Dynamics

a. S-15 drop test program. The S-15 test vehicle (T-1-type ballasted spaceframe) is being upgraded for use in the upcoming stability drop test program. Modifications to the vehicle include installation of the following items: (1) Class III landing gear, (2) triaxial gyro system, and (3) body block load-measuring devices. In addition, calculations are being made to determine the magnitude and location of ballast masses that will provide the desired vehicle mass properties. The S-15 is to weigh 650 lb, have a cg height of 19 in., and a radius of gyration of 32 in. for these stability investigations. Flight configuration shock absorbers and aluminum crushable components will be used for the test series.

The gyros for the triaxial gyro system have been received and are undergoing unit operational tests prior to integration into the vehicle. The mounting of this system will allow measurement of ±60 deg in both pitch and yaw, and 360 deg in roll.

Design of the body block load-measuring device has been completed, and a prototype is being built for testing to verify functional integrity. This device attaches the crushable body block to the spaceframe by means of strain-gaged supports. These supports are arranged so as to separate the measurement of vertical and lateral forces applied to the block during a landing. The measurements obtained will not only provide a time history of the vertical block crushing force, but also indicate the coefficient of friction between the blocks and the surface. In a further effort to determine the dynamic crushing properties of the body blocks, a series of tests will be conducted in the near future on individual blocks to determine the effect of velocity and angle of loading on the maximum crushing force of the aluminum honeycomb material.

Modifications to the drop test facility to be used for this series of tests are in progress. Work has begun on enlarging the steel scaffold which supports the vehicle, and final design has been completed for the new landing platform, which will rotate and tilt to facilitate cross-hill landing tests. A detailed analysis of the rigidity requirements for the landing surface indicates that 6- × 12-in. wood beams, laid flat, will be adequate instead of the 12- × 12-in. beams previously considered. This and other weight-saving measures have reduced the estimated weight from 40 to 22 tons. It appears that the fabrication of this landing platform is the pacing item for the S-15 stability drop test program.

3. Dynamic Analysis

a. S-2A drop test. A comparison of predicted and measured antenna solar panel positioner (A/SPP) bending moments is shown in Figs. 64 and 65. A listing of the drop test conditions is given in Table 33. Tests that simulated lunar landing conditions with Leg 1 and Leg 2 downhill are compared. Drops with Leg 1 downhill cause critical elevation motor housing torsion as shown by Fig. 64, and critical lower mast bending moment about the x-axis as shown by Fig. 65a. Drops with Leg 2 downhill cause critical lower mast bending moment about the y-axis (Fig. 65b).

The only failure observed for the A/SPP assembly used for Drops 5 through 9 was local yielding of the tapered

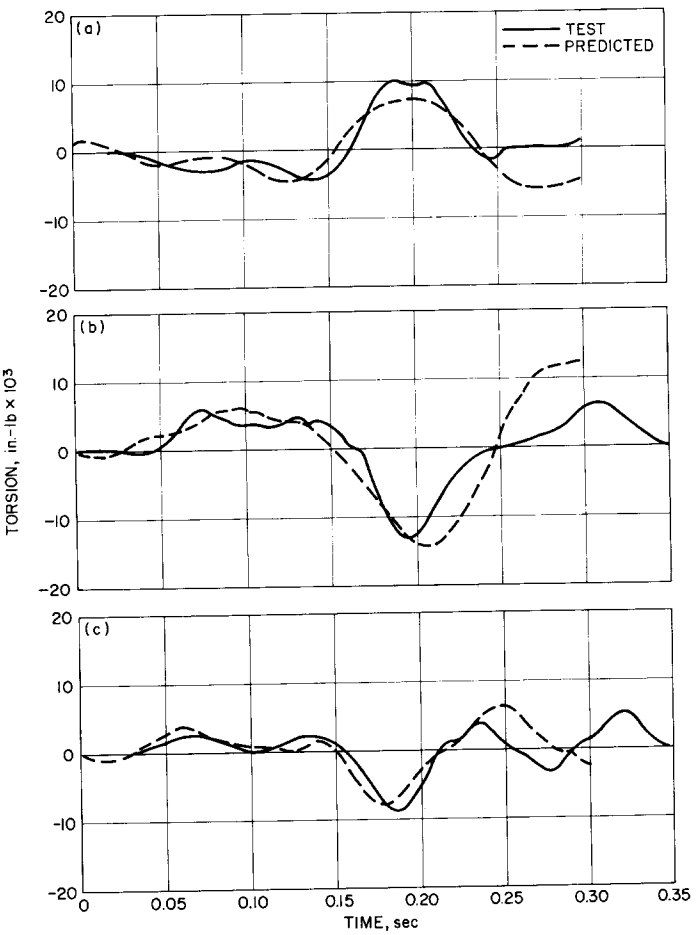

Fig. 64. Elevation motor housing torsion drop test: (a) Drop Test 2 on level surface, Leg 2 up 15 deg; (b) Drop Test 8 on 15-deg slope, Leg 1 downhill, polar angle of 0 deg; (c) Drop Test 9 on 15-deg slope, Leg 1 downhill, polar angle of 36.5 deg

UNCLASSIFIED

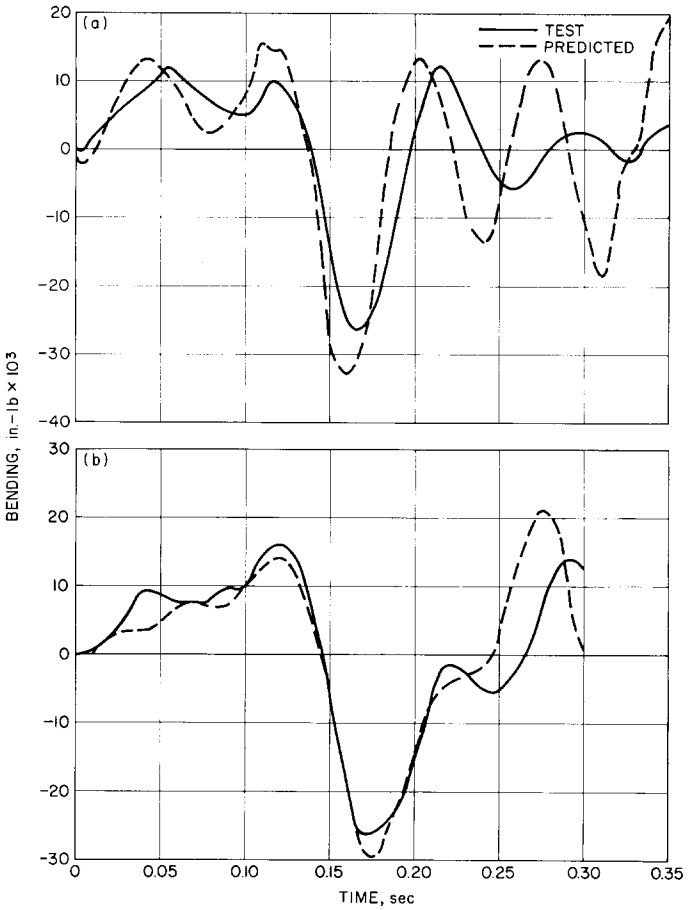

Fig. 65. Lower mast bending drop test: (a) Drop Test 5 about x-axis, on 15-deg slope, Leg 1 downhill; (b) Drop Test 2 about y-axis, on level surface, Leg 2 up 15 deg

pin hole in the elevation motor housing. These failures were noted in Drops 7 and 8 in which the A/SPP was at the polar angle of 0 deg. No failure was observed in the three drops covering the design range of 36.5 to 70.5 deg. This is substantiated by comparison of Figs. 64b and c, which show that the elevation motor housing torsion is smaller for the polar angle of 36.5 deg than for the polar angle of 0 deg. Thus, the drop tests indicate that the A/SPP is adequate in the design range of polar angle, although the solar panel arms will be strengthened in subsequent designs to cover a possible marginal situation.

b. Reduced velocities. The study of lunar landings at reduced velocities has continued with the objective of showing the variation of elevation motor housing torsion. The condition studied was a lunar landing on a 15-deg slope with a single leg downhill and with initial spacecraft incidence of 0 deg. The range of lateral velocities

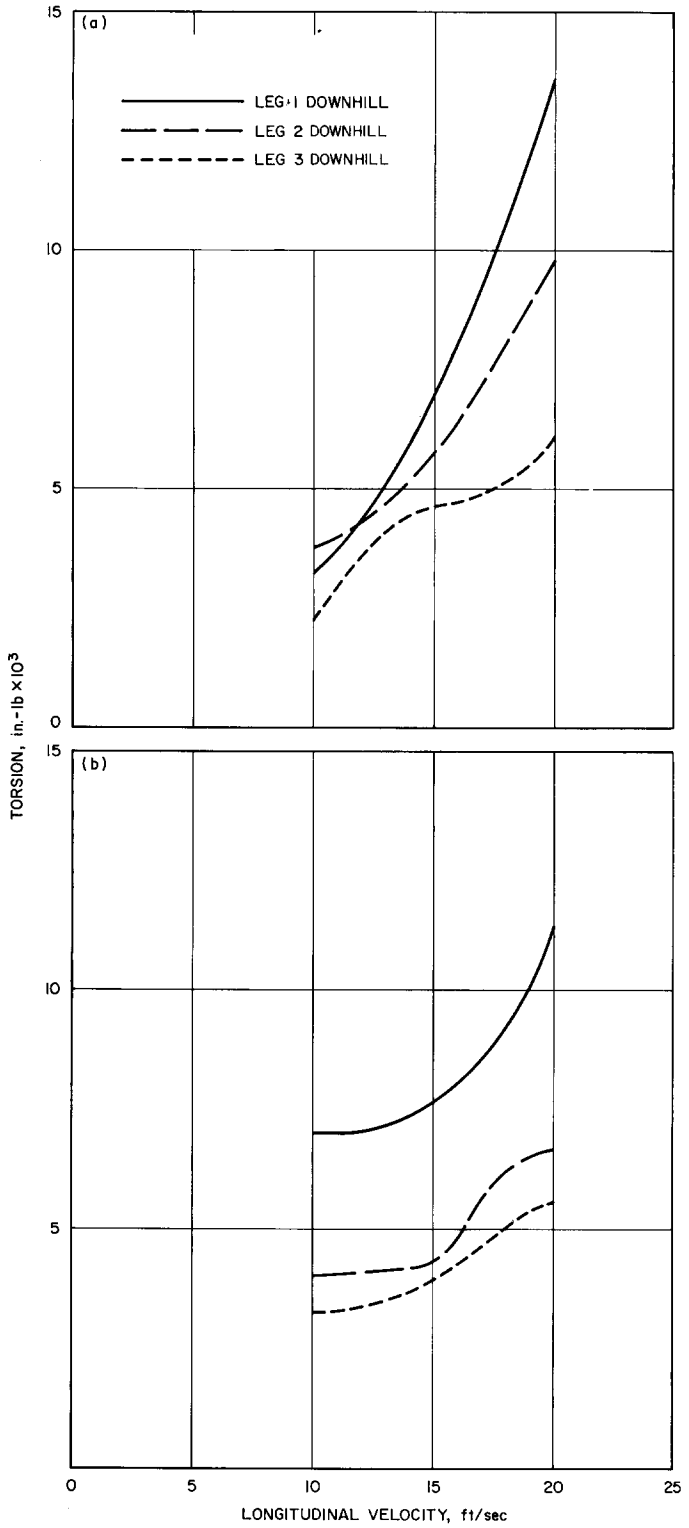

Fig. 66. Maximum elevation motor housing torsion vs longitudinal touchdown velocity: (a) polar angle = 0 deg; (b) polar angle = 18 deg

Table 33. Earth drop tests to simulate lunar landings

Test conditions	Spacecraft orientation	A/SPP position, deg	Worst-case lunar landings				Equivalent Earth drop tests (without horizontal velocity)			
			Touchdown velocities, ft/sec		θ_0,[a] deg	Slope of surface, deg	Vertical touchdown velocity, ft/sec	θ_0,[a] deg	Slope of surface, deg	Drop height, ft
			Longitudinal	Lateral						
1	Level	18	20	0	0	0	18.6	0	0	5.38
2	Leg 2 raised	18	20	6	0	15 (calculated for Leg 2 downhill)	19.0	16	0	5.61
3	Leg 1 downhill	18	20	2	2	15	18.0	0	15	5.04
4[b]	Leg 1 downhill	18	20	2	2	15	18.0	0	15	5.04
5	Leg 1 downhill	65	20	2	2	15	18.0	0	15	5.04
6	Leg 1 downhill	45	20	2	2	15	18.0	0	15	5.04
7	Leg 1 downhill	0	20	0	0	0	14.6	0	15	3.32
8	Leg 1 downhill	0	20	2	2	15	18.0	0	15	5.04
9	Leg 1 downhill	36.5	20	2	2	15	18.0	0	15	5.04

[a] θ_0 is initial incidence of spacecraft and is positive for single leg above horizontal.

[b] Drop 4 was not conducted.

investigated was from 6 ft/sec (uphill velocity in the direction of the double legs) to +2 ft/sec (downhill velocity in the direction of the single leg) and each of the three legs was taken as the single downhill leg. The position of the A/SPP was for each of two positions, a polar angle of 0 deg and a polar angle of 18 deg. The maximum elevation motor housing torsion versus longitudinal touchdown velocity is shown in Fig. 66a for landing with A/SPP at polar angle of 0 deg and in Fig. 66b for landing with A/SPP at polar angle of 18 deg.

4. Static Tests

a. Static load test of surface sampler. A static test is in progress to evaluate the current surface sampler mechanism and substructure design. The substructure was mounted to a rigid laboratory structure and no attempt was made to simulate the basic spaceframe (Fig. 67). The purpose of this test is to determine deflection characteristics of the surface sampler and substructure under simulated critical inertia loadings. This information will be used to determine spring rates of the assembly and the distribution of load between the main (lower) support and pin puller (upper) support. In addition, this test will be continued through the ultimate load condition to verify the structural integrity of the assembly during the most critical conditions of boost, transit, and touchdown loadings.

For the purpose of simulating the inertia loadings, the weight of the assembly was divided into six elements so that the total weight and loading cg would coincide with the weight and cg of the surface sampler. In general, these loading points coincide with the cg of the motor and gear box assemblies, which are the major concentrated weight items. In addition, loading points were established at the elevation pivot axis and on the linkage support in the vicinity of the pin puller. Instrumentation consisted of axial and bending strain gages installed on the six main substructure support tubes and dial gages to record rotation of the azimuth motor shaft and rotation plus deflection at the pin-puller support bracket, the elevation axis, the azimuth axis, and the main support.

Loads were applied in the three orthogonal axes of the linkage support for the stowed position. These loads were applied in 1-g increments with tare loading established at 1 g. In addition, combined conditions were applied consisting of lateral plus vertical loading combined. The most critical condition will be tested to the ultimate. The following critical loads were established:

(1) Lateral—17 g.

(2) Outboard—28 g.

(3) Down—28 g.

(4) Combined—15 g lateral plus 24 g down.

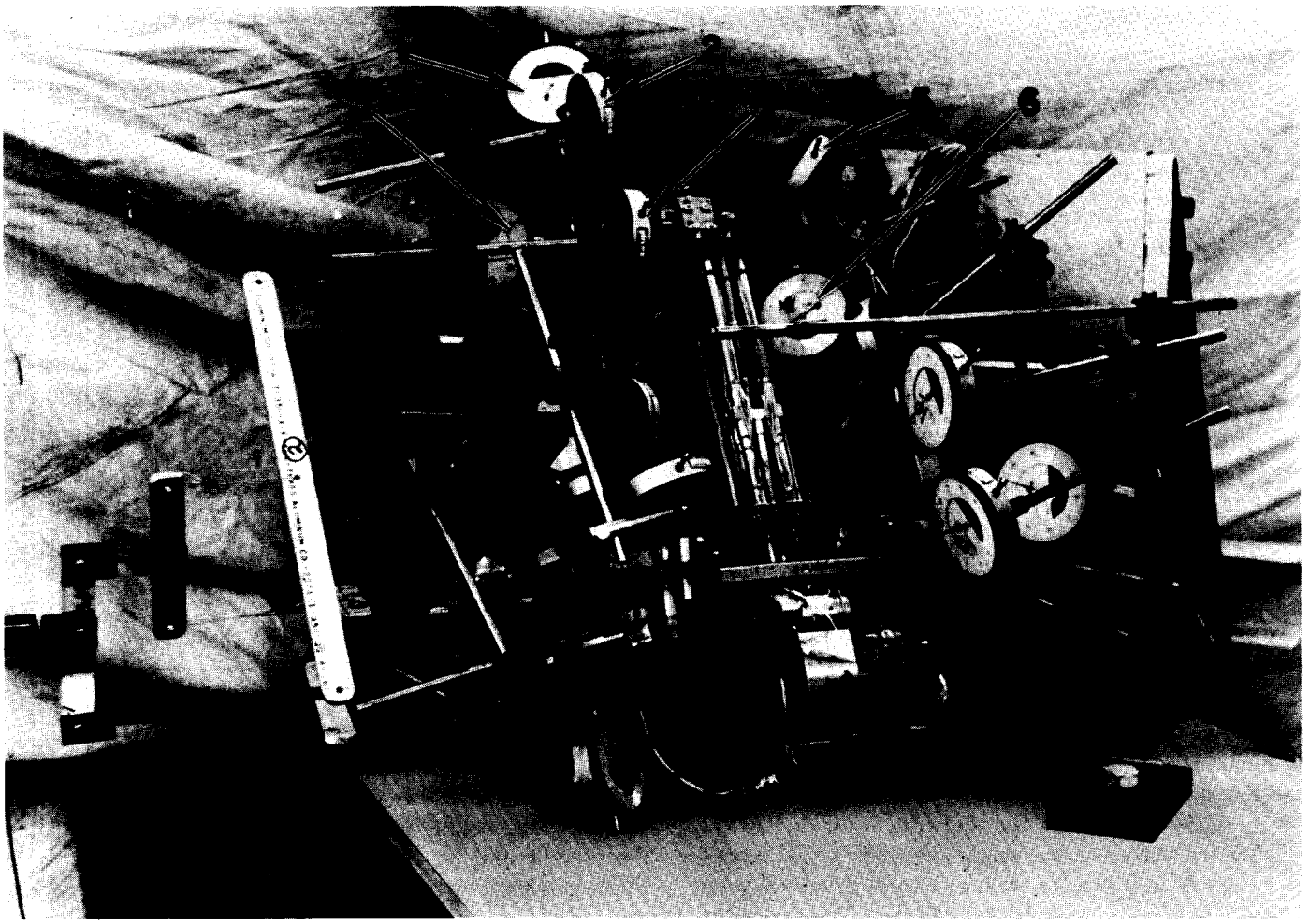

Fig. 67. Surface sampler test arrangement

Condition 1 represents boost phase loading that consists of 16 *g* vibration plus 0.4 *g* static. Conditions 2, 3, and 4 represent touchdown loads for a combined vertical load of 20 *g* and a lateral load of 15 *g*. The most critical load for the surface sampler structure is the loading in the lateral direction.

The test has now been completed to limit loads for the four conditions. As predicted by the previous stress analysis, plastic deformation of the azimuth pin occurred during the maximum lateral load condition (Condition 1). The pin is being redesigned to provide additional strength and will be installed in the test specimen. The test also indicated that the stiffness of the upper (pin-puller) supporting substructure is not sufficient to meet current functional requirements. Steps are now being taken to stiffen the upper support. After incorporation of this substructure modification in the test setup, Conditions 1 and 4 will be repeated, followed by a test to destruction.

b. Torque tests of titanium screws. The vernier system propellant tank assembly consists of a flanged titanium tank shell, an internal standpipe with a mating flange, a bladder, and associated seals. Six 8-32 titanium screws which engage tapped holes in the titanium flange are used to clamp and seal the standpipe to the tank, at the same time attaching the assembly to a "thermal standoff cup."

In the absence of published torque data for titanium-on-titanium threads, it was necessary to conduct appropriate tests to establish meaningful torque-preload curves. To accomplish this, an actual tank flange cut from a scrapped titanium propellant tank, and six titanium screws were used. Using a simple support fixture (Fig. 68) in conjunction with a Baldwin-Lima-Hamilton Mark G test machine, clamping forces generated by applied torque loads could be recorded in the test setup. All screw threads were cleaned and degreased according to

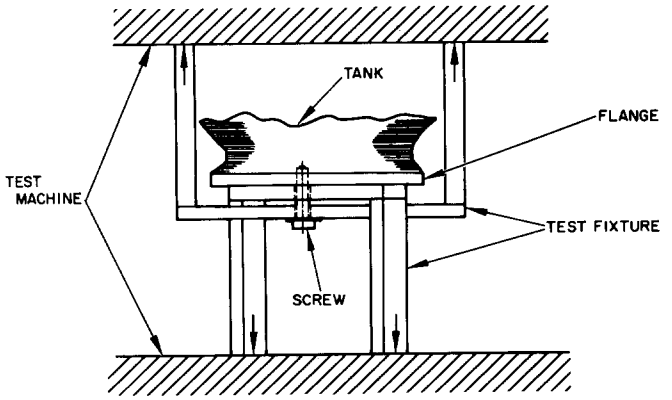

Fig. 68. Titanium screw torque test setup

standard *Surveyor* assembly procedures. The proper friction conditions under the screw head were simulated by using the same steel washer used in flight installation. The test results obtained from six screws are summarized in Fig. 69. The limiting torque in all cases was the torque at which the Allen head driver began to slip in the screw head socket.

Thus, no failure in screw or flange threads was produced. It is believed that the driver slippage was precipitated by cramped conditions in the test setup, which made proper insertion of the driver into the screw head and maintenance of its alignment throughout the application of the torque difficult. However, since the minimum torque of 38 in.-lb attained under the test condition exceeded the maximum installation torque of 23 in.-lb by a large margin, the driver failures are not considered significant. Additional tests of this type are currently in progress for larger size titanium screws.

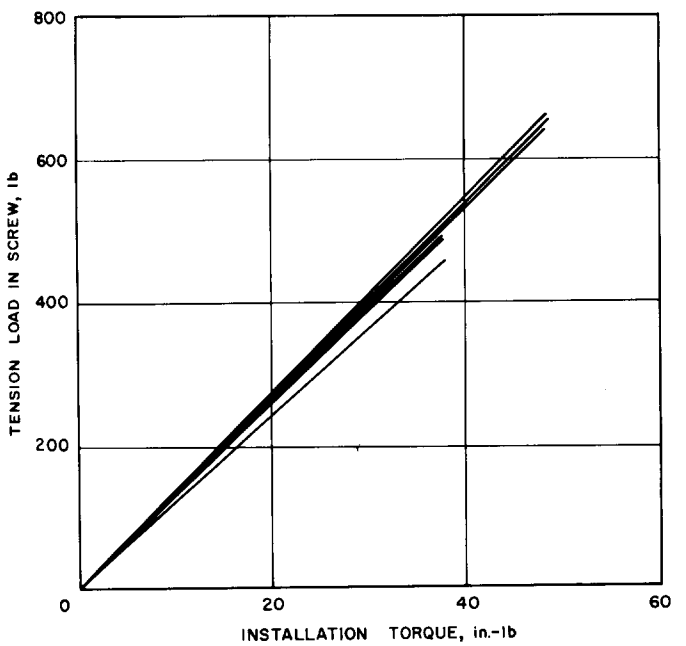

Fig. 69. Tension vs torque for titanium screws

c. Experimental evaluation of pressurized welded connections. The pressurized vernier plumbing system of the *Surveyor* spacecraft contains a number of welded connections. To demonstrate the structural adequacy of these weldments at low-temperature design extremes, pressure tests were performed on specimens designed to represent a typical joint configuration (Fig. 70). Pressurization of the test specimens (¼-in., 5/16-in., and ½-in. tubes) was accomplished using dry nitrogen gas controlled with a pressure regulator valve. For cooling purposes, the specimens with pressure line attached were placed in a wooden box lined with heat-insulating batting, and subjected to a stream of liquid nitrogen piped into the cavity. The temperature of the specimens was monitored by means of a thermocouple taped to them, and controlled by adjustment of the flow of the N_2 refrigerant.

The specimens pressurized to 2500 psig were inspected for cracks and other indications of incipient failure. Except for evidence of some yielding in the ½-in. specimens (where, at 31,000 psig of wall stress, the yield point of 5052-0 aluminum alloy had been exceeded) no damage was found.

No leakage was detected in any joint prior to rupture. All specimens tested to destruction failed by rupturing of the tube wall at acceptable pressure levels. Thus, in all thirty specimens tested there were no failures in the area of the welds, which is considered conclusive evidence of the structural adequacy of all welded connections in the vernier and attitude control systems.

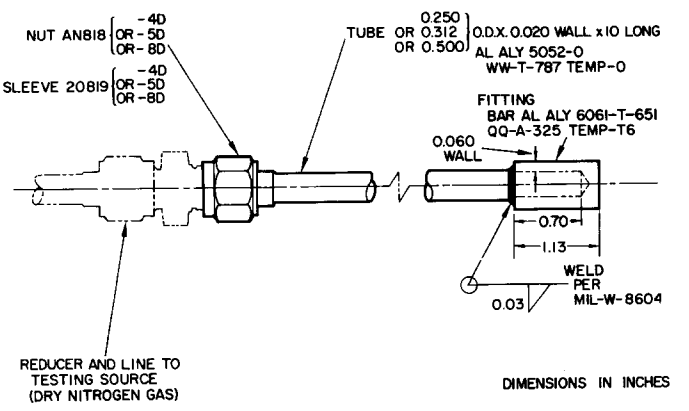

Fig. 70. Testing of typical vernier system joint specimens

M. Propulsion

The flight-acceptance main retrorocket engine fabricated in support of the SC-1 spacecraft was successfully fired on September 16 at Thiokol-Elkton. On September 29, the retrorocket engine for SC-1 (SN A-21-26) was shipped to the Air Force Eastern Test Range (AFETR). Final design, the development program, and the type-approval-test program for the A-21A retro-engine have been approved.

Because of the T-21 *Pathfinder* mission at AFETR, several changes have been made in procedures and in ground support equipment for the vernier propulsion system. Type approval tests were completed on the S-6 and S-7 vernier system test vehicles. A-21A vernier propulsion system component designs are complete and all hardware is being ordered.

1. Main Retrorocket Engine

a. A-21. The SC-1 flight-acceptance engine (A-21-25) was cut back to a propellant weight of 1238.5 lb on September 6 and was successfully fired at simulated altitude on September 16. The test data are being reduced. Engine A-21-26 was cut back on September 21 to a propellant weight of 1243.2 lb. Flight engine buyoff was conducted on September 28 and the engine was shipped to AFETR on September 29.

Flight-acceptance-test vibration of the SC-1 flight and spare safe-and-arm assemblies was conducted on September 17. Firing circuit resistances were monitored throughout the tests. No apparent changes in resistance levels were noted.

Approval to proceed with incorporation of the explosive-safe-area retro-heater assembly and the conductive mesh on the outer layer of the thermal control blanket was obtained. The mating controller will be supplied as part of the spacecraft ground support equipment. The mesh installation will consist of 304 stainless (0.003-in. diameter) wires sewn to the Teflon side of the aluminized Teflon cover with nylon thread.

The main retro-engine ignition squibs are currently undergoing flight-acceptance vibration testing.

b. A-21A. The final A-21A main retro-engine design will consist of a 6A1-4V titanium alloy case, having hemispherical dome ends joined by a 0.40-in. cylindrical section. Maximum calculated propellant loading capability is 1445 lb. The motor will be qualified for a maximum propellant loading of 1425 lb. The A-21A nozzle will incorporate a carbon-cloth phenolic rosette liner in place of the bulk-carbon phenolic material used in the A-21 design. The ignition system designed and qualified during the A-21 program will be used with no change in the A-21A retro-engine design. Similarly, no physical interface modifications are to be incorporated. The design performance levels for the A-21A retro-engine are listed in Table 34.

Table 34. A-21A main retro-engine performance

Thrust, 3σ maximum, 50°F	11,200 lb
Thrust, 3σ maximum, maximum gradient	11,500 lb
t_{3500},[a] 3σ maximum, 50°F bulk temperature	44.0 sec
Acceleration at t_{3500} + 12, maximum	6.8 ft/sec^2
Thrust, minimum	8330 lb at 32 sec 6000 lb at burnout
Total impulse variability	±0.75% of average value
Time to 3500-lb thrust	±1.0% of actual value

[a]Time from ignition until thrust drops to 3500 lb.

The A-21A retro-engine development program will consist of two nozzle over-test firings, one steel-case ballistic confirmation firing, and two prototype titanium case ballistic firings. All development firings are to be conducted at Thiokol.

The type-approval-test program will consist of four firings over the specified propellant loading range of 1370 to 1425 lb. The engines will be subjected to pre-firing sequential environmental conditions and tested at Arnold Engineering Development Center under simulated altitude conditions.

2. Vernier Propulsion System

a. A-21.

System analysis. Uncommanded thrust excursions noted during System Developmental Test S-6-055, as previously reported, were caused by free helium sucked into the propellant feed system. Studies conducted during this report period were concerned with the hydraulic characteristics of the standpipe and the effect of in-flight conditions of acceleration, temperature, and pressure on free helium ingestion.

The standpipe in each of the six propellant tanks is a ⅜-in. diameter tube in which there are sixty-four 0.030-in. diameter holes drilled to provide propellant flow from any part of the bladdered tank. Analysis and laboratory

tests have indicated that by enlarging the holes near the outlet of the standpipe helium ingestion can be minimized. Tests are being conducted to determine if helium will come out of solution and form a bubble during flight. If the tests show that helium can form a bubble, efforts will be made to redesign the standpipe to incorporate larger holes.

T-21 operations at AFETR. During the T-21 *Pathfinder* mission at AFETR, operational procedures, equipment, and techniques were demonstrated and refined. Vernier propulsion activities included:

(1) Validation of propulsion ground support equipment.

(2) Functional checkout of vernier propulsion system.

(3) Vernier propulsion system leak checks.

(4) Loading of propellants into ground support equipment.

(5) Loading of propellants into spacecraft.

(6) Demonstration of emergency abort procedures.

(7) Pressurizing helium tank.

(8) Depressurizing helium tank.

(9) Unloading of propellants from spacecraft.

(10) Deservicing ground support equipment.

As expected, several problem areas were identified and many necessary changes to procedures and techniques were discovered. All procedures were revised in preparation for use on SC-1.

System type-approval-test program. The thermal environment phase of the vernier-propulsion-system type-approval-test program was successfully completed at the Hughes Aircraft Company Placerita Canyon test facility. The S-6 test vehicle underwent a real-time simulated mission at each of the two temperature extremes of 0^{+5}_{-10} and 100^{+10}_{-5} °F. Each simulated mission consisted of a 50-sec midcourse firing and a programmed 175-sec descent firing. All firings were commanded and controlled by pre-recorded throttle-valve command tapes. Quality of data recovery was excellent and all program objectives were achieved.

The vibration environment phase of the vernier-propulsion-system type-approval test was also completed during this reporting period. The S-7 vehicle was used in this test program. This vehicle underwent vibration at flight-acceptance-test levels two times in each of three orthogonal axes and was then subjected to type-approval-test level vibration in both horizontal axes. These tests were conducted in the Hughes Aircraft Company Space Simulation Laboratory at El Segundo. The vehicle was then transferred to the JPL Edwards Test Station where it was subjected to a "hot shake" program consisting of the following tests, with live propellants and flight pressures:

(1) Simulated boost vibration at type-approval-test level.

(2) Two simulated midcourse firings without vibration.

(3) Simulated descent firing with retro vibration.

Results of the tests are being prepared.

Margin limits test program. Test plans were released for the margin limits tests to be conducted on S-6 and S-7. S-6 will undergo thermally-controlled real-time mission-cycle closed-loop firings, while S-7 will be subjected to a pressurized drop test. Refurbishment of S-6 and S-7 following type-approval tests was undertaken in preparation for the margin limits tests.

Helium tank and valve assembly. Three assemblies have failed the flight-acceptance-test post-vibration high-pressure leak test because of excessive leakage between the tank and the squib valve. One has been disassembled and is being analyzed for irregularities or defects. The other two, only slightly out of specification, are being held pending investigation of the first tank.

b. A-21A. After further consideration of the capability of the thrust chamber assembly, as well as system weight implications, it was decided not to increase the system feed pressure. Thus, the helium tank shell design has been fixed at the originally proposed 1750 in.[3]

The propellant tank has been designed for an 840-psi maximum working pressure. Modifications have been incorporated to improve bladder seal design and to provide for removal and replacement of a damaged thermal standoff without the need for disassembling the standpipe and bladder from the tank.

To facilitate production flight-acceptance testing and to reduce the severity of the environmental requirements, the helium check and relief valves have been removed from the helium tank assembly and moved to a location on the spacecraft. This eliminates the need to apply thermal paints to the relief valve, a process found to be detrimental to relief valve accuracy. This

redesign also provides a substantial decrease in the number of helium seals, facilitating assembly and improving system reliability.

Propellant line routing and configurations have been established and pressure budgets for the system analyzed, including the effects on the vernier propulsion system caused by one or two tanks running dry. When the thrust chamber assemblies are operated by feeding from tanks manifolded through the lines and anti-migration check valves, a decrease in propellant feed pressures results. Analytical studies, however, indicate that the thrust chamber assemblies will be capable of providing at least the 91-lb thrust under a combination of worst-case conditions, including 0°F propellants. It is anticipated that this thrust will be adequate during the final phase of the mission, when some of the tanks may be fully exhausted.

Analysis of the lunar dumping of residual propellants after landing has shown that contamination of the lunar surface may exceed the limits established for the alpha scattering experiment. Studies also indicate that lunar contamination by the exhaust plume of the descending spacecraft may substantially exceed the established limits. An experimental program has been initiated to evaluate the effects on the spacecraft of vapors generated during propellant dumping.

c. Thrust chamber assemblies. Thrust chamber assemblies were fired during the S-6 and S-7 vehicle test programs. Preliminary review of the data indicates that performance was satisfactory. Pre-test cold flow of the thrust chamber assemblies resulted in one unit being replaced with a spare on S-7 because of an out-of-specification mixture ratio. An additional spare was found to have a restricted oxidizer injector during cold flow testing. Both of these units are being analyzed.

d. T-2N vehicle. The vehicle propulsion system on the T-2N-1 descent test vehicle performed as required in two tether tests.

e. Ground support equipment. The set of propulsion ground support equipment used during the T-21 *Pathfinder* mission has been refurbished for use with SC-1. Some minor modifications were incorporated. In addition, the following improvements were adopted for SC-1 servicing:

(1) The method of attaching spill sleeves was changed.

(2) All ground-support-equipment quick-disconnect couplers were retrofitted to latest configuration and lubricated with Bray FX-45 lubricant.

(3) Manual shutoff valves were incorporated just upstream of each liquid quick-disconnect coupler.

(4) Spacecraft thermal finishes were protected by a layer of aluminum foil wrapped over plastic film.

All these techniques had been demonstrated satisfactorily during the S-6 type-approval-test program at the Placerita Canyon Facility and the S-7 type-approval-test program at the JPL Edwards Test Station. The latter program utilized the second set of operational ground support equipment.

3. Predicted Dissolved Helium Gas Levels in Propellants with Use of a Teflon–Aluminum-Foil Laminate Bladder[5]

a. Summary. An analysis of the Teflon–aluminum-foil laminate bladder (TFE/aluminum/FEP)[6] proposed for use in the A-21A *Surveyor* vernier feed system is presented. This analysis is based on data from bladder tests performed by Hughes Aircraft Company (HAC).

With use of this bladder on A-21A, the maximum expected helium concentration level in the oxidizer just prior to main-retro ignition under worst pre-launch conditions should be no greater than 45% of the full feed pressure saturated condition. The minimum predicted helium concentration level in the oxidizer under ideal pre-launch conditions should be about 21% of the full feed pressure saturated level.

This analysis indicates that for a 66-hr A-21A mission under worst pre-launch conditions the potential SC-1 problem of helium gas ingestion, due to sizable bubble formations in the bladders, will not exist when the oxidizer temperature remains above 20°F. Helium gas ingestion will be completely eliminated over the entire allowable temperature range (0–100°F) for propellants pressurized with 150-psia nitrogen for as long as two weeks prior to launch.

Calculations of the vernier-engine dynamic performance, operating at low thrust levels with high oxidizer temperatures (100°F), indicate, for worst pre-launch conditions, only slight improvement over predicted SC-1 performance under the same low thrust and high oxidizer temperature conditions. However, under more desirable pre-launch conditions (150-psia nitrogen pressurization)

[5]Prepared by JPL Technical Section 384.

[6]Laminations of tetrofluoroethylene, aluminum foil, and fluorinated ethylene propylene.

a significant improvement in engine dynamic performance is predicted. Also, helium-line freeze-up due to oxidizer vapors permeating the bladder may remain a potential problem.

b. Introduction. It is recognized that helium permeates the present Teflon laminate bladders (TFE/FEP)[7] of the *Surveyor* spacecraft vernier fuel and oxidizer feed system at rates such that the oxidizer is fully saturated after about 20 hr under any pressurization level. Such concentration levels are undesirable: (1) because of vernier-engine dynamic performance degradation at low thrust level operation, and (2) because of the potential problem of helium bubbles forming in the bladders due to oxidizer temperature or pressure reductions, causing uncontrolled thrust excursions when the bubbles are ingested into the engines. The present bladder is also permeable to oxidizer vapors. These vapors will diffuse into and saturate the helium manifold space. During a *Surveyor* mission the temperature of some parts of the helium manifolds is expected to be −100°F or lower. The freezing temperature of the oxidizer is −14°F. It is therefore presently feared that oxidizer vapors will condense and then freeze-up the helium pressurization lines.

An aluminum-foil laminate bladder (TFE/aluminum/FEP) has been proposed for use on A-21A. Tests performed with this bladder material by HAC indicate that the helium permeability is approximately only 1½% of that of the present bladders. However, if sufficient time exists, the oxidizer under pressure will approach the saturation level and the new bladders with reduced permeability will be little or no improvement over those employed on SC-1.

The permeability data for this bladder material were obtained after a 20-hr test. The concentration of helium dissolved at the end of this period was only about 4% of full saturation; however, it is possible that the permeability rate is actually lower than estimated here. Dissolved gas could be present in the oxidizer prior to the test due to oxidizer transfer operations or exposure to the atmosphere. It is possible that gas dissolved in the propellants prior to the permeability test could account for much of the apparent permeability of the foil bladder material, since the analysis for dissolved gas did not identify helium specifically.

The purpose of this study is to investigate the expected concentration levels of helium in the oxidizer at the end of various pressurization time intervals, and estimate the mass of oxidizer which can be transported to the helium manifold space. The analysis presented here assumes that the concentration rates measured are due directly to the foil material permeability. However, it is recognized that the actual permeability of the foil laminate bladder may be less than assumed in this analysis.

c. Analysis. Calculations based on the data obtained by HAC were made on the assumption that the oxidizer diffusive resistance is so small that the helium concentration within the oxidizer is substantially uniform at any instant. This can be stated mathematically as

$$U(C_0 - C) = \beta \frac{dC}{dt} \tag{1}$$

where U = overall bladder resistance which is related directly to the permeation constant, C_0 = saturated concentration level, C = instantaneous concentration level, β = oxidizer capacitance which is constant for any operating pressure and temperature, and t = time. This simplification is justified when the permeation resistance is so large compared to the internal diffusive resistance of the oxidizer that it controls the diffusion process.

The solution to Eq. (1) is

$$\frac{C - C_0}{C_i - C_0} = \epsilon^{-\frac{U}{\beta}t} \tag{2}$$

where C_i = initial concentration level at time $t = 0$.

Table 35 shows an extraction of the pertinent Hughes Aircraft Company bladder sample test data. Because the bladder-sample-area-to-oxidizer-volume ratio was different for the test setup than for the actual situation, the test storage time was adjusted to what it would have been had the test been conducted with the use of an actual bladder.

A plot of predicted concentration percentage versus time for the present SC-1 bladder is shown in Fig. 71. This curve was obtained by fitting the adjusted data in Row 1 of Table 35 to Eq. (2). Actual HAC tank-bladder storage test data of the present bladder are shown in Table 36. These data were averaged and are shown plotted in Fig. 71 for comparison. The permeability constant used to describe this curve was altered to include a 98.5% reduction in permeability constant for the proposed bladder. This reduction was determined by fitting the averaged data of Rows 3 and 4 of Table 35 to Eq. (2) and comparing the U/β with that previously calculated. The

[7]Laminations of tetrafluoroethylene and fluorinated ethylene propylene.

Table 35. Extracted HAC test results of small bladder samples separating oxidizer from gas

Material	Duration, hr	Corrected duration, hr	Temperature, °F	Weight of gas in solution, lb	Pressurizing gas
1. Present bladder (TFE/FEP)	4	2.8	48	37×10^{-6}	Helium
2. Present bladder (TFE/FEP)	20	14	48	79×10^{-6}	↓
3. Proposed bladder (TFE/aluminum/FEP)	20	14	49	2×10^{-6}	
4. Proposed bladder (TFE/aluminum/FEP)	18.8	11.2	53	3.8×10^{-6}	↓
5.[a] Present bladder (TFE/FEP)	20	14	74	147×10^{-6}	Nitrogen

[a]Average of four tests.
NOTE:
On a volumetric basis the permeability of nitrogen is about 10% of that of helium.

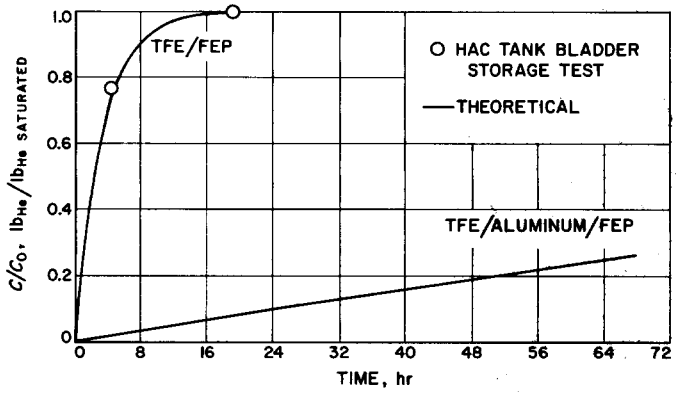

Fig. 71. Helium concentration in oxidizer vs time

result of this reduction with the oxidizer capacitance unchanged is also shown in Fig. 71.

Because it is possible that the propellants may be pressurized to 300 psia for as long as two weeks prior to launch, significant helium concentration levels are likely to exist before the propellants are fully pressurized for a *Surveyor* midcourse maneuver. Table 37 shows the expected helium concentration percentages an instant prior to final descent ignition using the proposed aluminum-foil laminate bladder. Different intervals of time during which the propellants may be required to sit under pad pressure were included in the calculations.

The results shown in Table 37 indicate that for a 66-hr *Surveyor* mission, the oxidizer, just prior to final descent ignition, will never be less than about 21% of the full-saturated condition. The maximum expected helium concentration level for a two-week period under a 300-psia pad pressure is 45% of the fully-saturated condition. With the pad pressure reduced to 150 psia the calculated maximum helium concentration level for a two-week pre-launch period under pad pressure is reduced to 33%. However, with 150-psia nitrogen pad pressurization for a two-week pre-launch period under pad pressure, the maximum expected concentration level will be about 25%.

Table 36. Extracted HAC data of *Surveyor* oxidizer tank pressurized storage tests to determine helium permeation through the bladder

Material	Weight of oxygen loaded into tanks, lb	Storage time, hr	Storage pressure, psia	Propellant temperature, °F	Weight of helium permeated through bladder, lb
Present bladder (TFE/FEP)	30.71	19.3	815	60	4.58×10^{-3}
↓	31.07	19.3	815	60	4.87×10^{-3}
	30.95	19.3	815	60	4.85×10^{-3}
	30.71	22.3	815	55	4.37×10^{-3}
	31.07	22.3	815	55	4.51×10^{-3}
	30.95	22.3	815	55	4.54×10^{-3}
	30.71	4.1	815	60	3.54×10^{-3}
	31.07	4.1	815	60	3.59×10^{-3}
	30.95	4.1	815	60	3.84×10^{-3}

Table 37. Calculated helium concentrations in oxidizer for a 66-hr *Surveyor* mission using the TFE/aluminum/FEP bladder

Time under pad pressure, hr[a]	Pressurizing gas and level, psia	$(C/C_0)_{720}$[b] due to time under pad pressure, %	$(C/C_0)_{720}$[b] due to time under previous pad pressure and 50-hr full pressure (approx. 720 psia) between midcourse and final descent, %
18	Helium, 300	3	22
168 (1 wk)	Helium, 300	22	37
336 (2 wk)	Helium, 300	32	45
18	Helium, 150	1.5	21
168 (1 wk)	Helium, 150	11	27
336 (2 wk)	Helium, 150	16	33
336 (2 wk)	Nitrogen, 150	~6 equivalent volumetric helium concentration %	25

[a]Includes 16 hr of flight time prior to midcourse maneuver.
[b]$(C/C_0)_{720}$ = 720 − psia saturation level.

Calculations of vernier-engine phase lag and gain attenuation based on a previously developed model (*SPS 37-35*, Vol. I, pp. 72–77) of engines using helium-saturated propellants using the equation

$$\frac{\Delta\,(\text{thrust})}{\Delta\,(\text{thrust command})} = \frac{\tau_1 S + 1}{\tau_2 S + 1} \qquad (3)$$

are shown (Table 38) for the maximum helium concentration level (45%) and the expected maximum level (25%) when nitrogen pressurization is used prior to launch.

Preliminary oxidizer vapor permeation rate data only of the TFE/FEP bladder have been obtained by HAC. Using N_2O_4 instead of MON-10 it was determined that about 3 mg of N_2O_4 vapor permeated a square inch of the TFE/FEP bladder per hour under standard temperature and pressure conditions. If it can be assumed that the permeation rate of oxidizer vapor is reduced by 98.5% for the TFE/aluminum/FEP bladders as was reduced for the helium, then the permeation rate of vapor for this bladder would be approximately 45 μg of vapor per square inch per hour. Even at this apparently low rate the helium line space will become saturated within less than two days. Because of the expected low temperatures on some parts of the helium lines it is inevitable that the vapor will condense. If this condensate were then to freeze out at one location, there would be enough oxidizer in the helium manifolds to freeze solid no less than a 2-in. section of the line. If this condition were to occur during the early part of the mission, it is conceivable that 6 to 8 in. of helium line could be frozen at main-retro ignition.

d. Conclusions. From the foregoing analysis it is definitely concluded that helium bubble ingestion will not be a problem with use of the TFE/aluminum/FEP bladder and nitrogen pad pressurization.

The dynamic performance of the vernier engines should be significantly improved with use of the proposed bladder and 150-psia nitrogen pad pressurization. This improvement, however, may be considerably better than shown in Table 38. More carefully controlled permeation tests of the TFE/aluminum/FEP bladders should provide accurate data from which a more realistic analysis can be made.

Oxidizer vapor freeze-up in the helium lines may remain a problem with use of the TFE/aluminum/FEP bladders. Representative tests will soon be conducted by JPL at Edwards Air Force Base using the TFE/FEP bladders to help determine the severity of this problem.

Table 38. Phase lag and gain attenuation calculations

Material	Pressurant	Pad pressure, psia	Time under pad pressure, hr	720-psia full saturation at final descent ignition, %	Phase lag for 100°F oxidizer at 5 cps, deg	Gain attenuation for 100°F oxidizer at 5 cps, db
Present bladder (TFE/FEP)	Helium	300	0+	100	25	−8.9
Proposed bladder (TFE/aluminum/FEP)	Helium	300	336	45	29	−7.9
Proposed bladder (TFE/aluminum/FEP)	Nitrogen	150	336	25	31	−3.5

4. *Vernier Propulsion Subsystem Testing at JPL*[8]

Work was continued at JPL on the program to perform limited environmental tests of selected upstream components for the purpose of evaluating, on an independent basis, the capability of these components to meet the *Surveyor* requirements.

The second component to be evaluated under this program is the helium relief valve. The purpose of these valves in the vernier propulsion subsystem is to prevent overpressurization of the propellant tanks in the event of a malfunction of regulator lock-up.

The original valve used in the system was one designed and manufactured for the Hughes Aircraft Company by the M.C. Manufacturing Corporation. Early in the development of this valve, design problems were encountered in the sealing of the valve at low temperatures. The original design used a butyl O-ring seal, but due to compatibility problems with the propellant vapors, a Teflon "Balseal" was incorporated. However, the use of the Teflon seal caused difficulty in assembly, since the seal had to be stretched during installation on the piston. The stretching deformed the seal and resulted in excessive leakage.

To solve the immediate need of flight hardware, a back-up design was produced for Hughes Aircraft Company by Carleton Controls Corporation using a bellows seal. Although this back-up unit functions acceptably, this valve design is more complex, heavier, and costlier than the M. C. Manufacturing Corporation unit. The M. C. Corporation relief valve (M.C. part No. 6031) is simpler and appears inherently more reliable if the leakage problem can be solved. Therefore a program was initiated at JPL to make changes to the piston design to eliminate the stretching of the Teflon seal and to demonstrate the suitability of the modified valve for *Surveyor* requirements.

Two M. C. Manufacturing Corporation valves were acquired from Hughes Aircraft Company for evaluation. One unit, SN-105, was subjected to testing in the "as-received" condition for reference purposes and the second valve, SN-106, in the modified version (with redesigned piston).

The scope of testing basically followed the Hughes Aircraft Company Approval Test Specification 262695. This sequence, which was modified to test the known problem areas first, is shown below.

Test No.	Description
1	Proof pressure
2	Leakage
3	Cracking pressure
4	Reseat
5	Leakage
6	Low temperature
6.1	Leakage at low temperature
6.2	Cracking at low temperature
6.3	Reseat at low temperature
7.0	High temperature
7.1	Leakage at high temperature
7.2	Cracking at high temperature
7.3	Reseat at high temperature
8.0	Functional
8.1	Cracking pressure
8.2	Capacity
8.3	Reseat
8.4	Response
9.0	Vibration
9.1	Leakage
9.2	Functional
10.0	Endurance
11.0	Leakage
12.0	Oxidizer compatibility

Valve SN-105 was started first through the test program per the sequence listed above. The initial test results were satisfactory except for the low reseat setting of this valve. The setting was 760 psig instead of the 800-psig minimum allowed by specification. This setting is adjustable, but was not readjusted for this particular valve.

A structural fatigue failure occurred at the fitting end of the valve during the high-temperature (100°F) cycling test. An ensuing investigation attributed the failure to poor body design in the area where the end thread relief interfaced with the body, forming an extremely sharp corner creating a stress riser. Due to the failure no further testing was accomplished on this valve. This body design must be modified before the valve type could be employed for flight use.

The modified valve, SN-106, followed the previous one into testing per the same sequence. Prior to this formal testing, however, the modified valve was cycled 1000 times

[8]Prepared by JPL Technical Section 384.

using the original piston to "wear-in" the Teflon seal, which had a leakage greater than the specification value. This cycling reduced the leakage to an acceptable value.

During the formal testing the valve passed all leakage tests with the exception of the post-vibration test, where the leakage was 1.3×10^{-3} standard cm³/sec of helium. The specification for this valve allows 0.28×10^{-3} standard cm³/sec leakage. Since subsequent leak checks were within tolerance, it was suspected that this failure was caused by some particulate matter in the test system that prevented complete closing of the valve. From the results of the tests conducted on this second valve, it appears that the modified-design two-piece piston apparently eliminated the piston seal leakage problem.

The crack and reseat pressures were within specification except after the high-temperature tests, where the reseat pressures were 5 psig below the specification limit. The initial setting of the valve was made at the mid-range of the pressure tolerance (830 psig). It is believed that had the initial settings been made 10 psig greater, the reseat pressure following high-temperature exposure would have met the specified values.

The valve response as defined by the specification was satisfactory. In every test the maximum upstream pressure was maintained below the required 900 psig during venting.

During each test the valve capacity was greater than the minimum acceptable value of 25 standard ft³/min. The average tested capacity was 78 standard ft³/min, indicating that adequate margin exists.

As an additional test the modified valve is to be given an exposure to oxidizer vapors to verify propellant compatibility. Results of these tests will be reported as data become available.

On the basis of the limited testing conducted to date, the M. C. Manufacturing Corporation helium relief valve appears to be able to meet the requirements of the *Surveyor* vernier propulsion system provided that relatively simple modifications are incorporated to prevent stretching of the Teflon "Balseal."

5. Thrust Chamber Assembly[9]

As a part of a continuing evaluation of the *Surveyor* vernier engines (RMD Model No. TD-339), five tests were performed at JPL Edwards Test Station during September and October. The tests are arranged in groups according to test goals.

Group	Test No.	Test date	Purpose
12	DY-77	9-1	Pre-chilled molybdenum-wrought nozzle extension tests
13	DY-78 and -79	10-1 to 10-6	Effect of saturated propellants on maximum thrust capability
14	DD-111 and -112	8-27 and 10-14	Cold-hard vacuum start tests

a. Group 12. This group of tests is intended to determine the suitability of the flight-type stress-relieved wrought-molybdenum nozzle material when test-fired after having been pre-chilled to successively lower temperatures.

The second test (DY-77) of this group was performed on September 1. (The first test was reported in *SPS* 37-35, Vol. I, pp. 79–80). The nozzle was pre-chilled to 0°F prior to the firing. The test duration was about 10 sec, at which time the engine was shut down as a result of a chamber pressure tap burnout. Subsequently, fuel leaked from the engine, reacted with peroxide from the Hyprox System and detonated (causing some damage to facility items). This engine (SN-05) has had a long history of firings prior to this test and can be considered to have passed its normal life expectancy. The wrought nozzle and the thrust chamber and injector assembly were undamaged by the detonation.

Additional testing of the wrought nozzle was suspended because of higher priority work at Edwards Test Station. The possibility of welding closed the chamber pressure tap and continuing the wrought nozzle evaluation will be considered at a later date.

b. Group 13. This group consisted of two tests performed with the SN-535 thrust chamber assembly (TCA) to determine any change in maximum thrust which might result from helium dissolved in the propellants. In both tests the firings were to be conducted at the minimum inlet pressures (about 686 psia) prescribed by the Hughes

[9]Prepared by JPL Technical Section 384.

Aircraft Company Interface Document No. 287015 and with nominally 100°F propellants. One test was to be conducted with minimum dissolved gas, the second test with maximum helium saturation. The firing profile for both tests involved steady operation at a nominal +80 Δma throttle valve setting.

The tests were successfully conducted during the first week in October. Inlet pressures were within 4 psi of the prescribed values and the command current was +79 Δma. Propellant temperatures were 82°F in Test DY-78 and 93°F in Test DY-79. The measured uncorrected thrust levels for the two runs were 103.8 and 103.6 lb, respectively. Correcting for the inlet pressure and temperature deviations to the worst-case specification conditions resulted in thrusts of 103.7 and 103.8 lb. Further correction to +80 Δma gave final levels of 104.0 and 104.2 lb for Tests DY-78 and -79, respectively.

The data indicate that helium dissolved in the propellants does not appreciably affect the maximum thrust capability of the RMD engine. These corrected maximum thrust data compare closely with the thrust of 104.5 lb predicted by RMD under worst-case specification inlet conditions at +80 Δma.

c. Group 14. This group of tests was to be performed with SN-07 TCA to demonstrate start characteristics in a cold, hard-vacuum environment. The test plan called for firings in a vacuum of about 10^{-5} torr and with propellants and TCA conditioned to as low as 0°F. This is representative of the environment to which the spacecraft Leg 2 engine may be exposed.

A special vacuum chamber was developed for maintaining the hard vacuum on the TCA (mounted within the chamber) during the ignition phase. This chamber was equipped with connections for a diffusion pump, ion gage, propellant lines, electrical leads, etc., and a special closure which falls away when the pressure within the chamber exceeds the external pressure. By mounting this special piece of test equipment within the Hyprox Facility, ignition at ultra-high-vacuum conditions, followed by about 5 sec of operation under the standard Hyprox vacuum, could be attained.

The first test (DD-111) was successfully accomplished on August 27. The start was made in a vacuum of 3.1×10^{-5} torr and with propellants conditioned to about 50°F. Ignition lag and start transient characteristics were comparable to that demonstrated by flight-type engine SN-538 in previous Tests DY-70 to -75 at a simulated altitude of about 120,000 ft (3.5 torr) (*SPS 37-34*, Vol I, p. 91 and *SPS 37-35*, Vol. I, pp. 79–80).

The second test (DD-112) was successfully performed on October 14. The start was made in a vacuum of 2.0×10^{-4} torr with propellants conditioned to about 20°F. The ignition lag was about 15 to 20 msec longer than that obtained in the prior test with 50°F propellants. Considerable difficulty has been experienced in maintaining a completely leak-tight system with cold propellants in the hard-vacuum environment. However, a third and final test is planned with propellants conditioned to 0°F.

N. Spaceflight Operations[10]

This article covers *Surveyor* Mission A spaceflight operations activities for the period September 1 through October 31.

1. Documentation

Surveyor documentation continues to be updated and published in accordance with existing *Surveyor* planning, and revision and expansion of *Surveyor* documentation is now being planned in terms of the recently revised launch schedule.

The revised test plan for the Spaceflight Operations Facility/Air Force Eastern Test Range (SFOF/AFETR) Compatibility (B-2.0) Test was completed during October and is scheduled for publication on November 15.

2. Surveyor Computer Program Development Status

Current user program development continues to lag behind the scheduled level of completion, specifically in the area of program certification. Efforts are continuing to bring the required number of programs for Mission A up to a status wherein they can be certified.

a. Flight Path Analysis and Command (FPAC). FPAC programs certified during the month of October were the Tracking Data Processor and Orbit Data Generator.

[10]Prepared by JPL Technical Section 316.

The Trajectory Program and Orbit Determination Program are currently being certified and may be bought off as operational and frozen by November 1.

A study comparing the output of the various FPAC programs has been initiated. Preliminary results show some discrepancies.

FPAC will extend its present capability to include Mode IV operation in computing orbits and transmitting predicts from the SFOF data processing system.

b. Spacecraft Performance Analysis and Command (SPAC). Power-thermal acceptance testing in accordance with the Program Test Specification was performed on September 2; the Attitude Determination Program was performed on July 22 and July 30. Test results are being studied and certification is expected shortly. Engineering data reduction has had major operational problems, but it is expected that the problems will be resolved in the near future.

c. Mission support/Space Science Analysis and Command (SSAC). The only problem with the Mission Support Programs which affects Mission A is the teletype telemetry processing in the IBM 7044. Work is underway to correct this problem.

The Command Verify/Transmit (CVT) Program has been certified for the prepare to transmit, display, and verify options. *Surveyor* command preparation (SCP) preliminary certification has been performed. A minor correction is to be made to the program and the SCP Program will be re-certified on November 11. TV command certification was performed on October 15.

3. Mission Operations Test Activity

The spacecraft/DSIF[11]-11/SFOF/Compatibility Tests (B-1.1) were completed during the week of September 10.

The Spacecraft/DSIF-51/SFOF Compatibility Tests were begun on September 20 and concluded during the first week of October. Spacecraft/DSIF-42/SFOF/ Compatibility Tests were also begun in early October and concluded during the week of October 15. Three special *Surveyor* Deep Space Network (DSN)/T-21 Interface Tests were also run on October 2, 5, and 8. Due to rescheduling of the *Surveyor* Mission A launch date, a revised test schedule was drafted wherein the remainder of the Mission B tests (the SFOF/AFETR Compatibility (B-2.0) and the TV Ground Data Handling System (B-3.0) were extended.) The SFO/DSN/AFETR Operational (Class C) Tests were also re-scheduled.

A number of SFOF/DSIF Program Integration Tests, as well as SFOF User Program Integration Tests were run during September and October.

As a result of the major redefinition of *Surveyor* Space Flight Operations System command procedure for Mission A, the following SPAC, SSAC, and Mission Support programs were transferred to a Mission B requirements status: Thermal Management, Power Management, TV/ ID Response Monitor, TV Command Generation, SCP Command Preparation, and CVT.

4. Surveyor FPAC Mission Operations Activity

a. Test activity. A number of FPAC Integration Tests run during September and October were provided with limited, but adequate FPAC support.

A test plan was drafted which defines and describes an additional FPAC A-1.2 test at the SFOF, for the purpose of verifying that the non-standard data processing system configuration and operations are feasible.

The FPAC Group rendered assistance to the Data Simulation Group of Mission Operations in preparing messages to interface AFETR and FPAC in the SFOF/ AFETR Compatibility Test Plan.

b. Documentation. Operational issues of the FPAC Orbit Determination, Computer Support, Trajectory, and Maneuver Analysis Detailed Operating Procedures were submitted for publication on September 20.

Revisions and corrections to the Space Flight Operations Plan, EPD[12]-180, Rev. 4, (including the Standard Sequence of Events) are currently being assembled by FPAC for publication of EPD-180, Rev. 5, scheduled for November 20.

5. Surveyor SPAC Mission Operations Activity

a. SFOF test activities. The complete SPAC Team participated in the T-21/DSIF-11/SFOF Compatibility (B-1.4) Test on September 8, 10, 14, and 16, and the special *Surveyor* DSN Interface Tests, again with T-21, on October 2, 5, and 8.

[11]DSIF—Deep Space Instrumentation Facility.

[12]EPD—Engineering Planning Document.

A reduced SPAC Team supported the Spacecraft/DSIF-11/SFOF Compatibility Test (B-1.1) on September 3, the Spacecraft/DSIF-51/SFOF Compatibility Tests on September 21 and 29, and the Spacecraft/DSIF-42/SFOF Compatibility Tests (B-1.3) on October 11 and 14.

In addition to the above scheduled tests, SPAC representative participated as Bus Chief in the special series of T-21/DSIF/SFOF Training Tests held on September 21, 27, 28, 29, and 30 and October 1.

b. Documentation. A number of updates and additions were submitted for approval and publication in the SFOF Detailed Operating Procedures (EPD-239). A number of non-standard operating procedures were also updated and submitted for approval. Specification 288143 on the "Command Sequence Glossary" for the *Surveyor* Command Preparation Program, and Command and Data Handling Console (CDC) Command Tape preparation (SC-1) was released on September 28.

c. CDC command tapes. The SPAC Group supplied a CDC Command Tape for the DSN/T-21 Interface Tests which were run during this reporting period.

d. General. The preliminary SPAC display requirement for SC-5 was prepared. Formulation of the standard command sequence for EPD-180, Rev. 5, was begun in mid-October.

6. Surveyor SSAC Mission Operations Activity

SSAC participated in the B-1.4 and the T-21/SFOF Compatibility Tests during the TV Functional Tests of September 15, 17, 25 and October 5. During these tests T-21 was used as the data source at Goldstone with the available ground support system utilized as it would be during a mission. Camera surveys were directed by SSAC from the SFOF using both punched tape and manual keyboard CDC command entry modes. Most of the basic SSAC test objectives of camera control were accomplished, although TV/ID had to be obtained by voice and in only a few cases was adequate video available in the SFOF.

Three T-21 Mission Sequence Interface Tests were conducted by the Space Flight Operations Director during October. SSAC provided support during the post-landing lunar phase by conducting a simulated TV sequence in narrow-band, simulated integrate modes under lunar night conditions. Valuable experience was obtained in exercising the interfaces with Mission Control, SPAC, and the DSIF *Surveyor* operations chief.

SSAC operations training was also carried out with SFOF exercises on TV survey sequences which simulated the lunar night mission as defined for Mission A. This training utilized the Hughes Aircraft Company prototype camera in the narrow-band (200 line), integrate mode at low lighting levels. On October 28 punched tape camera surveys were run where, for the first time, the PDP-1 computer program successfully provided TV/ID on the high-speed printer.

7. Surveyor Data Simulation

During the months of September and October, simulation data packages were supplied to support a variety of scheduled tests conducted in the SFOF, DSIF sites, and the AFETR. The data packages to support the Class B tests were developed and shipped to the required overseas sites. In addition, the telemetry tapes for the Class C tests were completed well ahead of schedule. The study effort, initiated prior to this reporting period, was supported during this period for the purpose of developing the simulation requirements for Missions E through G. Because of the complexity of this program it is indicated that this effort will be continuing for quite some time.

References

1. Davis, L., Meredith, C., and Ribarich, J., *Midcourse and Terminal Guidance Operations Programs,* SSD 4051R, Hughes Aircraft Company, Culver City, California, April 1964.

2. *AC-6 Firing Tables (Rev. 1),* BTDG5-04, General Dynamics/Convair, San Diego, California, July 6, 1965.

References (Cont'd)

3. *Surveyor Spacecraft Monthly Performance Assessment Report,* SSD 5397R, Hughes Aircraft Company, Culver City, California, August 21, 1965.

4. *Centaur Monthly Configuration, Performance, and Weight Status Report (U),* 63-0495-27, General Dynamics/Convair, San Diego, California, August 21, 1965.

5. "Intensity, Magnitude and Spacecraft Coordinates of Earth and Moon for Mission A," *Space Programs Summary No. 37-35,* Vol. I, Jet Propulsion Laboratory, Pasadena, California, September 30, 1965 (Confidential).

6. *Space Flight Operations Plan,* Engineering Planning Document 180, Jet Propulsion Laboratory, Pasadena, California, July 12, 1965.

7. "Antenna Radiation Measurements," *Space Programs Summary No. 37-35,* Vol. II, Jet Propulsion Laboratory, Pasadena, California, September 30, 1965.

8. Collin, R. F., *Field Theory of Guided Waves,* Chapter 11, McGraw-Hill Book Co., New York, N.Y., 1960.

9. Attwood, S. S., "Surface-Wave Propagation over a Coated Plane Conductor," *Journal of Applied Physics,* Vol. 22, No. 4, pp. 504–509, April 1951.

10. Jasik, H., *Antenna Engineering Handbook,* pp. 16–20, 16–21, McGraw-Hill Book Co., New York, N.Y., 1961.